Rapid Prototyping by Single Point Incremental Forming of Sheet Metal

Skjødt, Martin

Publication date:
2008

Document Version
Publisher's PDF, also known as Version of record

Rapid Prototyping by Single Point Incremental Forming of Sheet Metal

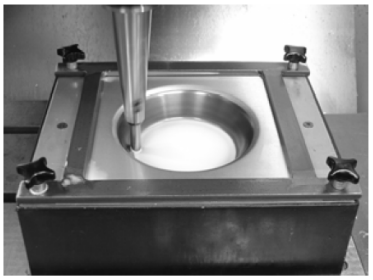

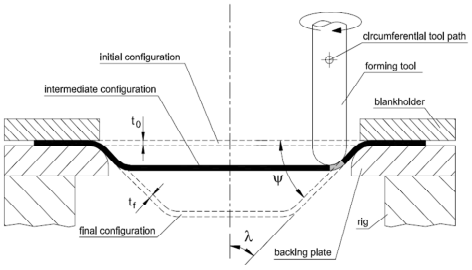

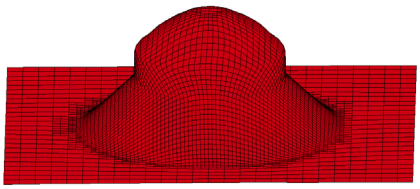

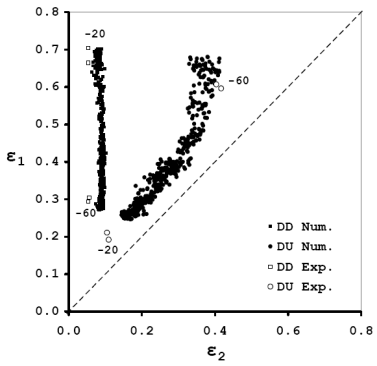

2008 PhD Project
by
Martin Skjødt

ISBN 978-87-89502-81-6

DTU Mechanical Engineering
Department of Mechanical Engineering

Papers included in the thesis

1) Creating helical tool paths for single point incremental forming, p. 55-64
M. Skjoedt, M. H. Hancock and N. Bay
SheMet 2007, 12th Int. Conf. on Sheet Metal, Palermo, Italy, Apr. 1-4, (2007)
Key Engineering Materials, vol. 344, p. 583-590

2) Single point incremental forming using a dummy sheet, p. 65-76
M. Skjoedt, M. B. Silva, N. Bay, P. A. F. Martins, T. Lenau
2nd ICNFT, 2nd Int. Conf. on New Forming Technologies
Bremen, Germany, Sep. 20-21, (2007)
Conference proceedings, BIAS-Verlag, p. 267-276

3) Estampagem incremental de 'tailored blanks', p. 77-93
M.B. Silva, M. Skjoedt, L.M. Alves, P. Vilaça, N. Bay, P.A.F. Martins
27o SENAFOR, 10a Conferencia Nacional de Conformaçao de Chapas
Porto Alegre, Brazil, Oct. 18-19, (2007)
Conference proceedings, p. 239-253

4) Revisiting the fundamentals of single point incremental forming by means of membrane analysis, p. 95-107
M.B. Silva, M. Skjoedt, N. Bay, P.A.F. Martins
International Journal of Machine Tools and Manufacture, (2008), vol. 48, p. 73-83

5) Single-point incremental forming & formability-failure diagrams, p. 109-131
M.B. Silva, M. Skjoedt, A.G. Atkins, N. Bay, P.A.F. Martins
The Journal of Strain Analysis, (2008), vol. 43, p. 15-35

6) Single point incremental forming of tailored blanks produced by friction stir welding, p. 133-162
M.B. Silva, M. Skjoedt, P. Vilaça, N. Bay, P.A.F. Martins
Journal of Materials Processing Technology, (2008), accepted for publication

7) Theory of single point incremental forming, p. 163-170
P.A.F. Martins, N. Bay, M. Skjoedt, M.B. Silva
CIRP Annals - Manufacturing Technology, (2008), vol. 57, p. 247-252

8) Multi stage strategies for single point incremental forming of a cup, p. 171-176
M. Skjoedt, N. Bay, B. Endelt, G. Ingarao
ESAFORM 2008, 11th Conf. on Material Forming, Lyon, France, Apr. 23-25, (2008)
International Journal of Material Forming, (2008), Springer/ESAFORM 2008

9) Strain paths and fracture in multi stage single point incremental forming, p. 177-184
M. Skjoedt, M.B. Silva, P.A.F. Martins, N. Bay
ICTP 2008, 9th Int. Conf. on Technology of Plasticity, Gyeongju, Korea, Sep. 7-11, (2008)
Conference proceedings, accepted

1 Preface

This thesis is the documentation of the PhD project *Rapid Prototyping by Single Point Incremental Forming of Sheet Metal* at Department of Mechanical Engineering, Technical University of Denmark.

The project was conducted from September 2005 to August 2008 by s973685 MSc Martin Skjødt (M. Skjoedt). Supervision of the project was done by Professor Niels Bay and Associate Professor Torben Anker Lenau.

I would like to thank all the different people involved with this project. My supervisors for always having confidence in me, being there when I needed help and giving me a lot of freedom. My fellow PhD students: Dr. Mike Halloway Hancock, MSc Morten Jerne Borrild and MSc Kasper Leth Friis for keeping me company and contributing to discussions regarding science and the life as a PhD student at this department.

I would also like to thank Professor Paulo Martins and MSc Beastriz Silva for welcoming me at Instituto Superior Technico (IST) in Lissabon, providing excellent guidance and making the four month stay such a nice experience. The collaboration between our department and IST has been very fruitful in terms of science and personal relations. The stay at IST was only possible thanks to financial support from: Otto Mønsteds Fond, Oticon Fonden and Augustinus Fonden, and for this support on short notice I am very grateful.

Also I would like to thank Professor Joachim Danckert and the Department of Production at Aalborg University for hosting me during the startup of my finite element (FE) simulation. I am also grateful to Professor Fabrizio Micari and the Department of Manufacturing and Management Engineering at University of Palermo for sharing their knowledge on FE simulation of SPIF.

Thanks also go to the students Peter Søe Nielsen and Benjamin Hald. I had the pleasure of supervising them in two projects and both of them contributed to my understanding of SPIF.

The thesis is based on papers and divided into three parts: 1) about SPIF in general, formability and numerical simulation, 2) summery of the papers, suggestions for future work and a conclusion, 3) reprint of all the papers. Some of the papers contain more than one page number and the one in the middle refers to this thesis. Before each paper a joint author statement is included. Original statements signed by all authors have been given to the PhD administration. The paper written in Portuguese is included as documentation only. A PDF file of this thesis can be downloaded at www.student.dtu.dk/~mask/thesis.pdf.

Now when twilight dims the sky above,
Recalling thrills of our love,
There's one thing I'm certain of:
Return I will
To old Brazil.
Aquarela do Brasil (Ary Barroso / S.K. Russell)

Date: 3/9 - 2008

martin_skjoedt@yahoo.dk

2 Abstracts

2.1 English abstract

Single Point Incremental Forming (SPIF) is a sheet forming process with a simple setup. The forming tool is a rod with a spherical end and the sheet is mounted in a rig which allows forming of the sheet into the cavity of the rig. SPIF is dieless forming since no dedicated dies are being used.

The process is incremental forming since plastic deformation takes place in a small local zone underneath the forming tool, i.e. the sheet is formed as a summation of the movement of the local plastic zone. The process is slow and therefore only suited for prototypes or small batch production. On the other hand it allows high strain compared to normal sheet forming processes, cheap tooling and a short product lead time.

The work in this project can be divided into the following topics all containing novel contributions to the science of SPIF:

Tool path generation in SPIF. A program has been developed which transforms a profile tool path into a helical tool path. This is an advantage since using a profile tool path results in scaring of the finished part and peaks in vertical forming force. The use of a helical tool path eliminates these problems.

SPIF using a dummy sheet. This is a new variant of SPIF which has been invented in this project. Two sheets are formed at the same time instead of one. The top sheet is just a dummy and protects the bottom sheet from the sliding of the forming tool. The use of a dummy sheet setup eliminates wear, increases surface roughness, improves visual appearance and only causes a small reduction in formability. This setup also allows forming of soft aluminium sheets without damage to the sheet surface.

Theory of SPIF and prediction of formability. Using membrane equilibrium equations a set of formulas have been developed for calculating principal stresses in the plastic zone. Using these it is demonstrated that the growth rate of accumulated damage in SPIF is small compared to conventional sheet forming processes. This combined with an explanation why necking is suppressed is a new theory stating that SPIF is limited by fracture and not necking. The theory explains a lot of experimental observation seen in the literature.

SPIF of tailored blanks produced by friction stir welding. It is demonstrated that SPIF of tailored sheets produced by friction stir welding is possible and a promising way of combining two innovative manufacturing processes.

Multi stage SPIF. A multi stage strategy is presented which allows forming of a cup with vertical sides in about half of the depth. It is demonstrated that this results in strain paths which are far from straight, but strains are still limited by a straight fracture line in the principal strain space. The multi stage process has been simulated and good correlation is found between simulated and experimental results.

2.2 Danish abstract

Single Point Incremental Forming (SPIF) er en pladeformgivningsproces med en simpel opsætning. Formgivningsværktøjet er en stang med en kugleformet ende og pladen er monteret i en holder som muliggør formgivning af pladen ned i holderens hulrum. SPIF er formfri formgivning, da der ikke bruges dedikerede forme til processen.

Processen er *incremental,* da den plastiske formgivning kun finder sted i et lille område under formgivningsværktøjet, dvs. pladen formgives som en summation af bevægelsen af det lokale plastiske område. Proccessen er langsom og derfor kun egnet til prototyper eller småserieproduktion. På den anden side tillader den store tøjninger sammenlignet med traditionel pladeformgivning, billige værktøjer og kort tid fra ide til produkt (*product lead time*).

Arbejdet i dette projekt kan inddeles i følgende emner, som alle indeholder nye bidrag til videnskaben indenfor SPIF:

Generering af værktøjsbaner til SPIF. Et program er udviklet, som transformerer en *profile* værktøjsbane til en *helical* værktøjsbane. Dette er en fordel, da brug af *profile* baner resulterer i et ar på den færdige del og spidsbelastninger i den lodrette proceskraft. Brugen af en *helical* bane fjerner disse problemer.

SPIF med brug af en dummy plade. Dette er en ny variant af SPIF, som er blevet opfundet i dette projekt. To plader formgives på samme tid istedet for en. Den øverste plade er bare en *dummy* og den beskytter den nederste plade mod gnidning fra formgivningsværktøj. Brugen af en *dummy* plader fjerner slid, øger overfladeruheden, forbedrer udseendet og sænker kun formbarheden en smule. En *dummy* plade muliggør også formgivning af bløde aluminiumsplader uden at overfladen på disse ødelægges.

SPIF teori og forudsigelse af formbarhed. Med brug af membranligevægtsligninger er der opstillet en række formler til udregning af hovedspændingerne den plastiske zone. Med brug af disse formler er det vist at vækstraten af akkumuleret *damage* i SPIF er lille i forhold til traditionel pladeformgivning. Dette, kombineret med en forklaring på hvorfor dannelse af indsnøringer er hæmmet, er samlet en teori, som siger at SPIF udelukkende er begrænset af brud og ikke indsnøring. Teorien forklarer mange af de eksperimentielle observationer i litteraturen.

SPIF af skræddersyet plader fremstillet med friction stir welding. Det er vist, at det er muligt at formgive skræddersyet plader fremstillet med *friction stir welding* ved brug af SPIF. Dette er en lovende kombination af to innovative fremstillingsprocesser.

Flertrins SPIF. En flertrins strategi er præsenteret, som muliggør formgivning af en kop med lodrette sider i ca. halvdelen af koppens dybde. Det er vist, at dette resulterer i en tøjningsvej som langt fra er lige, men tøjninger er stadig begrænset af en ret linie i hovedtøjningsrummet. Flertrins processen er nummerisk simuleret, og der er god overensstemmelse mellem simuleringer og eksperimenter.

3 Nomenclature

The nomenclature list below is only for the first two parts of thesis since the last part consists of papers which have different nomenclatures.

Symbol	Typical unit	Explanation
Stresses		
σ	MPa	True stress
$\bar{\sigma}$	MPa	Equivalent stress
$\sigma_1 > \sigma_2 > \sigma_3$	MPa	Principal stresses
σ_m	MPa	Hydrostatic stress / average principal stress
σ_{yield}	MPa	Yield stress / flow stress
σ_x	MPa	Stress in the direction of x
σ_y	MPa	Stress in the direction of y (yield stress in Table 3)
x		Ratio between stresses in the direction y and x
σ_t	MPa	Stress in thickness direction
σ_θ	MPa	Stress in circumferential direction
σ_ϕ	MPa	Stress in meridional direction
Strains		
ε		Logarithmic strain / true strain
$\bar{\varepsilon}$		Equivalent strain / effective strain
$\varepsilon_1 > \varepsilon_2 > \varepsilon_3$		Principal strains
ε_t		Strain in thickness direction
ε_θ		Strain in circumferential direction
ε_ϕ		Strain in meridional direction
$\bar{\varepsilon}_{diffuse}$		Equivalent strain at diffuse necking / diffuse instability
$\varepsilon_{x,diffuse}$		Strain in the direction of x at diffuse necking
$\varepsilon_{y,diffuse}$		Strain in the direction of y at diffuse necking
$\bar{\varepsilon}_{local}$		Equivalent strain at local necking / local instability
$\varepsilon_{x,local}$		Strain in the direction of x at local necking
$\varepsilon_{y,local}$		Strain in the direction of y at local necking

q		Value where a straight line crosses the ε_1 axis in the principal strain space / minus value of constant thickness strain for a straight line in the principal strain space with slope -1

Geometry

t	mm	Sheet thickness
t_0	mm	Initial sheet thickness
t_f	mm	Final sheet thickness / thickness after completion of forming
l_0	mm	Initial length
l_f	mm	Final length
ψ	degrees	Drawing angle / angle between formed side and flat configuration (90° is vertical)
λ	degrees	Angle between formed side and vertical ($\lambda = 90^\circ - \psi$)
ϕ	degrees	Angle between direction of local instability and tensile stress
r_{tool}	mm	Radius of forming tool
ΔZ	mm	Vertical distance between tool path contours
L_s	mm	Characteristic length of a shell element in FE simulation

Material

E	MPa	Elasticity modulus / youngs modulus
ρ	ton/mm^3	Mass density
υ		Poissons ratio
n		Strain hardening exponent in Hollomons expression
C	MPa	Strength coefficient in Hollomons expression
R		Normal anisotropi
D_c		Critical damage value

Time related

c	mm/s	Speed of sound
Δt	s	Time step in FE simulation

4 SPIF – Single Point Incremental Forming

4.1 Basics

SPIF is a sheet forming process and the setup is very simple. The forming tool is a rod with a spherical end. The sheet is mounted in a rig which allows forming of the sheet into the cavity of the rig. Beneath the sheet a backing plate can be used to get a clear definition of the transition between the flange part and the formed part, Fig. 1 and Fig. 2. SPIF is also called a dieless forming process since all information about the geometry comes from the path of the forming tool. In other words no dedicated dies are being used. Typical values for the main parameters in SPIF can be seen in Table 1.

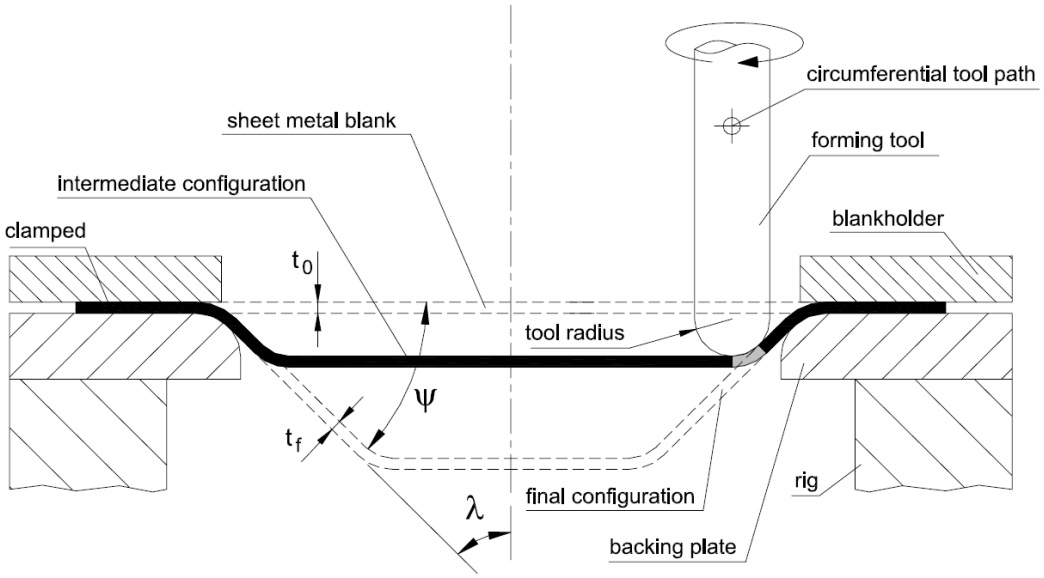

Fig. 1 Schematic presentation of SPIF

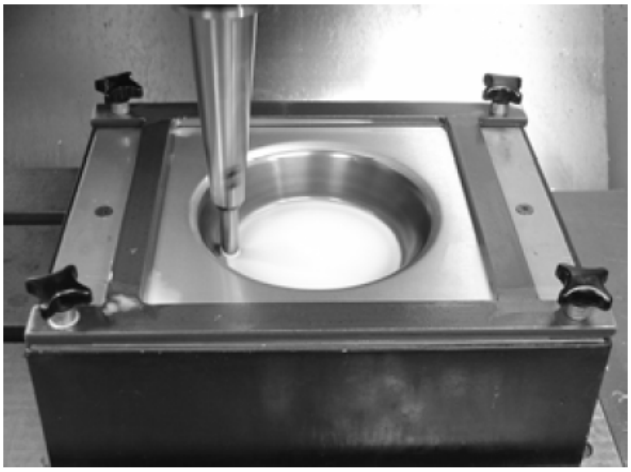

Fig. 2 Basic configuration of SPIF: rig, backing plate, sheet and forming tool

Forming tool radius	r_{tool}	5 – 15 mm
Initial sheet thickness	t_0	0.5 – 3 mm
Vertical step size	ΔZ	0.1 – 2 mm
Maximum drawing angle	$\psi_{\max}$	60-80°
Sheet material		Steel or aluminum
Forming speed		500 – 2000 mm/min
Forming time		30 – 60 min
Geometrical tolerances		± 0.5 - 2 mm
Equivalent strain values	$\bar{\varepsilon}$	0 - 2.5
Process forces:		300 – 1000 N vertical 100 – 500 N horizontal
Relations:		r_{tool} / t_0 ~ 5 – 20 Depth of part >> r_{tool} Radius of part >> r_{tool}

Table 1 Typical values in one stage SPIF

The influence of the main parameters on formability has been investigated by a lot of researchers. Conclusions are not consistent, except regarding the influence of tool size. However, the results lean towards the following relations: increasing sheet thickness, decreasing tool size and decreasing vertical step size all tend to increase formability. A possible explanation why results seem to vary is that the parameter ranges investigated are different. Also the possible presence of interactions between parameters will cause confusion if this is not included in the analysis. Only large variations of friction influence formability, i.e. when comparing forming with and without lubricant. Table 2 gives a short overview of the influence of various parameters on formality in SPIF as reported in literature.

$\uparrow t_0$ (intial thickness)	→	$\uparrow \psi_{\max}$ [1,2] /$\downarrow \psi_{\max}$ [3]
$\downarrow r_{tool}$ (tool radius)	→	$\uparrow \psi_{\max}$ [1,3,4]
$\downarrow \Delta Z$ (vertical step size)	→	$\uparrow \psi_{\max}$ [3,5] / None[1]
↓ forming speed	→	$\uparrow \psi_{\max}$ [1]
↑ tool rotational speed	→	$\uparrow \psi_{\max}$ [1]
↓ friction	→	$\uparrow \psi_{\max}$ [6]

Table 2 Influence on maximum drawing angle from process parameters

4.2 History

The history of SPIF begins in 1967 when Leszak obtained the patent: *Apparatus and Process for Incremental Dieless Forming* [7]. The idea was ahead of its time and the research did not start until the 1990s where research was primarily carried out on rotational symmetric geometries which could be formed on a turning machine. Most of the research toke place in Japan and some of the leading persons in the research were: Kitazawa [8], Iseki [9] and Matsubara [10].

In 2001 the use of an ordinary 3-axis CNC milling machine for SPIF of non rotational symmetrical components was introduced [11,12]. Before that only dedicated CNC machines

were being used for SPIF. This was the starting point for research outside of Japan. Some of the most active researchers since then have been Jeswiet [12], Hirt [13], Micari [5], Duflou [14] and Allwood [15].

SPIF is just one out of a group of processes called Incremental Sheet Forming (ISF). The different processes have a lot of similarities and the literature is often a mix of different variations. SPIF is the truly dieless version without any support under the sheet. Two point incremental forming (TPIF) has a partial or a full die.

4.3 Strains

Plotting measured strains in SPIF of different geometries in the principal strain space reveals that most strain values are in the stretching region, although exceptions do exist [16]. It is furthermore clear that the majority of measured strain values are close to plane strain [17]. A typical exception to this is sharp corners where the corner radius is limited by the radius of the forming tool.

Measuring the limiting strains for SPIF a number of researchers have independently found that the strains seem to be limited by a straight line having a slope around -1 in the principal strain space [9,11,17], Fig. 3. Intuition supports this since a line with the slope of -1 is the line of constant thickness strain. In other words defining the limit strains by this line is the same as stating that the thickness of the sheet can only be reduced until a certain value as seen in (1) to (4).

$$\varepsilon_1 = -\varepsilon_2 + q \tag{1}$$

$$\varepsilon_1 + \varepsilon_2 = q \tag{2}$$

$$\varepsilon_3 = \varepsilon_t = -q \tag{3}$$

$$t_f = \frac{t_0}{e^q} \tag{4}$$

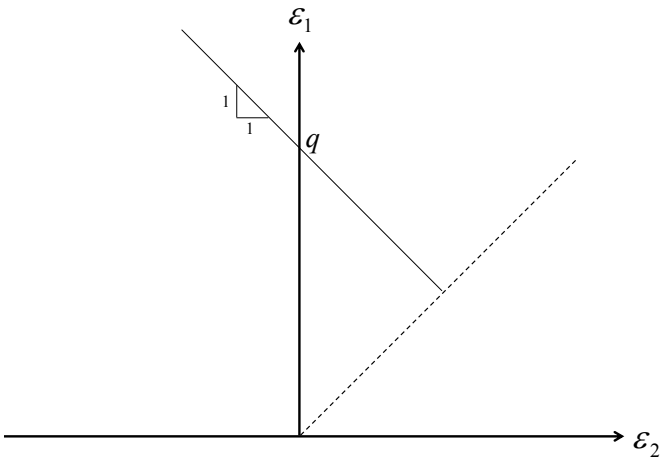

Fig. 3 Line with a slope of -1 in the principal strain space

4.4 The sine-law

The sine-law is a geometrical consequence of plane strain deformation and volume constancy. It was initially stated for shear spinning, but proved also to be valid in most cases of SPIF [18]. It relates initial thickness t_0 with thickness after forming t_f, Fig. 4 and (5) to (9).

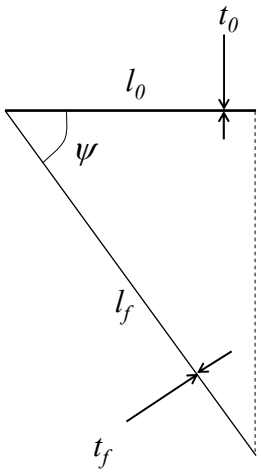

Fig. 4 Illustration of the sine-law

$$l_f = \frac{l_0}{\cos\psi} \tag{5}$$

$$\varepsilon_\phi = \ln\left(\frac{l_f}{l_0}\right) = \ln\left(\frac{1}{\cos\psi}\right) \tag{6}$$

$$\varepsilon_t = -\varepsilon_\phi \tag{7}$$

$$\varepsilon_t = \ln\left(\frac{t_f}{t_0}\right) = -\ln\left(\frac{1}{\cos\psi}\right) \tag{8}$$

$$t_f = t_0 \cdot \cos\psi = t_0 \cdot \sin(90^o - \psi) \tag{9}$$

The sine-law explains why high drawing angles approaching 90° can never be realized with one stage SPIF which is normally close to plane strain for the majority of the part. As ψ approaches 90° the strains goes towards infinity.

Assuming that ε_ϕ can be calculated as above and also assuming equal biaxial stretching, a similar law can be calculated for the case of equal biaxial stretching, (10) to (13).

$$\varepsilon_\phi = \varepsilon_\theta \tag{10}$$

$$\varepsilon_t = -2 \cdot \varepsilon_\phi \tag{11}$$

$$\varepsilon_t = -2 \cdot \ln\left(\frac{1}{\cos\psi}\right) \tag{12}$$

$$t_f = t_0 \cdot (\cos\psi)^2 \tag{13}$$

4.5 Deformation Type

Even though SPIF has been the subject of research for a number of years the type of deformation is yet to be identified with certainty. The two extremes in the ongoing discussion in literature are: 1) pure stretching with some bending at the edges and 2) pure vertical shear [19], Fig. 5. Another question in the discussion is whether a significant amount of through thickness shear is present [15].

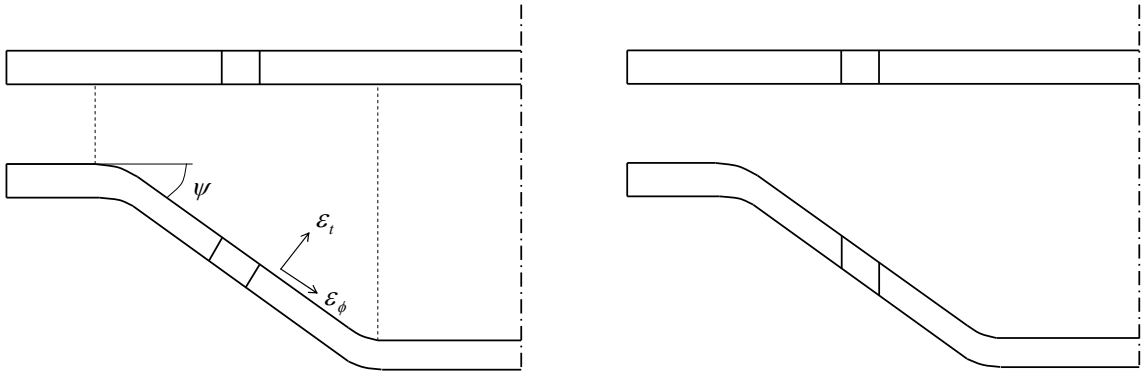

Fig. 5 Left: illustration of pure stretch, right: pure vertical shear

A good example why understanding the type of deformation is important is when measuring the strains. This is often done by applying a grid on the surface of the undeformed sheet and measuring the deformed grid after deformation. Using this procedure it is assumed that the strains measured provide two of the principal strains. This is the same as assuming the thickness strain to be a principal strain. This however is only the case for pure stretching. For vertical shear the strains found from a surface grid will not be the principal strains [19].

4.6 Stresses

Stresses are almost impossible to measure in SPIF, and this is the reason why literature only contains a small amount on this subject. Forces have been measured [14,20] but converting these into stresses is not easy. This would require information on the size of the contact area, and even this is difficult to get. Most information on stresses comes from simulation and comparisons with similar processes. In general it can be said that the state of stress in SPIF is still an open question.

Ambrogio et al. [21] used implicit simulation and found a compressive mean stress around 200 MPa in the area under the tool and a maximum principal stress of 100-250 MPa in the part wall close to the tool. The tool radius used was 6 mm and the sheet material was AA 1050 O.

4.7 Applications

SPIF can be classified as a rapid prototyping manufacturing process since no dedicated die is needed and the time from idea to final part can be less than 24 hours. It can also be classified as a layered technology process since the part is formed in layers by the tool path. The high machining time excludes SPIF as a mass production technology, but the low start up costs makes it suitable for one-of or small batch production. The price of producing a part with SPIF is difficult to estimate, but it is in many cases higher than initially guessed. The part must be created in a CAD system and a tool path must be generated in a CAM system. For a skilled technician this will take 2-5 hours depending on the complexity of the part. Including setup, occupation of a CNC machine about three hours is realistic and this will also include wages for a technician to operate the machine. In total a price of a SPIF part can easily reach 300-1000 €. This excludes a lot of trivial uses for normal consumers, such as customized dog bowls and sinks. In short the product segment for SPIF can be categorized as: high value - low volume [22].

In the medico industry the price of equipment and material can often be considered low compared to prices of wages for doctors and other medical related costs. The human body is a good example of a complicated one-of "product" and custom manufactured parts to fit a specific person is an area where SPIF has a large potential. Tanaka et al. [23] showed this by using SPIF instead of casting to produce a denture plate out of titanium sheet, Fig. 6. Verbert et al. [24] used multi stage SPIF to produce a titanium skull implant, Fig. 7.

Fig. 6 Incrementally formed denture plate in titanium [23]

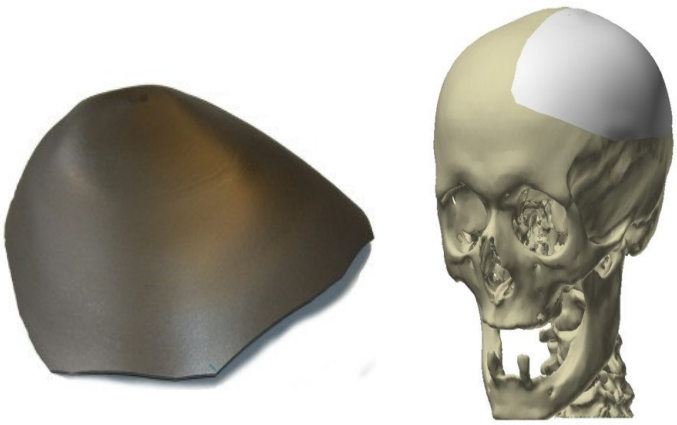

Fig. 7 Titanium skull implant made by multi stage SPIF [24]

A structured search for applications has been done by Allwood et al. [22]. A total of 28 existing sheet metal products are compared with economical and technological capabilities of incremental sheet forming. Geometrical tolerance is identified as the most critical parameter. Out of 28 possible applications only two have tolerance demands wide enough for the 2 mm tolerance limit estimated for incremental sheet forming, Fig. 8.

Thickness tolerance is not included in the work. All parts formed with SPIF have very poor thickness tolerances. A 60° cone formed out of a 1 mm sheet has a side thickness of about 0.5 mm but the undeformed bottom of the part is still 1 mm. The thickness tolerance for this example is 0.75 mm ± 0.25 mm.

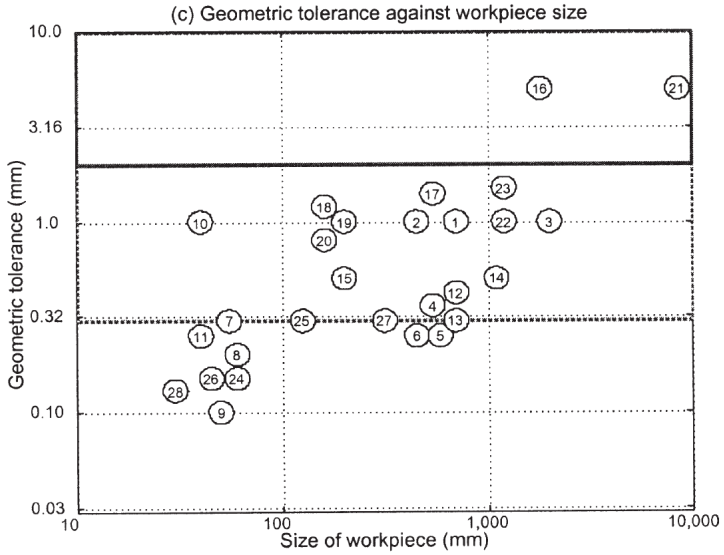

Fig. 8 Tolerances for 28 possible applications of ISF, limit for ISF is set to 2 mm [22]

Another possible application for SPIF is production of dies and moulds for polymer and metal forming, and this application has been investigated by Allwood et al. [25]. The geometry formed by SPIF is only intended as the surface of the die or mould and back support is needed behind the sheet. This could be concrete, sand or any other substance which can be poured into a mould. Allwood successfully produced a male and female die using this technique and used them to form a sheet metal part, Fig. 9.

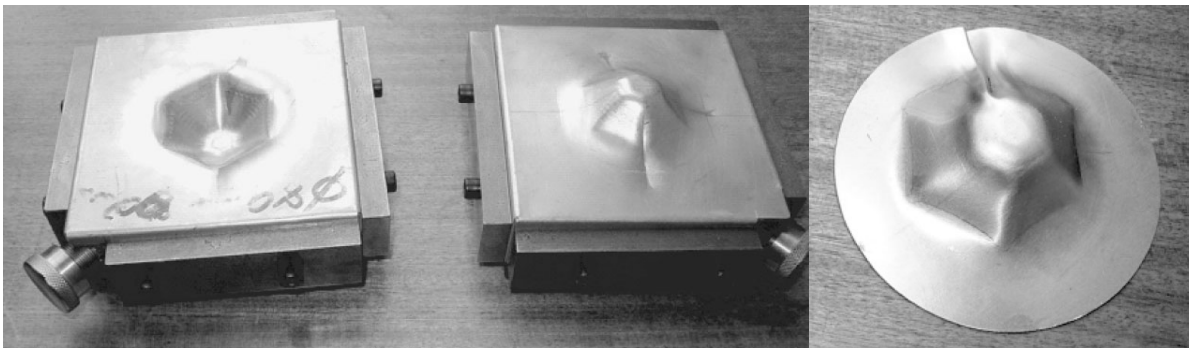

Fig. 9 Left: male and female die made with SPIF, right: part produced with dies [25]

Jeswiet et al. investigated using SPIF for production of prototypes for the automotive industry. A prototype of a manifold heat shield [17] and a headlight reflector [26] were successfully produced, Fig. 10 and Fig. 11.

Fig. 10 Left: original manifold heat shield, right: prototype produced by SPIF [17]

Fig. 11 Left: prototype of headlight reflector, right: reflector after surface treatment [26]

5 Formability in sheet forming

5.1 Classical instability theories in sheet forming

The present chapter is based on [27,28]. Instability theories in sheet forming typically deal with two types of instability or necking: diffuse and local. The two types of instability can be seen in a tensile test of a metal strip, Fig. 12. Instability occurs when strain hardening of the material can no longer out balance the reduction in cross sectional area. After this point deformation is no longer homogenous, but concentrated in a small zone in the work piece. All further deformation will happen within this zone.

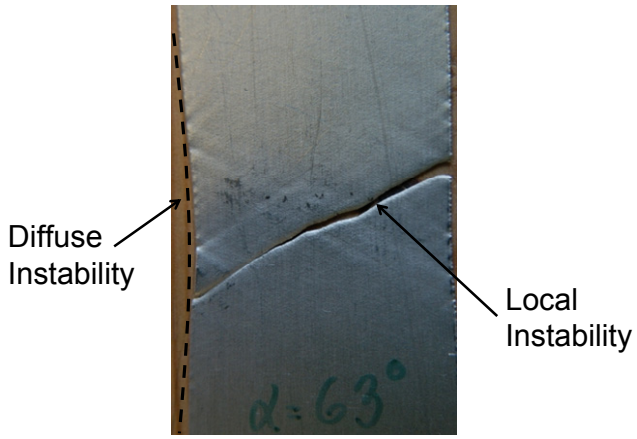

Fig. 12 Diffuse and local instability in tensile test of an aluminium strip

Diffuse instability occurs before local and causes a gradual reduction in thickness in the instability zone. At some point a local instability is formed within the diffuse instability zone. The local instability zone has a width in the same order of magnitude as the strip thickness. Deformation in the local instability zone can be considered plane strain since no deformation occurs in the longitudinal direction of the zone due to surrounding material which is now rigid.

In the following sections material is assumed to be isotropic (14) and following the Hollomon expression for yield stress (15).

$$R = 1 \tag{14}$$

$$\sigma_{yield} = C\bar{\varepsilon}^{n} \tag{15}$$

5.2 The Swift criterion for diffuse instability

The Swift instability criterion can be described as the point in a tensile test where further deformation can occur without increasing the load. This follows the intuition of an unstable situation where deformation is continuing although the load is constant or decreasing.

A small sheet work piece is loaded in biaxial stress in two directions x and y in the plane of the sheet which are also the principal directions for stresses and strains, Fig. 13.

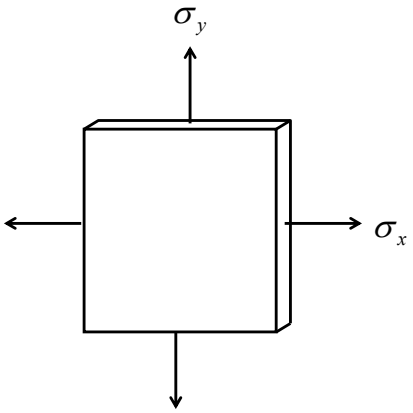

Fig. 13 Small sheet element loaded in two directions

In this situation the Swift criterion can be expressed as:

$$d(\sigma_x A_x) = 0 \tag{16}$$

Using the assumptions (14) and (15) together with von Mises yield criterion and the Levy-Mises flow rule the following expression for the effective strain when diffuse instability occurs can be derived from (16):

$$\bar{\varepsilon}_{diffuse} = n \cdot \frac{4(1 - x + x^2)^{\frac{3}{2}}}{4 - 3x - 3x^2 + 4x^3} \tag{17}$$

In (17) x is the ratio between the principal stresses:

$$x = \frac{\sigma_y}{\sigma_x} \tag{18}$$

For a uniaxial tensile test in the direction of σ_x the stress ratio x is equal to zero which results in an effective diffuse instability strain equal to n. The strains in the principal directions in the plane of the sheet can be calculated as seen in (19) and (20). Fig. 14 shows the Swift criterion for diffuse instability for $n = 0.25$ in the principal strain space.

$$\varepsilon_{x,diffuse} = \frac{2 - x}{2\sqrt{1 - x + x^2}} \cdot \bar{\varepsilon}_{diffuse} \tag{19}$$

$$\varepsilon_{y,diffuse} = \frac{2x - 1}{2\sqrt{1 - x + x^2}} \cdot \bar{\varepsilon}_{diffuse} \tag{20}$$

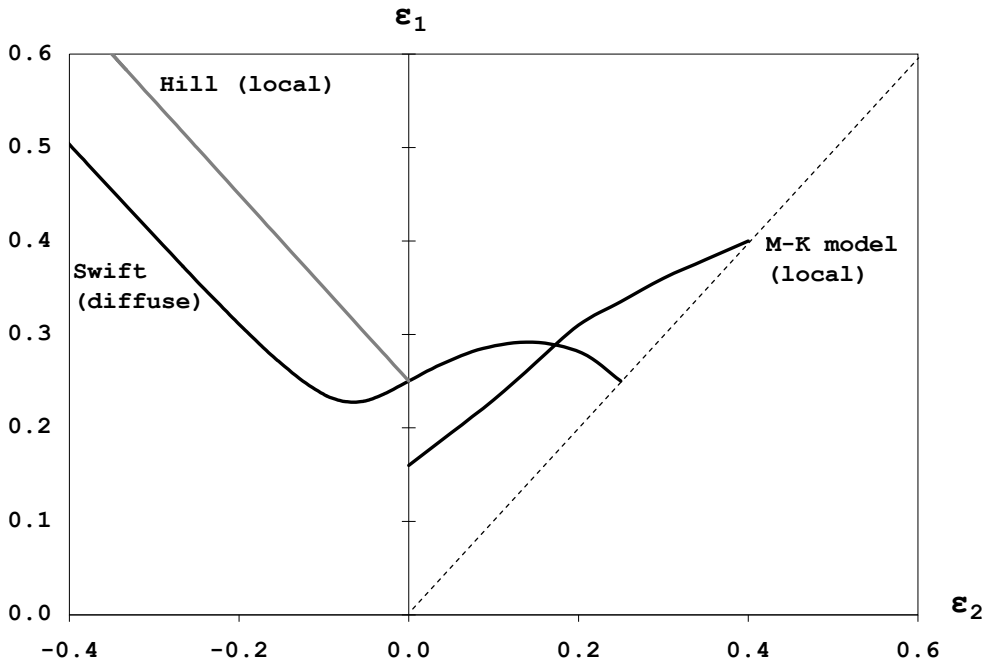

Fig. 14 The Swift and Hill criteria for instability and the M-K model

5.3 The Hill criterion for localized instability

Fig. 15 shows the formation of a localized instability zone within the diffuse instability zone. The width of the zone is of the same order of size as the thickness. The condition for a local instability to appear is that the strain in the longitudinal direction of the instability zone is zero as expressed in (21).

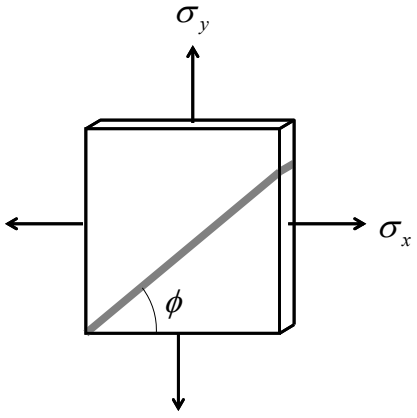

Fig. 15 Formation of a localized instability zone

$$0 = \varepsilon_x \cos^2 \phi + \varepsilon_y \sin^2 \phi \tag{21}$$

(21) can also be expressed as the following equations:

$$\tan^2 \phi = -\frac{\varepsilon_x}{\varepsilon_y} \tag{22}$$

$$\tan^2 \phi = \frac{x-2}{2x-1} \tag{23}$$

For a uniaxial tensile test x is equal to zero which results in a localized instability forming an angle of 55° to the direction of tension. From (22) and (23) it is clear that the right hand side of the equation must remain positive to get a solution. This means that a local instability can only form in the drawing section of the principal strain space where ε_2 is negative. The right hand side of equation (23) is only positive for stress ratios lower than 0.5. This means that for stress ratios higher than 0.5 only diffuse instability will form. For stress ratios lower than 0.5, diffuse instability will occur followed by a local instability.

A localized instability is formed when the increase in stress due to strain hardening perpendicular to the direction of the localized instability is balanced out by the decrease in cross sectional area of the local instability. This is called the Hill criterion and can be expressed as (24), which leads to (25). For a uniaxial tensile test in the direction of σ_x the effective local instability strain will be equal to $2n$. The strains in the principal directions can be calculated using (26) and (27). The Hill criterion can be seen in Fig. 14 for n = 0.25.

$$d(\sigma_{\phi+\pi/2} A_\phi) = 0 \tag{24}$$

$$\bar{\varepsilon}_{local} = n \cdot \frac{2\sqrt{1-x+x^2}}{1+x} \tag{25}$$

$$\varepsilon_{x,local} = \frac{2-x}{2\sqrt{1-x+x^2}} \cdot \bar{\varepsilon}_{local} \tag{26}$$

$$\varepsilon_{y,local} = \frac{2x-1}{2\sqrt{1-x+x^2}} \cdot \bar{\varepsilon}_{local} \tag{27}$$

5.4 The Marciniak Kucynski model for local instability

According to the Hill criterion a local instability will never appear for positive strain ratios, which is the right hand side of principal strain space. This is not in agreement with the model put forward by Marciniak and Kucynski (M-K model) which describes the limit for local instability for positive strain ratios.

The M-K model is more complicated than the Hill criterion and the formulas will not be given here. The model assumes that a sheet material will always have some degree of inhomogeneity in the form of local areas with a thickness lower than the surrounding sheet material.

Fig. 14 shows the M-K model for an inhomogeneity factor of 0.98, n = 0.25 and a strain increment of 0.0001. For plane strain the M-K limit is much lower than the Swift limit, but for equal biaxial stretching it is the opposite.

5.5 Terminology

The curve formed by combining the Hill criterion in the drawing region and the Swift criterion in the stretching region is often called the forming limit curve (FLC) or instability curve and the diagram is called a forming limit diagram (FLD). An FLC can also be a curve fitted to experimental values for necking. In general the terms FLC and FLD are used for theoretical or experimental curves for the necking limit in the principal strain space.

A fundamental and sometimes overlooked assumption which needs to be fulfilled in order to use the curves for necking as displayed in Fig. 14 is that the strain path must be straight. If this is not the case the theoretical limits for necking are of little value [29]. Measuring strain with a grid applied on the sheet surface will provide strain values in the plane of the sheet. There is no guarantee that these strains are principal strains and this measuring technique does not provide information about the strain path.

To use strains from a grid analysis in combination with the theoretical instability limits it must first be verified or assumed that the thickness strain is a principal strain and that the strain path is linear.

5.6 Fracture forming limit curves

Fracture forming limit curves (FFLC) are normally more associated with bulk forming than sheet forming. As a result diagrams showing an FLC and an FFLC at the same time are rare. Another reason is that most sheet forming processes are limited by necking and the increase in strain within the neck until fracture is therefore of little interest. Fig. 16 shows measured strain values for necking and fracture. The necking strains are similar to the theoretical curve for diffuse necking in the stretching area and the curve for local necking in the drawing area. The FFLC is seen to be much higher than the FLC, but as seen in Fig. 17 this is not always the case.

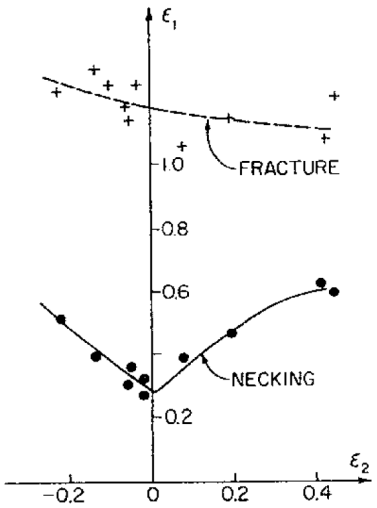

Fig. 16 Experimental strains for necking and fracture in stretch forming of fine-grained aluminium [29]

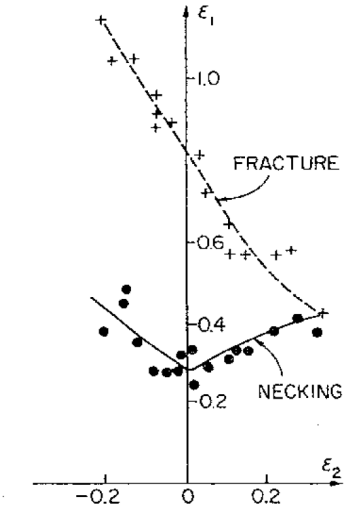

Fig. 17 Experimental strains for necking and fracture in stretch forming of aluminium 5154-O [29]

5.7 Experimental values for necking and fracture

Experimental values for necking and fracture can be obtained using the same experiments. Bulge-testing is used for values in the stretching region and tensile tests are used for values in the drawing region.

For diffuse necking the strains are measured outside the necking region to get the limit for this type of necking. Since all deformation occurs within the diffuse necking zone after formation, the measured values will be the strain values just before diffuse necking. For local necking the strain is measured inside the diffuse necking zone but outside the local neck. Since all deformation occurs within the local necking zone after its formation, these strain values will be the strain values just before local necking.

Fracture strains are measured as close to the fracture as possible. The thickness strain is measured at the edge of the crack. A second principal strain is measured as the change of width in the direction of the local neck, i.e. comparing initial length in this direction of the undeformed strip with the length of the local neck after fracture.

6 Increased formability in SPIF

It is commonly accepted that the formability of SPIF is much higher than traditional sheet forming processes [18], but the reason or reasons for this is far from agreed upon. The present state of the research – without including the findings of this project – offers the following very different explanations:

1) Through thickness shear (Allwood et al.)
2) Serrated strain paths (Eyckens et al.)
3) Bending under tension (Emmens et al.)
4) Compressive mean stress, small strain increment and low maximum principal stress (Micari)

6.1 Through thickness shear

Allwood et al. [15] used a forming tool shaped as a paddle to create a process with features similar to SPIF, i.e. small contact area and repeated contacts between tool and sheet. Experiments showed that the paddle increases formability about 35% compared with a rotational symmetric punch of the same shape. The paddle process was simulated using ABAQUS/explicit and five solid elements in thickness. The simulation demonstrated through thickness shear. An extension of the M-K model was developed to include the influence from through thickness shear in a process having proportional loading. The resulting surface strains at instability increased with increasing through thickness shear, Fig. 18. Using a grid on the upper and lower surface, experiments confirmed the presence of through thickness shear in forming of a truncated pyramid. The experiments also indicated that the deformation was not vertical shear.

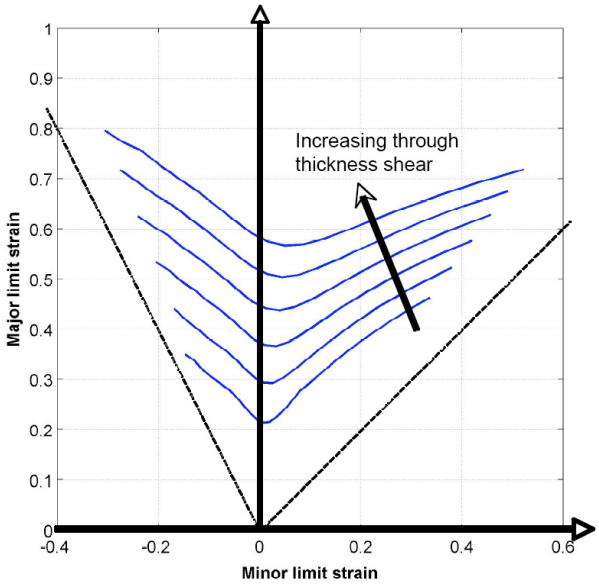

Fig. 18 Surface strains at the onset of instability with increasing through thickness shear [15]

6.2 Serrated strain paths

Eyckens et al. [30] simulated forming of a slice of a 50° cone using ABAQUS/standard. The strain path was found to be far from linear having a non-monotonic serrated path. The strain

paths were used as input in a M-K model. The results showed a higher forming limit when using different isotropic and anisotropic flow laws.

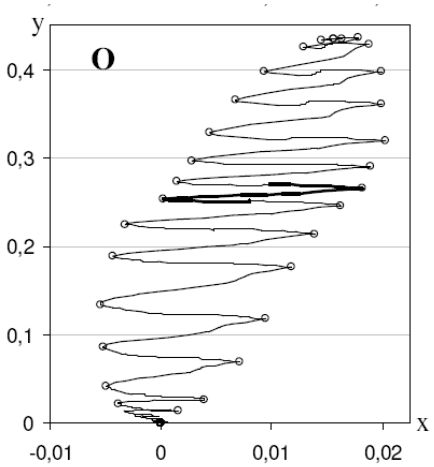

Fig. 19 Serrated strain path found by simulation of 50° cone (y is ε_1 and x is ε_2) [30]

6.3 Bending under tension

In a fundamental study of material properties Emmens et al. [31] developed a tension test with repetitive bending and unbending. Experiments showed that large uniform strains could be achieved without necking, Fig. 20 and Fig. 21. Decreasing the bending radius increased formability similar to how decreasing tool radius increases formability in SPIF.

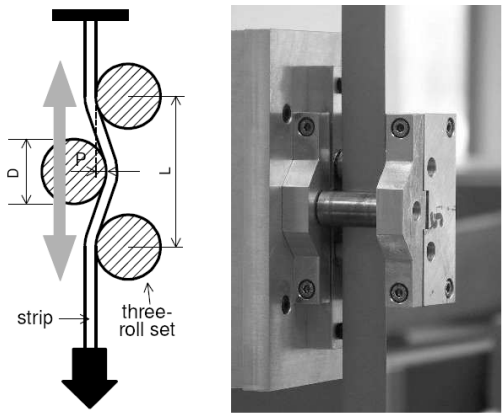

Fig. 20 Experimental setup for bending and unbending during tensile test [31]

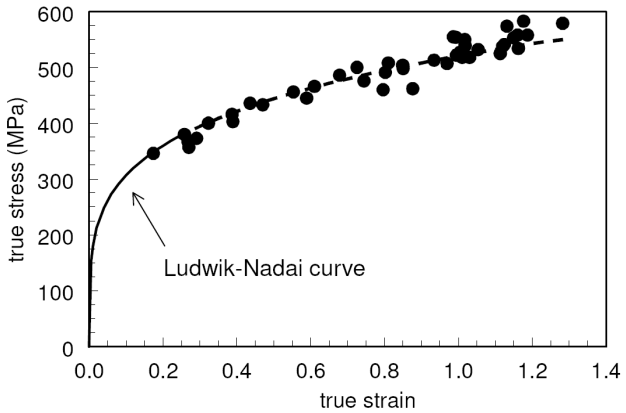

Fig. 21 Stress-strain curve obtained from tested specimens [31]

6.4 Compressive mean stress, small strain increments and low maximum principal stress

Micari [5] simulated SPIF using explicit time integration and calculated a compressive mean stress under the tool. This was believed to reduce both nucleation and growth of micro voids, i.e. to work against ductile fracture in the process. Low values of the maximum principal stress were also stated to increase formability since this stress is known to cause fracture in conventional deep drawing. In general the high formability in SPIF was believed to be the result of a synergy between compressive mean stress, low value of maximum principal stress and small and localized strain increments.

6.5 Necking versus fracture

Whatever the reason for the increased formability in SPIF is, it remains to be determined what happens with the fracture line which is seen in Fig. 16 and Fig. 17. As necking is delayed, the position of the necking limit is raised in the principal strain space and maybe the shape also changes. The question is whether the fracture limit also moves upwards to keep the strain between necking and fracture constant or the fracture line remains in the same position? If the fracture line is more or less constant the necking limit will, if raised enough, pass the fracture line implying that deformation will be uniform thinning until fracture.

Fracture without previous necking is not an unknown phenomenon. As seen in Fig. 17 the fracture line is in some cases close to or lower than the necking line at equal biaxial strain. A bulge test with a circular die will in this case produce uniform thinning until fracture.

In fracture mechanics studies of sheet forming the fracture curve based on experiments and theory of ductile damage evolution is often a straight line with a slope of -1 [32], Fig. 22. This combined with the knowledge that the limiting strains in SPIF can be displayed as a line with a slope of -1 is not a proof that SPIF is limited by fracture only, but it is a strong indication. It does not tell anything about why necking is delayed or simply not present. In fact the reason could be any of the mechanisms described earlier in this chapter. A statement that SPIF is limited by fracture only, i.e. uniform thinning until fracture, does not exclude: serrated strains paths, through thickness shear or bending under tension as the cause/causes for the absence of necking.

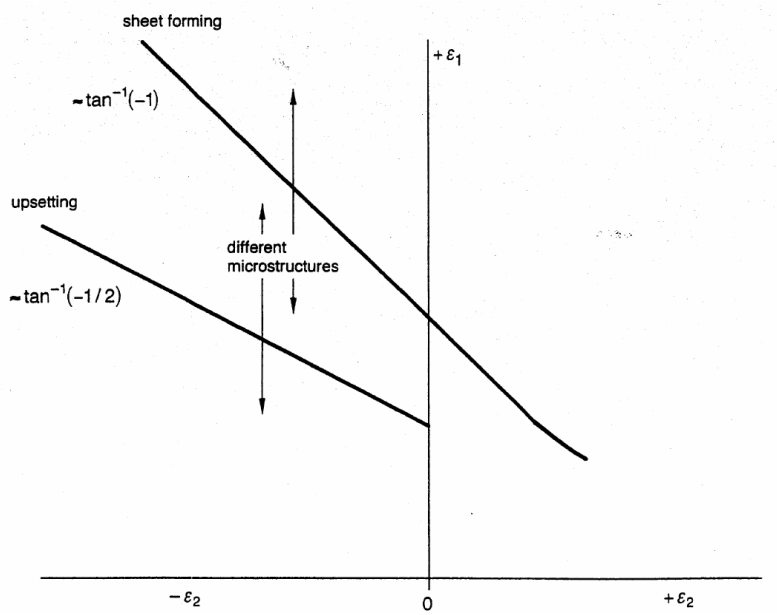

Fig. 22 Typical locations of fracture lines in bulk and sheet forming [32]

Damage is related to fracture and not necking, so any attempt to explain the increased formability in SPIF by calculation of damage is basically the same as assuming that the process is limited by fracture. A number of researches have looked at damage in relation to formability in SPIF [4,5,33], but this has not lead to the conclusion that SPIF is limited by fracture instead of necking.

Identifying whether SPIF is limited by necking or fracture seems like an easy task, but the literature shows that this is not the case. Another reason for the confusion is that a simple analysis of strains from a surface grid close to a fracture does not provide information on the possible appearance of necking previous to fracture. Examples of parts formed to necking without fracture are not common, and this indicates that the straining between necking and fracture is very small, assuming that a neck does exist.

7 Numerical Simulation

Numerical simulation of SPIF is challenging due to the long duration of the process and the constantly changing contact between tool and work piece. The geometries which need to be meshed for a simulation are very simple and all information about the geometry lies in the movement of the forming tool.

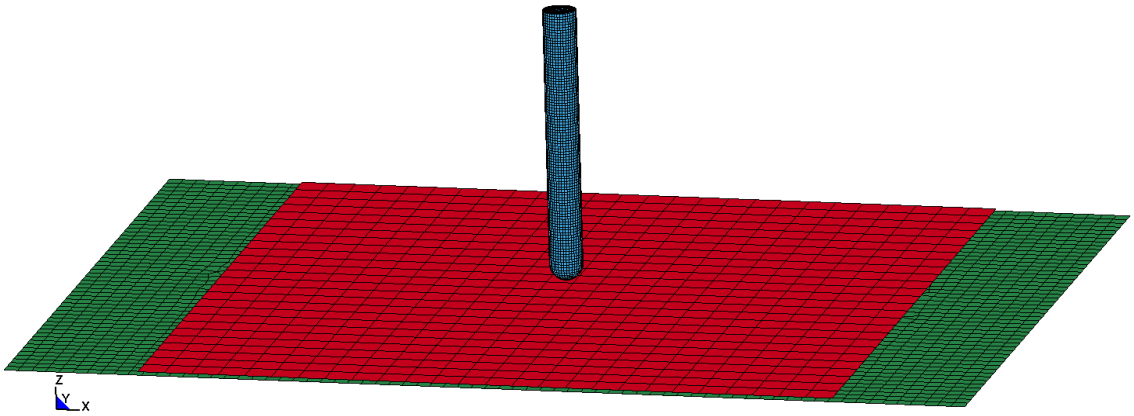

Fig. 23 Basic geometries (tool, sheet and backing plate) for numerical simulation of SPIF

Simulation has been done with both explicit and implicit time integration, but explicit is by far the most common choice. Using implicit time integration it not feasible to simulate forming of the whole part and only a section is simulated [30]. With explicit time integration the whole part can be simulated but mass scaling, time scaling and rigid tools must be used to ensure a reasonable calculation time [34].

7.1 Element choice

The most common element is a fully integrated shell with five or more integration points in thickness. Using integration points in the thickness direction places this element somewhere between a solid element and a membrane element which only has one integration point in thickness. It can take bending effects into account and the state of stress is not plane-stress. Using solid elements normally requires that only a section of the geometry is simulated to make calculation time reasonable.

Most shells assume that the normal stresses are zero in the thickness direction, but since the shear stresses in this direction can still be different from zero, the state of stress is not plane stress. Some shells can also include normal stresses in the thickness direction and they are often referred to as solid shells or thick shells.

7.2 Friction and Material Data

Getting input data for simulation of SPIF is not an easy task. The coefficient of friction between the forming tool and the sheet has not been measured by any researchers. Measurements of process forces have been carried out, but these can not easily be converted into a coefficient of friction. Common values are guessed to lie between 0.05 and 0.125.

Another challenge is getting reliable material data. Even though almost all research is done with standard materials only a few publications report material data found by experiments. Material data is found by tensile and bulge tests, but these tests will only provide results for rather low strain values, much smaller than those observed in SPIF. As a result a high degree of extrapolation is needed, Fig. 24.

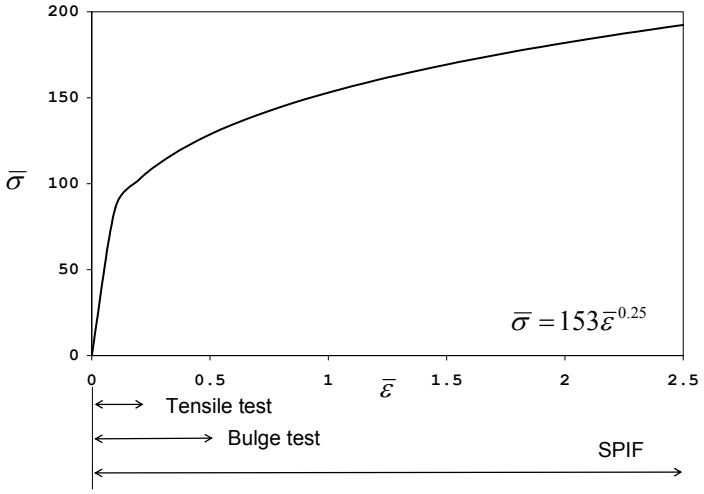

Fig. 24 Stress-strain curve for equivalent strain values observed in SPIF and values from tensile and bulge testing

7.3 Time scaling

Time scaling is done by simulating the process with a higher feed rate than what is used in experiments. Typical scale factors are 500-2500 which causes the simulated process to last a couple of seconds compared to experiments with duration of about an hour. This increases the kinetic energy in the process, and a general rule often used is that the kinetic energy may not exceed 5% of the deformation energy. For simulation of SPIF this global criteria is not always enough since the amount of kinetic energy is almost constant, but the deformation energy is constantly increasing throughout the process. Any violation of the 5% criterion is therefore most likely to be seen in the beginning of the process where the total amount of deformation energy is small or if peaks in the kinetic energy exist [35].

An example of excessive time scaling in a simulation carried out by the author can be seen in Fig. 25. The first stage in a two stage operation is completed without problems for both time scaling levels, but the second stage is only possible at the lower level of time scaling. The observed difference is most likely caused by a more complicated stress-strain situation during the second stage. This also serves as an example that multi stage SPIF is more difficult to simulate compared to normal SPIF.

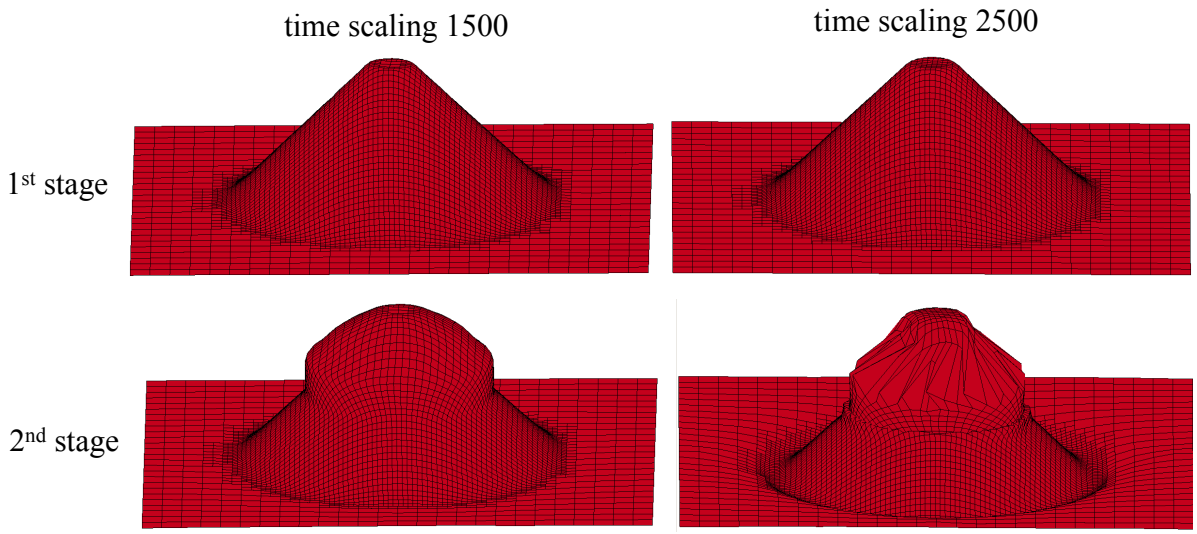

Fig. 25 Different time scaling levels (shell 16, no mass scaling)

7.4 Mass scaling

Mass scaling is a method for increasing the maximum time step set by the Courant stability criterion (28) in explicit time integration [36]. L_s is the characteristic length of the shell and can be the shell area divided by the largest side or diagonal. c is the speed of sound in the material. For steel with a shell side length of 2 mm the time step Δt is about $3 \cdot 10^{-7}$s. Mass scaling allows a higher time step and as a result a reduced calculation time, but it also increases the mass and thereby the kinetic energy. To keep total mass increase at a minimum only shells which require mass scaling to fulfil the Courant criterion are scaled [37]. An example of excessive mass scaling in a simulation by the author can be seen in Fig. 26. As in the case of time scaling, multi stage SPIF is more sensitive to mass scaling than normal SPIF.

$$\Delta t = \frac{L_s}{c} \tag{28}$$

$$c = \sqrt{\frac{E}{\rho(1-\upsilon^2)}} \tag{29}$$

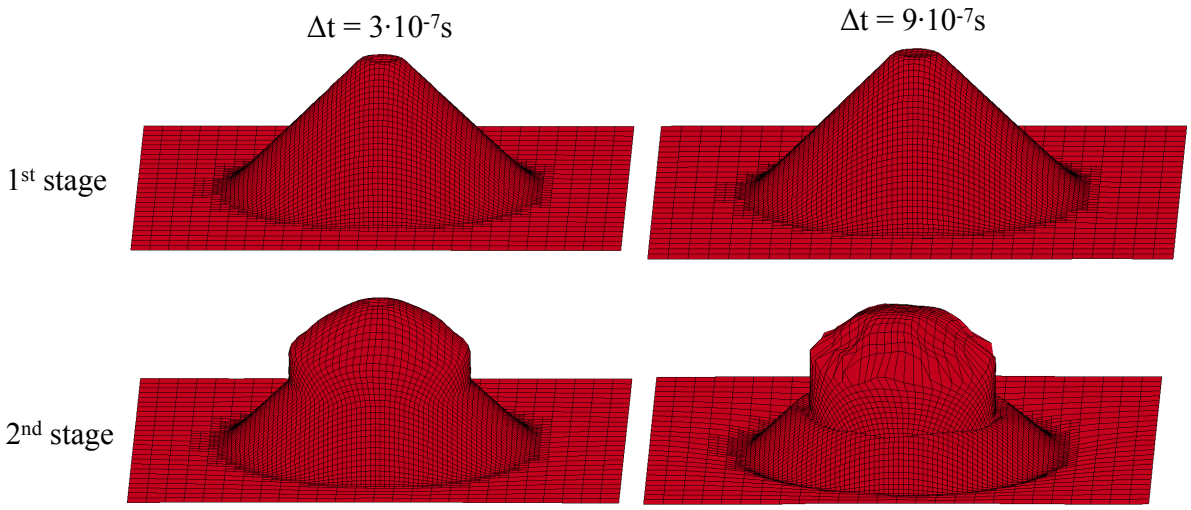

Fig. 26 Different levels of mass scaling (shell 16, time scaling 1500)

Both time and mass scaling offers the possibility to reduce calculation time. The price payed is a lower quality output and it is not easy to determine an appropriate level of scaling. Time and mass scaling can be used together or individually.

7.5 LS-DYNA

LS-DYNA from Livermore Software Technology Corporation, version LS-DYNA_971, is the numerical software used in this project. LS-DYNA is originally a dynamic explicit program but the current version also offers implicit time integration [36].

8 Summery of Papers

In the present chapter the papers appended to the thesis are listed and summarized. To structure the summery the papers are divided into five main topics.

8.1 List of papers

1) Creating helical tool paths for single point incremental forming
[38], p. 55-64
M. Skjoedt, M. H. Hancock and N. Bay
SheMet 2007, 12th Int. Conf. on Sheet Metal, Palermo, Italy, Apr. 1-4, (2007)
Key Engineering Materials, vol. 344, p. 583-590

2) Single point incremental forming using a dummy sheet
[39], p. 65-76
M. Skjoedt, M. B. Silva, N. Bay, P. A. F. Martins, T. Lenau
2nd ICNFT, 2nd Int. Conf. on New Forming Technologies
Bremen, Germany, Sep. 20-21, (2007)
Conference proceedings, BIAS-Verlag, p. 267-276

3) Estampagem incremental de 'tailored blanks'
[40], p. 77-93
M.B. Silva, M. Skjoedt, L.M. Alves, P. Vilaça, N. Bay, P.A.F. Martins
27º SENAFOR, 10ª Conferencia Nacional de Conformaçao de Chapas
Porto Alegre, Brazil, Oct. 18-19, (2007)
Conference proceedings, p. 239-253

4) Revisiting the fundamentals of single point incremental forming by means of membrane analysis
[41], p. 95-107
M.B. Silva, M. Skjoedt, N. Bay, P.A.F. Martins
International Journal of Machine Tools and Manufacture, (2008), vol. 48, p. 73-83

5) Single-point incremental forming & formability-failure diagrams
[42], p. 109-131
M.B. Silva, M. Skjoedt, A.G. Atkins, N. Bay, P.A.F. Martins
The Journal of Strain Analysis, (2008), vol. 43, p. 15-35

6) Single point incremental forming of tailored blanks produced by friction stir welding
[43], p. 133-162
M.B. Silva, M. Skjoedt, P. Vilaça, N. Bay, P.A.F. Martins
Journal of Materials Processing Technology, (2008), accepted for publication

7) Theory of single point incremental forming
[44], p. 163-170
P.A.F. Martins, N. Bay, M. Skjoedt, M.B. Silva
CIRP Annals - Manufacturing Technology, (2008), vol. 57, p. 247-252

8) Multi stage strategies for single point incremental forming of a cup
[45], p. 171-176
M. Skjoedt, N. Bay, B. Endelt, G. Ingarao
ESAFORM 2008, 11th Conf. on Material Forming, Lyon, France, Apr. 23-25, (2008)
International Journal of Material Forming, (2008), Springer/ESAFORM 2008

9) Strain paths and fracture in multi stage single point incremental forming
[46], p. 177-184
M. Skjoedt, M.B. Silva, P.A.F. Martins, N. Bay
ICTP 2008, 9th Int. Conf. on Technology of Plasticity, Gyeongju, Korea, Sep. 7-11, (2008)
Conference proceedings, accepted

Some of the papers overlap considerably. [42] is an expanded version of [41] and also includes geometries which are not formed in plane strain. [40] is a Portuguese conference version of [43]. [44] is a summery of [39,42,43].

All material is basically covered by the following papers: [38,39,42,43,45,46].

8.2 Main topics of papers

The content of the papers can be divided into five main topics:

1) Tool path generation for SPIF
2) SPIF using a dummy sheet
3) Theory of SPIF and prediction of formability
4) SPIF of tailored blanks produced by friction stir welding
5) Multi stage SPIF

In the natural flow of research the different topics flow into each other and papers often contain more than one of the five topics. Examples: helical tool paths are used in work on all the topics, dummy sheets are used in the work on SPIF of tailored blanks produced by friction stir welding and the developed theoretical analysis of SPIF is used to explain observations in the dummy sheet work and to construct a fracture line in the multi stage work. To link the different topics one of the papers [44] is an overview of three topics 2), 3) and 4). This strategy is justified by the fact that it has made it possible to explain previous observations with newer developments, thus facilitating reading of the thesis.

In the following sections the five topics within the nine papers are summarized.

8.2.1 Tool path generation for SPIF

[38]

SPIF is often performed on a CNC milling machine and the tool movement is programmed using CAM software intended for surface milling. Often the function called profile milling or contour milling is applied. Using this milling function the tool only has a continuous feed rate in two directions X and Y, which represents the planes parallel to the undeformed sheet. The feed in the Z direction is done in the same angular position in the XY plane along a line down the side of the work piece. This causes a scarring of the side and furthermore results in a peak in the axial force when the tool is moved down.

The present paper offers a solution to this problem. A dedicated program is created which uses the coordinates from the profile milling code and converts them into a helical tool path with continuous feed in all three directions, Fig. 27. The program is called HeToPac. Using the helical tool path the scarring is removed, the part is otherwise unchanged and a major disadvantage of using milling software for SPIF is removed, Fig. 28. The solution is demonstrated by SPIF of three different geometries: a pyramid, a cone and a complex part.

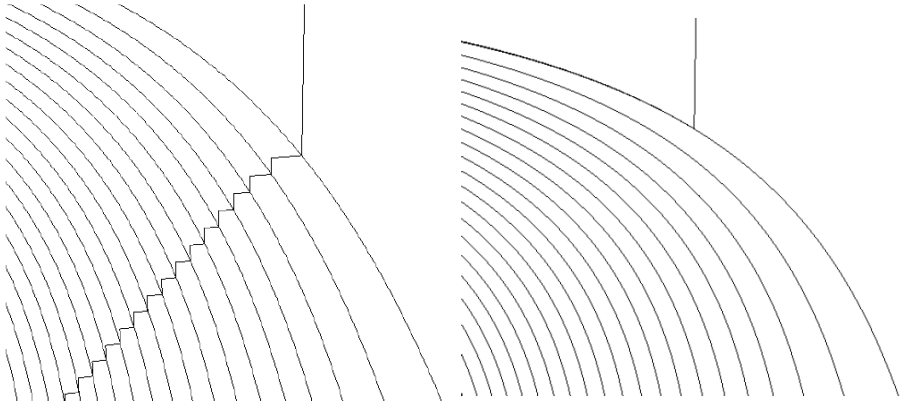

Fig. 27 Left: profile tool path, right: helical tool path generated by HeToPac [38]

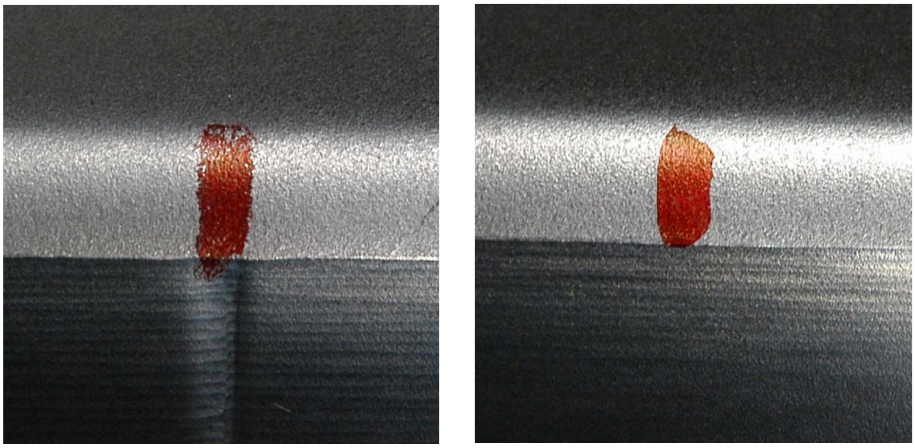

Fig. 28 Left: inside scaring from profile tool path, right: same surface by using HeToPac [38]

The paper presents a solution to a small practical problem caused by using milling software for SPIF. HeToPac was used in work for all the other papers included in this thesis. By request HeToPac is now exported to a couple of other universities, Fig. 29.

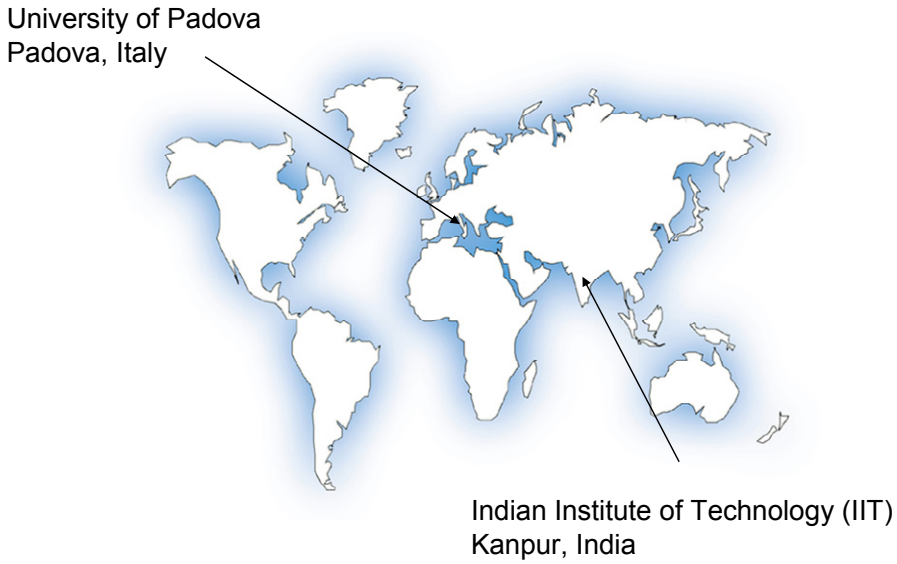

Fig. 29 Locations of universities which have requested the HeToPac program

8.2.2 SPIF using a dummy sheet

[39]

A new variant of SPIF is invented in this work. This version includes a dummy sheet on top of the work piece sheet, i.e. forming two sheets instead of one, Fig. 30. The dummy sheet, which is in contact with the rotating tool pin, can be discarded after forming. This new setup influences the process and offers a number of new possibilities for solving some of the remaining problems in SPIF.

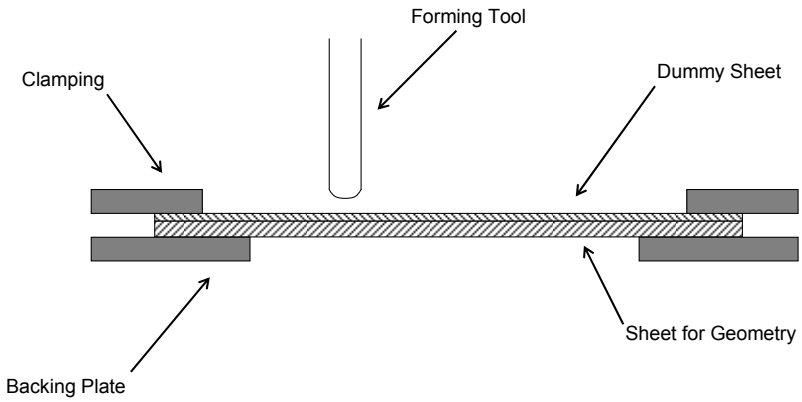

Fig. 30 SPIF using a dummy sheet setup [39]

It is investigated how the use of a dummy sheet influences: formability, wear, surface quality and bulging of planar sides. This is done by forming two test shapes: a truncated cone with increasing drawing angle, Fig. 31, and a truncated pyramid. The possible influence of the level of friction between the two sheets is also investigated.

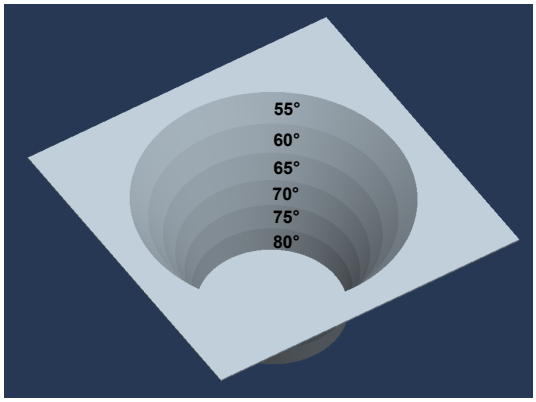

Fig. 31 Truncated cone with step wise increasing drawing angle [39]

The results show that the use of a dummy sheet reduces wear of the work piece to almost zero, but it also causes a decrease in formability. Bulging of the planar sides of the pyramid is reduced. Surface roughness is increased, but the general appearance is improved. Lowering the friction between the two sheets by lubrication only influences roughness. Suggestions for applications of this new technique are discussed, among those SPIF of tribologically difficult materials such as titanium and soft aluminium.

The invention of the dummy sheet version of SPIF soon proved its worth. It was used in forming thick tailored AA 1050 H111 blanks produced by friction stir welding. Without the dummy sheets, the experiments could not be performed without severe galling of the soft aluminium sheets.

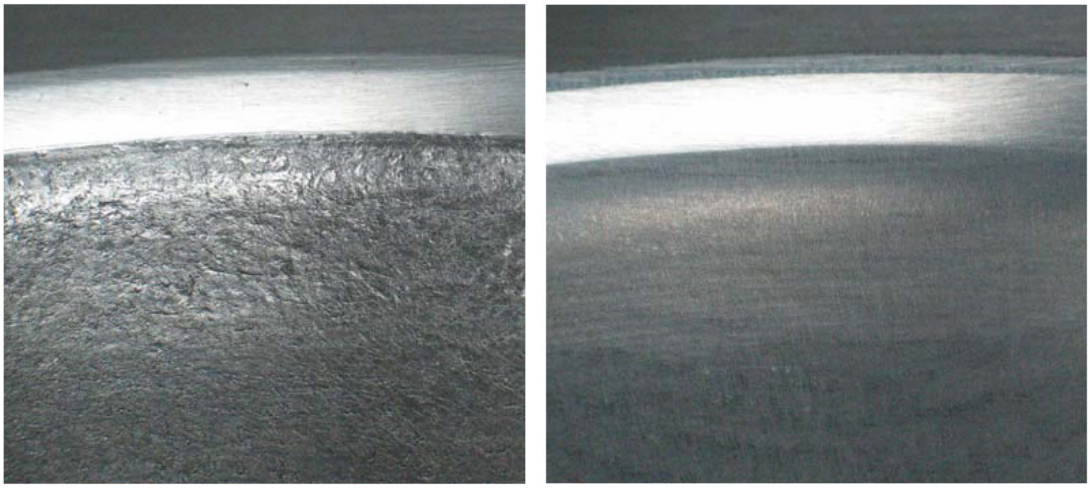

Fig. 32 Left: signs of galling in SPIF of 1.5 mm AA1050 H111, right: surface quality in SPIF of 1.5 mm AA1050 H111 using a 0.63 mm DC04 steel dummy sheet [39]

8.2.3 Theory of SPIF and prediction of formability

[41,42,44]

In this work membrane equilibrium equations are used to derive a set of equations to describe the state of stresses and strains in the plastic zone of SPIF, Table 3. Assumptions and conditions are listed below:

1) The governing mode of deformation is in-plane stretching.
2) The plastic zone is small and placed right underneath the forming tool.
3) Three basic modes of deformation are considered the extremes and all shapes are assumed to be combinations of these: 1) flat and 2) rotational symmetric surfaces, which are considered to deform under plane strain, and 3) corners, which are considered equal biaxial stretching.
4) Bending moment is neglected and friction is considered small. This is necessary to assume that the principal stresses are coinciding with the following directions: meridional, circumferential and thickness.
5) No strain hardening, i.e. rigid-perfectly plastic.
6) Friction can be treated as two in-plane components: meridional friction and circumferential friction.
7) Tresca is yield criterion and Levy-Mises flow rule is adapted.

	Assumption	State of strain	State of stress	Hydrostatic stress
SPIF (flat and rotational symmetric surfaces)	plane strain conditions	$d\varepsilon_\phi = -d\varepsilon_t > 0$ $d\varepsilon_\theta = 0$ $d\varepsilon_t < 0$	$\sigma_\phi = \sigma_1 = \frac{\sigma_Y}{(1+t/r_{tool})} > 0$ $\sigma_\theta = \sigma_2 = \frac{1}{2}(\sigma_1 + \sigma_3)$ $\sigma_t = \sigma_3 = -\sigma_Y \frac{t}{(r_{tool}+t)} < 0$	$\sigma_m = \frac{\sigma_Y}{2}\left[\frac{r_{tool}-t}{r_{tool}+t}\right]$
SPIF (corners)	equal bi-axial stretching	$d\varepsilon_\phi = d\varepsilon_\theta > 0$ $d\varepsilon_t < 0$	$\sigma_\phi = \sigma_\theta = \sigma_1 = \frac{\sigma_Y}{(1+2t/r_{tool})} > 0$ $\sigma_t = \sigma_3 = -2\sigma_Y \frac{t}{(r_{tool}+2t)} < 0$	$\sigma_m = \frac{2\sigma_Y}{3}\left[\frac{r_{tool}-t}{r_{tool}+2t}\right]$

Table 3 Equations for calculating principal stresses in the plastic zone in SPIF [44]

The work also presents a theorem to explain the high formability in SPIF:

> . . . the suppression of necking seems to be the key mechanism that, together with the low growth rate of accumulated damage, is capable of ensuring the high levels of formability in SPIF.

Fig. 33 Quotation from [42]

The theorem can be broken down in two parts: 1) the suppression of necking and 2) the low growth rate of accumulated damage. Another way of saying this is to describe the deformation

in SPIF as uniform thinning until fracture, i.e. deformation is limited by fracture only and not necking, Fig. 34.

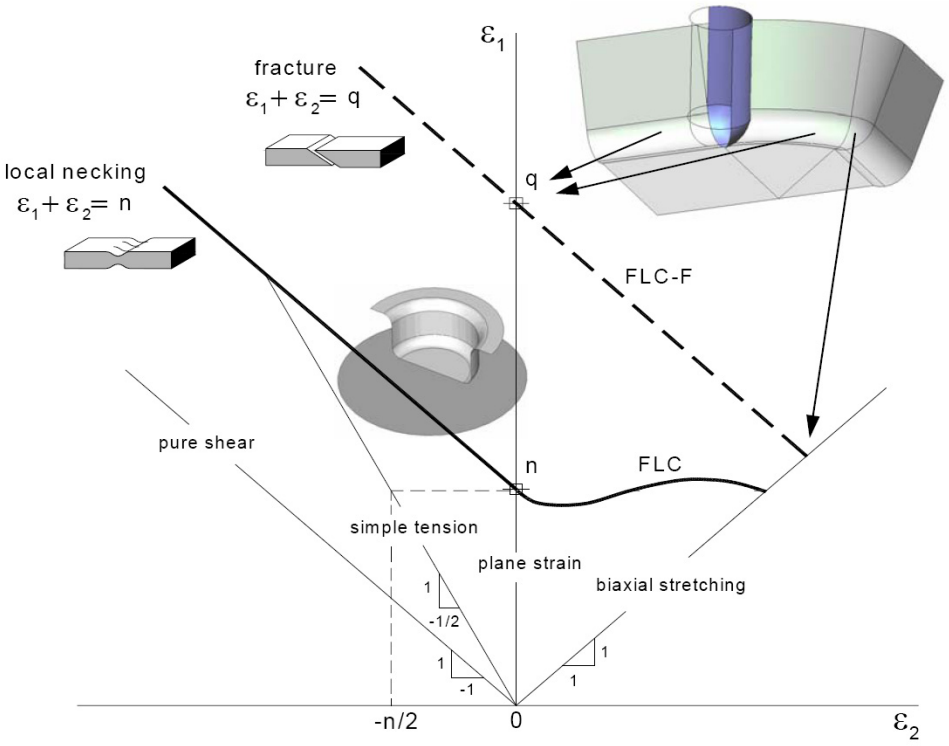

Fig. 34 Fracture line limiting the SPIF process in the principal strain space and theoretical FLC [42]

The low growth rate of accumulated damage is explained by looking at the triaxiality ratio (hydrostatic stress divided by flow stress) using the theoretical hydrostatic stress as seen in Table 3. Comparing the triaxiality ratio of stamping with SPIF it is clear that the growth rate of damage can be expected to be higher in stamping than in SPIF, (30) and (31), [42].

The suppression of necking is explained qualitatively by the inability of a neck to grow in the small plastic zone surrounded by material which is close to being rigid or at least only deformed elastically.

$$\left(\frac{\sigma_m}{\sigma_Y}\right)_{stamping} > \left(\frac{\sigma_m}{\sigma_Y}\right)_{bi-axial} > \left(\frac{\sigma_m}{\sigma_Y}\right)_{plane\ strain} \tag{30}$$

$$\frac{2}{3}\left[\frac{r_{punch}-t/2}{r_{punch}+t}\right] > \frac{2}{3}\left[\frac{r_{tool}-t}{r_{tool}+2t}\right] > \frac{1}{2}\left[\frac{r_{tool}-t}{r_{tool}+t}\right] \tag{31}$$

Critical damage values (D_c) based on the triaxiality ratios are used to calculate a theoretical slope for the straight line which limits SPIF in the principal strain space, Fig. 34 and (32), [42]. Please note: (32) is different than the same expression seen in the papers [42,44,46]. This is due to errors in the papers, (32) is correct. The error causes a small change in the calculated slope.

$$\frac{\Delta\varepsilon_1}{\Delta\varepsilon_2} = -\frac{5\left(\frac{r_{tool}}{t}\right)+2}{3\left(\frac{r_{tool}}{t}\right)+6} \tag{32}$$

The work also contains experimental evidence that no necking is formed before fracture. This is shown in the form of thickness measurements along the sides of a cone with increasing drawing angles. The thickness in the area of cracking is not different from the thickness in a zone with no cracking at the same depth. Also, close up pictures of the cracks reveal no necking, Fig. 35.

Fig. 35 Close up picture revealing no necking [42]

Novel contributions in this work are listed below:

1) Theoretical explanation to the experimentally observed influence from initial sheet thickness (t_0) and tool radius (r_{tool}) on formability.
2) Equations for calculating the principal stresses in the plastic zone.
3) Theory to explain the high formability in SPIF, i.e. why necking is suppressed and damage growth rate is low.
4) Theoretical explanation to why the curve limiting the strains in the principal strain is a straight line with a negative slope.
5) Theoretical calculation of the slope of the fracture line in the principal strain space.
6) Theoretical explanation why the inclined wall adjacent to the tool is only elastically deformed.
7) Theoretical explanation to why cracking occurs in the upper part of the plastic zone and not under the tool.
8) Experimental evidence that no necking is present.

8.2.4 SPIF of tailored blanks produced by friction stir welding

[40,43]

This work is dealing with SPIF of tailored blanks produced by friction stir welding. The work also investigates the use of dummy sheets to protect the welding joint and the soft aluminium sheets from the rotating forming tool. Formability of the welded blanks is evaluated by tests carried out on truncated conical and pyramidal shapes with step wise increasing drawing angles. Results are compared with similar tests performed on conventional reference sheets of the same material, Fig. 36.

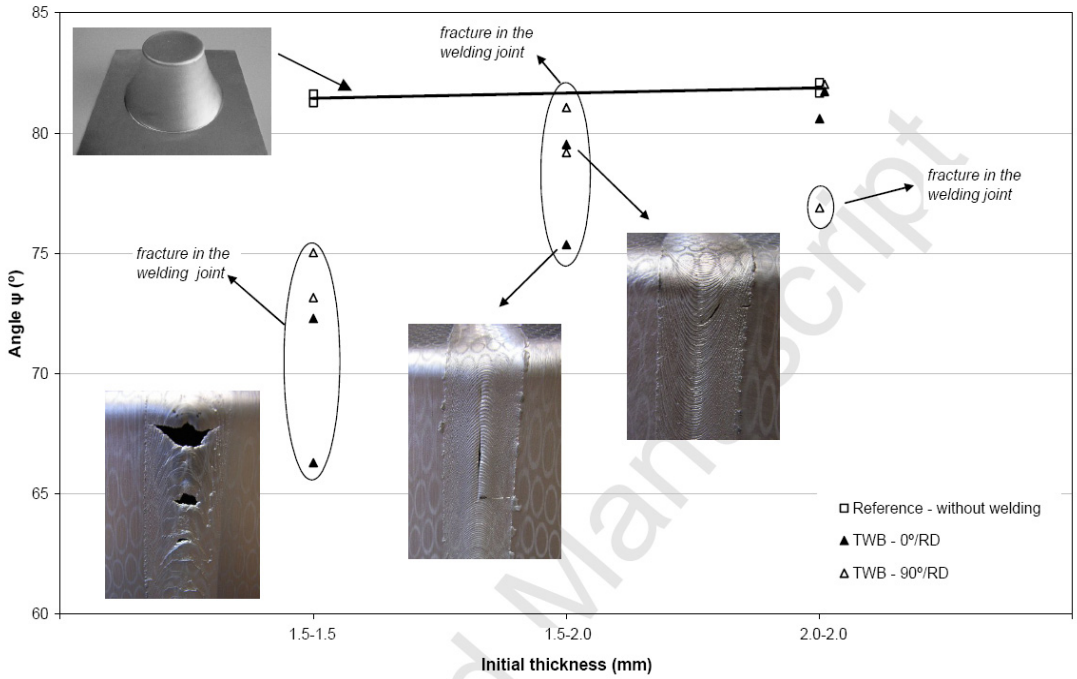

Fig. 36 Maximum drawing angles for tailored blanks and reference blanks as a function of t_0 during SPIF of Aluminium AA1050-H111. A 0.63 mm DC04 steel dummy sheet was used in all the experiments [43]

Results show that the combination of SPIF with friction stir welding seems promising in the manufacture of complex sheet metal parts with high depths and drawing angles up to 60°, Fig. 37.

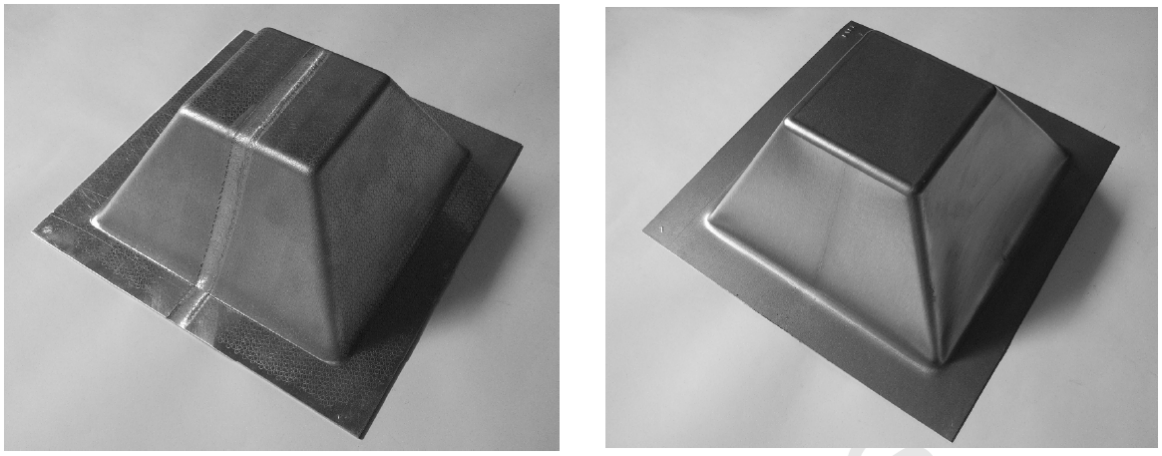

Fig. 37 Right: 60° pyramid with friction stir welding without fracture, left: steel dummy used during forming [43]

This work is dealing with the subject of maturing SPIF for applications. It is likely that SPIF will have to be used together with other advanced manufacturing technologies once the process moves from research into areas of applications. This is in agreement with the product segment for SPIF being high value - low volume. A part produced by a combination of friction stir welding and SPIF will contain a large amount of know-how and processing time, and will present a significant value.

8.2.5 Multi Stage SPIF

[45,46]

In this work a five stage forming strategy for SPIF of a round cylindrical cup with a height/radius ratio of one is developed. Geometrical relations are discussed and theoretical strains are calculated. The influence of forming direction (upwards or downwards) is investigated comparing explicit FE analysis with experiments.

Good agreement is found between calculated and measured thickness distribution, overall geometry and strains, Fig. 38 and Fig. 39. Using the developed multi stage strategy it is shown possible to produce a cup with a depth almost as large as the radius and vertical sides in about half of the depth, Fig. 40.

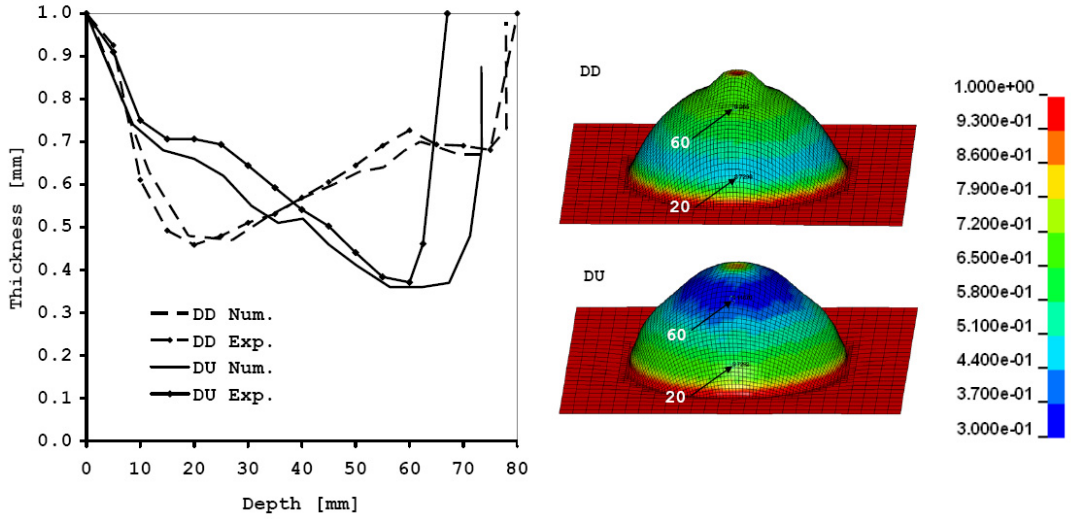

Fig. 38 Left: sheet thickness as a function of depth for down-down (DD) and down-up (DU) strategy, right: shapes determined by FE simulation with marking of elements at depths of 20 and 60 mm, scale is thickness in mm [46]

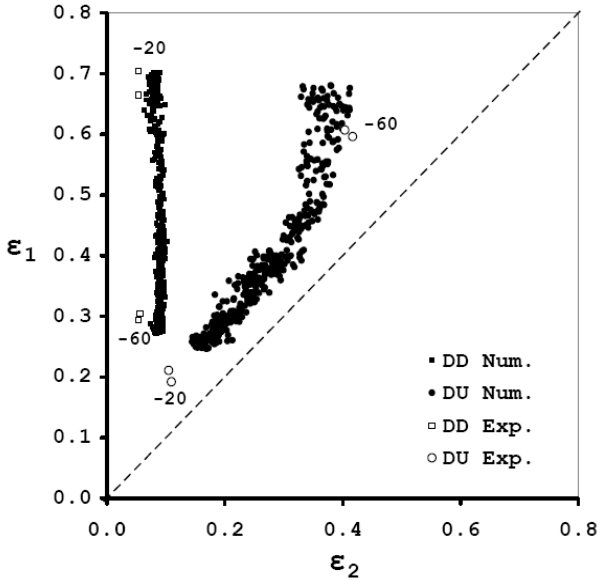

Fig. 39 Experimental and nummerical strains for strategies DD and DU in zone -20 < Z < -60 mm [46]

Fig. 40 Cup with 90° walls formed in four stages [46]

Strain paths are found to be straight in the first stage of forming and far from straight in the second stage. Fracture strains seem to follow a line with a slope of -1 indicating that the fracture line is not very dependent on strain paths.

The subject of multi stage SPIF is aimed at two areas: expanding the range of possible geometries by increasing the maximum drawing angle and improving the thickness tolerance. The two subjects go hand in hand since the requirement for increasing the maximum drawing angle is to use all material available, i.e. achieving a more uniform thickness. The work could also be described as investigating possible ways to get biaxial strains for rotational symmetric geometries, or how to move away from the limitations prescribed by the sine-law.

9 Suggestions for future work

One Topic could be to verify the theoretical principal stresses in Table 3 by comparing them with results from FE simulations. This could be done by running simulations with a constant yield stress and using geometries to cover the assumed basic geometrical shapes: 1) flat and 2) rotational symmetric surfaces, which are considered to deform under plane strain, and 3) corners, which are considered equal biaxial stretching. This would also allow a validation of the assumed strain situations, i.e. plane and equal biaxial strain.

The proposed multi stage strategy is far from ideal. Using this strategy it has been possible to produce vertical walls but the measurements of thickness reveals that the distribution of material is far from ideal. The residual centre part of the geometry is only formed in the first stage and this causes the thickness to be high compared to the rest of the part. Since the distribution of material is not ideal it opens for the possibility to form deeper geometries or walls with drawing angles higher than 90°. In theory this can be done without passing the fracture line in the principal strain space. Another topic within this area could be to use multi stage strategies for geometries which are not axis symmetric. It is expected that the corners in a square cup are the most difficult to form without fracture. The reason is that corners of a pyramid are already experiencing biaxial stretching in one stage SPIF.

The use of dummy sheets opens a number of possibilities. Using a steel dummy on top of soft aluminium sheets has already proven to be a success. A logical step would be to try different thicknesses and material combinations. Also the idea of using the dummy sheet beneath instead of on the top has not been investigated yet. A few preliminary experiments have shown that an increase in formability is possible with this configuration.

10 Conclusion

The work of this PhD project has lead to a number of advances within the science of SPIF. When the project was started 3 years ago no analytical models for SPIF existed and the reason for the high formability was still an open question.

This project has put forward a new theory for explaining the high formability. Within the same time period other researchers have come up with other explanations as seen in chapter 6. Time will tell which theories are correct, but the possibility also exist that the whole explanation includes elements from the different theories.

The analytical model presented in this work is unique. So far no other researchers have presented a way of calculating stresses in SPIF without using numerical simulation. A lot of assumptions had to be made, but even with these the model helps understanding the process and is able to explain a lot of experimental observations in the literature. This must be considered a milestone in SPIF research.

The invention of the dummy sheet variant of SPIF has already proved its worth during this work and all the possibilities for this variant have not been investigated yet. This work together with SPIF of tailored sheets produced by friction stir welding can be considered maturing the process for use outside the laboratories. Often variations of manufacturing processes or combinations with other new processes are necessary to expand the use into new areas.

For a long time it was considered impossible to achieve a 90° drawing angle using SPIF. The sine-law was considered a universal law. From the beginning of this project it was a clear goal to prove that it could be done. This was accomplished by only four stages of forming with the proposed multistage strategy and this result must also be considered a milestone in SPIF.

SPIF can still be considered a relatively new process and it still has the ability to impress people who see it running for the first time. A lot of suggestions have been presented for use of SPIF in the industry, but so far examples of SPIF being used for other purposes than research are rare.

The number of research groups working with SPIF has doubled over the last three years. There is a risk that SPIF will become “old news” within the next couple of years. It is not enough to keep the process interesting that researchers can come up with new things to investigate in laboratories. The jump to industry must be made in the near future.

11 References

1. Ham, M. and Jeswiet, J., *Single point incremental forming and the forming criteria for AA3003,* CIRP Annals - Manufacturing Technology, 55, (2006), 241-244.

2. Jeswiet, J., Hagan, E., and Szekeres, A., *Forming parameters for incremental forming of aluminium alloy sheet metal,* Proceedings of the Institution of Mechanical Engineers, Part B: Journal of Engineering Manufacture, 216, (2002), 1367-1371.

3. Ham, M. and Jeswiet, J., *Forming limit curves in single point incremental forming,* CIRP Annals - Manufacturing Technology, 56, (2007), 277-280.

4. Hirt, G., Junk, S., Bambach, M., and Chouvalova, I., *Process limits and material behaviour in incremental sheet forming with CNC-tools,* Materials Science Forum, 426-432, (2003), 3825-3830.

5. Micari, F., *Some remarks on material formability in single point incremental forming of sheet metal*, ICTP, Verona Italy, (2005).

6. Carrino, L., Di Meo, N., Sorrentino, L., and Strano, M., *The influence of friction in the negative dieless incremental forming*, ESAFORM, Glasgow Scotland, (2006).

7. Leszak, E., *Apparatus and process for incremental dieless forming,* Patent US3342051A, (19-9-1967).

8. Kitazawa, K. and Okaku, H., *Possibility of CNC incremental stretch-expanding of sheet metal by single-tool-path process,* Nippon Kikai Gakkai Ronbunshu, C Hen/Transactions of the Japan Society of Mechanical Engineers, Part C, 62, (1996), 2012-2017.

9. Iseki, H., Kato, K., and Sakamoto, S., *Forming limit of flexible and incremental sheet metal bulging with a spherical roller*, ICTP, (1993), 1635-1640.

10. Matsubara, M., Tanaka, S., and Nakamura, T., *Development of incremental sheet-metal-forming system using elastic tools (1st Report, principle of forming process and formation of some fundamental curved shapes),* Nippon Kikai Gakkai Ronbunshu, C Hen/Transactions of the Japan Society of Mechanical Engineers, Part C, 60, (1994), 1835-1842.

11. Filice, L., Fratini, L., and Micari, F., *Analysis of material formability in incremental forming,* CIRP Annals - Manufacturing Technology, 51, (2002), 199-202.

12. Jeswiet, J., *Incremental single point forming,* Technical Paper - Society of Manufacturing Engineers, MF, (2001).

13. Hirt, G., Ames, J., Bambach, M., and Ziegler S., *New developments in incremental forming*, 2nd ICNFT, Bremen Germany, 2nd ICNFT, (2007), 31-40.

14. Duflou, J. R., Szekeres, A., and Vanherck, P., *Force measurements for single point incremental forming: An experimental study,* Sheet Metal 2005 - Proceedings of the 11th International Conference, SheMet'05, 6-8, (2005), 441-448.

15. Allwood, J. M., Shouler, D. R., and Tekkaya, A. E., *The increased forming limits of incremental sheet forming processes*, Key Engineering Materials, (2007), 621-628.

16. Bambach, M., Todorova, M., and Hirt, G., *Experimental and numerical analysis of forming limits in CNC incremental sheet forming*, Key Engineering Materials, (2007), 511-518.

17. Jeswiet, J. and Young, D., *Forming limit diagrams for single-point incremental forming of aluminium sheet,* Proceedings of the Institution of Mechanical Engineers, Part B: Journal of Engineering Manufacture, 219, (2005), 359-364.

18. Jeswiet, J., Micari, F., Hirt, G., Bramley, A., Duflou, J., and Allwood, J., *Asymmetric single point incremental forming of sheet metal,* CIRP Annals - Manufacturing Technology, 54, (2005), 623-649.

19. Emmens, W. C. and van den Boogaard, A. H., *Strain in shear and material behaviour in incremental forming*, Key Engineering Materials, (2007), 519-526.

20. Jeswiet, J., Duflou, J. R., and Szekeres, A., *Forces in single point and two point incremental Forming,* Sheet Metal 2005 - Proceedings of the 11th International Conference, SheMet'05, 6-8, (2005), 449-456.

21. Ambrogio, G., Filice, L., Fratini, L., and Micari, F., *Process mechanics analysis in single point incremental forming*, NUMIFORM, (2004).

22. Allwood, J. M., *A structured search for novel manufacturing processes leading to a periodic table of ring rolling machines,* Journal of Mechanical Design, Transactions of the ASME, 129, (2007), 502-511.

23. Tanaka, S., Nakamura, T., Hayakawa, K., Nakamura, H., and Motomura, K., *Incremental sheet metal forming process for pure titanium denture plate*, ICTP, Verona Italy, (2005).

24. Verbert, J., Belkassem, B., Henrard, C., Habraken, A. M., Gu, J., Sol, H., Lauwers, B., and Duflou, J. R., *Multi-Step toolpath approach to overcome forming limitations in single point incremental forming*, ESAFORM 2008, Lyon France, (2008).

25. Allwood, J. M., Bramley, A. N., Ridgman, T. W., and Mileham, A. R., *A novel method for the rapid production of inexpensive dies and moulds with surfaces made by incremental sheet forming,* Proceedings of the Institution of Mechanical Engineers, Part B (Journal of Engineering Manufacture), 220, (2006), 323-327.

26. Jeswiet, J. and Hagan, E., *Rapid proto-typing of a headlight with sheet metal,* Technical Paper - Society of Manufacturing Engineers, (2002), 1-6.

27. Danckert, J., *Yield criteria and flow rule for anisotropic materials*, Institute for production, Ålborg University, Denmark, (1989).

28. Marciniak, Z., Duncan, J. L., and Hu, S. J., *Mechanics of sheet metal forming*, Butterworth Heineman, (2002).

29. Embury, J. D. and Duncan, J. L*., Formability maps,* Annual review of materials science.Vol.11, (1981), 505-521.

30. Eyckens, P., He, S., Van Bael, A., Van Houtte, P., and Duflou, J*., Forming limit predictions for the serrated strain paths in single point incremental sheet forming*, AIP Conference Proceedings - American Institute of Physics, (2007), 141-146.

31. Emmens, W. C. and van den Boogaard, A. H*., Tensile tests with bending: a mechanism for incremental forming.*, ESAFORM, Lyon France, (2008).

32. Atkins, A. G*., Fracture mechanics and metal forming: Damage mechanics and the local approach of yesterday and today,* Fracture research in retrospect, (1997), 327-350.

33. Pohlack, M., Kuttner, R., and Majak, J*., Modelling and optimal design of sheet metal RP&M processes,* Rapid prototyping journal, (2005), 304-311.

34. Qin Q., Masuku E.S., Bramley A., Mileham A.R., and Owen G.W*., Incremental sheet forming simulation and accuracy*, 8th ICTP, Proceedings of 8th ICTP, (2005).

35. Bambach, M. and Hirt, G*., Error analysis in explicit finite element analysis of incremental sheet forming*, AIP Conference Proceedings, (2007), 859-864.

36. *LS-DYNA Theory Manual*, Livermore Software Technology Corporation (LSTC), (2006).

37. *LS-DYNA Keyword Users manual*, Livermore Software Technology Corporation (LSTC), (2007).

38. Skjoedt, M., Hancock, M. H., and Bay, N*., Creating helical tool paths for single point incremental forming*, Key Engineering Materials, (2007), 583-590.

39. Skjoedt, M., Silva , M. B., Bay, N., Martins, P. A. F., and Lenau, T*., Single point incremental forming using a dummy sheet*, 2nd ICNFT, Bremen Germany, (2007), 267-276.

40. Silva, M. B., Skjoedt, M., Alves, L. M., Vilaça, P., Bay, N., and Martins, P. A. F*., Estampagem incremental de 'tailored blanks'*, XXVII SENAFOR, (2007), 239-253.

41. Silva, M. B., Skjoedt, M., Martins, P. A. F., and Bay, N*., Revisiting the fundamentals of single point incremental forming by means of membrane analysis,* International Journal of Machine Tools and Manufacture, 48, (2008), 73-83.

42. Silva, M. B., Skjoedt, M., Atkins, A. G., Bay, N., and Martins, P. A. F., *Single-point incremental forming and formability-failure diagrams,* Journal of Strain Analysis for Engineering Design, 43, (2008), 15-35.

43. Silva, M. B., Skjoedt, M., Vilaça, P., Bay, N., and Martins, P. A. F., *Single point incremental forming of tailored blanks produced by friction stir welding,* Journal of Materials Processing Tech., (2008).

44. Martins, P. A. F., Bay, N., Skjoedt, M., and Silva, M. B., *Theory of single point incremental forming,* CIRP Annals - Manufacturing Technology, 57, (2008), 247-252.

45. Skjoedt, M., Bay, N., Endelt, B., and Ingarao, G., *Multi stage strategies for single point incremental forming of a cup*, ESAFORM, Lyon France, (2008).

46. Skjoedt, M., Silva, M. B., Martins, P. A. F., and Bay, N., *Strain paths and fracture in multi stage single point incremental forming*, ICTP, Gyeongju Korea, (2008).

February 2008

Joint author statement

If a thesis contains articles made in collaboration with other researchers, a joint author statement about the PhD-student's part of the article shall be made by each of the co-authors, cf. article 12, section 4 of the Ministerial Order No. 18 February 2008 about the PhD degree

Title of the article: Creating helical tool paths for single point incremental forming

Author(s): M. Skjoedt, M. H. Hancock and N. Bay

Journal: Conference paper, SheMet 07 – 12th Int. Conf. on Sheet Metal, Palermo, Italy, Apr. 1-4, (2007), Key Engineering Materials, vol. 344, p. 583-590.

PhD-student: Martin Skjødt Cpr.nr:

Signature of the PhD-student: Date:

Co-author: Signature:

Description of each author's contribution to the above-mentioned article:

M. Skjoedt: Development of theory for helical program, CAM programming of parts, planning and conduction of experiments, literature study, writing of paper, pictures and graphics for paper, final editing.

M. H. Hancock: Development of theory for helical program, programming of the helical program, writing of paper, final editing.

N. Bay: Initiation of problem formulation and final editing.

Key Engineering Materials Vol. 344 (2007) pp. 583-590
online at http://www.scientific.net

Online available since 2007/07/15

Department of Mechanical Engineering
Technical University of Denmark

Creating Helical Tool Paths for Single Point Incremental Forming

M. Skjoedt[1,a], M. H. Hancock[2,b] and N. Bay[3,c]

[1, 2, 3] Technical University of Denmark, Department of Manufacturing Engineering and Management
DTU - Building 425, DK-2800, Kgs. Lyngby, Denmark
[a]msk@ipl.dtu.dk, [b]mhh@ipl.dtu.dk, [c]nbay@ipl.dtu.dk

Keywords: Incremental Sheet Forming, Helical Tool Path, Spiral Tool Path, CAM

Abstract. Single point incremental forming (SPIF) is a relatively new sheet forming process. A sheet is clamped in a rig and formed incrementally using a rotating single point tool in the form of a rod with a spherical end. The process is often performed on a CNC milling machine and the tool movement is programed using CAM software intended for surface milling. Often the function called profile milling or contour milling is applied. Using this milling function the tool only has a continuous feed rate in two directions X and Y, which is the plane of the undeformed sheet. The feed in the vertical Z direction is done in the same angular position in the XY plane along a line down the side of the work piece. This causes a scarring of the side and also results in a peak in the axial force when the tool is moved down.

The present paper offers a solution to this problem. A dedicated program uses the coordinates from the profile milling code and converts them into a helical tool path with continuous feed in all three directions. Using the helical tool path the scarring is removed, the part is otherwise unchanged and a major disadvantage of using milling software for SPIF is removed. The solution is demonstrated by SPIF of three different geometries: a pyramid, a cone and a complex part.

Introduction

SPIF originated back in 1967 when Leszak patented the concept of forming sheets incrementally by using a single point tool [1]. This concept and the use of an ordinary milling machine was investigated by Jeswiet et al. who used this to produce a prototype of a headlight for a car [2] and Filice et al. who used different geometries to investigate formability [3]. An overview of SPIF may be found in the keynote paper by Jeswiet et al. [4].

Since SPIF is a relatively new sheet forming process and often performed on a CNC milling machine most researchers use CAM software designed for milling to program the movement of the tool. The ideal tool path is helical where the tool has continuous feed in all three directions. For unknown reasons most CAM programs do not have this option, instead profile milling is often used [4]. A profile milling tool path works well for all parts, but has a major drawback since a scarring is created where the tool steps down in the vertical direction. Another drawback is that a peak occurs in the axial force as the tool steps down [4]. As SPIF becomes more commonly applied it might be expected that CAM programs will have a SPIF option for producing helical tool paths suitable for SPIF. Until this happens other solutions must be found.

The program Pro Engineer, which is applied in the present work, has a surface milling feature called “helical”, but it only works for SPIF if the geometry is axis symmetric. For non axis symmetric geometries the tool moves axially within one contour and the path cannot be considered helical. For a pyramid the tool plunges deeper in the corners causing a bulging of the bottom. This bulging results in fracture or non-planar bottom after forming.

Filice et al. used a helical tool path for formability testing [3]. This tool path was made using an Excel worksheet instead of commercial CAM software. This approach only works where the overall part geometry may be given as a simple mathematical expression. This paper presents a solution in the form of a dedicated program which converts a profile tool path to a helical tool path. The input for the program is the coordinates from the profile tool path. This means that milling software is still needed and the program can be thought of as an extra post processing.

Geometries

Three geometries are used for testing the program. Fig. 1 is a 196x196x55 mm pyramid with a 60° wall angle. Fig. 2 is a 196 mm diameter cone, 90 mm deep with a 45° wall angle converging into a triangle. Fig. 3 is a complex part inspired from the upper part of a truck muffler with wall angles ranging from 0° to 65°. The geometries are chosen to see how the program removes the scarring on planar sides on the pyramid, on curved sides on the cone and how it works for a complex part, such as the muffler part.

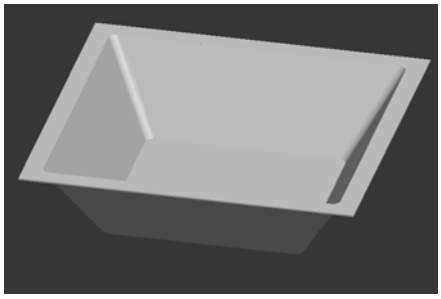

Fig. 1 Pyramid

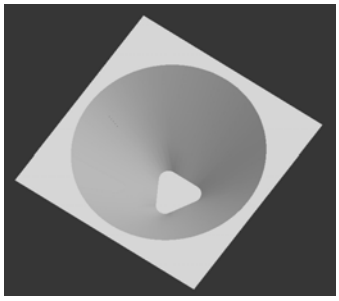

Fig. 2 Cone

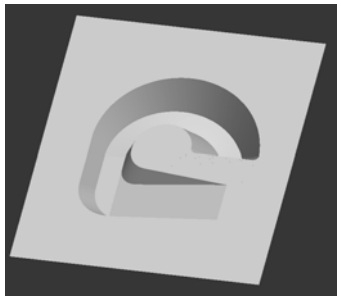

Fig. 3 Muffler

The program

The idea of the program is simple. Instead of going directly from a CAD model to a helical tool path, a profile tool path is used as an intermediate step. The coordinates of a profile tool path contain information about the geometry and also divides the geometry into layers. The thickness of the layers is the same as the chosen step size.

A simple example is used to illustrate how the program calculates the coordinates. Fig. 4 shows the points of two profiles belonging to two subsequent planes or layers of a geometry. For simplicity the number of points in each profile is limited to five and the profiles have been folded out. Points number 1 and 5 are the first and the last point on the periphery, which are coinciding. To begin with the program calculates the distance between the points in plane 1. They are summed up to $L_{1,total}$ see Eq. 1. The program also calculates the distances between each point in plane 1 and all the points in plane 2. As an example the distance between $P_{1,1}$ and $P_{2,1}$ is calculated in Eq. 2. This is used by the program to identify which point in plane 2 which is closest to each of the points in plane 1.

$P_{2,1}$ is identified as the closest point to $P_{1,1}$ in plane 2. The three coordinates for the first helical point is calculated in Eq. 3 to 5. The first helical point becomes the same point as $P_{1,1}$. The X coordinates for the second and third helical points are calculated in Eq. 6 and 7. Y and Z coordinates can be calculated in the same way. The X coordinate for the final helical point is calculated in Eq. 8 and this point is the same as $P_{2,5}$. The helical points and helical tool path are indicated in Fig. 4. The helical points are located where the helical tool path crosses the dashed lines.

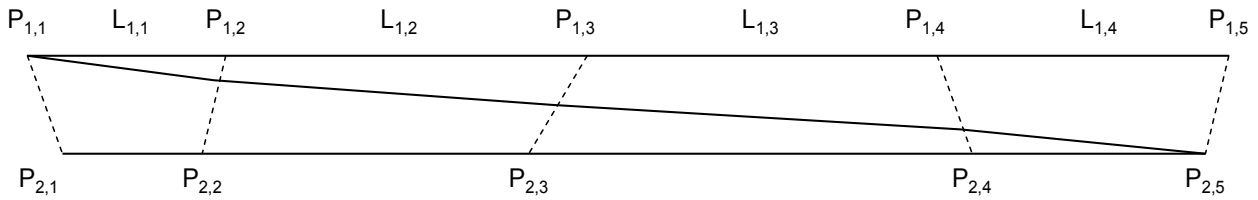

Fig. 4 Schematic outline of two subsequent, out-folded profiles and calculated points along helical tool path

In Fig. 4 the helical tool path is not a straight line between $P_{1,1}$ and $P_{2,5}$. For a real profile tool path $L_{1,total}$ will be much larger than the step size which will result in a much more continuous helical tool path.

$$L_{1,total} = L_{1,1} + L_{1,2} + L_{1,3} + L_{1,4} \tag{1}$$

$$D_{P1,1-P2,1} = \sqrt{\left(x_{2,1} - x_{1,1}\right)^2 + \left(y_{2,1} - y_{1,1}\right)^2 + \left(z_2 - z_1\right)^2} \tag{2}$$

$$x_{hel,1} = \frac{0}{L_{1,total}} \cdot \left(x_{2,1} - x_{1,1}\right) + x_{1,1} = x_{1,1} \tag{3}$$

$$y_{hel,1} = \frac{0}{L_{1,total}} \cdot \left(y_{2,1} - y_{1,1}\right) + y_{1,1} = y_{1,1} \tag{4}$$

$$z_{hel,1} = \frac{0}{L_{1,total}} \cdot \left(z_2 - z_1\right) + z_1 = z_1 \tag{5}$$

$$x_{hel,2} = \frac{L_{1,1}}{L_{1,total}} \cdot \left(x_{2,2} - x_{1,2}\right) + x_{1,2} \tag{6}$$

$$x_{hel,3} = \frac{L_{1,1} + L_{1,2}}{L_{1,total}} \cdot \left(x_{2,3} - x_{1,3}\right) + x_{1,3} \tag{7}$$

.
.

$$x_{hel,5} = \frac{L_{1,1} + L_{1,2} + L_{1,3} + L_{1,4}}{L_{1,total}} \cdot \left(x_{2,5} - x_{1,5}\right) + x_{1,5} = x_{2,5} \tag{8}$$

Generalized expressions for helical coordinates $x_{hel,n}$, $y_{hel,n}$, $z_{hel,n}$, for a given point *n* in a given plane *p* can be seen in Eq. 9 to Eq. 11.

$$x_{hel,n} = \sum_{i=1}^{n-1} \frac{L_{p,i}}{L_{p,total}} \cdot \left(x_{p+1,cl} - x_{p,n}\right) + x_{p,n} \tag{9}$$

$$y_{hel,n} = \sum_{i=1}^{n-1} \frac{L_{p,i}}{L_{p,total}} \cdot \left(y_{p+1,cl} - y_{p,n}\right) + y_{p,n} \tag{10}$$

$$z_{hel,n} = \sum_{i=1}^{n-1} \frac{L_{p,i}}{L_{p,total}} \cdot (z_{p+1} - z_p) + z_p \tag{11}$$

Where $x_{p+1,cl}$ and $y_{p+1,cl}$ are the coordinates in the plane $p+1$ which are closest to the coordinates $x_{p,n}$ and $y_{p,n}$ in the plane p as seen in Eq. 12. The last term in Eq. 12 could be removed, but is kept so as to use the actual distance. The distance between a given point n in the plane p and the following point $n+1$ is given in Eq. 13. The total curve length from the first to the last point in the plane p *is* given in Eq. 14 where t is the total number of points in the plane p.

$$D_{\min} = \sqrt{(x_{p+1,cl} - x_{p,n})^2 + (y_{p+1,cl} - y_{p,n})^2 + (z_{p+1} - z_p)^2} \tag{12}$$

$$L_{p,n} = \sqrt{(x_{p,n+1} - x_{p,n})^2 + (y_{p,n+1} - y_{p,n})^2} \tag{13}$$

$$L_{p,total} = \sum_{i}^{t-1} L_{p,i} \tag{14}$$

To get a clear definition of the part, the program preserves the first and the last layer of the profile tool path. This means that the program starts out with a constant Z value for the first layer. As it passes the starting point it starts the helical tool path. When it reaches the lowest Z value it finishes this layer with a constant Z value. In Fig. 5 for illustrative purposes the step size is set to 10 mm for the pyramid and the helical tool path is shown in Fig. 6. Fig. 7 and Fig. 8 compare a section of the tool path for the cone before and after the helical program is used.

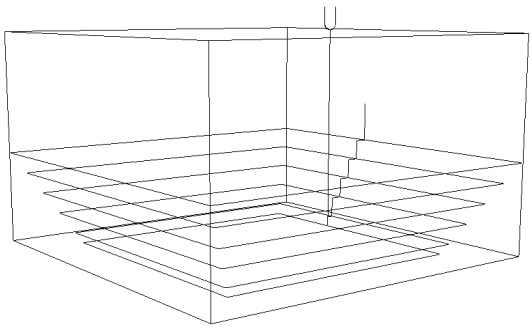

Fig. 5 Profile tool path for pyramid with 10 mm step size

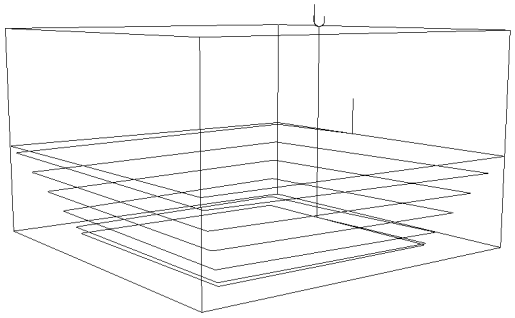

Fig. 6 Helical tool path for pyramid with 10 mm step size

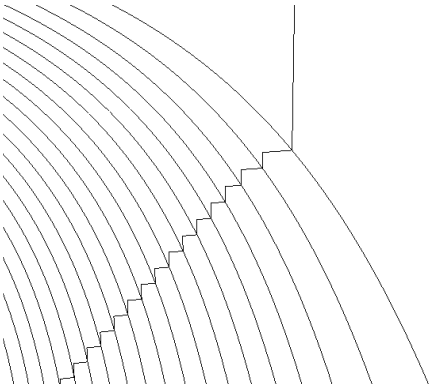

Fig. 7 Profile tool path for the cone

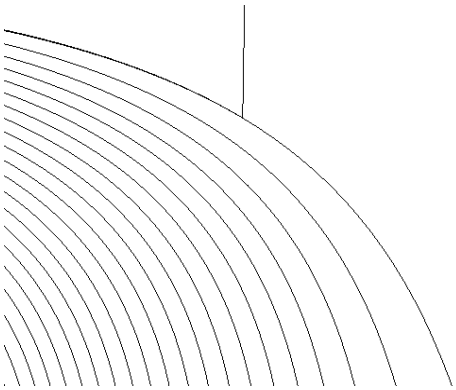

Fig. 8 Generated helical tool path for the cone

Testing

The testing is aimed at demonstrating that the program works. A visual comparison is made between the parts made with the original profile tool path and the parts made with the helical tool path. The process parameters are: tool diameter 12 mm, feed rate 1000 mm/min, step size 0.5 mm, tool rotational speed 35 1/min and ProE tolerance is 0.01 mm. Lubrication is diluted cutting fluid and the milling machine is a Cincinnati Milacron - Sabre 750.

Pyramid. A big difference is noticed between the pyramid made with a profile tool path and a helical tool path. On the outer surface the scarring is removed completely, see Fig. 9 and Fig. 10. Also on the inside the scarring is removed, but a shadow remains where the scarring used to be. This is caused by a change in point density which causes the actual feed rate of the CNC machine to decrease a bit. The change in point density is created because the helical program leaves a point where the step down used to be. Since these points are placed along a line down the side they become visible. The shadow is barely visible, cannot be felt and is difficult to catch with a camera, see Fig. 11 and Fig. 12.

Fig. 9 Outer surface of pyramid made with profile tool path

Fig. 10 Outer surface of pyramid made with helical tool path

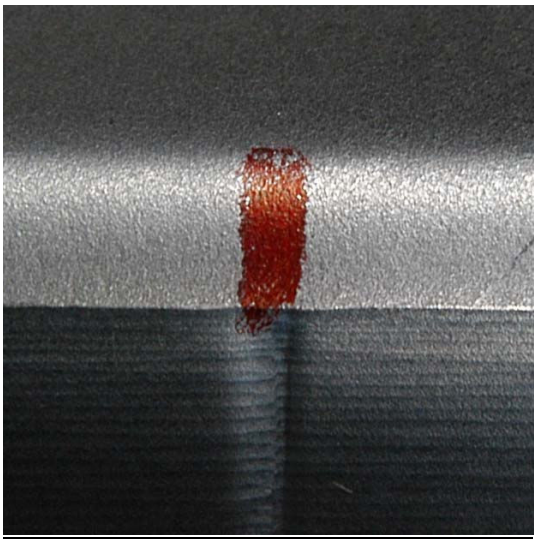

Fig. 11 Inner surface of pyramid made with profile tool path

Fig. 12 Inner surface of pyramid made with helical tool path

Cone. Like for the pyramid the scarring is removed completely on the outside. On the inside a barely visible shadow remains, see Fig. 13 to Fig. 16.

Fig. 13 Outer surface of cone made with profile tool path

Fig. 14 Outer surface of cone made with helical tool path

Fig. 15 Inner surface of cone made with profile tool path

Fig. 16 Inner surface of cone made with helical tool path

Muffler. The muffler is an example of a geometry where the program does not work without modifications. The output contains an error in the layer which contains a horizontal plateau connecting the upper and the lower two sections of the muffler seen in Fig. 17 and Fig. 18. The error, which is marked with an arrow in Fig. 19, is a logical result of the way the program calculates. When determining the helical points for the last plane in section 1 and finding the corresponding points closest in the first plane in section 2, these points will be far from each other. This happens because the geometry contains a horizontal plateau which is not the bottom of the geometry.

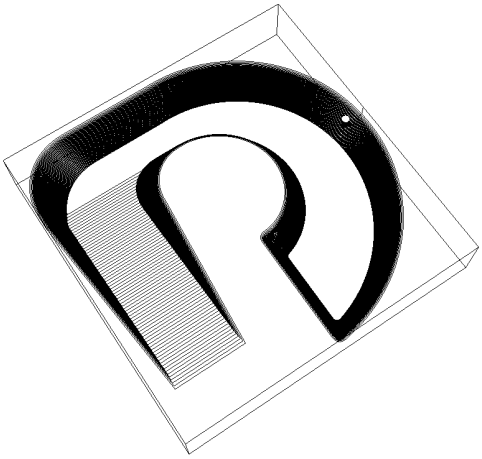

Fig. 17 Section 1 of the muffler,
tool path for Z from 0 mm to -35.5 mm

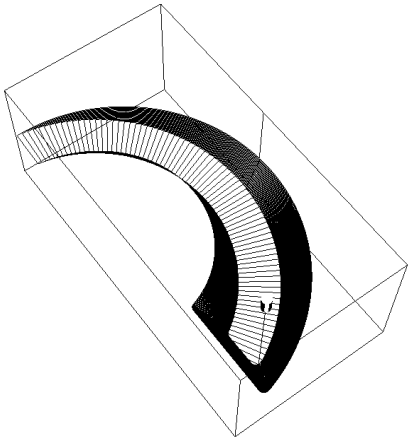

Fig. 18 Section 2 of the muffler,
tool path for Z from -35.5 mm to -74 mm

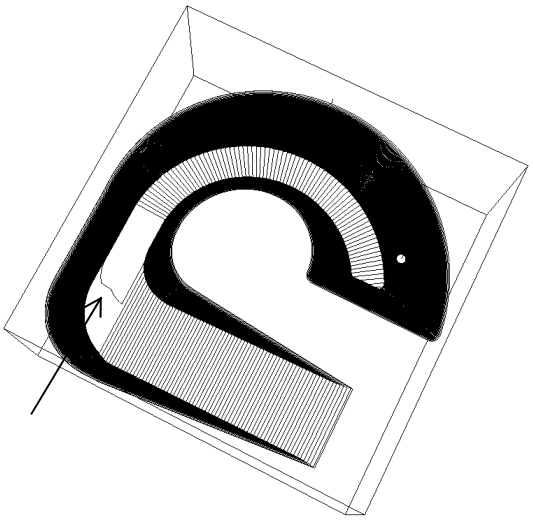

Fig. 19 Helical tool path for muffler

A way to work around this is to use the helical program on each section separately and then combine the two helical outputs. This results in a working tool path with only one non helical layer where the two helical outputs are linked. Compared with the muffler made with a profile tool path the result is still a huge improvement, see Fig. 20 and Fig. 21.

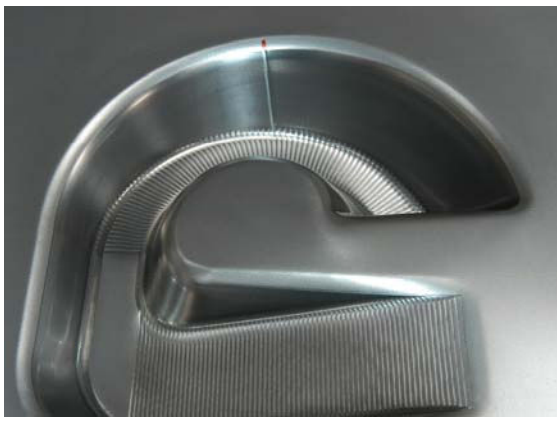

Fig. 20 Muffler made with profile tool path

Fig. 21 Muffler made with helical tool path

Discussion

The helical program works as expected for the pyramid and the cone. For the muffler the coordinates have to be split up into two sections in order to produce the required part. This is not practical so the helical program does not remove the need for CAM software designed for SPIF entirely. However for most parts the program will work without problems.

Using continues feed in three directions can be a problem for some CNC milling machines. The Cincinnati machine used for testing has problems maintaining a constant feed rate when applying feed in all three directions X, Y and Z at the same time. For feed rates higher than 1000 mm/min the machine starts to vibrate. Using the profile tool path the machine can handle 2000 mm/min without problems since it only moves in two axes at a time. This problem is caused by the high feed rates used in SPIF compared to milling. It has not been investigated whether this is only a problem for the machine applied or a general problem.

For the three geometries the step size is set to 0.5 mm. If another step size or point density is requested this can be done by creating a profile tool path with the required settings and converting this into a helical tool path. The use of the helical program does not prevent adjustments of step size or point density.

Conclusion

The helical program offers an easy and inexpensive way of using helical tool paths for SPIF parts. All that is needed is a CAM program for creating a profile tool path and the helical program. In this way the scarring created by a profile tool path is removed.

The helical program can be required by contacting the authors.

Acknowledgement

The authors would like to thank Joergen Dai Jensen, Kasper Leth Friis, Benjamin Hald and Peter Soee Nielsen for providing Pro Engineer files of the geometries used for testing.

References

[1] E. Leszak: *Apparatus and Process for Incremental Dieless Forming*, Patent US3342051A1, published 1967-09-19

[2] J. Jeswiet, E. Hagan: *Rapid Proto-typing of a Headlight with Sheet Metal*, Technical Paper - Society of Manufacturing Engineers, 2002, p. 1-6

[3] L. Filice, L. Fratini, F. Micari: *Analysis of Material Formability in Incremental Forming*, Annals of the CIRP 51/1/2002, p.199

[4] J. Jeswiet, F. Micari, G. Hirt, A. Bramley, J. Duflou, J. Allwood: *Asymmetric Single Point Incremental Forming of Sheet Metal*, Annals of the CIRP 54/2/2005, p.623

February 2008

Joint author statement

If a thesis contains articles made in collaboration with other researchers, a joint author statement about the PhD-student's part of the article shall be made by each of the co-authors, cf. article 12, section 4 of the Ministerial Order No. 18 February 2008 about the PhD degree

Title of the article: Single point incremental forming using a dummy sheet

Author(s): M. Skjoedt, M. B. Silva, N. Bay, P. A. F. Martins, T. Lenau

Journal: Conference paper, 2nd ICNFT (2nd Int. Conf. on New Forming Technologies), Bremen, Germany, Sep. 20-21, (2007) Conference proceedings, BIAS-Verlag, p. 267-276.

PhD-student: Martin Skjødt Cpr.nr: _____

Signature of the PhD-student: _____ Date: _____

Co-author: _____ Signature: _____

Description of each author's contribution to the above-mentioned article:

M. Skjoedt: Original idea of using a dummy sheet, CAD drawing of parts, CAM programming of parts, planning and conduction of experiments, measurements, statistical analysis of results, literature study, writing of paper, pictures and graphics for paper, final editing.

M. B. Silva: Conduction of experiments, final editing.

N. Bay: Discussions and final editing.

P. A. F. Martins: Final editing.

T. Lenau: Final editing.

2nd International Conference on New Forming Technology, Bremen, September 20-21, 2007

Single Point Incremental Forming using a Dummy Sheet

M. Skjoedt[1], M. B. Silva[2], N. Bay[1], P. A. F. Martins[2], T. Lenau[1]

[1]Technical University of Denmark, Department of Manufacturing Engineering and Management, DTU - Building 425, DK-2800, Kgs. Lyngby, Denmark

[2]IDMEC, Instituto Superior Tecnico, TULisbon, Av. Rovisco Pais, 1049-001 Lisboa, Portugal

Keywords: Incremental forming, dummy sheet, friction, wear, surface quality, roughness.

Abstract

A new version of single point incremental forming (SPIF) is presented. This version includes a dummy sheet on top of the work piece, thus forming two sheets instead of one. The dummy sheet, which is in contact with the rotating tool pin, is discarded after forming. The new set-up influences the process and furthermore offers a number of new possibilities for solving some of the problems appearing in SPIF. Investigations of the influence of dummy sheet on: formability, wear, surface quality and bulging of planar sides is done by forming to test shapes: a hyperboloid and a truncated pyramid. The possible influence of friction between the two sheets is furthermore investigated. The results show that the use of a dummy sheet reduces wear of the work piece to almost zero, but also causes a decrease in formability. Bulging of the planar sides of the pyramid is reduced and surface roughness is increased. Lowering of friction between the two sheets by lubrication only influences roughness. Suggestions for applications of this new technique are discussed, among those SPIF of tribologically difficult materials like titanium and soft aluminium.

1 Introduction

SPIF is a relatively new sheet forming process. A sheet is clamped in a rig and formed incrementally using a rotating single point tool in the form of a rod with a spherical end, **Figure 1**. The process was discovered in 1967 when Leszak patented the concept of forming sheets incrementally by using a single point tool [1]. This concept was proven by Kitazawa et al. [2] by forming rotational symmetric parts in aluminium. The use of an ordinary milling machine for this process was later investigated by Jeswiet et al. [3] and Filice et al. [4]. A comprehensive overview of research on SPIF may be found in the keynote paper by Jeswiet et al. [5].

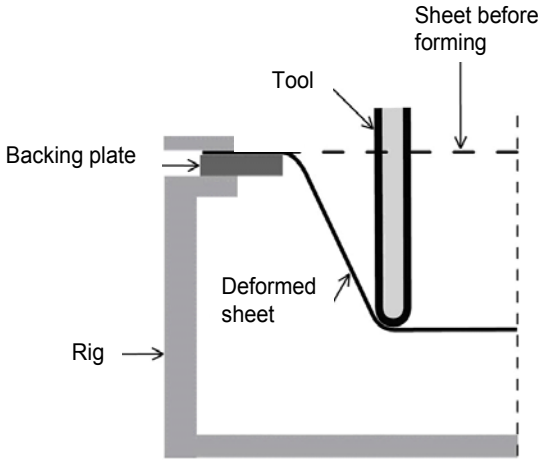

Figure 1: Schematic illustration of SPIF

1.1 Dummy sheet setup

The set-up with a dummy sheet implies forming two sheets together, **Figure 2**. The top sheet is the dummy, which may be discarded after forming. In traditional SPIF the work piece surface will be affected by the sliding of the forming tool. Using a dummy sheet the sliding is only affecting the dummy. The relative movement between dummy and work piece sheet is neglible. The dummy is an extra cost, but since SPIF is only an option for small quantity production or prototyping, the price of the dummy sheet is small compared to initial costs and the production costs.

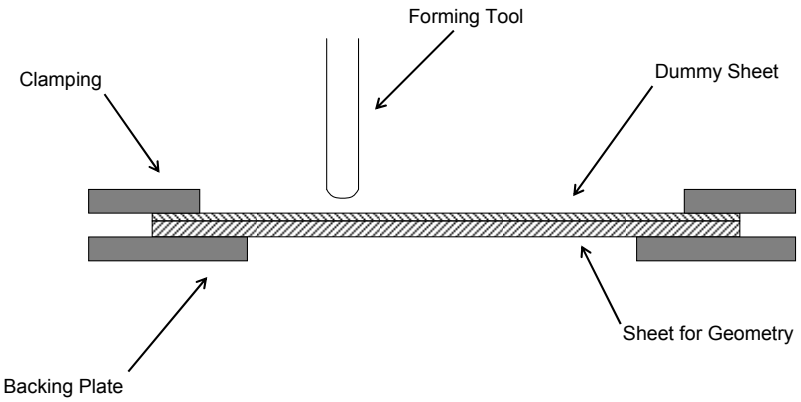

Figure 2: SPIF using a dummy sheet

Forming two sheets together will increase applied forming loads. In most cases it will be desirable to keep the thickness of the dummy sheet at a minimum. Interface friction and difference in stress-strain characteristics of work piece and dummy sheet will determine, whether the sheets act like one sheet or like two separate sheets during forming.

1.2 Geometries

Two geometries are used for testing. **Figure 3** is a 55 mm deep 196x196 mm truncated pyramid with a 60° wall angle. **Figure 4** is a hyperboloid with increasing wall angle in vertical 15 mm sections and an initial diameter of 162 mm.

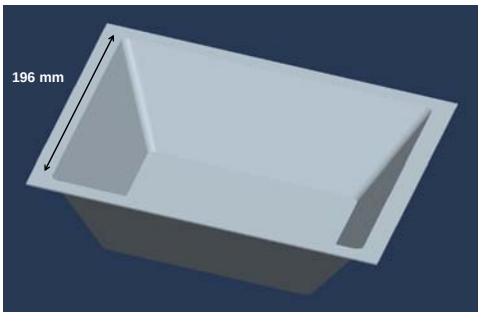

Figure 3: Truncated pyramid

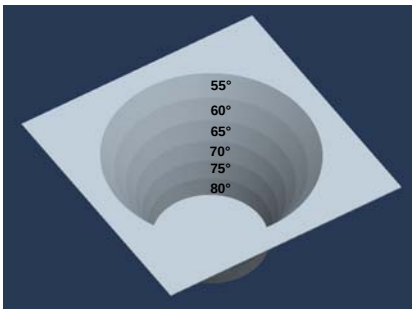

Figure 4: Hyperboloid in steps

The pyramidal geometry is chosen to investigate whether the dummy may suppress the problem of bulging of the four planar sides, which has been shown experimentally and by modelling [6;7]. The hyperboloid is used to compare formability with and without the dummy sheet. The increasing wall angle ensures a fracture before the tool reaches the bottom, **Figure 5**. In the present investigation the maximum depth before fracture is used as a measure of formability, but this depth also indicates the maximum wall angle for geometries similar to a cone.

Figure 5: Fracture when forming the hyperboloid

2 Experimental set-up

All experiments in the main investigation are carried out using DC01 deep drawing steel. The dummy sheet is 0.5 mm thick and the work piece sheet is 1 mm. Three methods are compared:

a) traditional SPIF of a single sheet

b) SPIF with a dummy sheet with lubrication between the two sheets

c) SPIF with a dummy sheet with dry friction between the two sheets

The lubricant applied between the forming tool and the top sheet (dummy or work piece) is diluted cutting fluid. The tool path is a helical tool path generated with the program HeToPaC [8]. This is done because the CAM program used is not able to generate a truly helical tool path. The step size per revolution is 0.5 mm and a backing plate is used. The forming tool has a diameter of ø12 mm and a spherical tip. The speed of rotation is 35 rpm and feed rate is 1000 mm/min. As lubricant between the

two sheets a high viscosity plain mineral oil is applied. In the tests with dry friction between sheets these are cleaned with alcohol. Two replicates are done for each combination of method and geometry which allows for a statistical analysis. The experiments are performed in a random order.

3 Results

Results are analyzed using STATGRAPHICS plus 5.1. In all graphs the bars indicate 95% least significant difference. This means that there is a significant difference between the mean values when the arrows do not overlap.

3.1 Formability

Formability is tested by comparing the fracture depths of the hyperboloid. As seen from **Figure 6** the introduction of a dummy sheet clearly decreases formability. For traditional SPIF the average fracture depth is 69 mm which is in the 75° section of the hyperboloid. There is no significant difference between dry friction and lubrication between the sheets. The average fracture depth is around 54 mm corresponding to the 70° section of the hyperboloid. The use of a dummy sheet thus seems to reduce the maximum wall inclination about 5° for this geometry.

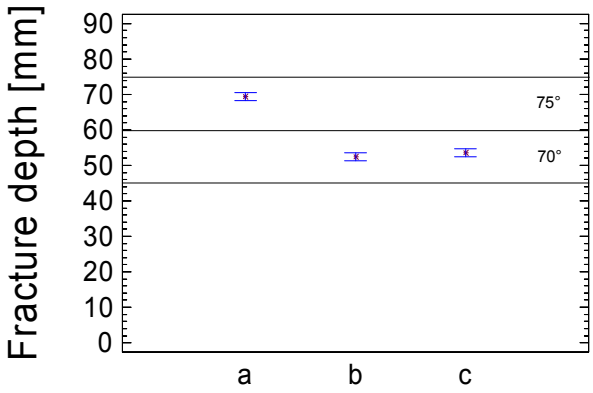

Figure 6: Fracture depth for the hyperboloid for three SPIF methods

It is of interest to compare these results with fracture depths of single sheets in the same material but with different thicknesses. **Figure 7** shows increasing formability with increasing thickness in accordance with results by Jeswiet et al. [9] for aluminium. The combination of dummy sheet and a work piece sheet has a thickness of 1.5 mm, but as seen from **Figure 6** the formability is far lower than for a single 1.5 mm sheet, which can be formed with an 80° angle. In fact the formability of the combined sheets is lower than that of a single 0.5 mm sheet, which can be formed to 75°.

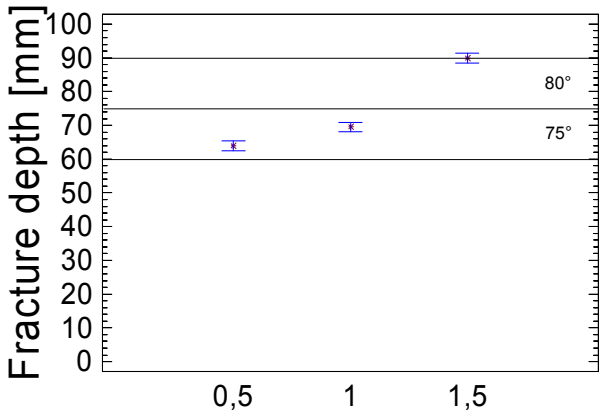

Figure 7: Fracture depth as function of sheet thickness in mm for DC01 steel

The reasons for the reduced formability are not investigated in detail in the present work. A possible explanation is that forming with a dummy sheet corresponds to forming the work piece sheet with a larger tool diameter. It has been shown by Hirt et al. [10] that increasing the tool diameter decreases the formability when forming a pyramid in DC04 steel.

3.2 Wear

Wear of the formed components is determined by comparing the weight before and after forming for both geometries. The wear (in grams) is converted into an average thickness by using the deformed area. The level of friction between the sheets has no significant influence on wear. Therefore method b and c are merged to compare traditional SPIF with SPIF using a dummy sheet, **Figure 8**. The average wear found in traditional SPIF is 0.25 µm and wear is close to zero when using a dummy sheet.

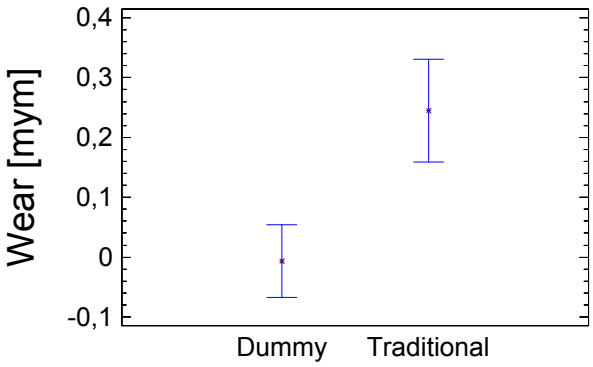

Figure 8: Average wear for traditional SPIF vs. SPIF using a dummy sheet

3.3 Surface Quality

A clear difference is noticed in appearance between the parts made by traditional SPIF and the parts made with a dummy sheet as seen in **Figure 9** to **Figure 12**. The upper surface is rougher when using a dummy sheet because the smoothening effect of the tool is lost. Another phenomenon contributing to the rough surface could be that the dummy sheet allows free change in grain orientation during deformation. The rough

surface is not due to wear since wear is measured to being zero when using a dummy sheet. Measured roughness is also increased using a dummy sheet, **Figure 13**. Dry condition between sheets result in a lower roughness compared to using mineral oil between sheets.

Figure 9: Pyramid formed with traditional SPIF

Figure 10: Pyramid formed using a dummy sheet with dry friction

Figure 11: Surface of hyperboloid formed with traditional SPIF

Figure 12: Surface of hyperboloid using a dummy sheet with dry friction

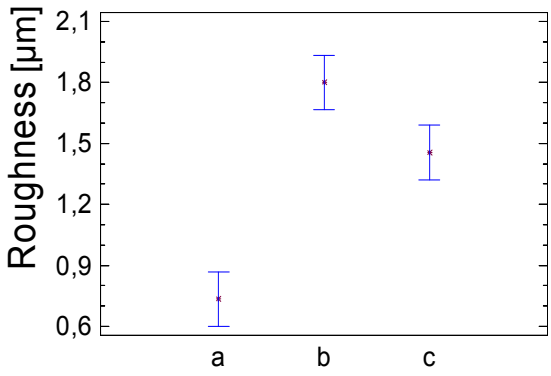

Figure 13: Measured R_a roughness for the three SPIF methods

3.4 Bulging of pyramidal sides

Bulging of the planar sides of the pyramid is measured using a hole depth caliper placed on side of the pyramid. The measured distance is between the middle of a straight line going from the corners of the pyramid and the formed surface, **Figure 14**.

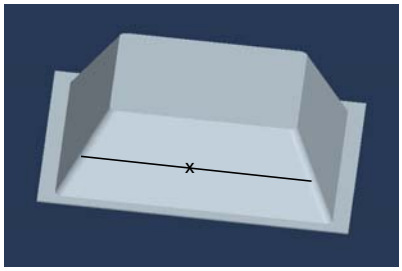

Figure 14: Position of measuring bulging on pyramid sides

The use of a dummy sheet reduces the bulging from 1.93 mm to 1.73 mm, which is a 10% reduction, **Figure 15**. No difference between method b and c is observed.

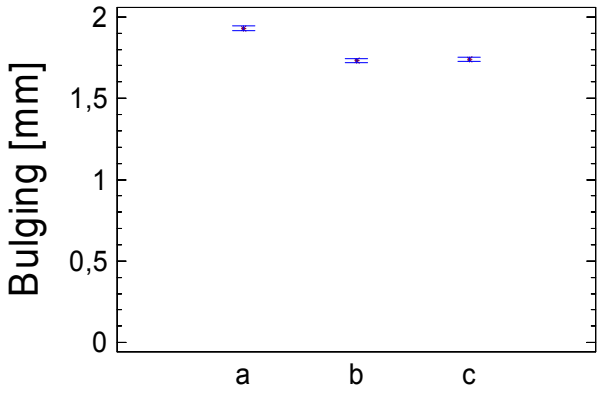

Figure 15: Results for bulging of the sides of the pyramid

4 Applications

4.1 Forming of soft aluminum sheets

Forming of AA1050 H111 aluminum sheets of 1.5 mm thickness or more causes surface quality problems due to galling (pick-up of work piece material on the tool and subsequent scoring of the work piece surface). In some cases the tool removes considerable amount of work piece surface resulting in very poor surface quality, **Figure 16**. This problem can be solved using a steel dummy sheet avoiding direct contact of the tribologically difficult work piece material with the rotating tool, **Figure 17** and **Figure 18**.

Figure 16: Severe galling in forming of hyperboloid in 2 mm AA1050 H111

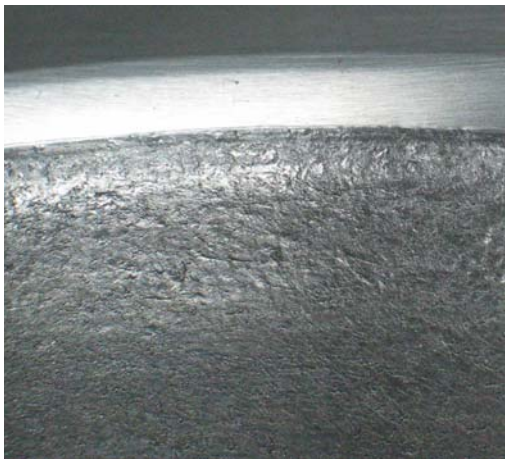

Figure 17: Signs of galling in SPIF of 1.5 mm AA1050 H111

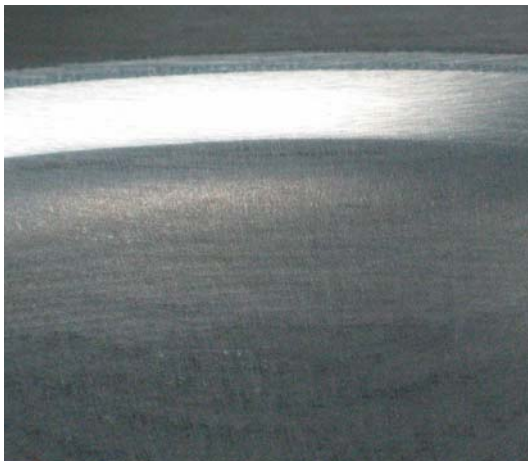

Figure 18: Surface quality in SPIF of 1.5 mm AA1050 H111 using a 0.63 mm DC04 steel dummy sheet

To ensure that the good surface quality obtained with a 1 mm sheet compared to 1.5 and 2.0 mm, is not due to variations in material properties, two 1 mm sheets are formed on top of each other. The result is galling similar to that obtained with the 2 mm sheet, **Figure 19** and **Figure 20** The problem might also be solved by using a larger tool or decreasing the step size, but this has yet to be investigated.

Similar results as those shown in **Figure 17** and **Figure 18** are found when using a 2 mm AA1050 H111 sheet and when forming a pyramid. The increase in roughness seen in **Figure 9** to **Figure 12**, when forming two sheets of the same material, is not observed when forming AA1050 H111 with a steel dummy sheet. In fact the work piece surface changes from a rough and worn surface to a smooth surface.

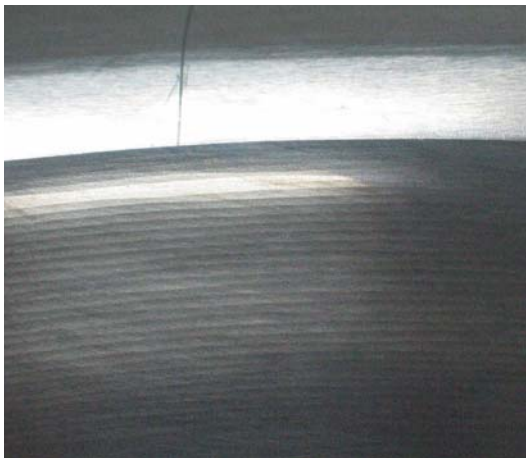

Figure 19: No signs of galling in SPIF of 1 mm AA1050 H111

Figure 20: Galling on top sheet when forming two 1 mm AA1050 H111 sheets

The reduction of formability observed when forming two steel sheets together in **Figure 6**, is not observed when combining an aluminum sheet with a steel dummy sheet. In case of AA1050 H111 sheets of thickness 1.5 and 2 mm formability seems to be increased about 5° when using a 0.63 mm DC04 dummy sheet. The improved formability of 1.5 and 2 mm AA1050 H111, when using a dummy compared to that without, is most likely due to the poor surface quality in the latter case causing an early fracture.

4.2 Other possible applications

The possible applications of a dummy sheet on top of the work piece sheet are numerous. In cases where the contact between forming tool and part causes tribological problems the dummy sheet has already proven to be a solution as regards forming of aluminum. A similar application is suggested to solve the problem of galling of titanium sheets mentioned by Tanaka et al. [11] in forming a denture plate. Other applications could be forming of precoated sheets, perforated sheets and wire meshes.

4.3 Dummy sheet as the bottom sheet

The dummy sheet is not limited to being the top one contacting the tool pin. It might also be placed beneath the work piece sheet in order to increase formability. This idea will be subject for future work by the authors. In special cases two dummy sheets might be used creating a sandwich construction. The top dummy solves the tribological problems and the bottom one increases formability.

5 Conclusion

The use of dummy sheets offers a number of potentials for improving the SPIF process. The three most obvious variables to study as regards the dummy sheet are thickness, material and position (top or bottom). It has been shown that wear of the work piece sheet is removed and that bulging of planar sides is reduced. Further

investigations need to be done as regards the influence of thickness and different material combinations. It is believed that the right combinations will also allow for improving formability using the dummy as the bottom sheet.

6 Acknowledgement

Beatriz Silva and Paulo Martins would like to acknowledge PTDC/EME-TME/64706/2006 FCT/Portugal for the financial support.

7 References

1. Leszak E: Apparatus and Process for Incremental Dieless Forming. Patent US3342051A 1967.

2. Kitazawa K, Wakabayashi A, Murata K, Yaejima K: Metal-flow phenomena in computerized numerically controlled incremental stretch-expanding of aluminum sheets. Keikinzoku/Journal of Japan Institute of Light Metals 1996;46:65-70.

3. Jeswiet J: Incremental Single Point Forming. Technical Paper - Society of Manufacturing Engineers MF 2001.

4. Filice L, Fratini L, Micari F: Analysis of material formability in incremental forming. CIRP Annals - Manufacturing Technology 2002;51:199-202.

5. Jeswiet J, Micari F, Hirt G, Bramley A, Duflou J, Allwood J: Asymmetric single point incremental forming of sheet metal. CIRP Annals - Manufacturing Technology 2005;54:623-649.

6. Bambach M, Hirt G, Ames J: Modeling of optimization strategies in the incremental CNC sheet metal forming process. AIP Conference Proceedings 2004;1969-1974.

7. Qin Q, Masuku ES, Bramley A, Mileham AR, Owen GW: INCREMENTAL SHEET FORMING SIMULATION AND ACCURACY. ICTP Verona 2005.

8. Skjoedt M, Hancock MH, Bay N: Creating Helical Tool Paths for Single Point Incremental Forming. Key Engineerint Materials - Sheet Metal 07 2007;344:583-590.

9. Jeswiet J, Hagan E, Szekeres A: Forming parameters for incremental forming of aluminium alloy sheet metal. Proceedings of the Institution of Mechanical Engineers, Part B: Journal of Engineering Manufacture 2002;216:1367-1371.

10. Hirt G, Junk S, Bambach M, Chouvalova I: Process limits and material behaviour in incremental sheet forming with CNC-tools. Materials Science Forum 2003;426-432:3825-3830.

11. Tanaka S, Nakamura T, Hayakawa K, Nakamura H, Motomura K: INCREMENTAL SHEET METAL FORMING PROCESS FOR PURE TITANIUM DENTURE PLATE. ICTP Verona 2005.

February 2008

Joint author statement

If a thesis contains articles made in collaboration with other researchers, a joint author statement about the PhD-student's part of the article shall be made by each of the co-authors, cf. article 12, section 4 of the Ministerial Order No. 18 February 2008 about the PhD degree

Title of the article: Estampagem incremental de 'tailored blanks'

Author(s): M.B. Silva, M. Skjoedt, L.M. Alves, P. Vilaça, N. Bay, P.A.F. Martins

Journal: Conference paper, XXVII SENAFOR, Porto Alegre, Brazil, Oct. 18-19, (2007), Conference proceedings, p. 239-253.

PhD-student: Martin Skjødt Cpr.nr:

Signature of the PhD-student: Date:

Co-author: Signature:

Description of each author's contribution to the above-mentioned article:

M. B. Silva: Planning and conduction of experiments, measurement of strains, analysis of results, friction stir welding, pictures and graphics for paper, literature study, final editing.

M. Skjoedt: CAD drawing of parts, CAM programming of parts, planning and conduction of experiments, final editing.

L. M. Alves: Final editing.

P. Vilaça: Friction stir welding, Final editing.

N. Bay: Final editing.

P. A. F. Martins: Planning of experiments, writing of paper, graphics for paper, final editing.

ESTAMPAGEM INCREMENTAL DE 'TAILORED BLANKS'

Silva M. B. (1),
Skjoedt M. (2),
Alves L. M. (1),
Vilaça P. (1),
Bay N. (2)
Martins P. A. F. (1,)*
(1) IDMEC, Instituto Superior Técnico, TULisbon,
Av. Rovisco Pais, 1049-001 Lisboa; Portugal
(2) Technical University of Denmark, Department of Manufacturing Engineering and Management, DTU - Building 425, DK-2800, Kgs. Lyngby, Denmark

RESUMO

Este artigo apresenta um estudo experimental inédito que se desenvolve em torno da avaliação do desempenho de 'tailored blanks' de alumínio AA1050-H111 durante operações de estampagem incremental. O trabalho envolveu a produção de 'tailored blanks' por intermédio de soldadura por fricção linear e a realização de ensaios de enformabilidade destinados a comparar a enformabilidade dos 'tailored blanks' com a de chapas de referência não-soldadas do mesmo material.

Os 'tailored blanks' foram produzidos a partir de sub-conjuntos de chapas com espessuras de 1.5 mm e 2 mm e os cordões de soldadura foram realizados segundo direcções paralelas e perpendiculares à de laminagem. A opção por limitar o trabalho de investigação a 'tailored blanks' em que apenas se faz variar a espessura, mantendo-se inalteravel o tipo material e de acabamento superficial, teve por objectivo reduzir o número de variáveis e, desta forma, analisar exclusivamente a influência do cordão de soldadura na enformabilidade geral da estampagem incremental.

Palavras-chave: Estampagem incremental, soldadura por fricção linear, experimentação.

(*) Autor para correspondência. Fax: +351-21-8419058 E-mail: pmartins@ist.utl.pt

1. INTRODUÇÃO

Os processos de deformação plástica incremental têm vindo a registar um desenvolvimento crescente uma vez que as suas características se adequam muito bem a algumas das novas exigências do mercado, como sejam o fabrico rápido de protótipos, a produção de pequenas séries de fabrico e a produção de peças que, por possuírem uma complexidade geométrica elevada, sejam muito difíceis, ou até mesmo impossíveis, de obter por intermédio de tecnologias convencionais.

A estampagem incremental é um novo processo de deformação plástica de chapa que associa as características anteriormente referidas ao facto de poder ser realizada nas máquinas-ferramenta CNC que são habitualmente utilizadas em corte por arranque de apara, sem que para tal seja necessário proceder a investimentos significativos.

A figura 1 apresenta os elementos básicos do processo; (i) a chapa a deformar plasticamente, (ii) o encostador, (iii) a placa-espera e (iv) a ferramenta de extremidade esférica. A ferramenta tem movimento de rotação em torno do seu eixo e movimento de translação. O movimento de translacção da ferramenta é gerado no comando numérico da máquina-ferramenta onde se realiza a operação e é acompanhado de indexação vertical progressiva de modo a deformar plasticamente a chapa até ser obtida a forma final desejada.

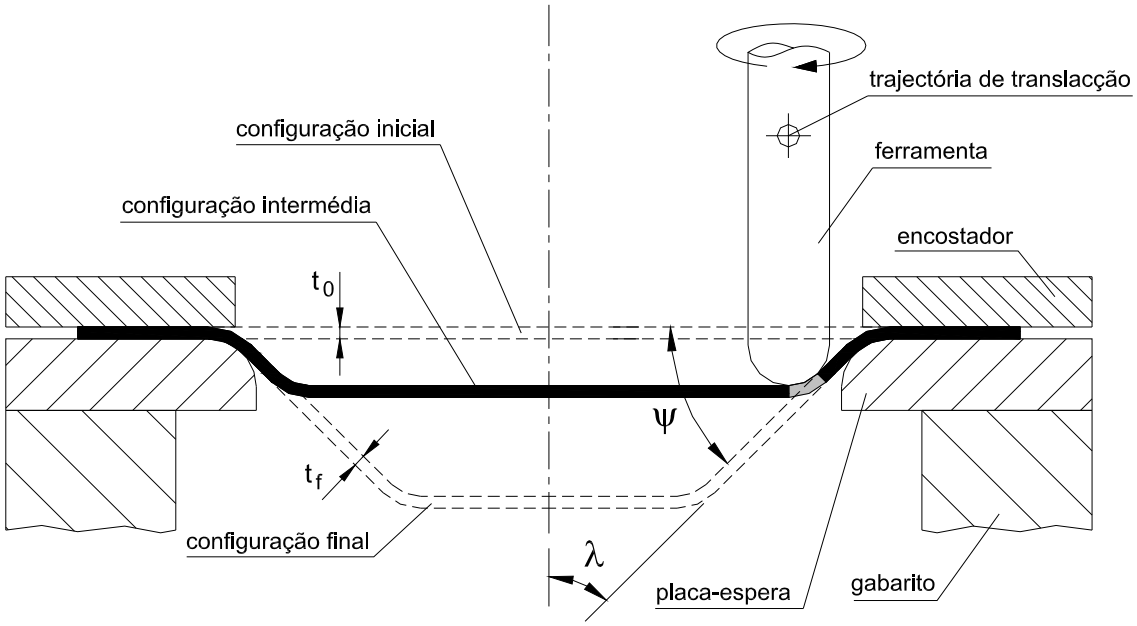

Figura 1 – Representação esquemática do processo de estampagem incremental.

A estampagem incremental foi patenteada por Leszak em 1967 [1] mas a sua viabilidade tecnológica apenas foi demostrada em 1996 após Kitazawa e colaboradores [2] terem fabricado com sucesso um componente de alumínio com simetria de revolução. Os trabalhos subsequentes de Jeswiet [3], Micari [4] e colaboradores não só vieram confirmar a viabilidade do processo bem como

permitiram dar-lhe um impulso tecnológico decisivo através da demonstração que a estampagem incremental podia ser realizada numa máquina-ferramenta CNC convencional destinada a operações de corte por arranque de apara.

A consulta da literatura da especialidade permite concluir que a generalidade dos trabalhos de investigação e desenvolvimento no domínio da estampagem incremental estão focalizados nas aplicações e nos limites de enformabilidade do processo envolvendo chapas com espessura, propriedades mecânicas e acabamentos uniformes. Esta observação pode igualmente ser extendida aos estudos teóricos e numéricos baseados na aplicação do método dos elementos finitos [5-11]. De facto, tanto quanto os autores têm conhecimento, a única excepção ao actual enfoque da investigação e desenvolvimento deve-se ao trabalho de Kopp e colaboradores [12] em que se estuda a enformabilidade da estampagem incremental de chapas com espessura variável fabricadas por intermédio de laminagem flexível.

A utilização de sub-conjuntos de chapa soldados (designados na terminologia Inglesa por 'tailored blanks') com diferentes espessuras e/ou diferentes propriedades mecânicas e/ou acabamentos destinados a operações de estampagem incremental não tem sido objecto de interesse industrial embora no caso do alumínio possam existir aplicações potenciais ao nível dos veículos automóveis topo de gama e de desporto, dos veículos ferroviários de alta velocidade e dos bens de consumo domésticos e decorativos.

As aplicações estruturais de 'tailored blanks' de alumínio a veículos automóveis e ferroviários de elevado desempenho permite aumentar a segurança e a performance dos veículos ao mesmo tempo que possibilita economias substanciais de peso e, consequentemente, de combustível. No caso dos bens de consumo domésticos e decorativos é possível antecipar o fabrico de novos produtos que envolvam design e concepções avançadas e que procurem tirar partido de caracteristicas estéticas inovadoras obtidas à custa de diferentes tipos de acabamento superficial ao nível de cores e texturas.

A razão principal para esta aparente falta de interesse tem a ver com a produção de 'tailored blanks' de alumínio adequados a operações subsequentes de estampagem incremental. De facto, a utilização da soldadura laser CO2 habitualmente utilizada na produção industrial de 'tailored blanks' de aço não é adequada para o alumínio e suas ligas em virtude da alta reflectividade das chapas impedir uma adequada absorção da energia contida no feixe de laser e, consequentemente, impedir que a soldadura laser se realize em boas condições operatórias. A utilização de revestimentos à base de grafite para eliminar o problema da alta reflectividade do alumínio permite resolver o problema da soldadura mas dá origem a outro tipo de problemas relacionados com a sua aplicação e remoção.

Por outro lado, a utilização de processos de soldadura alternativos ao laser não é viável por razões de natureza económica e/ou tecnológica. Citam-se com exemplos (i) a soldadura por feixe de electrões que exige investimentos e tempos de 'set-up' muito elevados e (ii) os processos de soldadura por fusão que fazem geralmente intervir densidades de potência calorífica reduzidas e velocidades de soldadura baixas. Os processos de soldadura por fusão contribuem para um aumento

exagerado da zona afectada pelo calor a qual, no caso dos 'tailored blanks', é responsável pela diminuição dos seus limites de enformabilidade.

A tecnologia da laminagem flexível proposta por Kopp e colaboradores [12] permite ultrapassar alguns dos problemas específicos da soldadura laser do alumínio e, desta forma, garantir a produção de 'tailored blanks' multi-espessura adequados a operações subsequentes de deformação plástica. Contudo, a implementação industrial do processo de laminagem flexível exige investimentos substanciais ao nível do controlo do processo e não permite produzir 'tailored blanks' com diferentes propriedades

mecânicas e acabamentos.

Em face do exposto, pode-se concluir que os recentes desenvolvimentos ao nível da soldadura por fricção linear merecem ser avaliados sob o ponto de vista da produção de 'tailored blanks' de alumínio com diferentes espessuras, propriedades mecânicas e acabamentos destinados a operações de estampagem convencional e incremental. No caso concreto da estampagem incremental é interessante referir que existe a possibilidade de utilizar a mesma máquina-ferramenta CNC para a soldadura e para a deformação plástica das chapas.

Este artigo apresenta um estudo experimental inédito destinado a avaliar o desempenho de 'tailored blanks' de alumínio em operações de estampagem incremental. O trabalho envolveu a produção de 'tailored blanks' por intermédio de soldadura por fricção linear e a realização de ensaios experimentais de estampagem incremental destinados a comparar a enformabilidade dos 'tailored blanks' com a de chapas de referência não-soldadas do mesmo material.

2. EXPERIMENTAÇÃO

A estampagem incremental de 'tailored blanks' foi realizada a partir de chapas de alumínio AA1050-H111 com espessuras de 1.5 mm e 2 mm. Esta secção do artigo fornece informações detalhadas sobre o processo de fabrico dos 'tailored blanks' por intermédio de soldadura por fricção linear e apresenta o plano de ensaios e os parâmetros operatórios mais relevantes que foram utilizados nas operações de estampagem incremental de peças cónicas e pirâmidais destinadas ao estudo da enformabilidade dos 'tailored blanks'.

A opção por realizar a totalidade do trabalho de investigação com 'tailored blanks' em que apenas se faz variar a espessura, mantendo-se o tipo de material e de acabamento superficial, tem como objectivo limitar o número de variáveis e, desta forma, analisar exclusivamente a influência do cordão de soldadura na enformabilidade geral da estampagem incremental.

2.1 FABRICO DE TAILORED BLANKS

Os 'tailored blanks' de alumínio AA1050-H111 foram produzidos por intermédio de soldadura por fricção linear. Este processo de união de materiais no estado sólido foi desenvolvido e patenteado pelo TWI (The Welding Institute) [13], apresenta um elevado potencial na ligação do Alumínio e suas ligas e é considerado

um dos maiores avanços que se verificaram na tecnologia da soldadura nas últimas décadas.

A soldadura por fricção linear faz intervir uma ferramenta cilíndrica rotativa, não consumível, em cuja extremidade se destacam uma base e um pino com um perfil especial que é inserido na junta definida pelos bordos das chapas e movimentado linearmente ao longo da junta a soldar [14] (figura 2a)). A união dos materiais resulta de mecanismos de deformação plástica e de atrito que têm lugar a temperaturas inferiores à temperatura de fusão dos materiais de base.

No caso concreto deste trabalho utilizou-se uma ferramenta de aço para trabalho a quente H13 (AISI) que após tratamento térmico de tempera e nitruração iónica e oxidação apresenta uma dureza de 52 HRc na zona de processamento. A base da ferramenta tem 14 mm de diâmetro e o pino tem uma geometria cilíndrica roscada ISSO M3 e um comprimento variável entre os 1.9 e 2.6 mm.

Os 'tailored blanks' de alumínio AA1050-H111 foram produzidos numa fresadora convencional equipada com um gabarito para fixação mecânica das chapas a soldar (figura 2). Utilizou-se uma velocidade de rotação de 1120 rpm e uma velocidade de avanço linear igual a 320 mm/min, no caso das chapas a soldar terem a mesma espessura, e igual a 160 mm/min no caso das espessuras serem diferentes. O angulo de ataque na ferramenta de soldadura por fricção linear é nulo porque a base é estriada e plana.

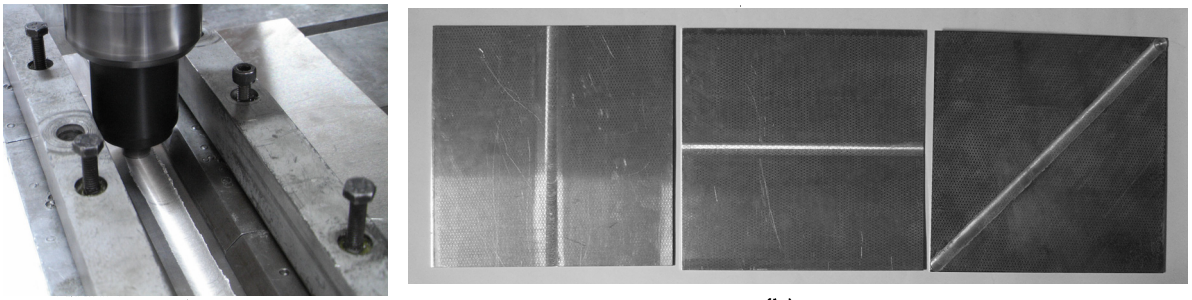

(a) (b)

Figura 2 – Produção de 'tailored blanks' de alumínio AA1050-H111 por intermédio de soldadura por fricção linear.

a) Detalhe em que se observam a ferramenta, o cordão de soldadura e o gabarito para fixação das chapas.
b) Disposições do cordão de soldadura segundo direcções paralelas e perpendiculares à direcção de laminagem. O cordão orientado segundo a diagonal foi realizado na direcção de laminagem de cada uma das chapas.

As juntas a soldar foram previamente preparadas de modo a garantir um paralelismo perfeito entre os dois lados das chapas a soldar e os cordões de soldadura foram realizados paralela e perpendicularmente à direcção de laminagem. Após concluídas as soldaduras procedeu-se à remoção mecânica das rebarbas que se desenvolvem ao longo dos cordões.

2.2 ESTAMPAGEM INCREMENTAL

Os ensaios de estampagem incremental foram realizados num centro de maquinagem Cincinnati Milacron equipado com um gabarito e uma ferramenta de ponta hemisférica com 6 mm de raio. A velocidade de rotação da ferramenta é de 35 rpm e a velocidade de translacção (avanço) é da ordem de grandeza dos 1000 mm/min. As trajectórias, de natureza helicoidal com indexação vertical progressiva, foram geradas através do programa HeToPac [15] e a indexação vertical total por volta é de 0.5 mm. O lubrificante utilizado nos ensaios é uma emulsão à base de óleo de corte.

Foram utilizadas chapas de alumínio AA1050-H111 de 1.5 mm e 2.0 mm bem como 'tailored blanks' produzidos por soldadura por fricção linear de 1.5 mm, 2.0 mm e (1.5+2.0) mm. Porque a estampagem incremental de chapas de alumínio AA1050-H111 com espessuras iguais ou superiores a 1.5 mm dá origem a peças finais com graves problemas de qualidade superficial, tiveram de se utilizar soluções tecnológicas inovadoras baseadas na utilização de chapas descartáveis que permitem ultrapassar com sucesso este tipo de problemas e fabricar componentes com bom acabamento superficial [16]. De facto, a utilização de chapas com espessuras elevadas faz aumentar significativamente a pressão e a penetração da ferramenta na superfície da chapa ao ponto de ser energeticamente mais favoravel deformar e remover o material sob a forma de pequenas aparas (figura 3a) do que apenas deformar o material da chapa.

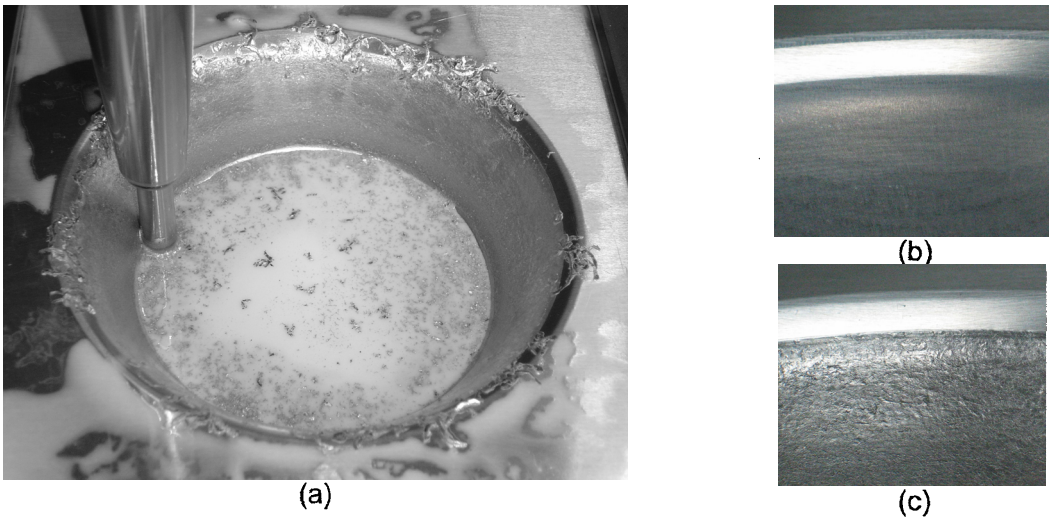

Figura 3 – Estampagem incremental de chapas de alumínio AA1050-H111.

a) Baixa qualidade superficial e formação de aparas durante a estampagem incremental de uma geometria cónica numa chapa de alumínio AA1050-H111 com 1.5 mm de espessura.
b) Pormenor em que se pode observar a boa qualidade superficial resultante da estampagem incremental de uma chapa de alumínio AA1050-H111 com 1.5 mm de espessura em foi utilizada uma chapa descartável de aço DC04 com 0.63 mm de espessura.

c) Pormenor em que se pode observar a baixa qualidade superficial final resultante da estampagem incremental de uma chapa de alumínio AA1050-H111 com 1.5 mm de espessura.

A utilização de uma chapa descartável colocada entre a ferramenta e a chapa de alumínio permite resolver o problema da baixa qualidade superficial e eliminar a eventual formação de aparas. No caso concreto deste trabalho optou-se por utilizar uma chapa descartável de aço DC04 com 0.63 mm de espessura. As figuras 3b) e c) apresentam um pormenor da qualidade superficial de uma peça fabricada por intermédio de estampagem incremental com e sem utilização de chapa descartável. Como se pode observar as diferenças de qualidade são muito significativas.

No caso da estampagem incremental de 'tailored blanks' a utilização de chapas descartáveis assume um papel ainda mais relevante na medida em que permite evitar o contacto directo da ferramenta com o cordão de soldadura. Por outras palavras, a chapa descartável acaba por ter uma função adicional protectora do cordão de soldadura.

A tabela 1 apresenta um resumo do trabalho experimental. O plano de ensaios foi concebido de modo a isolar a influência de alguns dos parâmetros mais importantes do processo de fabrico; (i) a existência de cordão de soldadura, (ii) a orientação do cordão de soldadura relativamente à direcção de laminagem da chapa, (iii) a orientação do cordão de soldadura relativamente à geometria da peça, (iv) a posição da raíz do cordão de soldadura relativamente à ferramenta de estampagem incremental, (v) a espessura da chapa e (vi) a eventual existência de diferentes espessuras nos dois lados das chapas soldadas.

Geometria	Chapa	Espessura [mm]	Observações
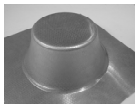		1.5	-
		2.0	
		1.5	Cordão de soldadura paralelo à direcção de laminagem.
		2.0	
		1.5 + 2.0	
		1.5	Cordão de soldadura perpendicular à direcção de laminagem.
		2.0	
		1.5 + 2.0	
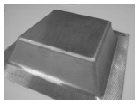		1.5	-
		2.0	
		1.5	Cordão de soldadura paralelo à direcção de laminagem.
		2.0	
		1.5 + 2.0	
		1.5	Cordão de soldadura paralelo à direcção de laminagem.
		2.0	Cordão de soldadura paralelo à direcção de laminagem. Posição de estampagem invertida relativamente ao cordão de soldadura.
		2.0	Cordão de soldadura perpendicular à direcção de laminagem. Posição de estampagem invertida relativamente ao cordão de soldadura.

Tabela 1 – Plano dos ensaios experimentais

Os ensaios foram realizados de modo a fabricar geometrias cónicas e piramidais truncadas em que o valor do ângulo ø aumenta com a posição vertical da ferramenta (figura 4). Cada tipo de ensaio indicado na tabela 1 foi, no mínimo, repetido duas vezes de modo a viabilizar o tratamento estatístico dos resultados. A sequência de ensaios foi aleatória.

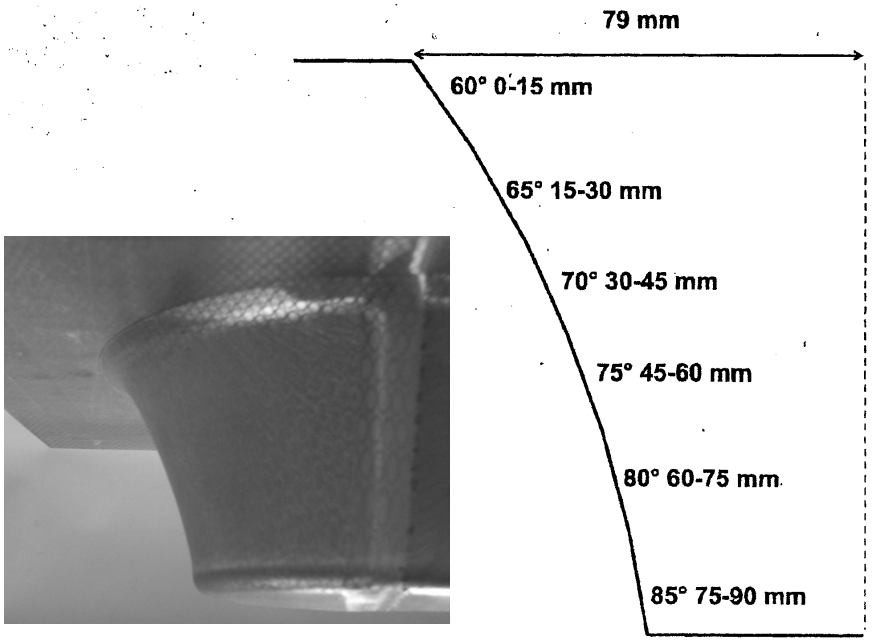

Figura 4 – Peça cónica truncada obtida a partir de um 'tailored blank' com 2 mm de espessura e representação esquemática da secção transversal da peça onde se assinala a variação do ângulo ø com a posição vertical da extremidade da ferramenta.

3. RESULTADOS E DISCUSSÃO

A figura 5 apresenta alguns exemplos de peças cónicas e piramidais fabricadas por estampagem incremental de 'tailored blanks' obtidos por intermédio de soldadura por fricção linear. São apresentadas peças em que as soldaduras se encontram alinhadas com a direcção de laminagem, peças em que as soldaduras são perpendiculares à direcção de laminagem e, no caso da pirâmide, peças em que a soldadura se encontra posicionada nas zonas que são mais e menos solicitadas durante o processo de fabrico. A análise da figura 6 permite concluir que a qualidade final da peça é muito dependente da qualidade do cordão de soldadura do 'tailored blank'. De facto, é possível obterem-se peças em que a rotura se dá fora do cordão de soldadura (figura 6a)), confirmando, o elevado potencial dos 'tailored blanks' produzidos por soldadura por fricção linear para operações de estampagem incremental, e peças em que a rotura se dá prematuramente no cordão de soldadura do 'tailored blank'.

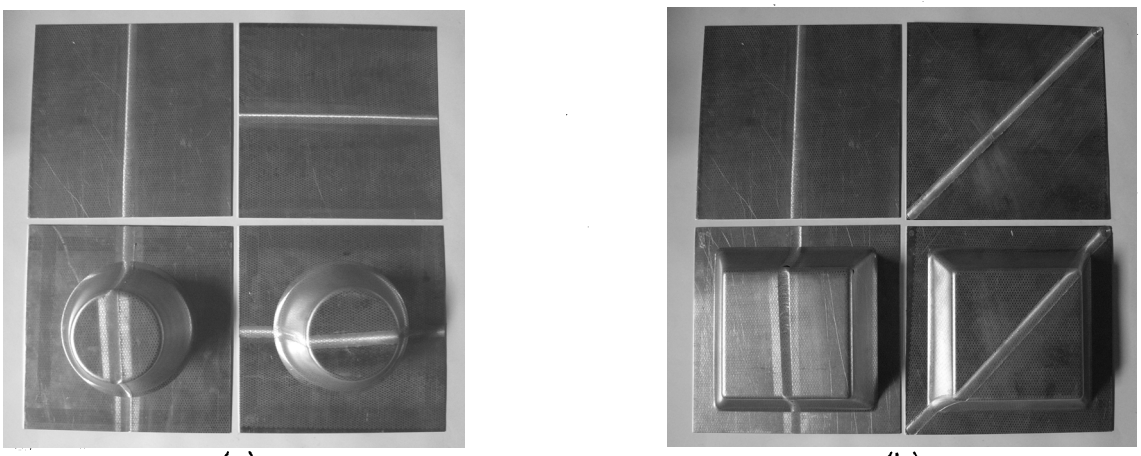

Figura 5 – Estampagem incremental de (a) geometrias cónicas e (b) piramidais truncadas a partir de 'tailored blanks' de alumínio AA1050-H111.

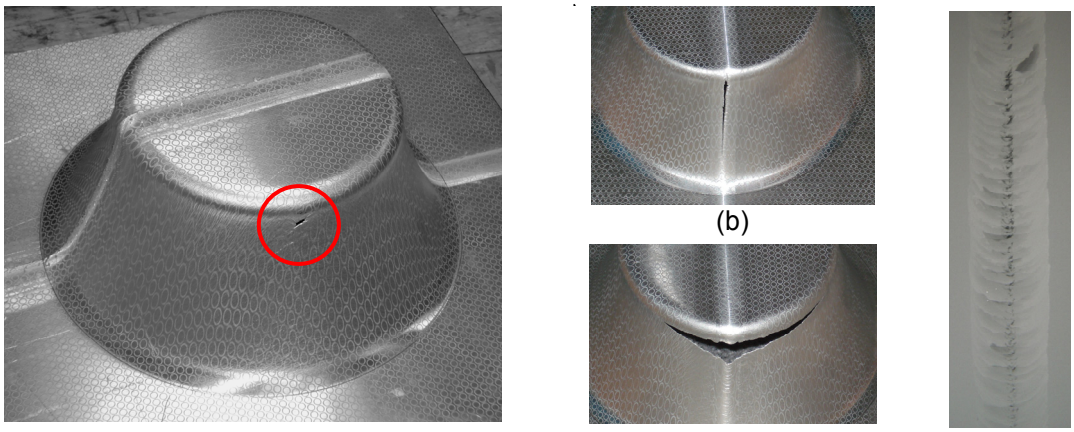

Figura 6 – Peças cónicas truncadas em que o valor do ângulo ø aumenta com a posição vertical da extremidade da ferramenta fabricadas por estampagem incremental de 'tailored blanks'.

a) Bom nível de enformabilidade com uma rotura fora do cordão de soldadura ('tailored blank' de 2.0 mm de espessura).
b) Baixo nível de enformabilidade com uma estricção muito acentuada seguida de rotura ao longo do cordão de soldadura ('tailored blank' de 1.5 mm de espessura).
c) Baixo nível de enformabilidade com uma rotura perpendicular ao cordão de soldadura ('tailored blank' de 1.5 mm de espessura).
d) Radiografia de um cordão de soldadura de um 'tailored blank' com 1.5 mm de espessura em que se podem observar defeitos no cordão de soldadura.

As figuras 6b) e c) apresentam dois tipos distintos de defeitos que têm origem no cordão de soldadura e a figura 6d) apresenta o resultado do controlo não-destrutivo por intermédio de raio-X em que se observam defeitos no cordão de soldadura. Estes defeitos que se revelaram particularmente críticos no fabrico de 'tailored blanks' envolvendo sub-conjuntos de chapa de 1.5 mm, devido a dificuldades na execução da soldadura, dão origem a ligações de má qualidade na zona da raíz do cordão e justificam as roturas prematuras com origem no cordão de soldadura que se verificaram na estampagem incremental de algumas peças (figuras 6b) e c)).

A razão pela qual a qualidade dos cordões de soldadura por fricção linear tende a diminuir com a diminuição da espessura das chapas tem a ver com o facto do fluxo do material em torno da ferramenta ir perdendo características tridimensionais à medida que a espessura vai diminuindo.

A figura 7 apresenta uma peça com geometria piramidal truncada obtida por estampagem incremental de 'tailored blanks' em que o valor do ângulo ø aumenta com a posição vertical da ferramenta. Os cordões de soldadura estão posicionados nos cantos da peça sendo estas zonas as que estão mais solicitadas durante o processo de fabrico. Conforme se pode observar na figura 7 as roturas ocorrem simultaneamente nos cantos da peça com e sem cordão de soldadura (figura 7a)) evidenciando a boa enformabilidade dos 'tailored blanks' produzidos por intermédio de soldadura por fricção linear. A análise das figuras 7b) e c) permite igualmente concluir que a rotura apenas ocorre num dos cantos do cordão de soldadura na medida em que o outro canto, localizado na diagonal oposta da peça, não apresenta qualquer tipo de rotura.

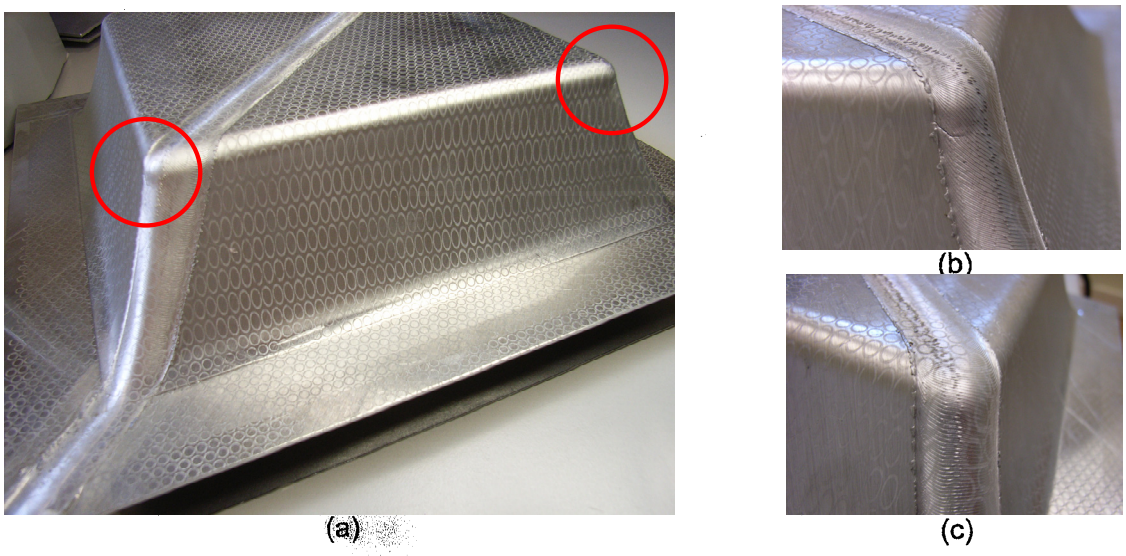

Figura 7 – Peça piramidal truncada em que o valor do ângulo ø aumenta com a posição vertical da extremidade da ferramenta fabricada por estampagem incremental de 'tailored blanks' (2.0 mm de espessura).

a) Roturas quase simultâneas em cantos com e sem cordão de soldadura.
b) Detalhe do canto que apresenta rotura no cordão de soldadura.
c) Detalhe do canto situado na diagonal oposta que não apresenta rotura no cordão de soldadura.

As figuras 8 e 9 apresentam os resultados experimentais do valor do ângulo max ø a partir do qual surgem roturas em função da espessura inicial das chapas. São apresentados valores para chapas sem cordão de soldadura (que são utilizadas como termo de referência) e para 'tailored blanks' do mesmo material e com o mesmo tipo de acabamento em que se utilizaram espessuras de chapa iguais (1.5 mm e 2 mm) e diferentes (1.5+2 mm) nos dois lados da chapa.

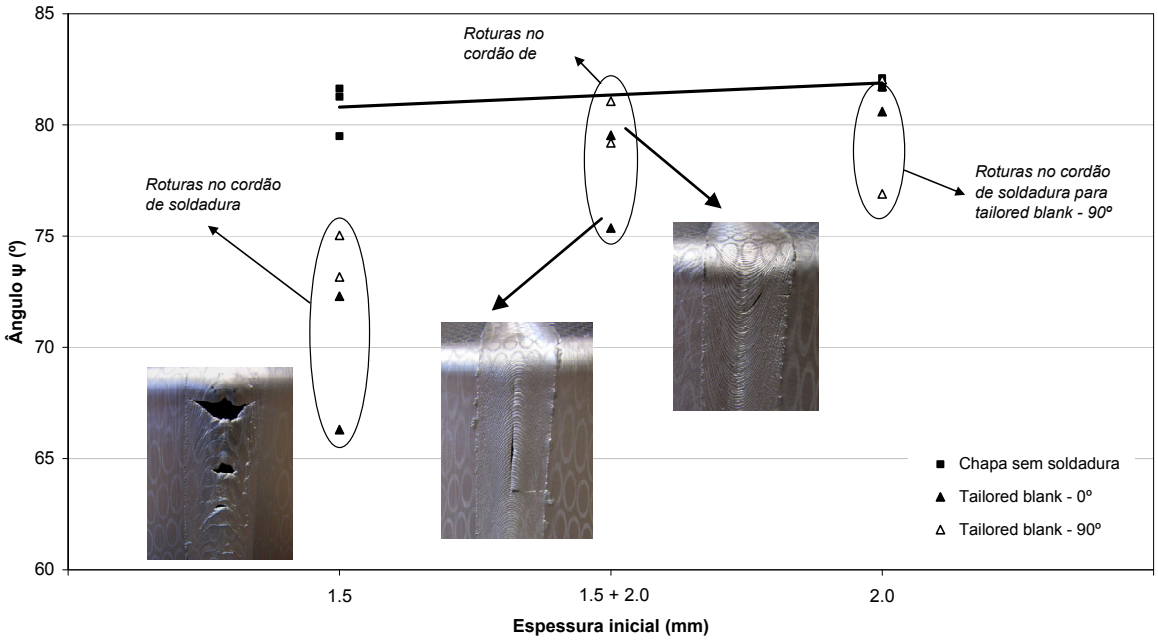

Figura 8 – Valor do ângulo ø a partir do qual surgem roturas em função da espessura inicial das chapas para peças cónicas truncadas.

A análise das figuras 8 e 9 permite concluir que o valor máximo do ângulo ø diminui com a espessura inicial das chapas de referência não-soldadas em conformidade com aquilo que tem sido observado experimentalmente por outros investigadores [5]. No caso dos 'tailored blanks' observam-se dois grupos de resultados distintos conforme a espessura é igual ou superior a 1.5 mm. De facto a enformabilidade dos 'tailored blanks' mais espessos é muito idêntica à das chapas não-soldadas e também é insensível ao facto da raiz do cordão de soldadura se poder apresentar virado ou invertido para a ferramenta de estampagem incremental. Os 'tailored blanks' fabricados a partir de chapas de 1.5 mm apresentam uma grande dispersão de resultados. Nalguns casos obtêm-se enformabilidades análogas às das chapas não-soldadas enquanto que noutros casos se obtêm reduções muito significativas dos índices de enformabilidade. Este elevado nível de incerteza deve-

se a dificuldades experimentais que foram sentidas na produção dos 'tailored blanks' envolvendo sub-conjuntos de chapa de 1.5 mm, conforme foi referido anteriormente.

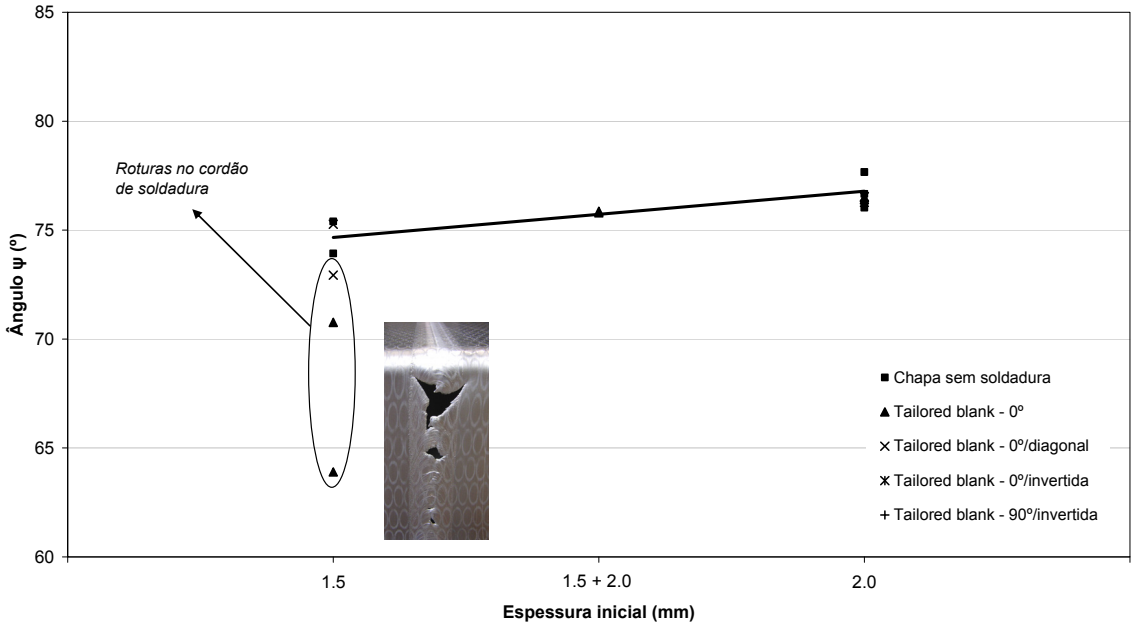

Figura 9 – Valor do ângulo ø a partir do qual surgem roturas em função da espessura inicial das chapas para peças pirâmidais truncadas.

Uma forma alternativa de estudar a enformabilidade de peças fabricadas por intermédio de estampagem incremental consiste na utilização do espaço das extensões principais (2 1 ,å å) que se encontra representado na figura 10. No caso de peças cónicas truncadas em que o valor do ângulo ø aumenta com a posição vertical da ferramenta observa-se que a medição das extensões a partir de grelhas de círculos impressas electroquímicamente na superfície da chapa permite obter um campo de extensões típico de condições de deformação plástica plana (3 1 2 , 0 å - =å =å). O campo de extensões das chapas não-soldadas é muito semelhante ao dos 'tailored blanks' o que permite concluir acerca do excelente nível de enformabilidade dos cordões de soldadura produzidos através de soldadura por fricção linear. De facto, os 'tailored blanks' apresentam roturas fora do cordão de soldadura para valores da extensão principal 3 . 1 1 .å e as chapas não-soldadas apenas permitem alcançar valores de extensão ligeiramente mais elevados 35 . 1 1 .å sem que ocorra qualquer tipo de rotura.

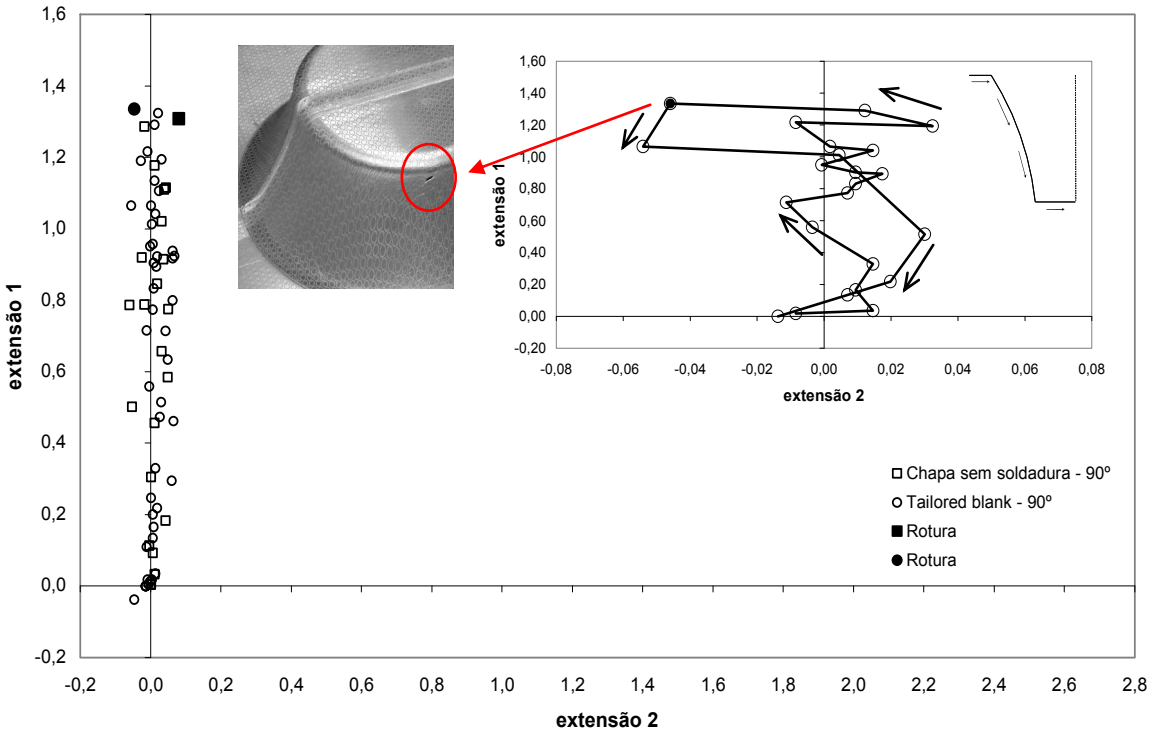

Figura 10 – Evolução do valor das extensões 2 1 ,å å em peças com geometria cônica truncada em que o valor do ângulo ø aumenta com a posição vertical da extremidade da ferramenta[1] .

Os estudos de enformabilidade realizados anteriormente (figura 9) permitem concluir acerca da viabilidade de fabricar uma peça com geometria pirâmidal truncada com um ângulo º 60 =ø constante a partir de 'tailored blanks' de alumínio AA1050-H111 obtidos por intermédio de soldadura por fricção linear de chapas de 1.5 mm e/ou 2 mm. De facto, com este valor do ângulo ø é possível fabricar peças semelhantes às que se encontram ilustradas na figura 11 sem que apareçam quaisquer indícios de rotura.

Também os problemas associados a roturas prematuras com origem na dificuldade de execução de soldaduras envolvendo sub-conjuntos de chapa de 1.5 mm ficam devidamente salvaguardados com a utilização de um ângulo º 60 =ø .

1 - As medições foram realizadas na direcção perpendicular à de laminagem numa chapa sem soldadura e num 'tailored blank' com 2.0 mm de espessura.

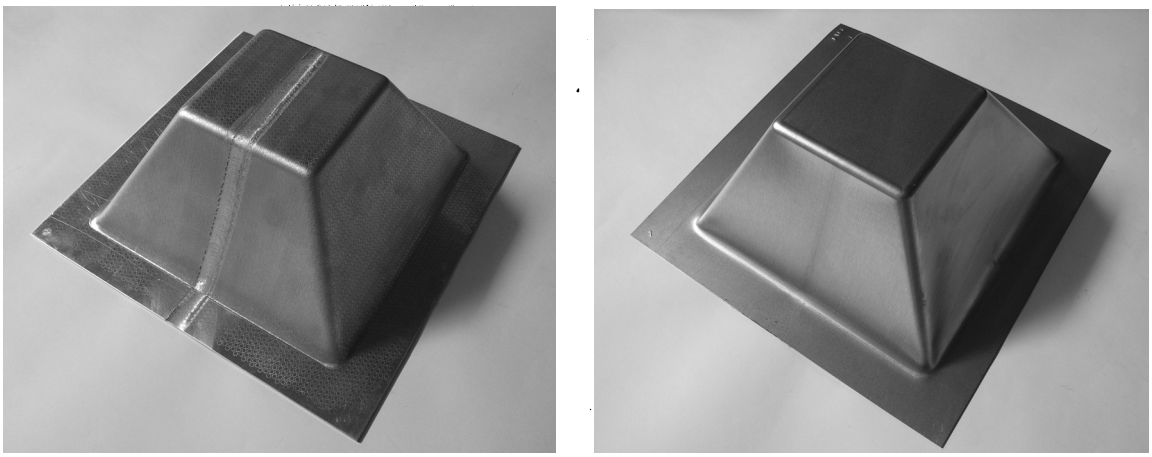

Figura 11 – (a) Geometria pirâmidal truncada (° 60 =ø , constante) obtida por estampagem incremental de um 'tailored blank' de alumínio AA1050-H111 com 2.0 mm de espessura em que foi utilizada (b) uma chapa descartável de aço DC04 com 0.63 mm de espessura.

4. CONCLUSÕES

O fabrico de peças por estampagem incremental pode ser extendido aos 'tailored blanks' produzidos por intermédio de soldadura por fricção linear.

O estudo experimental permite concluir que as reduções de enformabilidade que se verificaram relativamente a geometrias de referência fabricadas a partir de chapas não-soldadas estão, na generalidade dos casos, ligadas a dificuldades de execução das soldaduras envolvendo sub-conjuntos de chapa com espessuras reduzidas (1.5 mm).

A utilização de uma chapa de aço descartável colocada entre o 'tailored blank' de alumínio e a ferramenta permite ultrapassar os problemas de qualidade superficial associados à estampagem incremental de chapas de alumínio AA1050-H111 com espessuras superiores a 1 mm e oferece a vantagem adicional de proteger o cordão de soldadura da acção directa da ferramenta.

AGRADECIMENTOS

Os autores Portugueses agradecem o apoio financeiro da FCT/Portugal através do projecto PTDC/EME-TME/64706/2006. O Prof. Paulo Martins quer igualmente agradecer o apoio da Universidade Técnica da Dinamarca durante a sua licença sabática.

REFERÊNCIAS

[1] Leszak E., Apparatus and process for incremental dieless forming. Patent US3342051A (1967).

[2] Kitazawa K., Wakabayashi A., Murata K. and Yaejima K., Metal-flow phenomena in computerized numerically controlled incremental stretch-

expanding of aluminum sheets, *Keikinzoku/Journal of Japan Institute of Light Metals*, **46**, 65-70, (1996).
[3] Jeswiet J., Incremental single point forming, *Trans. of North American Manufacturing Research Institute*; **29**, 75-79, (2001).
[4] Filice L., Fratini L., Micari F., Analysis of material formability in incremental forming. *Annals of CIRP*, **51**, 199-202, (2002).
[5] Jeswiet J., Micari F., Hirt G., Bramley A., Duflou J. and Allwood J., Asymmetric single point incremental forming of sheet metal, *Annals of CIRP*, **54**, 623-650, (2005).
[6] Hagan E. and Jeswiet J., A review of conventional and modern single point sheet metal forming methods". *Journal of Engineering Manufacture*, **217**, 213–225, (2003).
[7] Leach D., Green A. J. and Bramley A. N. A new incremental sheet forming process for small batch and prototype parts, *9th International Conference on Sheet Metal*, Leuven, Belgium, 211-21, (2001).
[8] Fratini L., Ambrogio G., Di Lorenzo R., Filice L., Micari F., Influence of mechanical properties of the sheet material on formability in single point incremental forming, *Annals of CIRP*, **53**, 207-210, (2004).
[9] Allwood J. M., King G. P. F. and Duflou J. R., A structured search for applications of the Incremental Sheet Forming process by product segmentation, *Journal of Engineering Manufacture*, **219**, 239-244, (2004).
[10] Bambach M., Hirt G., and Ames J., Quantitative validation of FEM simulations for incremental sheet forming using optical deformation measurement, *Advanced Materials Research*, **6-8**, 509-516, (2005).
[11] Duflou J. R., Lauwers B., Verbert J., Gelaude F. and Tunckol Y., Medical application of single point incremental forming: cranial plate manufacturing, *Virtual Modelling and Rapid Manufacturing*, Taylor & Francis, London, 161-166, (2005).
[12] Kopp R., Wiedner C. and Meyer A., Forming strategies and process modelling for CNC incremental sheet forming, *Advanced Materials Research*, **6-8**, 81-92, (2005).
[13] Thomas W. M., Nicholas E. D., Needham J. C., Church M. G., Templesmith P and, Dawes C. J. Friction stir butt welding, International Patent Application No. PCT/GB92/02203, (1991).
[14] Vilaça P., Santos J. P.,Góis A., Quintino L., Joining Aluminium Alloys Dissimilar in Thickness by Friction Stir Welding and Fusion Process, *Welding in the World - Journal of the International Institute of Welding (IIW)*, **49**, 56-62, (2005).
[15] Skjoedt M., Hancock M. H., Bay N:, Creating helical tool paths for single point incremental forming, *Key Engineering Materials*, **344**, 583-590, (2007).
[16] Skjoedt M., Silva M. B., Bay N., Martins P. A. F., Lenau T., Single point incremental forming using a dummy sheet, *2 nd International Conference on New Forming Technology*, Bremen, Germany, (2007).

February 2008

Joint author statement

If a thesis contains articles made in collaboration with other researchers, a joint author statement about the PhD-student's part of the article shall be made by each of the co-authors, cf. article 12, section 4 of the Ministerial Order No. 18 February 2008 about the PhD degree

Title of the article: Revisiting the fundamentals of single point incremental forming by means of membrane analysis

Author(s): M.B. Silva, M. Skjoedt, N. Bay, P.A.F. Martins

Journal: International Journal of Machine Tools and Manufacture, (2008), vol. 48, p. 73-83.

PhD-student: Martin Skjødt Cpr.nr: _____

Signature of the PhD-student: _____ Date: _____

Co-author: _____ Signature: _____

Description of each author's contribution to the above-mentioned article:

M. B. Silva: Planning and conduction of experiments, literature study, further discussion and development of theory, final editing.

M. Skjoedt: CAD drawing of parts, CAM programming of parts, planning and conduction of experiments, pictures for paper, literature study, further discussion and development of theory, final editing.

N. Bay: Planning of experiments, further discussion and development of theory, final editing.

P. A. F. Martins: Development of initial theory including formulas and assumptions, further discussion and development of theory, planning of experiments, writing of paper, pictures and graphics for paper, final editing.

Available online at www.sciencedirect.com
ScienceDirect
ELSEVIER
International Journal of Machine Tools & Manufacture 48 (2008) 73–83
INTERNATIONAL JOURNAL OF MACHINE TOOLS & MANUFACTURE DESIGN, RESEARCH AND APPLICATION
www.elsevier.com/locate/ijmactool

Revisiting the fundamentals of single point incremental forming by means of membrane analysis

M.B. Silva[a], M. Skjoedt[b], P.A.F. Martins[a,*], N. Bay[b]

[a]IDMEC, Instituto Superior Tecnico, TULisbon Avenue Rovisco Pais, 1049-001 Lisboa, Portugal
[b]Technical University of Denmark, Department of Manufacturing Engineering and Management, DTU-Building 425, DK-2800, Kgs. Lyngby, Denmark

Received 12 June 2007; received in revised form 19 July 2007; accepted 19 July 2007
Available online 27 July 2007

Abstract

Knowledge of the physics behind the fracture of material at the transition between the inclined wall and the corner radius of the sheet is of great importance for understanding the fundamentals of single point incremental forming (SPIF). How the material fractures, what is the state of strain and stress in the small localized deformation zone and how these two subjects are brought together in order to explain the overall formability of SPIF in terms of ductile damage are still not well understood. However, they are of great importance for improving the robustness and enhancing the predictability of currently existing numerical models and for extending the scope of industrial applications of the process. This paper attempts to provide answers to these questions by means of a new theoretical model for rotational symmetric SPIF that was developed under membrane analysis with bi-directional in-plane contact friction forces.

Keywords: Single point incremental forming; Fundamentals; Membrane analysis

1. Introduction

Single point incremental forming (SPIF) is a new sheet metal forming process with a high potential economic payoff for rapid prototyping applications and for small quantity production.

Fig. 1 presents the basic components of the process: (i) the sheet metal blank; (ii) the blankholder; (iii) the backing plate; and (iv) the single point forming tool. The tool path is generated in a CNC machining center and is utilized to progressively form the sheet into a component. During the process there is no backup die supporting the back surface of the sheet.

Most investigations of SPIF have concerned applications and formability limits of the process [1]. This observation applies equally to experimental investigations as to the small available amount of finite element studies.

The experimental investigations lead to the conclusion that the formability of the process can be defined in terms of four major parameters: (i) thickness of the sheet; (ii) size of the step down; (iii) speed; and (iv) radius of the forming tool [1]. The influence of the first and second parameters is commonly explained by means of the sine law $t_f = t_0 \sin\lambda$, where t_0 is the initial thickness, t_f is the final thickness, λ is the semi-cone angle and $\psi = \pi/2 - \lambda$ is the drawing angle between the inclined wall surface and the initial flat configuration of the sheet. The speed of the forming tool is known to influence formability because of its direct influence on the frictional conditions at the tool–sheet interface. In what concerns the radius of the forming tool it is experimentally observed that better formability is achieved with the utilization of smaller tools. Smaller tools are claimed to be able to concentrate the strain at the zone of deformation in the sheet under the forming tool, whereas larger tools tend to distribute the strains over a more extended area making the process more similar to conventional stamping.

Despite the major contributions made by Matsubara [2], Iseki and Kumon [3], Jeswiet and Hagan [4], Micari et al. [5], Allwood et al. [6], Bramley et al. [7], Hirt et al. [8], Duflou et al. [9] and many others, on the development of industrial applications and better characterization of the forming limits of the process, the mechanics of deformation

*Corresponding author. Fax: +351 21 8419058.
E-mail address: pmartins@ist.utl.pt (P.A.F. Martins).

0890-6955/$ - see front matter © 2007 Elsevier Ltd. All rights reserved.
doi:10.1016/j.ijmachtools.2007.07.004

Nomenclature

σ_θ	circumferential stress
σ_ϕ	meridional stress
σ_t	thickness stress
σ_Y	yield stress
μ	coefficient of friction
λ	half cone angle of the component
ψ	draw angle between the inclined wall and the initial flat configuration of the sheet
t	thickness of the sheet
t_0	initial thickness of the sheet
t_f	final thickness of the sheet
r	radial coordinate
r_2	radius of the element normal where it cuts the z-axis
r_1	radius of curvature of meridian at the element (radius of the SPIF tool)

remains little understood due to the complexity and low predictive ability of the finite element models that, so far, have been employed to study the process. In fact, nowadays, SPIF is one of the very few if not the only sheet metal forming process in which the advantage of experimentation over theory is absolute even for solving the simplest practical problem.

From what was mentioned before it can be concluded that there is a need for a simple but effective theoretical model that allows the influence of major fundamental process parameters and their mutual interaction to be studied both qualitatively and quantitatively.

Such a model must draw from the characterization of the small plastic zone created by the single point forming tool during incremental deformation to the physics behind the onset of cracking at the region where the inclined wall of the sheet is tangent to the corner in contact with the tool. How material separates and cracks propagate along the circumferential direction is still not well understood, although being of great importance for understanding the mechanics of deformation and for improving formability and extending the applicability of the process.

In fact, the incremental nature of SPIF raises important key questions that need to be properly addressed: What is the state of strain and stress at the small plastic zone created by the forming tool? What is the physics behind cracking at the transition between the inclined wall and the corner radius of the sheet being formed? Are the cracks formed by shear or by tensile stresses? Is it possible to explain the formability of SPIF being higher than that of conventional stamping by means of damage based concepts?

This paper attempts to provide answers to these issues by means of a theoretical investigation based on membrane analysis of the small plastic zone created by the single point tool during forming of rotational symmetric components.

2. Membrane analysis of rotational symmetry SPIF components

The governing mode of deformation in SPIF is subject of controversy in the metal forming community [10]. Some authors claim that deformation takes place by stretching instead of shearing while others claim the opposite, but assertions are mainly based on 'similarities' with well-known processes of stamping and shear-spinning rather than on achieved results or experimental evidence.

As it will be shown later in Section 3, examination of the likely mode of material failure at the transition zone between the inclined wall and the corner radius of the sheet

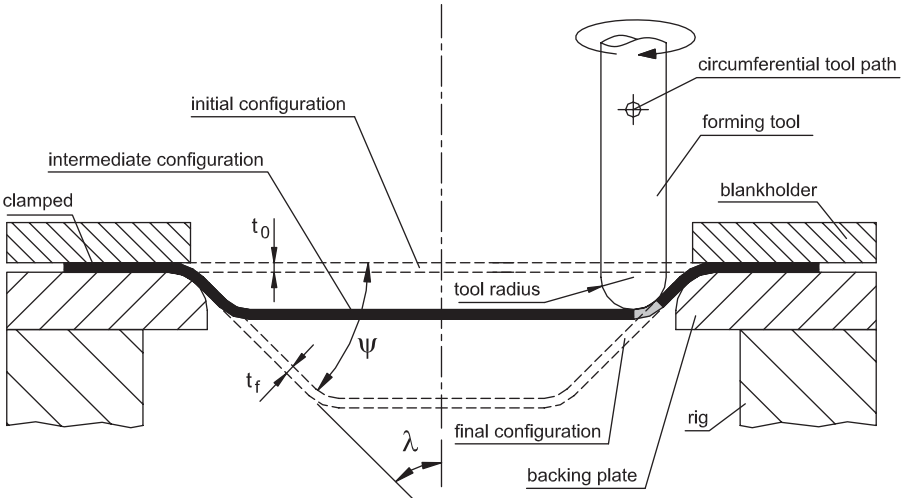

Fig. 1. Schematic representation of a cross section view of the rotational symmetric single point incremental forming (SPIF) process. The tool rotates while performing a round (or helical) path.

is consistent with stretching, rather than shearing, being the governing mode of deformation in SPIF.

This is the starting point for setting up an analytical model for rotational symmetric SPIF based on membrane analysis.

2.1. Small localized plastic zone

Fig. 2 shows a forming tool acting on a sheet during rotational symmetric SPIF. The metal is stretched by membrane forces, so that it conforms to the hemispherical shape of the tool, forming a contact area between the tool and the part of the sheet placed immediately ahead of the moving tool. The contact area is characterized as a small zone localized at the corner of the deforming sheet with a shape resembling that of a radial slice (refer to picture in Fig. 2b).

The schematic drawings included in Figs. 2c and d illustrate the shape of the localized plastic zone in two limiting situations: (i) forming tool path without step down during a circular tour yet not finished (Fig. 2c) and (ii) forming tool path with a large step down (Fig. 2d). The examination of these drawings together with the analysis of the picture showing the experimentally observed smear–mark interference between the tool and the surface of the sheet (Fig. 2b) allows us to conclude that the instantaneous small plastic zone typical of rotational symmetric SPIF can be approximated by a local shell element CDEF as depicted in Fig. 3.

The stress state acting in this element will be derived from membrane equilibrium conditions under bi-directional contact friction forces.

2.2. Membrane equilibrium conditions

In general terms, the surface of revolution of a SPIF part is described by the rotation of a radial slice containing the local shell element about the symmetry z-axis. The normal to the surface of the local shell element cuts the z-axis at the point O and r_2 is defined as the corresponding radius. The center of curvature lies at point Q on the normal and r_1 is the radius of curvature of the local shell element along the meridian direction.

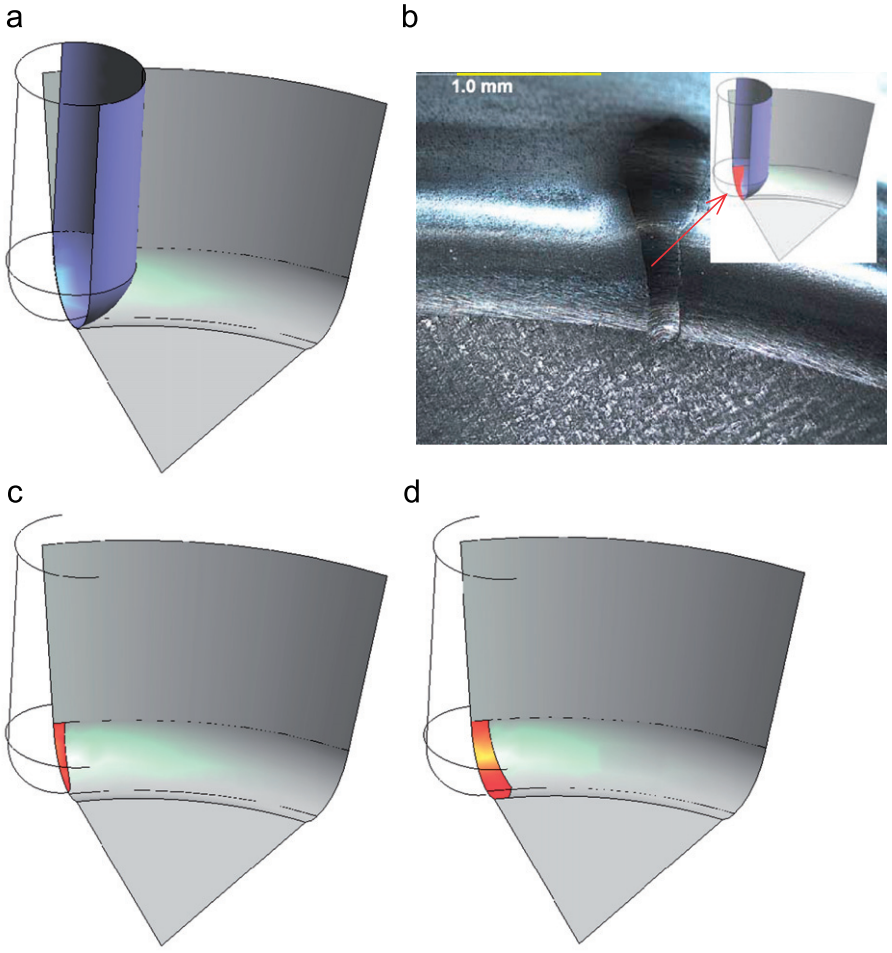

Fig. 2. Rotational symmetric single point incremental forming: (a) schematic representation of the tool and sheet; (b) smear-mark resulting from the local contact between the tool and sheet placed immediately ahead of tool; (c) schematic representation of the smear-mark in case of a forming tool path without step down during a round tour yet not finished; (d) schematic representation of the smear-mark in case of a forming tool path with a large step down.

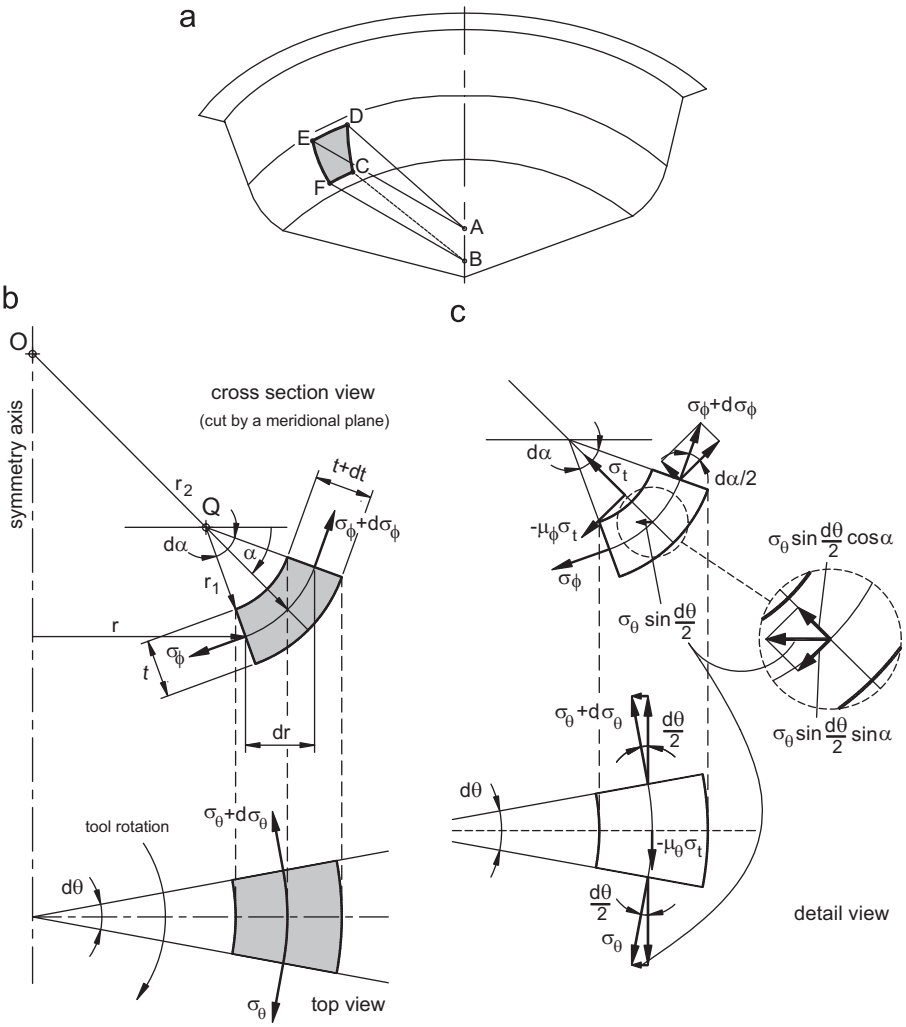

Fig. 3. Rotational symmetric single point incremental forming: (a) schematic representation of the shell element in perspective; (b) schematic representation of the shell element after being cut by an axial meridional plane and as it is seen from the top; (c) detail of (b) showing the acting stresses.

In SPIF the local shell element is subjected to normal forces, shear forces, and bending moments. However, the membrane analysis of plastically deforming shells will neglect the bending moments and, because of axial symmetry, assume the circumferentional, meridional, and thickness stresses to be principal stresses. Further simplifying assumptions that will be made in the following sections of the present paper are: (i) material is assumed as rigid-perfectly plastic; i.e. no strain-hardening effects are taken into consideration; (ii) material is assumed isotropic; i.e. no anisotropic effects are taken into consideration; and (iii) the resultant friction stress exerted at the tool–sheet contact interface is assumed to be made of two in-plane components—a meridional component $-\mu_\phi\sigma_t$ due to the step down movement of the tool and a circumferential component $-\mu_\theta\sigma_t$ due to circular (or helical) movement of the tool combined with the rotational speed of the tool. This last assumption, which is an untraditional way of modeling friction introduced for convenience, implies that the coefficient of friction $\mu = \sqrt{\mu_\phi^2 + \mu_\theta^2}$.

2.2.1. Circumferential direction

The stresses acting on the local shell element are illustrated in Figs. 3b and c. The $\mu_\theta\sigma_t$ stress term along the circumferentional direction is due to the tool–sheet frictional contact interface and its point of application is assumed to coincide with the center of element. Its sign is dependent on the balance of the relative velocity between the tool and the surface of the sheet.

Resolving the force equilibrium along the circumferential direction one obtains

$$\sigma_\theta r_1 \,\mathrm{d}\alpha\left(t+\frac{\mathrm{d}t}{2}\right) - \mu_\theta\sigma_t r_1 \,\mathrm{d}\alpha\left(r+\frac{\mathrm{d}r}{2}\right)\mathrm{d}\theta = (\sigma_\theta + \mathrm{d}\sigma_\theta) r_1 \,\mathrm{d}\alpha\left(t+\frac{\mathrm{d}t}{2}\right) \quad (1)$$

or,

$$\mathrm{d}\sigma_\theta = -\mu_\theta\sigma_t\frac{r\,\mathrm{d}\theta}{t} \cong -\mu_\theta\sigma_t \quad (2)$$

after neglecting higher order terms and assuming $rd\theta \approx t$. The latter assumption comes from observation of micrograph in Fig. 2b showing the width of the smear mark in circumferential direction to be of approximately the same size as the sheet thickness, an approximation that also is physical sensible.

2.2.2. Thickness direction

Resolving the force equilibrium along the thickness direction (refer to Fig. 3c) one obtains,

$$\begin{aligned}&\sigma_t r\,d\theta r_1\,d\alpha + \sigma_\phi r\,d\theta t\,\sin\frac{d\alpha}{2}\\&+(\sigma_\phi+d\sigma_\phi)(r+dr)\,d\theta(t+dt)\,\sin\frac{d\alpha}{2}\\&+\sigma_\theta r_1\,d\alpha t\,\sin\frac{d\theta}{2}\cos\alpha+(\sigma_\theta+d\sigma_\theta)\\&\times r_1\,d\alpha t\,\sin\frac{d\theta}{2}\cos\alpha=0.\end{aligned}\tag{3}$$

After neglecting higher order terms and simplifying the above equation by taking into account that $r_2 = r/\cos\alpha$ and the identity in (2) one obtains

$$\sigma_t\left(\frac{1}{t}-\frac{\mu_\theta}{2r_2}\right)+\frac{\sigma_\phi}{r_1}+\frac{\sigma_\theta}{r_2}=0.\tag{4}$$

Because the term $\mu_\theta/2r_2$ placed inside the brackets is very small when compared with $1/t$ it follows that Eq. (4) can be further simplified as

$$\frac{\sigma_t}{t}+\frac{\sigma_\phi}{r_1}+\frac{\sigma_\theta}{r_2}=0.\tag{5}$$

In physical terms this last simplification implies that the frictional effects in the circumferential direction are neglected in the analysis. This result will be very advantageous in the forthcoming sections of the paper.

2.2.3. Meridional direction

The equilibrium condition of the local shell element in the meridional direction gives (refer to Fig. 3c)

$$\begin{aligned}&(\sigma_\phi+d\sigma_\phi)(r+dr)d\theta(t+dt)-\sigma_\phi r\,d\theta t\\&+\mu_\phi\sigma_t r\,d\theta r_1\,d\alpha-\sigma_\theta\frac{d\theta}{2}r_1\,d\alpha t\,\sin\alpha\\&-(\sigma_\theta+d\sigma_\theta)\frac{d\theta}{2}r_1\,d\alpha t\,\sin\alpha=0,\end{aligned}\tag{6}$$

where, $\mu_\phi\sigma_t$ is the average or net frictional stress in the meridional direction and $d\sigma_\theta \cong \mu_\theta\sigma_t$, included in the last term of Eq. (6), derives from the projection of the circumferential build-up of friction along the meridional direction.

After neglecting higher order terms and simplifying the above equation by taking into account that $dr = r_1\,d\alpha\sin\alpha$, one obtains

$$\frac{d\sigma_\phi}{dr}+\frac{\sigma_\phi-\sigma_\theta}{r}+\sigma_t\left(\frac{\mu_\phi}{t\,\sin\alpha}+\frac{\mu_\theta}{2r}\right)+\frac{\sigma_\phi}{t}\frac{dt}{dr}=0.\tag{7}$$

Because $r \gg t\sin\alpha$, the previous equation can be rewritten in the following simplified form:

$$\frac{d\sigma_\phi}{dr}+\frac{\sigma_\phi-\sigma_\theta}{r}+\frac{\mu_\phi\sigma_t}{t\,\sin\alpha}+\frac{\sigma_\phi}{t}\frac{dt}{dr}=0.\tag{8}$$

In physical terms this last equation confirms, once again, that the frictional effects in the circumferential direction may be neglected in the analysis. As a result of this, the forthcoming sections of the paper will make use of the following approximation of the friction coefficient, $\mu \cong \mu_\phi$.

3. Applications

This section combines the characterization of the opening mode of the cracks found in rotational symmetry SPIF with the analysis of the states of strain and stress, the role of friction and the evolution of thickness in the small localized plastic zone. The analysis is performed by means of the new proposed theory of rotational symmetric SPIF based on membrane analysis that was presented in Section 2 and its overall objective is to provide answers for the fundamental key questions that were listed in the introductory section of the paper (Section 1).

3.1. Opening mode of cracks

Examination of the likely mode of material failure at the transition zone between the inclined wall and the corner radius of the sheet (refer to Fig. 4) allow us to conclude that the opening mode of the cracks occurring in rotational symmetric SPIF (e.g. truncated cone shape) is similar to that of conventional stamping or deep drawing. Cracks are opened by meridional tensile stresses σ_ϕ (mode I of fracture mechanics) and not by in-plane $\tau_{\theta\phi}$ shearing stresses (mode II of fracture mechanics).

The characterization of the typical crack propagation paths that are experimentally observed in SPIF will only be addressed at the end of the paper but the explanation that will then be given is compatible with the above mentioned

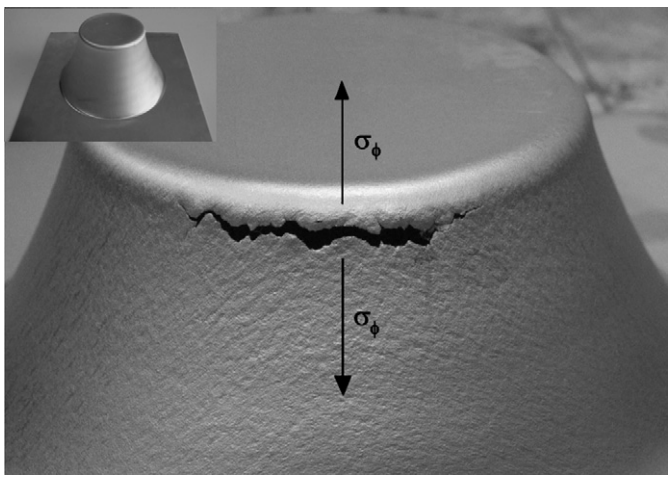

Fig. 4. Typical cracks that may occur in a rotational symmetric SPIF component (truncated cone shape).

key role of the meridional tensile stresses σ_ϕ in the opening mode of cracks.

Under these circumstances, the governing mode of deformation in rotational symmetric SPIF is stretching although some minor shearing effects are expected to arise as a consequence of the contact with friction between the forming tool and the surface of the sheet. The shearing effects are not taken into account by the membrane analysis presented in Section 2 and may be responsible for eventual deviations between the actual and the assumed principal stresses. This sort of deviation is a well-known limitation of the analysis of metal forming processes by means of slab-based methodologies that is frequently referred in classical textbooks.

3.2. State of stress and strain

The stress state acting in the local shell element that conforms to the hemispherical shape of the tool (refer to BC in Fig. 5) can be derived from the previous membrane equilibrium equations under plane strain conditions.

Using the simplified form of the membrane equilibrium equation in the thickness direction (5) and taking into account the geometrical conditions prevailing in BC ($r_2 \gg r_1$ and $r_2 \gg t$, refer to Fig. 3 for definition of these variables), it follows that the ratio between the circumferential stress σ_θ and the radius r_2 normal to the surface of the local shell element in Eq. (5) can be neglected,

$$\frac{\sigma_\theta}{r_2} \cong 0. \tag{9}$$

Hence, Eq. (5) can take the following simplified form:

$$\frac{\sigma_t}{t} + \frac{\sigma_\phi}{r_1} = 0. \tag{10}$$

Under these circumstances, the following relation between the normal contact pressure $p = -\sigma_t$ acting on the local shell element, the meridional stress σ_ϕ, the thickness of the sheet t and the radius of the forming tool ($r_1 = r_{tool}$) can be derived,

$$\sigma_t = -\sigma_\phi \frac{t}{r_{tool}}. \tag{11}$$

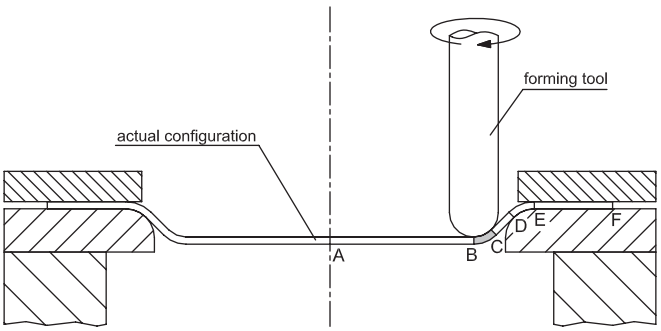

Fig. 5. Schematic representation of a cross section view of the SPIF process by a meridional plane. The shaded zone BC illustrates the local shell element on the surface of the intermediate configuration of the sheet that conforms to the hemispherical shape of the forming tool.

The full characterization of the state of stress in the small localized plastic zone can now be easily obtained after assuming that SPIF of a rotational symmetric truncated cone shape is performed under plane strain conditions. This assumption is experimentally corroborated by the work of Jeswiet et al. [1,11] and Micari et al. [5].

By considering the Levy–Mises constitutive equations in plane strain conditions,

$$d\varepsilon_\theta = 0 \rightarrow \sigma_\theta = \tfrac{1}{2}(\sigma_t + \sigma_\phi) \tag{12}$$

the principal stresses acting on the element can be identified as

$$\begin{aligned} &\sigma_\phi = \sigma_1 > 0, \\ &\sigma_\theta = \sigma_2, \\ &\sigma_t = \sigma_3 < 0, \end{aligned} \tag{13}$$

where, $|\sigma_t| < |\sigma_\phi|$, because $r_{tool} > t$ (refer to Eq. (11)).

Although the relative values of the principal stresses may vary with process parameters related to the thickness t of the sheet and to the radius r_{tool} of the forming tool (Fig. 6), the term σ_1–σ_3 should be constant according to Tresca yield criterion and equal to the flow stress of the sheet (σ_Y under perfectly plastic material assumptions). Inserting in Eq. (11) this leads to the following equation for calculating the meridional stress σ_ϕ acting in the local shell element:

$$\sigma_\phi = \frac{\sigma_Y}{\left(1 + \left(t/r_{tool}\right)\right)}. \tag{14}$$

It is worth noticing that σ_Y is to be replaced by $\sigma = K\varepsilon^n$ in case of a material obeying a power law strain hardening curve and $t = t_0 \sin\lambda$ according to the geometric relationship provided by the sine law.

3.3. Damage and formability

Because cracks are opened by meridional tensile stresses σ_ϕ it is possible to conclude from the analysis of Eq. (14) that formability is expected to decrease when the thickness t of the sheet diminishes or when the radius r_{tool} of the forming tool increases. In addition to this, material strain-hardening is expected to be advantageous in terms of formability since strain hardening results in the expansion of the deformation zone leading to less strain localization. These qualitative predictions based on the new proposed theory are in agreement with the excellent state-of-the-art review of SPIF technology performed by Jeswiet et al. [1] and also with results reported by Micari et al. [12].

As it is shown in Fig. 6 a decrease in the thickness t of the sheet and/or an increase in the radius r_{tool} of the forming tool will result in a shift of the Mohr circle further into the tensile region. This will lead to an increase of the hydrostatic stress $\sigma_m = \sigma_\theta$ and, hence, to a higher rate of accumulated damage. The reduction of the overall formability of the process is, therefore, inevitable. This conclusion is consistent with the damage coupled finite

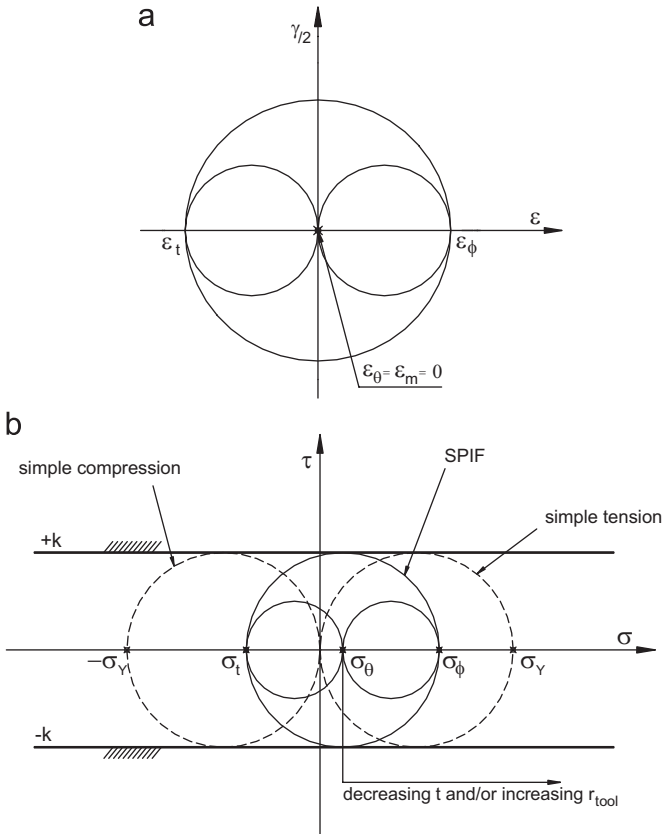

Fig. 6. Schematic representation of the state of strain (a) and stress (b) during rotational symmetric SPIF.

element investigation on the influence of the radius of the forming tool on formability by Hirt et al. [13].

As it will be seen in Section 3.5, the friction at the tool–sheet contact interface will result in a build-up $(\Delta\sigma_\phi)_{BC}$ of the meridional stresses that will lead to an additional shift of the Mohr circle into the tensile region. Contact with friction is therefore expected to decrease the overall formability of the forming process. Experimental results provided by Carrino et al. [14] confirm this fact.

A recurrent question in SPIF is why formability is higher than that of alternative stamping (or deep-drawing) processes [1,11]. A possible answer to this question is often provided in terms of the benefits of concentrating the strain at the zone of deformation in the sheet under the forming tool. However, an alternative answer can be provided by comparing the principal stresses acting in the corner of the rotational symmetric sheet metal parts formed by SPIF and by conventional stamping (or deep-drawing) processes,

SPIF (rotational symmetric)

$$\sigma_\phi = \sigma_1 = \frac{\sigma_Y}{\left(1+\left(t/r_{\text{tool}}\right)\right)} > 0$$

$$\sigma_\theta = \sigma_2 = \frac{1}{2}(\sigma_1+\sigma_3),$$

$$\sigma_t = \sigma_3 = -\sigma_Y \frac{t}{(r_{\text{tool}}+t)} < 0,$$

Conventional stamping [15]

$$\sigma_\phi \cong \sigma_\theta = \sigma_1 = \frac{\sigma_Y}{\left(1+\left(t/r_{\text{punch}}\right)\right)} > 0.$$

$$\sigma_t = \sigma_3 = -\sigma_Y \frac{t}{(r_{\text{punch}}+t)} < 0. \quad (15)$$

The principal stresses in Eq. (15) show that the circumferential stress σ_θ in stamping (or at the punch nose in deep drawing) is equal to the meridional stress σ_ϕ giving rise to biaxial stretching. Because the level of hydrostatic stress σ_m in biaxial stretching is higher than that of plane strain stretching conditions it follows that the rate of accumulated damage in stamping (or deep drawing) grows faster than in SPIF (Fig. 7). This result explains why the overall forming limit line of SPIF is higher than that of conventional stamping processes.

The forming limit line of rotational symmetric SPIF is included in Fig. 7 as a dashed line $\varepsilon_1+\varepsilon_2 = C$ located in the plane strain region of the principal strain space $(\varepsilon_1,\varepsilon_2)$. This limiting line is drawn based on experimental data for the truncated cone provided in literature [5,11]. The line is parallel to the strain path for pure shear $\varepsilon_1 = -\varepsilon_2$ as well as to the limiting condition for local necking $\varepsilon_1+\varepsilon_2 = n$ of a deforming sheet of a material that obeys a general stress–strain power law $\sigma = K\varepsilon^n$.

3.4. Friction at the tool–sheet contact interface

The resultant friction force exerted at the tool–sheet contact interface is made of two in-plane components; a meridional component due to the step down movement of the tool and a circumferential component due to the circular (or eventually helical) tool path of the rotating tool. It was shown in Section 2.2 that the frictional effects along the circumferential direction can be neglected implying that only the friction forces exerted in the meridional directional need to be taken into account.

Starting from the simplified form of the membrane equilibrium condition in the meridional direction (8) and neglecting the variation in thickness $dt/dr \cong 0$ one obtains

$$\frac{d\sigma_\phi}{dr} + \frac{\sigma_\phi - \sigma_\theta}{r} + \frac{\mu\sigma_t}{t\sin\alpha} = 0. \quad (16)$$

Substituting σ_t and σ_θ by Eqs. (11) and (12) one obtains

$$\frac{d\sigma_\phi}{dr} + \frac{1}{2}\frac{\sigma_\phi}{r}\left(1+\frac{t}{r_{\text{tool}}}\right) + \frac{\mu\sigma_t}{t\sin\alpha} = 0. \quad (17)$$

The above equation can be further simplified by neglecting the second term, due to the fact that r is a large number and $(1+t/r_{\text{tool}}) \approx 1$, and by substituting σ_t in accordance to Eq. (11),

$$\frac{d\sigma_\phi}{dr} - \sigma_\phi \frac{\mu}{r_{\text{tool}}\sin\alpha} = 0. \quad (18)$$

Integration of Eq. (18) along the meridional length of the small localized plastic zone originated by the geometrical interference between the contour of the tool and that of the

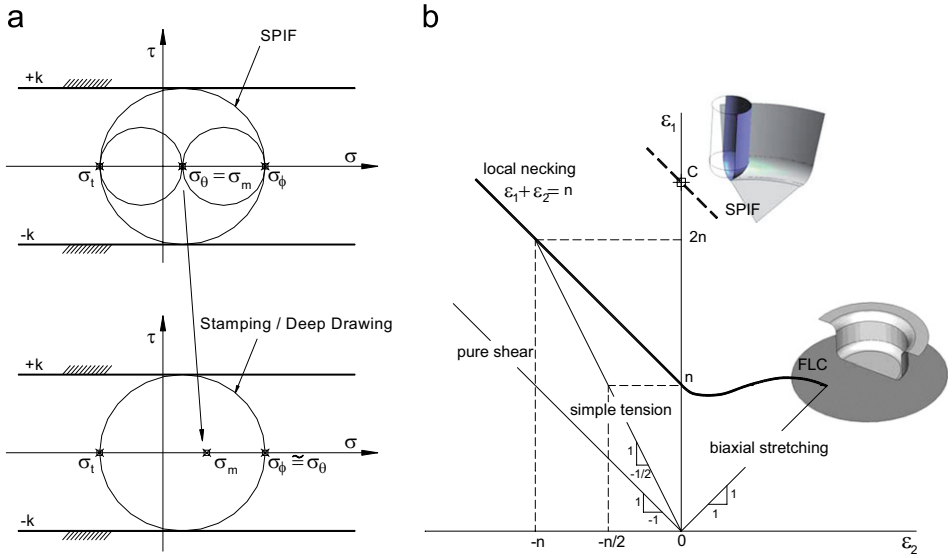

Fig. 7. Forming limit of single point incremental forming against that of conventional stamping and deep drawing processes: (a) state of stress and correspondent hydrostatic (or mean) stress; (b) schematic representation of the forming limit curve in the principal strain space (ε_1,ε_2).

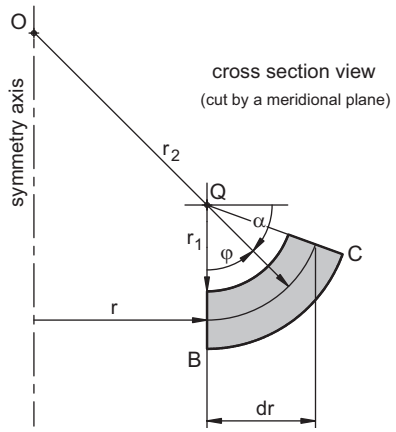

Fig. 8. Detail of the cross-sectional view of the local shell element with variables utilized in the integration of friction along the meridional direction.

sheet placed immediately ahead (noting that $dr/d\alpha = r_{tool}\sin\alpha$), gives

$$\sigma_\phi = \sigma_{\phi_B}\exp^{\mu\varphi}, \tag{19}$$

where the angle φ is defined in Fig. 8.

The change in the meridional stress $(\Delta\sigma_\phi)_{BC}$ due to friction can be estimated as

$$(\Delta\sigma_\phi)_{BC} = \sigma_{\phi_C} - \sigma_{\phi_B} = \sigma_{\phi_B}(\exp^{\mu\Delta\varphi} - 1). \tag{20}$$

This result indicates that the meridional stress σ_ϕ will increase with r as a result of friction at the tool–sheet contact interface. It also explains why the onset of cracking is placed at the transition between the inclined wall and the corner radius of the component being formed (refer to Fig. 4).

However, the increase of meridional stresses due to friction is not expected to greatly influence the overall formability of the process due to small variations in the exponential term of Eq. (20) in the typical range of friction coefficients μ. This result is in agreement with the work of Carrino et al. [14] experimentally observing the differences in formability of SPIF due to friction only to be significant at extreme conditions (e.g. lubricated vs. non-lubricated).

The analysis of thinning that will be performed in the following section of the paper will further corroborate the above mentioned localization of the onset of cracking.

3.5. Thinning at the corner radius

As the sheet is formed under the single point incremental tool, it is also thinned. Starting from the following simplified form of the membrane equilibrium condition in the meridional direction neglecting friction (refer to Eq. (8)),

$$\frac{d\sigma_\phi}{dr} + \frac{\sigma_\phi - \sigma_\theta}{r} + \frac{\sigma_\phi}{t}\frac{dt}{dr} = 0 \tag{21}$$

and substituting σ_t and σ_θ by Eqs. (11) and (12) one obtains

$$\frac{d\sigma_\phi}{dr} + \frac{1}{2}\frac{\sigma_\phi}{r}\left(1 + \frac{t}{r_{tool}}\right) + \frac{\sigma_\phi}{t}\frac{dt}{dr} = 0. \tag{22}$$

The above equation can be further simplified by neglecting the second term (refer to Section 3.4),

$$\frac{d\sigma_\phi}{dr} + \frac{\sigma_\phi}{t}\frac{dt}{dr} = 0. \tag{23}$$

Integration of Eq. (23) along the meridional length of the local shell element gives

$$\ln\sigma_\phi = -\ln t + C \tag{24}$$

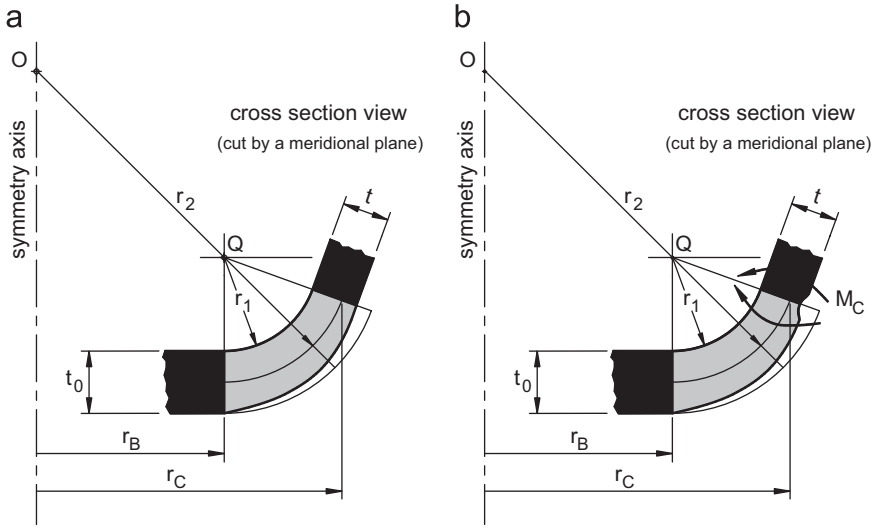

Fig. 9. Schematic representation of the variation in thickness along the meridional direction in the local shell element utilized for modeling the small plastic zone located at the corner of the rotational symmetric components: (a) evolution of thinning as predicted by the new proposed membrane analysis; (b) localization of thinning in point C as a result of bending effects that were not taken into consideration in the membrane analysis.

and for the boundary conditions at $r = r_B$, $\sigma_\phi = \sigma_{\phi B}$ and $t = t_0$,

$$\ln\frac{\sigma_\phi}{\sigma_{\phi_B}} = \ln\frac{t_0}{t} \rightarrow \sigma_\phi = \sigma_{\phi_B}\frac{t_0}{t}. \tag{25}$$

The physical meaning of Eq. (25) is that reduction in thickness t tends to balance the rise in the meridional stress σ_ϕ so that $\sigma_\phi t$ is constant in the small localized zone being plastically deformed. The schematic geometrical interpretation is provided in Fig. 9.

From what was mentioned before it follows that although the variation in the wall thickness of the inclined surface of the sheet can be adequately estimated by means of the sine law $t = t_0 \sin\lambda$, the reason why thinning occurs has to do with the meridional tensile stresses σ_ϕ acting in the small localized zone being plastically deformed. According to Eq. (25) and Fig. 9a thinning is most pronounced at the transition between the inclined wall and the corner radius of the sheet. Increase in the meridional stress σ_ϕ due to bending over point C [15],

$$(\Delta\sigma_\phi)_{\text{bend}} = \frac{\sigma_Y t}{4r_{\text{tool}}}\left\{1 + \left(\frac{(\sigma_\phi)_C}{\sigma_Y}\right)^2\right\} \tag{26}$$

is expected to promote additional localized thinning as it is schematically shown in Fig. 9b.

Eq. (26) is similar to that usually accounted in stamping (or deep drawing) [15] and further corroborates the experimentally observed onset of cracking in rotational symmetric SPIF components.

3.6. The inclined wall surface of the sheet adjacent to the forming tool

To conclude the characterization of the stress field in the radial slice of the component containing the small localized plastically deforming region it is interesting to extend the membrane analysis to the inclined wall of the sheet placed at the vicinity of the single point forming tool (refer to zone CD in Fig. 5).

Using the simplified form of the membrane equilibrium equation in the thickness direction (5) and noticing the absence of curvature $r_1 = \infty$ as well as the contact pressure $\sigma_t = 0$ on the surface of the local element CD, one obtains

$$\frac{\sigma_t}{t} + \frac{\sigma_\phi}{r_1} + \frac{\sigma_\theta}{r_2} = 0 \rightarrow \sigma_\theta = 0. \tag{27}$$

In physical terms this result is compatible with the fact that during rotational symmetric SPIF with a constant draw angle ψ the inclined wall maintains its geometry after being formed.

Since the meridional stresses σ_ϕ are the only stresses acting in this region it is possible to set-up the following equilibrium condition based on the stretching force that is supported by the inclined wall of the sheet,

$$\sigma_{\phi_C} r_C t_C \, d\theta = \sigma_{\phi_D} r_D t_D \, d\theta \tag{28}$$

or

$$\sigma_{\phi_D} = \sigma_{\phi_C}\frac{r_C}{r_D}, \tag{29}$$

considering that the thickness of the inclined wall of the sheet remains unchanged, $t_C = t_D = t_0 \sin\lambda$.

According to Eq. (29), the meridional stress σ_ϕ decreases along the inclined wall of the sheet being higher at the transition point C and smaller at point D. Because the meridional stress at point C must be kept below the yield stress (for a perfectly-plastic material), it follows that the inclined wall surface of the sheet adjacent to the forming tool is elastic,

$$\begin{aligned} &0 < \sigma_\phi = \sigma_1 < \sigma_Y, \\ &\sigma_\theta = \sigma_t = 0, \end{aligned} \tag{30}$$

This result together with the stress analysis performed in the previous sections of the paper allows plotting the schematic representation of the stress field in a radial slice of the SPIF component that contains the small localized plastic zone as it is depicted in Fig. 10.

To conclude the analysis of the fundamentals of SPIF it is necessary to explain the origin of the two different types of crack propagation paths that are usually found in rotational symmetric parts (Fig. 11); (i) the circumferential straight crack propagation path and (ii) the circumferential 'zigzag' crack propagation path.

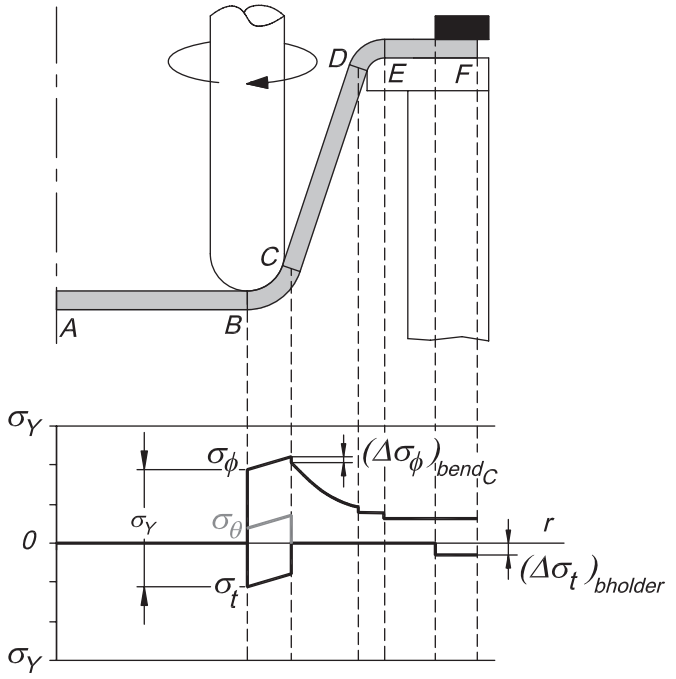

Fig. 10. Schematic representation of the stress field in the radial slice of the component being formed that contains the local shell element utilized for the membrane analysis of SPIF.

The circumferential straight propagation path (Fig. 11c) is similar to that usually found in conventional stamping or deep drawing operations (Fig. 11d) and it is a clear evidence that crack opening in SPIF is triggered by stretching mechanisms due to meridional tensile stresses σ_ϕ.

The 'zigzag' crack propagation path (Fig. 11b) is also triggered by meridional tensile stresses σ_ϕ but its morphology, bouncing around the circumferential direction, is probably caused by friction towards the rotating forming tool. In fact, the position of the neutral velocity line at the contact interface between the tool and the sheet may cause crack propagation, after attainment the onset conditions at point 'o', to follow at some angle δ with the meridional direction (Fig. 11a). After reaching point 'a' the crack will be considerably away from the small plastic deformation zone, where the level of applied stresses is high, and will be located within the inclined (conical) surface of the component undergoing elastic deformation. In other words, the tip of the crack in 'a' will be under a much lower level of meridional stresses than at the onset point 'o'. As a consequence, propagation of the crack will stop and the rotation of the tool will drag it to point 'b' where the level of applied stresses will be, once again, capable of restoring the onset conditions and restarting crack propagation. This mechanism of crack initiation and propagation will be recursively repeated leading to the 'zigzag' morphology of the cracks that can be experimentally observed in SPIF.

Another possibility for explaining the experimentally observed differences between the propagation paths

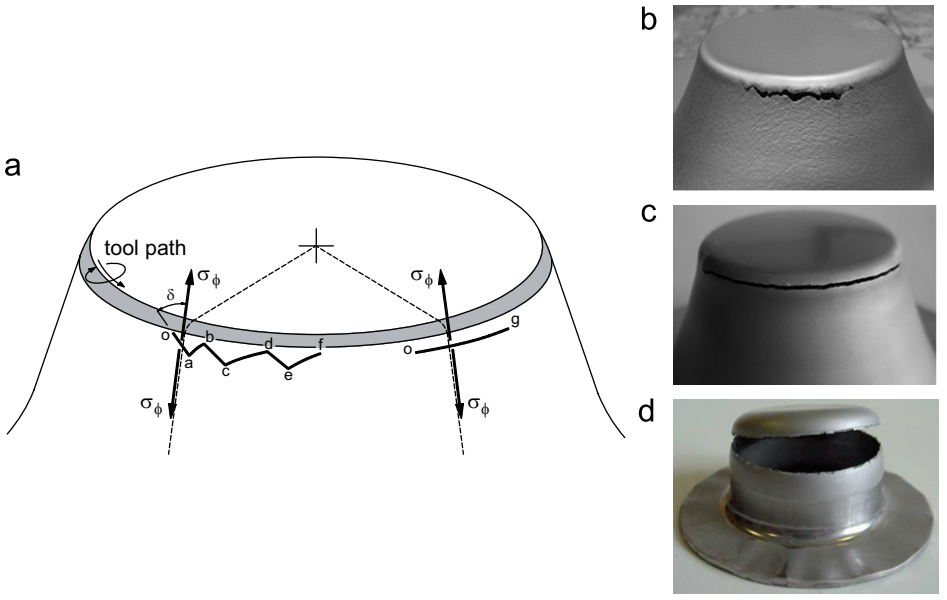

Fig. 11. Crack propagation in SPIF: (a) schematic illustration of the typical crack propagation path in SPIF; (b) circumferential zigzag crack propagation path; (c) circumferential straight crack propagation path; (d) circumferential straight crack propagation path in a rotational symmetric partobtained by conventional deep-drawing.

depicted in Fig. 11 can be set-up on the basis of the physics behind crack opening mechanisms. This possibility, yet to be evaluated, argues that in some materials the attainment of a maximum value of the meridional tensile stresses σ_ϕ permits localized necking to develop in the form of a groove at some angle δ with the meridional direction (refer to Fig. 11a and b) while in other materials this will only account for the development of diffuse necking (Fig. 11c). The reason why this possibility must be further analyzed is due to the fact that the part in Fig. 11b is made of conventional deep drawing steel, while the part in Fig. 11c is made of deep drawing stainless steel. Stainless steel is known to have a much higher strain hardening coefficient than conventional steel and, therefore, a much lower tendency to experience local necking crack growing mechanisms.

4. Conclusions

The paper presents the first closed-form analytical model for SPIF. The model is built upon membrane analysis and is based on the experimental observation of the smear-mark interference between the tool and the surface of the sheet and on the examination of the likely mode of material failure at the transition zone between the inclined wall and the corner radius of the sheet. Cracks in SPIF are claimed to be opened by meridional tensile stresses and not by in-plane shearing stresses.

The new proposed model is able to address the fundamentals of the process and to qualitatively explain the experimental and numerical results that were made available in the literature for the past couple of years.

Strain hardening and anisotropy were not taken into consideration while bending effects were only indirectly included in the analysis. However, the proposed model can be further enhanced to include some of these limitations.

Acknowledgments

The first author and the corresponding author would like to acknowledge PTDC/EME-TME/64706/2006 FCT/Portugal for the financial support. The corresponding author would like to acknowledge the support of IPL/DTU during his sabbatical license in Denmark.

Revision of the manuscript and suggestions for future work provided by Professor Anthony G. Akins are also greatly acknowledged.

References

[1] J. Jeswiet, F. Micari, G. Hirt, A. Bramley, J. Duflou, J. Allwood, Asymmetric single point incremental forming of sheet metal, Annals of CIRP 54 (2005) 623–650.
[2] S. Matsubara, Incremental backward bulge forming of a sheet metal with a hemispherical head tool, Journal of the Japan Society for Technology of Plasticity 35 (1994) 1311–1316.
[3] H. Iseki, O. Kumon, Forming limit of incremental sheet metal stretch forming using spherical rollers, Journal of the Japan Society for Technology of Plasticity 35 (1994) 1336–1341.
[4] E. Hagan, J. Jeswiet, A review of conventional and modern single point sheet metal forming methods, Journal of Engineering Manufacture 217 (2003) 213–225.
[5] L. Filice, L. Fratini, F. Micari, Analysis of material formability in incremental forming, Annals of the CIRP 51 (2002) 199–202.
[6] J.M. Allwood, G.P.F. King, J.R. Duflou, A structured search for applications of the incremental sheet forming process by product segmentation, Journal of Engineering Manufacture 219 (2004) 239–244.
[7] D. Leach, A.J. Green, A.N. Bramley, A new incremental sheet forming process for small batch and prototype parts, in: 9th International conference on sheet metal, Leuven, Belgium, 2001, pp. 211–221.
[8] M. Bambach, G. Hirt, J. Ames, Quantitative validation of FEM simulations for incremental sheet forming using optical deformation measurement, Advanced Materials Research 6–8 (2005) 509–516.
[9] J.R. Duflou, B. Lauwers, J. Verbert, F. Gelaude, Y. Tunckol, Medical application of single point incremental forming: cranial plate manufacturing, in: Virtual modelling and rapid manufacturing, Taylor & Francis, London, 2005, pp. 161–166.
[10] W.C. Emmens, A.H. van den Boogaard, Strain in shear and material behaviour in incremental forming, Key Engineering Materials 344 (2007) 519–526.
[11] J. Jeswiet, D. Young, Forming limit diagrams for single point incremental forming of aluminum sheet, Journal of Engineering Manufacture 219 (2005) 359–364.
[12] L. Fratini, G. Ambrogio, R. Di Lorenzo, L. Filice, F. Micari, Influence of mechanical properties of the sheet material on formability in single point incremental forming, Annals of CIRP 53 (2004) 207–210.
[13] G. Hirt, J. Ames, M. Bambach, R. Kopp, Forming strategies and process modeling for CNC incremental sheet forming, Annals of the CIRP 53 (2004) 203–206.
[14] L. Carrino, N. Di Meo, L. Sorrentino, M. Strano, The influence of friction in negative dieless incremental forming, in: 9th International ESAFORM conference on materials forming, Glasgow, UK, 2006, pp. 203–206.
[15] J.M.C. Rodrigues, P.A.F. Martins (Eds.), Tecnologia da deformação plástica: aplicações industriais, Escolar Editora (2005) (in Portuguese).

February 2008

Joint author statement

If a thesis contains articles made in collaboration with other researchers, a joint author statement about the PhD-student's part of the article shall be made by each of the co-authors, cf. article 12, section 4 of the Ministerial Order No. 18 February 2008 about the PhD degree

Title of the article: Single-point incremental forming & formability-failure diagrams

Author(s): M.B. Silva, M. Skjoedt, A.G. Atkins, N. Bay, P.A.F. Martins

Journal: The Journal of Strain Analysis, (2008), vol. 43, p. 15-35.

PhD-student: Martin Skjødt Cpr.nr: _____

Signature of the PhD-student: _____ Date: _____

Co-author: _____ Signature: _____

Description of each author's contribution to the above-mentioned article:
M. B. Silva: Planning and conduction of experiments, thickness measurements, literature study, further discussion and development of theory, final editing.

M. Skjoedt: CAD drawing of parts, CAM programming of parts, planning and conduction of experiments, pictures for paper, literature study, further discussion and development of theory, final editing.

A. G. Atkins: Planning of experiments, further discussion and development of theory, final editing.

N. Bay: Planning of experiments, further discussion and development of theory, final editing.

P. A. F. Martins: Development of initial theory including formulas and assumptions, further discussion and development of theory, planning of experiments, writing of paper, pictures and graphics for paper, final editing.

Single-point incremental forming and formability–failure diagrams

M B Silva[1], **M Skjoedt**[2], **A G Atkins**[3], **N Bay**[2], and **P A F Martins**[1*]
[1] IDMEC, Instituto Superior Tecnico, TULisbon, Lisboa, Portugal
[2] Technical University of Denmark, Department of Manufacturing Engineering and Management, Kgs. Lyngby, Denmark
[3] Department of Engineering, University of Reading, Reading, UK

The manuscript was received on 6 August 2007 and was accepted after revision for publication on 21 September 2007.

DOI: 10.1243/03093247JSA340

Abstract: In recent work, the present authors constructed a closed-form analytical model that is capable of dealing with the fundamentals of single-point incremental forming (SPIF) and explaining the experimental and numerical results published in the literature over the past couple of years. The model is based on membrane analysis with in-plane contact frictional forces but is limited to plane strain, rotationally symmetric conditions.

The aim of the present paper is twofold: first, to extend the previous closed-form analytical model into a theoretical framework that can easily be applied to the different modes of deformation that are commonly found in general single-point incremental forming processes and, second, to investigate the formability limits of SPIF in terms of ductile damage mechanics and the question of whether necking does, or does not, precede fracture.

Experimentation by the present authors, together with data retrieved from the literature, confirms that the proposed theoretical framework is capable of successfully addressing the influence of the major parameters of the SPIF process. It is demonstrated that neck formation is suppressed in SPIF, so that traditional forming limit diagrams are inapplicable to describe failure. Instead fracture forming limit diagrams should be employed.

Keywords: single-point incremental forming, membrane analysis, formability

1 INTRODUCTION

Single-point incremental forming (SPIF) is a new sheet-metal-forming process with a high-potential economic pay-off for rapid prototyping applications and for small-quantity production.

Figure 1 presents the basic components of the process:

(a) the sheet metal blank;
(b) the blank holder;
(c) the backing plate;
(d) the rotating single-point forming tool.

The tool path is generated in a computer numerical control (CNC) machining centre and is utilized to form progressively the sheet into a component. During the process there is no backup die supporting the back surface of the sheet.

SPIF was patented in 1967 by Leszak [**1**] and was proven to be feasible by Kitazawa *et al.* [**2**] in forming rotational symmetric parts in aluminium. The capability study of using an ordinary CNC milling machine instead of a special-purpose machine-tool apparatus later performed by Jeswiet [**3**] and Filice *et al.* [**4**] was the starting point for the successful and rapid development of the process.

Most studies on SPIF have concerned experimental investigations on applications and formability limits, and also a limited number of finite element studies have been carried out. A comprehensive overview of the research on SPIF may be found in the keynote paper by Jeswiet *et al.* [**5**] and other

*Corresponding author: Departamento de Engenharia Mecanica, Instituto Superior Tecnico, Seccao de Tecnologia Mecanica, Avenida Rovisco Pais, Lisboa, 1049-001, Portugal. email: pmartins@ist.utl.pt

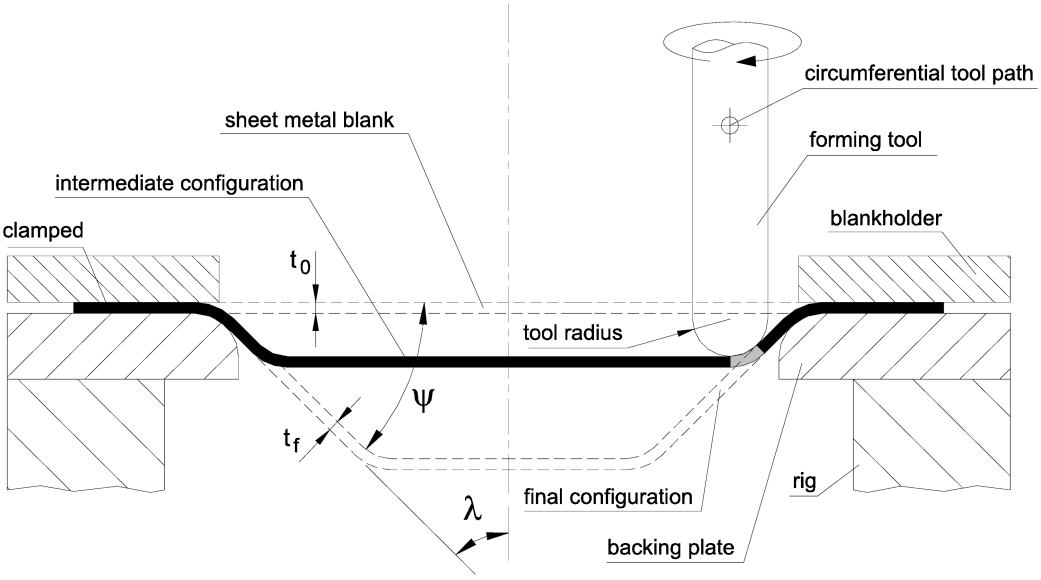

Fig. 1 Schematic representation of a cross-sectional view of the rotationally symmetric SPIF process. The tool rotates while performing a round (or helical) path

significant contributions to the development of industrial applications, and characterization of the formability limits of the process can be found in the papers by Hagan and Jeswiet [**6**], Leach *et al.* [**7**], Fratini *et al.* [**8**], Allwood *et al.* [**9**], Bambach *et al.* [**10**], and Duflou *et al.* [**11**].

So far, the experimental investigations lead to the conclusion that the formability of the process can be defined in terms of four major parameters [**5**]:

(a) thickness of the sheet;
(b) relative size of the step down per revolution (or the drawing angle);
(c) speed (both rotational and feed rate);
(d) radius of the forming tool.

The influence of the first and second parameters is commonly explained by means of the sine law $t_f = t_0 \sin\lambda$, where t_0 is the initial thickness, t_f is the final thickness, λ is the semicone angle, and $\psi = \pi/2 - \lambda$ is the drawing angle between the inclined wall surface and the initial flat configuration of the sheet (see Fig. 1). The speed of the forming tool is known to influence formability because of its direct influence on the frictional conditions at the tool–sheet interface [**5**]. In what concerns the radius of the forming tool it is experimentally observed that better formability is achieved with the utilization of smaller tools. It is claimed that smaller tools are able to concentrate the strain at the zone of deformation in the sheet under the forming tool, whereas larger tools tend to distribute the strains over a more extended area, making the process more similar to conventional stamping [**5**].

In what concerns finite element analysis, studies reported in the literature have been mainly disclosing that numerical modelling of SPIF is a complex task, requiring the utilization of a large number of very small elements everywhere on the sheet, which often leads to prohibitive central processing unit times. Moreover, such studies are generally limited to examples where experimentation had been previously performed, meaning that computations are not being employed predictively.

The widespread utilization of dynamic explicit finite element computer programs for increasing the 'know-how', and to compensate for the gap of understanding of the mechanics of SPIF, often gives answers that are not helpful owing to poor accuracy of the overall numerical predictions. In fact, the limitations of dynamic explicit formulations in properly characterizing quasi-static sheet-metal-forming processes due to the artificial increase in the inertia terms in the equilibrium equations is a well-known problem that is comprehensively documented in the literature [**12**]. This means that more concentrated efforts must be made to develop alternative quasi-static implicit formulations that are capable of effectively and efficiently modelling SPIF [**13**].

Even if the great difficulties in analysing SPIF by the finite element method were not actual, it is good practice to obtain improved understanding of the process by establishing a simple but effective algebraic theoretical model that allows the major process parameters to interact with each other in a set of equations that can be employed in both

qualitative and quantitative predictions. This research will shortly appear [**14**].

The aim of the present paper is to extend the previous closed-form analytical model for plane strain, rotationally symmetric conditions into a theoretical framework, founded on the physics of the process, that can easily handle the different modes of deformation that are commonly found in SPIF. The approach is based on the utilization of membrane equilibrium conditions under contact frictional forces in conjunction with the characterization of the small localized region being incrementally plastically deformed, and a better understanding of the ductile damage mechanisms behind the onset and propagation of cracks. The overall presentation is supported by experimental results obtained by the present authors and by data retrieved from the literature.

2 THEORETICAL BACKGROUND

The governing mode of deformation in SPIF has been subject to controversy in the metal-forming community [**15**]. Some researchers have claimed that deformation takes place by stretching instead of shearing while others have claimed the opposite, but assertions are mainly based on 'similarities' with well-known processes of stamping and shear spinning rather than on experimental evidence from SPIF itself.

As will be shown later in section 3, examination of the likely mode of material failure at the transition zone between the inclined wall and the corner radius of the sheet is consistent with the fact that stretching, rather than shearing, is the governing mode of deformation in SPIF. This agrees with a recent published work by Allwood *et al.* [**16**] which identifies the mechanics of SPIF as being a combination of stretching and bending deformation modes instead of vertical shear as initially proposed by other workers. In connection with this it is important to distinguish vertical shear from the concept of through-thickness shear that is presented in reference [**16**] as a possible explanation for the increased forming limits of SPIF.

The aforementioned conclusion that in-plane stretching is the principal mode of deformation in SPIF is the starting point for setting up the theoretical framework of SPIF presented in the following sections of the paper.

2.1 Small localized plastic zone

Figure 2(a) shows a schematic outline of the forming tool acting on a (transparent) sheet during SPIF. The metal is stretched by membrane forces, so that it conforms to the hemispherical shape of the tip of the pin tool, forming a contact area between the tool and the part of the sheet placed immediately ahead of the moving tool.

Parts produced by SPIF may have complex shapes but, in general terms, it is possible to classify all possible tool paths as combinations of those that are schematically depicted in Fig. 2. This leads to the identification of three basic modes of deformation that are associated with the following:

(a) flat surfaces under plane strain stretching conditions;
(b) rotationally symmetric surfaces under plane strain stretching conditions;
(c) corners under equal biaxial stretching conditions.

It is worth noting that in between these modes of deformation there are other possibilities where neither plane strain stretching nor equal biaxial stretching appears. However, the analytical model to be presented in the paper will be focused only on the extreme modes of deformation that are likely to be found in SPIF.

The examination of these modes of deformation together with the analysis of the pictures showing the experimentally observed smear-mark interferences between the tool and the surface of the sheet (Fig. 2(b)) allows it to be concluded that the instantaneous small plastic zone typical of SPIF can be approximated by one of the shapes plotted in Fig. 2(c). The states of strain and stress acting in these zones will be derived from the membrane equilibrium conditions of a local shell element CDEF under contact frictional forces (Fig. 3).

2.2 Membrane equilibrium conditions

The surface of a SPIF part is characterized by the local shell element depicted in Fig. 3. The normal to the surface of the local shell element cuts the z axis at the point O and r_2 is defined as the corresponding radius. The centre of curvature lies at point Q on the normal and r_1 is the radius of curvature of the local shell element along the meridian direction.

In SPIF the local shell element is subjected to normal forces, shear forces, and bending moments. However, the membrane analysis of plastically deforming shells will neglect the bending moments and, assuming axial symmetry and friction to be rather small, the circumferential, meridional, and thickness stresses may be considered as principal

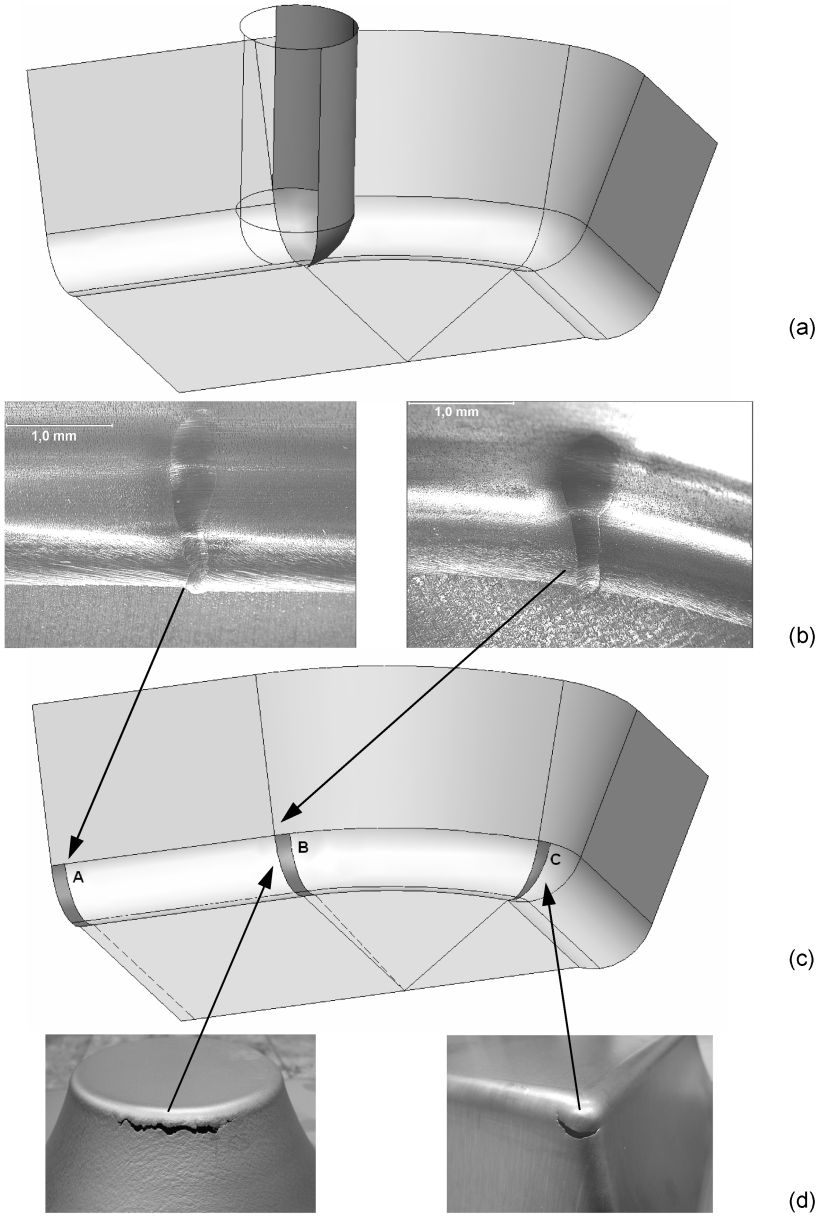

Fig. 2 Schematic representation of the volume element resulting from the local contact between the tool and sheet placed immediately ahead of tool, and identification of the basic modes of deformation of SPIF: A, flat surface under plane strain stretching conditions; B, rotationally symmetric surface under plane strain stretching conditions; C, corner under biaxial stretching conditions. Note that the insets show images of typical cracks occurring in deformation modes B and C

stresses. Further simplifying assumptions that will be made in the following sections of the present paper are as follows.

1. The material is assumed to be rigid–perfectly plastic, i.e. no strain-hardening effects are taken into consideration.
2. The material is assumed to be isotropic, i.e. no anisotropic effects are taken into consideration.
3. The resultant frictional stress exerted at the tool–sheet contact interface is assumed to be made of two in-plane components: a meridional component $\mu_\phi \sigma_t$ due to the step-down movement of the tool and a circumferential component $\mu_\theta \sigma_t$ due to the circumferential feed combined with the rotation of the tool. This last assumption, which is an untraditional way of modelling friction

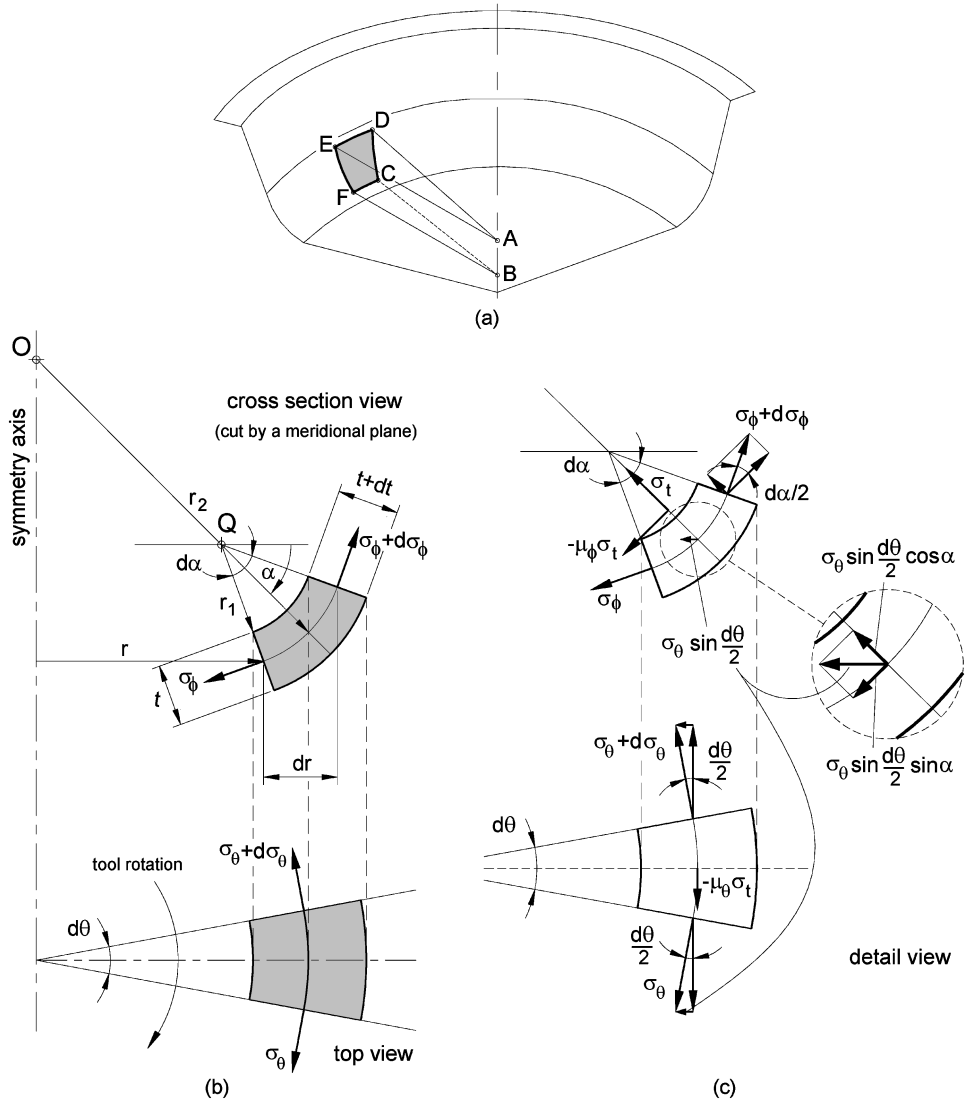

Fig. 3 Membrane analysis for the SPIF: (a) schematic representation of the shell element in perspective; (b) schematic representation of the shell element after being cut by an axial meridional plane and as it is seen from the top; (c) detail of (b) showing the acting stresses

introduced for convenience, implies that the coefficient of friction $\mu = \sqrt{\mu_\phi^2 + \mu_\theta^2}$.

2.2.1 *Circumferential direction*

The stresses acting on the local shell element are illustrated in Figs 3(b) and (c). The $\mu_\theta \sigma_t$ stress term along the circumferential direction is due to the tool–sheet frictional contact interface, and its point of application is assumed to coincide with the centre of the element. Its sign is dependent on the balance of the relative velocity between the tool and the surface of the sheet.

Resolving the force equilibrium along the circumferential direction results in

$$\sigma_\theta r_1 \, \mathrm{d}\alpha \left(t + \frac{\mathrm{d}t}{2}\right) - \mu_\theta \sigma_t r_1 \, \mathrm{d}\alpha \left(r + \frac{\mathrm{d}r}{2}\right) \mathrm{d}\theta = (\sigma_\theta + \mathrm{d}\sigma_\theta) r_1 \, \mathrm{d}\alpha \left(t + \frac{\mathrm{d}t}{2}\right) \quad (1)$$

Which, after neglecting higher-order terms and assuming $r \, \mathrm{d}\theta \approx t$, gives

$$\mathrm{d}\sigma_\theta = -\mu_\theta \sigma_t \frac{r \mathrm{d}\theta}{t} \approx -\mu_\theta \sigma_t \quad (2)$$

The latter assumption, $r\,\mathrm{d}\theta \approx t$, comes from observation of the micrographs in Fig. 2(b) showing the width of the smear mark in the circumferential direction to be of approximately the same size as the sheet thickness, an approximation that also is physically sensible.

2.2.2 *Thickness direction*

Resolving the force equilibrium along the thickness direction (see fig. 3(c)) gives

$$\begin{aligned}&\sigma_t r\,\mathrm{d}\theta\, r_1\,\mathrm{d}\alpha + \sigma_\phi r\,\mathrm{d}\theta\, t\sin\left(\frac{\mathrm{d}\alpha}{2}\right)\\&+(\sigma_\phi+\mathrm{d}\sigma_\phi)(r+\mathrm{d}r)\,\mathrm{d}\theta\,(t+\mathrm{d}t)\sin\left(\frac{\mathrm{d}\alpha}{2}\right)\\&+\sigma_\theta r_1\,\mathrm{d}\alpha\, t\sin\left(\frac{\mathrm{d}\theta}{2}\right)\cos\alpha\\&+(\sigma_\theta+\mathrm{d}\sigma_\theta)r_1\,\mathrm{d}\alpha\, t\sin\left(\frac{\mathrm{d}\theta}{2}\right)\cos\alpha = 0\end{aligned} \tag{3}$$

After neglecting higher-order terms and simplifying the above equation by taking into account that $r_2 = r/\cos\alpha$ and the identity in equation (2)

$$\sigma_t\left(\frac{1}{t}-\frac{\mu_\theta}{2r_2}\right)+\frac{\sigma_\phi}{r_1}+\frac{\sigma_\theta}{r_2}=0 \tag{4}$$

Because the term $\mu_\theta/2r_2$ placed inside the parentheses is very small when compared with $1/t$ it follows that equation (4) can be further simplified to

$$\frac{\sigma_t}{t}+\frac{\sigma_\phi}{r_1}+\frac{\sigma_\theta}{r_2}=0 \tag{5}$$

In physical terms this last simplification implies that the frictional effects in the circumferential direction are neglected in the analysis. This result will be very advantageous in the forthcoming sections of the paper.

2.2.3 *Meridional direction*

The equilibrium condition of the local shell element in the meridional direction gives (see Fig. 3(c))

$$\begin{aligned}&(\sigma_\phi+\mathrm{d}\sigma_\phi)(r+\mathrm{d}r)\,\mathrm{d}\theta\,(t+\mathrm{d}t)-\sigma_\phi r\,\mathrm{d}\theta\, t\\&+\mu_\phi\sigma_t r\,\mathrm{d}\theta\, r_1\,\mathrm{d}\alpha-\sigma_\theta\frac{\mathrm{d}\theta}{2}\,r_1\,\mathrm{d}\alpha\, t\sin\alpha\\&-(\sigma_\theta+\mathrm{d}\sigma_\theta)\frac{\mathrm{d}\theta}{2}r_1\mathrm{d}\alpha\, t\sin\alpha=0\end{aligned} \tag{6}$$

where $\mu_\phi\sigma_t$ is the average or net frictional stress in the meridional direction and $\mathrm{d}\sigma_0 \approx -\mu_\theta\sigma_t$, included in the last term of equation (6), derives from the projection of the circumferential build-up of friction along the meridional direction.

After neglecting higher-order terms and simplifying the above equation by taking into account that $\mathrm{d}r = r_1\,\mathrm{d}\alpha\,\sin\alpha$

$$\frac{\mathrm{d}\sigma_\phi}{\mathrm{d}r}+\frac{\sigma_\phi-\sigma_\theta}{r}+\sigma_t\left(\frac{\mu_\phi}{t\sin\alpha}+\frac{\mu_\theta}{2r}\right)+\frac{\sigma_\phi}{t}\frac{\mathrm{d}t}{\mathrm{d}r}=0 \tag{7}$$

Because $r \gg t\,\sin\alpha$, the previous equation can be rewritten in the simplified form

$$\frac{\mathrm{d}\sigma_\phi}{\mathrm{d}r}+\frac{\sigma_\phi-\sigma_\theta}{r}+\frac{\mu_\phi\sigma_t}{t\sin\alpha}+\frac{\sigma_\phi}{t}\frac{\mathrm{d}t}{\mathrm{d}r}=0 \tag{8}$$

In physical terms this last equation confirms, once again, that the frictional effects in the circumferential direction may be neglected in the analysis. As a result of this, the forthcoming sections of the paper will make use of the following approximation of the friction coefficient: $\mu \approx \mu_\phi$.

3 THEORY APPLIED TO GENERAL SPIF PARTS

This section combines the characterization of the opening mode of the cracks found in rotationally symmetric SPIF with the analysis of the states of strain and stress, the role of friction, and the evolution of thickness in the small localized plastic zones depicted in Fig. 2. The analysis is performed by means of the membrane equilibrium conditions presented in section 2, and it is aimed to set up a theoretical framework that can help the physics of the process to be understood and can model the basic modes of deformation that are usually found in general SPIF parts.

3.1 State of stress and strain

The stress state acting in the local shell element that conforms to the hemispherical shape of the tool (see BC in Fig. 4) can be derived from the previous membrane equilibrium equations applied to the three basic modes of deformation associated with the following:

(a) flat surfaces under plane strain stretching conditions (shell element A in Fig. 2(c));
(b) rotationally symmetric surfaces under plane strain stretching conditions (shell element B in Fig. 2(c));

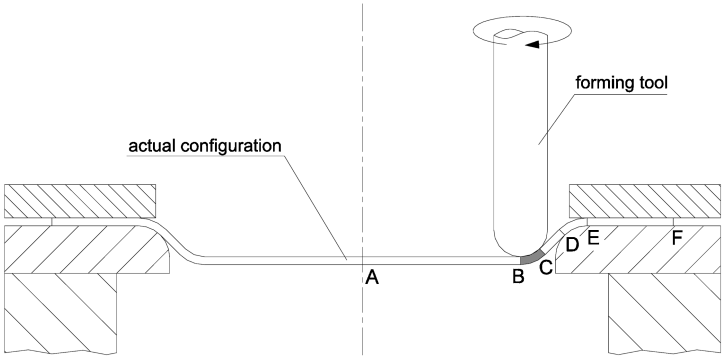

Fig. 4 Schematic representation of a cross-sectional view of the SPIF process by a meridional plane. The shaded zone BC illustrates the local shell element on the surface of the intermediate configuration of the sheet that conforms to the hemispherical shape of the forming tool

(c) corners under equal biaxial stretching conditions (shell element C in Fig. 2(c)).

3.1.1 *Flat and rotationally symmetric surfaces (shell elements of type A and B)*

Combining the simplified form of the membrane equilibrium equation in the thickness direction (equation (5)) with the geometrical conditions prevailing in BC ($r_2 \gg r_1$ and $r_2 \gg t$; see Figs 3 and 4 for definition of these variables), it follows that the ratio of the circumferential stress σ_θ to the radius r_2 normal to the surface of the local shell element can be neglected; thus

$$\frac{\sigma_\theta}{r_2} \approx 0 \tag{9}$$

Hence, equation (5) can take the following simplified form

$$\frac{\sigma_t}{t} + \frac{\sigma_\phi}{r_1} = 0 \tag{10}$$

Under these circumstances, the relation between the normal contact pressure $p = -\sigma_t$ acting on the local shell element, the meridional stress σ_ϕ, the thickness of the sheet t, and the radius of the forming tool ($r_1 = r_{\text{tool}}$) can be derived as

$$\sigma_t = -\sigma_\phi \frac{t}{r_{\text{tool}}} \tag{11}$$

The full characterization of the state of stress in the small localized plastic zone can now be easily obtained after assuming that SPIF of flat and rotationally symmetric surfaces is performed under plane strain conditions ($\mathrm{d}\varepsilon_\theta = 0$ and $\mathrm{d}\varepsilon_\phi = -\mathrm{d}\varepsilon_t$). This assumption is experimentally corroborated by the work of Jeswiet and co-workers [**5**, **17**], Filice *et al.* [**4**], and Hirt *et al.* [**18**].

By considering the Levy–von Mises constitutive equations in plane strain conditions

$$\mathrm{d}\varepsilon_\theta = 0 \rightarrow \sigma_\theta = {}^1\!/_2\left(\sigma_t + \sigma_\phi\right) \tag{12}$$

the principal stresses acting on the element can be identified as

$$\begin{aligned} &\sigma_\phi = \sigma_1 > 0 \\ &\sigma_\theta = \sigma_2 \qquad (\sigma_1 > \sigma_2 > \sigma_3) \\ &\sigma_t = \sigma_3 < 0 \end{aligned} \tag{13}$$

where $|\sigma_t| < |\sigma_\phi|$, because $r_{\text{tool}} > t$ (see equation (11)).

Although the relative values of the principal stresses may vary with process parameters related to the thickness t of the sheet and to the radius r_{tool} of the forming tool, the term $\sigma_1 - \sigma_3$ should be constant according to the Tresca yield criterion and equal to the flow stress of the sheet (σ_{Y}, under perfectly plastic material assumptions). Inserting this in equation (11) leads to the equation for calculating the meridional stress σ_ϕ acting in the local shell element, given by

$$\sigma_\phi = \frac{\sigma_{\text{Y}}}{(1 + t/r_{\text{tool}})} \tag{14}$$

It is worth noting that σ_{Y} is to be replaced by $\sigma = K\varepsilon^n$ in the case when the material obeys a power law strain-hardening curve and $t = t_0 \sin\lambda$ according to the geometric relationship provided by the sine law.

3.1.2 *Corners (shell element of type C)*

The corners of the sheet metal parts produced by SPIF are assumed to be plastically deformed under

equal biaxial stretching conditions ($d\varepsilon_\phi = d\varepsilon_\theta > 0$, $d\varepsilon_t < 0$, and $\sigma_\phi = \sigma_\theta$). This complies with the state-of-the-art review by Jeswiet *et al.* [**5**] and the numerical modelling by Hirt *et al.* [**19**], who disclosed biaxial stretching conditions at the corners of a pyramid shape component.

Using the simplified form of the membrane equilibrium equation (5) in the thickness direction and taking into account the geometrical conditions prevailing in BC ($r_2 = r_1$; see Figs 3 and 4 for definition of these variables), it follows that

$$\frac{\sigma_t}{t} + 2\frac{\sigma_\phi}{r_1} = 0 \tag{15}$$

Under these circumstances, the relation between the normal contact pressure $p = -\sigma_t$ acting on the local shell element, the meridional stress σ_ϕ, the thickness of the sheet t, and the radius of the forming tool ($r_1 = r_{\text{tool}}$) can be derived as

$$\sigma_t = -2\sigma_\phi \frac{t}{r_{\text{tool}}} \tag{16}$$

The full characterization of the state of stress in the small localized plastic zone located at the corners of the SPIF parts can be easily obtained, after taking into consideration the aforementioned assumption of equal biaxial stretching conditions, as

$$\begin{aligned} &\sigma_\phi = \sigma_\theta = \sigma_1 > 0 \\ &\sigma_t = \sigma_3 < 0 \end{aligned} \tag{17}$$

where $|\sigma_t| < |\sigma_\phi|$, because $r_{\text{tool}} > 2t$ (see equation (16)).

Although the relative values of the principal stresses may vary with process parameters related to the thickness t of the sheet and to the radius r_{tool} of the forming tool, the term $(\sigma_1 - \sigma_3)$ should be constant according to the Tresca yield criterion and equal to the flow stress of the sheet (σ_Y, under perfectly plastic material assumptions). Inserting this in equation (16) leads to the following equation for calculating the meridional stress σ_ϕ acting in the local shell element given by

$$\sigma_\phi = \sigma_\theta = \frac{\sigma_Y}{(1 + 2t/r_{\text{tool}})} \tag{18}$$

Table 1 summarizes the states of stress and strain that are commonly found in general SPIF processes and compares their values with those of conventional stamping. These values will be of major importance in the following sections of the paper.

3.2 Friction at the tool–sheet contact interface

The resultant frictional force exerted at the tool–sheet contact interface consists of two in-plane components: a meridional component due to the step-down movement of the tool and a circumferential component due to the circular (or eventually helical) tool path of the rotating tool. It was shown in section 2.2 that the frictional effects along the circumferential direction can be neglected, implying that only the frictional forces exerted in the meridional direction need to be taken into account.

Starting from the simplified form of the membrane equilibrium condition in the meridional direction (8) and neglecting the variation in thickness, $dt/dr \approx 0$, gives

$$\frac{d\sigma_\phi}{dr} + \frac{\sigma_\phi - \sigma_\theta}{r} + \frac{\mu\sigma_t}{t\sin\alpha} = 0 \tag{19}$$

Solving equation (19) is divided into the three basic modes of deformation:

Table 1 States of stress and strain that are commonly found in general SPIF processes and conventional stamping

	Assumption	State of strain	State of stress	Hydrostatic stress
SPIF (flat and rotational symmetric surfaces)	Plane strain conditions	$d\varepsilon_\phi = -d\varepsilon_t > 0$ $d\varepsilon_\theta = 0$ $d\varepsilon_t < 0$	$\sigma_\phi = \sigma_1 = \frac{\sigma_Y}{1 + t/r_{\text{tool}}} > 0$ $\sigma_\theta = \sigma_2 = {}^1/_2(\sigma_1 + \sigma_3)$ $\sigma_t = \sigma_3 = -\sigma_Y \frac{t}{r_{\text{tool}} + t} < 0$	$\sigma_m = \frac{\sigma_Y}{2}\frac{r_{\text{tool}} - t}{r_{\text{tool}} + t}$
SPIF (corners)	Equal biaxial stretching	$d\varepsilon_\phi = d\varepsilon_\theta > 0$ $d\varepsilon_t < 0$	$\sigma_\phi = \sigma_\theta = \sigma_1 = \frac{\sigma_Y}{1 + 2t/r_{\text{tool}}} > 0$ $\sigma_t = \sigma_3 = -2\sigma_Y \frac{t}{(r_{\text{tool}} + 2t)} < 0$	$\sigma_m = \frac{2\sigma_Y}{3}\frac{r_{\text{tool}} - t}{r_{\text{tool}} + 2t}$
Conventional stamping (rotational symmetric surfaces) [**21**]	Equal biaxial stretching	$d\varepsilon_\phi = d\varepsilon_\theta > 0$ $d\varepsilon_t < 0$	$\sigma_\phi = \sigma_\theta = \sigma_1 = \frac{\sigma_Y}{1 + t/r_{\text{punch}}} > 0$ $\sigma_t = \sigma_3 = -\sigma_Y \frac{t}{(r_{\text{punch}} + t)} < 0$	$\sigma_m = \frac{2\sigma_Y}{3}\frac{r_{\text{punch}} - t/2}{r_{\text{punch}} + t}$

(a) flat surfaces under plane strain stretching conditions (shell element A in Fig. 2(c));
(b) rotationally symmetric surfaces under plane strain stretching conditions (shell element B in Fig. 2(c));
(c) corners under equal biaxial stretching conditions (shell element C in Fig. 2(c)).

3.2.1 *Flat surfaces under plane strain stretching conditions*

In this case, $r = \infty$, implying that equation (19) is reduced to

$$\frac{\mathrm{d}\sigma_\phi}{\mathrm{d}r} + \frac{\mu\sigma_t}{t\sin\alpha} = 0 \tag{20}$$

Inserting (11) and introducing α instead of r by the relation $\mathrm{d}r = r_{\text{tool}}\sin\alpha\ \mathrm{d}\alpha$ give

$$\frac{\mathrm{d}\sigma_\phi}{\sigma_\phi} = \mu\,\mathrm{d}\alpha \tag{21}$$

which by integration along the meridional line leads to

$$\sigma_\phi = \sigma_{\phi_\mathrm{B}}\exp^{\mu\varphi} \tag{22}$$

where the angle $\varphi = \pi/2 - \alpha$ is shown in Fig 5.

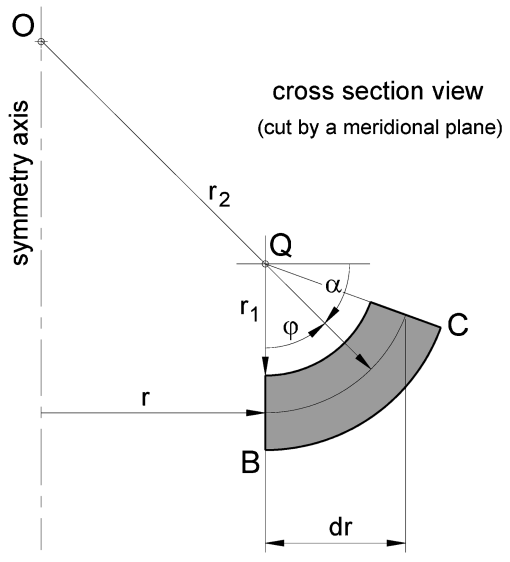

Fig. 5 Detail of the cross-sectional view of the local shell element with the variables utilized in the integration of friction along the meridional direction

3.2.2 *Rotationally symmetric surfaces under plane strain stretching conditions*

Substituting σ_t and σ_θ in equation (19) using equations (11) and (12) and inserting again $\mathrm{d}r = r_{\text{tool}}\sin\alpha\ \mathrm{d}\alpha$ result in

$$\frac{\mathrm{d}\sigma_\phi}{\mathrm{d}r} + \frac{1}{2}\frac{\sigma_\phi}{r}\left(1 + \frac{t}{r_{\text{tool}}}\right) - \frac{\mu\sigma_\phi}{r_{\text{tool}}\sin\alpha} = 0 \tag{23}$$

The above equation can be rewritten as

$$\frac{\mathrm{d}\sigma_\phi}{\sigma_\phi} = \mu\,\mathrm{d}\alpha - \frac{1}{2r}\left(1 + \frac{t}{r_{\text{tool}}}\right)\mathrm{d}r \tag{24}$$

which by integration leads to

$$\sigma_\phi = \sigma_{\phi_\mathrm{B}}\left(\frac{r_\mathrm{B}}{r}\right)^{(1+t/r_{\text{tool}})/2}\exp^{\mu\varphi} \tag{25}$$

For $r_\mathrm{B} \gg r_1$ it follows that $r \approx r_\mathrm{B}$, implying that

$$\sigma_\phi = \sigma_{\phi_\mathrm{B}}\exp^{\mu\varphi} \tag{26}$$

giving rise to an equation identical with that obtained for the flat surface.

3.2.3 *Corners under equal biaxial stretching conditions*

Applying equal biaxial stretching conditions ($\sigma_\phi = \sigma_\theta$) in equation (19)

$$\frac{\mathrm{d}\sigma_\phi}{\mathrm{d}r} + \frac{\mu\sigma_t}{t\sin\alpha} = 0 \tag{27}$$

and substituting σ_t from equation (16) gives

$$\frac{\mathrm{d}\sigma_\phi}{\sigma_\phi} = 2\mu\,\mathrm{d}\alpha \tag{28}$$

which by integration leads to

$$\sigma_\phi = \sigma_{\phi_\mathrm{B}}\exp^{2\mu\varphi} \tag{29}$$

i.e. an expression similar to the foregoing cases of plane strain conditions except for the factor 2 in the exponent. A general expression for the meridional stress including plane strain as well as equal biaxial stress is then given by

$$\sigma_\phi = \sigma_{\phi_\mathrm{B}}\exp^{k\mu\varphi} \tag{30}$$

where k takes a value equal to 1 or 2 for plane strain or equal biaxial strain respectively.

The change in the meridional stress $(\Delta\sigma_\phi)_{\mathrm{BC}}$ due to friction can be estimated as

$$\left(\Delta\sigma_\phi\right)_{\mathrm{BC}} = \sigma_{\phi_{\mathrm{C}}} - \sigma_{\phi_{\mathrm{B}}} = \sigma_{\phi_{\mathrm{B}}}\left(\exp^{k\mu\,\Delta\varphi} - 1\right) \tag{31}$$

This result indicates that the meridional stress σ_ϕ will increase with increasing r as a result of friction at the tool–sheet contact interface and that the rate of increase in the corners (where $k = 2$) is higher than in the flat and rotationally symmetric surfaces (where $k = 1$). It also explains why the onset of cracking is placed at the transition between the inclined wall and the corner radius of the component being formed (see Fig. 2).

However, the increase in meridional stresses due to friction is not expected to influence greatly the overall formability of the process, owing to small variations in the exponential term of equation (31) in the typical range of friction coefficients μ. This result is in agreement with the experimental work of Carrino *et al.* [**20**], who observed that the differences in formability of SPIF due to friction were only significant in extreme conditions (e.g. lubricated versus non-lubricated).

3.3 Thinning at the corner radius

As the sheet is formed under the single-point incremental tool, it is also thinned. Starting from the simplified form of the membrane equilibrium condition in the meridional direction neglecting friction (see equation (8)) given by

$$\frac{\mathrm{d}\sigma_\phi}{\mathrm{d}r} + \frac{\sigma_\phi - \sigma_\theta}{r} + \frac{\sigma_\phi}{t}\frac{\mathrm{d}t}{\mathrm{d}r} = 0 \tag{32}$$

the solution of this equation is divided into two different cases – first, plane strain stretching conditions (shell elements A and B in Fig. 2(c)) and, second, equal biaxial stretching conditions (shell element C in Fig. 2(c)).

3.3.1 Plane strain stretching conditions

Substituting equations (11) and (12) into equation (32) gives

$$\frac{\mathrm{d}\sigma_\phi}{\mathrm{d}r} + \frac{1}{2}\frac{\sigma_\phi}{r}\left(1 + \frac{t}{r_{\mathrm{tool}}}\right) + \frac{\sigma_\phi}{t}\frac{\mathrm{d}t}{\mathrm{d}r} = 0 \tag{33}$$

Flat surfaces where $r = \infty$ and rotationally symmetric surfaces where $r \gg t$ imply that the relation between the second and third terms of equation (33) is

$$\frac{1}{2}\frac{\sigma_\phi}{r}\left(1 + \frac{t}{r_{\mathrm{tool}}}\right) \ll \frac{\sigma_\phi}{t}\frac{\mathrm{d}t}{\mathrm{d}r} \tag{34}$$

which inserted in equation (33) gives

$$\frac{\mathrm{d}\sigma_\phi}{\mathrm{d}r} + \frac{\sigma_\phi}{t}\frac{\mathrm{d}t}{\mathrm{d}r} = 0 \tag{35}$$

3.3.2 Equal biaxial stretching conditions

Inserting equal biaxial stretching conditions, $\sigma_\theta = \sigma_\phi$, in equation (32) leads back to the same equation (35) as for plane strain, implying that solving equation (35) is the same for all three basic modes of deformation. Integration of equation (35) along the meridional length of the local shell element gives

$$\ln\sigma_\phi = -\ln t + C \tag{36}$$

and for the boundary conditions at $r = r_{\mathrm{B}}$, $\sigma_\phi = \sigma_{\phi_{\mathrm{B}}}$, and $t = t_0$

$$\ln\frac{\sigma_\phi}{\sigma_{\phi_{\mathrm{B}}}} = \ln\frac{t_0}{t} \rightarrow \sigma_\phi = \sigma_{\phi_{\mathrm{B}}}\frac{t_0}{t} \tag{37}$$

The physical meaning of equation (37) is that the reduction in thickness t tends to balance the rise in the meridional stress σ_ϕ so that $\sigma_\phi t$ is constant in the small localized zone being plastically deformed. The schematic geometrical interpretation is provided in Fig. 6.

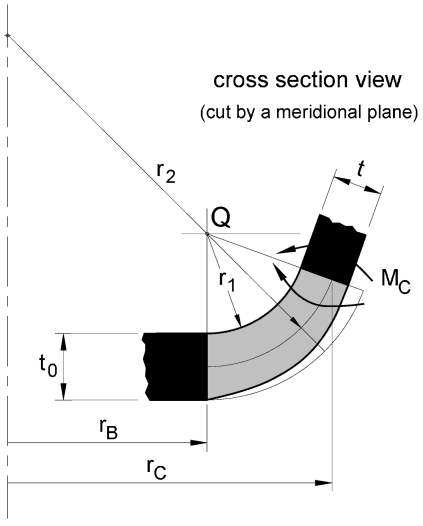

Fig. 6 Schematic representation of the evolution of thinning along the meridional direction in the local shell element utilized for modelling the instantaneous small plastic deformation zone typical of SPIF

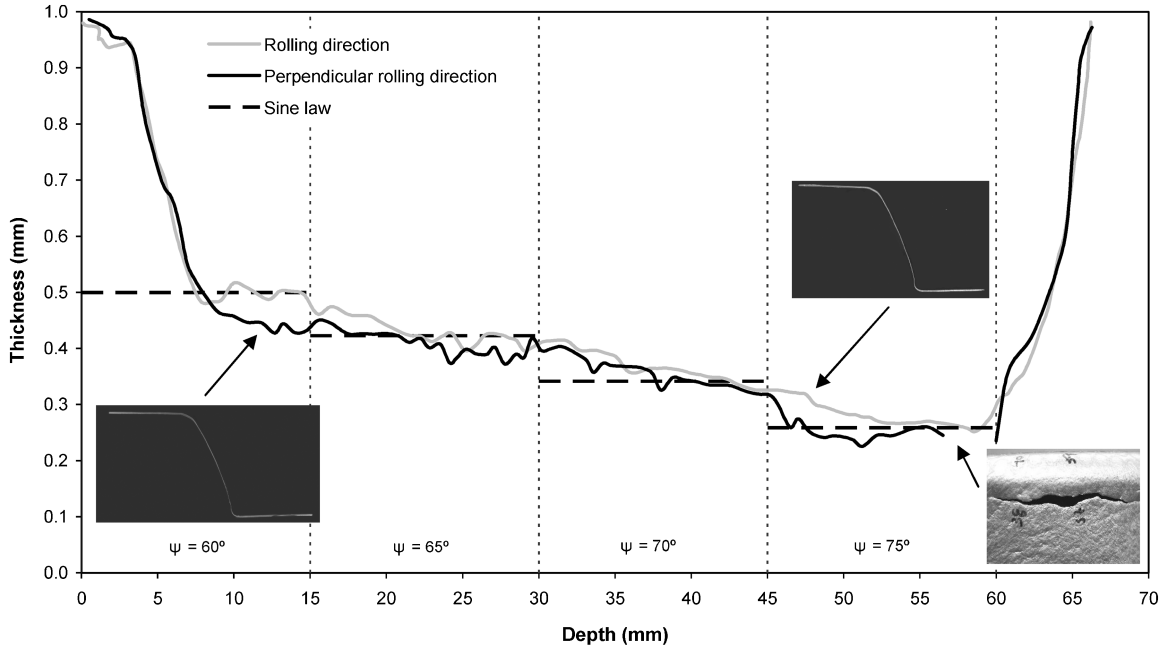

Fig. 7 Experimental variation in the thickness with the depth along two meridional cross-sections of a truncated conical shape with various drawing angles ψ. The horizontal dashed lines included in the figure present the thickness estimates provided by the sine law. Note that the material is aluminium AA1050-H111 and the insets show pictures of the cross-sections parallel and perpendicular to the rolling direction and a detail of a crack triggered in a location perpendicular to the rolling direction

From what was mentioned before, it follows that, although the variation in the wall thickness of the inclined surface of the sheet can be approximately estimated by means of the sine law $t = t_0 \sin\lambda$ for plane strain conditions (Fig. 7), the reason why thinning occurs has to do with the meridional tensile stresses σ_ϕ rather than shear acting in the small localized zone being plastically deformed. According to equation (37) and Figs 6 and 7, thinning is most pronounced at the transition point C between the inclined wall and the corner radius of the sheet.

The increase in the meridional stress σ_ϕ due to bending over point C can be computed in a similar way to that currently performed in stamping (or deep drawing) [**21**] and is given by

$$(\Delta\sigma_\phi)_{\text{bend}} = \frac{\sigma_Y t}{4r_{\text{tool}}}\left\{1+\left[\frac{(\sigma_\phi)_C}{\sigma_Y}\right]^2\right\} \tag{38}$$

and further corroborates the experimentally observed location of the onset of cracking in SPIF components.

3.4 The inclined wall surface of the sheet adjacent to the forming tool

To conclude the characterization of the stress field in the radial slice of the component containing the small localized plastically deforming region, it is interesting to extend the membrane analysis to the inclined wall of the sheet placed at the vicinity of the single-point forming tool (see zone CD in Fig. 4).

Using the simplified form of the membrane equilibrium equation (5) in the thickness direction and noting the absence of curvature $r_1 = \infty$ as well as the contact pressure $\sigma_t = 0$ on the surface of the local element CD, it is found that

$$\frac{\sigma_t}{t}+\frac{\sigma_\phi}{r_1}+\frac{\sigma_\theta}{r_2}=0 \rightarrow \sigma_\theta = 0 \tag{39}$$

In physical terms this result is compatible with the fact that during SPIF with a constant draw angle ψ the inclined wall maintains its geometry after being formed.

Since the meridional stresses σ_ϕ are the only stresses acting in this region, it is possible to set up the equilibrium condition based on the stretching force that is supported by the inclined wall of the sheet according to

$$\sigma_{\phi_C} r_C t_C \, d\theta = \sigma_{\phi_D} r_D t_D \, d\theta \tag{40}$$

or

$$\sigma_{\phi_D} = \sigma_{\phi_C}\frac{r_C}{r_D} \tag{41}$$

considering that the thickness of the inclined wall of the sheet remains unchanged if the half-cone angle λ of the component is kept constant: $t_C = t_D = t_0 \sin\lambda$.

According to equation (41) the meridional stress σ_ϕ decreases along the inclined wall of the sheet, being higher at the transition point C and smaller at point D. Because the meridional stress at point C must be kept below the yield stress (for a perfectly plastic material), it follows that the inclined wall surface of the sheet adjacent to the forming tool is elastic according to

$$0 < \sigma_\phi = \sigma_1 < \sigma_Y$$
$$\sigma_\theta = \sigma_t = 0 \tag{42}$$

This result together with the stress analysis performed in the previous sections of the paper allow the schematic representation of the stress field to be plotted in a radial slice of the SPIF component that contains the small localized plastic zone as depicted in Fig. 8, for the case of plane strain.

4 FORMABILITY

There are two basic experimental procedures for determining whether a sheet metal part of a specific material can be made by SPIF. Both procedures make use of simple benchmark tests performed with different shapes with various angles (e.g. truncated cone and the pyramid shapes, among others) in order to represent all the possible combinations of shapes that are usually found in a production part. One experimental procedure makes use of conventional circle grid analysis to characterize the forming limit curve in the principal strain space (ε_1, ε_2); the other employs the maximum drawing angle ψ_{max} that a material can undertake as a function of the initial thickness t_0 of the sheet.

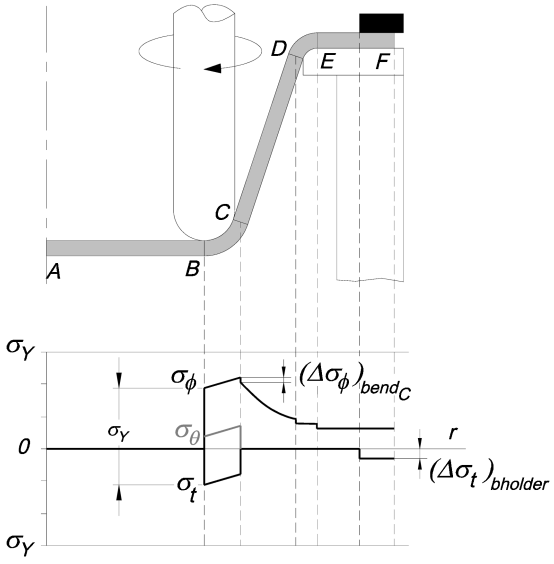

Fig. 8 Schematic representation of the stress field in the radial slice of the component being formed that contains the local shell element utilized for the membrane analysis of SPIF. Note that the distribution of stress shown above is valid only for plane strain conditions because, in the case of biaxial stretching, $\sigma_\phi = \sigma_\theta$ in the small plastic zone BC located at the corner of the components

As far as circle grid analysis is concerned, limit curves found for SPIF are often referenced to the usual type of forming limit diagram employed in sheet metal processing, where necking is the criterion of 'failure'. However, as will be shown, experiments demonstrate that formation of necks is suppressed in SPIF and failure is by fracture directly following uniform material thinning. As far as the present authors are aware, there is no theoretical background behind the second procedure of using ψ_{max} as a criterion of failure, nor how the two procedures may be related.

All these aspects of spifability will be examined in the following sections.

4.1 Variation in the thickness of SPIF parts and absence of necking

Experimenters, in relating limit strains in SPIF with the limit strains given in conventional forming limit diagrams, have observed that limit strains from SPIF when plotted in principal strain space (ε_1, ε_2) are usually placed much higher than those of conventional sheet-metal-forming processes [**4**, **17**]. Now to link the conventional forming limit diagram strains with SPIF limiting strains presumes that the failure modes in the two processes are the same, i.e. necking is the limiting criterion. If SPIF limiting strains seem to exceed those of the forming limit diagram, it could be that the presumption of necking as the limit in SPIF is in error.

To answer this question any possible experimental evidence of localized necking in SPIF should be checked first. This is crucial, because the existence of strain levels well above the forming limit curve of conventional sheet-metal-forming processes may instead be taken as a sign that SPIF parts are formed without necking. Indeed, it will be shown that the locus of failure strains in SPIF much more resembles the so-called fracture forming limit diagram [**22**].

Careful measurements were taken of the evolution of thickness with depth along two meridional cross-sections of a truncated conical shape with various drawing angles ψ made from an aluminium AA1050-H111 sheet of 1 mm initial thickness. Figure 7 reveals that plastic deformation takes place by uniform thinning until fracture. In other words, there is no experimental evidence that localized necking takes place before reaching the onset of fracture.

As far as theory is concerned, if SPIF were to be limited by necking, flat and rotationally symmetric surfaces (shell elements A and B) would only be able to trigger necks along the circumferential direction because of Hill's condition for a localized neck to be formed along a line of zero extension $d\varepsilon_w = 0$, under plane strain loading $\sigma_\theta = \sigma_\phi/2$ (anisotropy is neglected – see Fig. 9 (a)); thus

$$d\varepsilon_w = d\varepsilon_\phi \cos^2\alpha + d\varepsilon_\theta \sin^2\alpha = 0$$
$$\tan^2\alpha = -\frac{d\varepsilon_\phi}{d\varepsilon_\theta} = \frac{2\sigma_\phi - \sigma_\theta}{\sigma_\phi - 2\sigma_\theta} \Rightarrow \alpha = \frac{\pi}{2} \quad (43)$$

where α is the angle of the neck to the meridional direction. If SPIF were to be limited by necking at the equally biaxial stretched corners of a SPIF part (shell element C), it would be difficult to conclude anything because localized neck formation in the positive ε_1–positive ε_2 quadrant is still an open

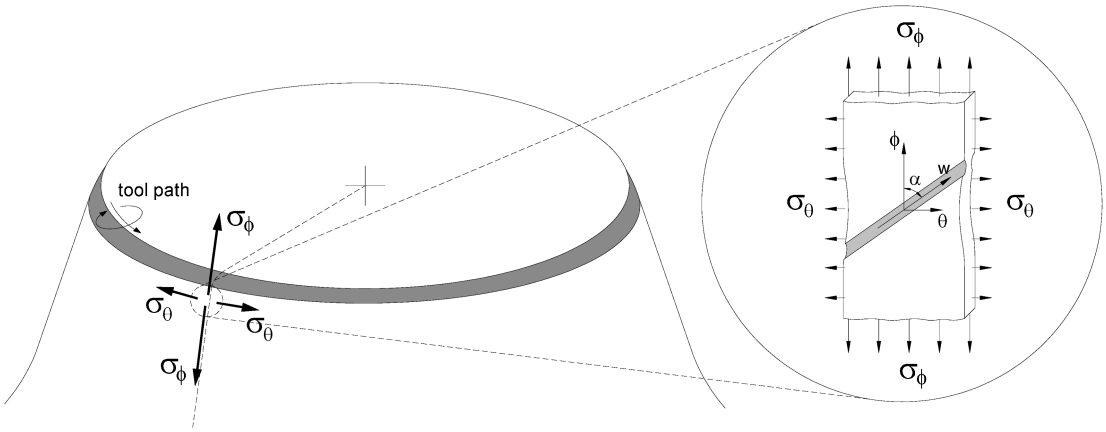

(a)

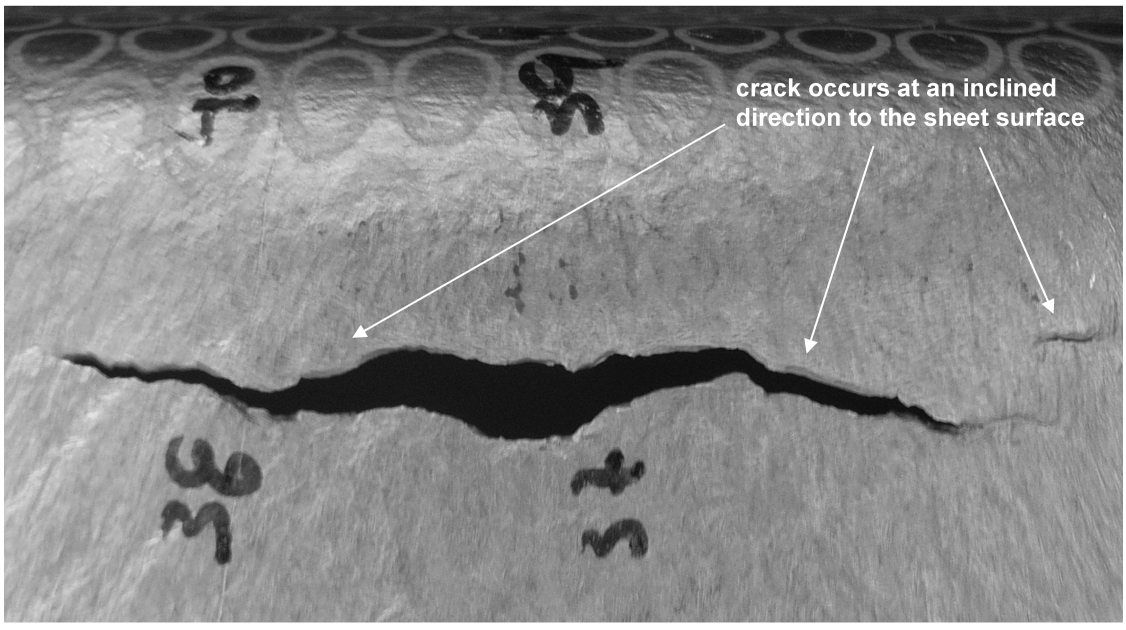

(b)

Fig. 9 Forming limits due to necking (tearing) and fracture: (a) schematic illustration of the hypothetical principle that SPIF is limited by necking; (b) experimental evidence that SPIF is limited by fracture without necking

research topic in plasticity (experimentally, necks tend to form at right angles to the principal strain direction in such circumstances). Irrespective of that theoretical gap, the experimental evolution of thickness with depth along two meridional cross-sections of a truncated conical shape with various drawing angles ψ depicted in Fig. 7 reveals that plastic deformation takes place by uniform thinning until fracture without experimental evidence of localized necking.

Additional evidence that formability is limited by fracture without previous necking is the inclined cross-sectional shape of the crack to the sheet surface depicted in Fig. 9(b).

Under these circumstances the suppression of necking seems to be the key mechanism that, together with the low growth rate of accumulated damage, is capable of ensuring the high levels of formability in SPIF.

Suppression of necking is not unknown in sheet metal forming. For example, Arndt *et al.* [**23**] investigated the formation of multiple necks in the biaxial expansion of annuli of ductile sheets, and showed that the continuous growth of necks was only possible if the following two necessary and sufficient conditions for the formation of necks in plane strain were fulfilled.

1. The incremental strain parallel to the neck must be zero.
2. The strain perpendicular to the neck should be equal to the plane strain necking limit (i.e. equal to n). This is the same as the familiar uniaxial condition of axial strain $\varepsilon_1 = 2n$ for localized necking when the neck is inclined to the direction of tension and the axes of the neck are not the axes of the specimen.

In other work, Hu and Daehn [**24**] also showed that limit strains are expected to increase under high-velocity sheet-metal-forming conditions owing to the suppression of necking.

In the case of SPIF, suppression of necking is not concerned with inertial effects as with high-velocity sheet metal forming, and the lack of necking is concerned with the inability to grow. Thus, if a neck were to form in the small plastic deformation zone in contact with the incremental forming tool, it would have to grow around the circumferential bend path that circumvents the tool (see equation (43) for the circumferential direction of propagation). This is difficult and creates problems of neck development. Even if the conditions for localized necking could be met in the small plastic deformation zone in contact with the tool, growth would be inhibited by the surrounding material which experiences considerably lower levels of stress.

The conditions for suppression of localized necking mentioned above do not occur in conventional sheet-metal-forming processes owing to uniform loading and deformation conditions. In fact, differences between neighbouring, plastically deforming regions in conventional sheet-metal-forming processes are much smaller than in SPIF and, therefore, growth of necking is easily ensured.

4.2 Hydrostatic stress in SPIF

Assuming proportional loading, it is possible to conclude that the level of the hydrostatic stress σ_m at the corners of a SPIF part (shell element C) is approximately 33 per cent higher than that exerted in the other flat and rotationally symmetric surfaces (shell elements A and B). This is caused by the aforementioned differences between the existing modes of deformation – equal biaxial stretching at the corners and plane strain at the other surfaces, given by

$$\frac{(\sigma_m)_{\text{biaxial}}}{(\sigma_m)_{\text{plane strain}}} = \frac{4}{3}\frac{r_{\text{tool}}+t}{r_{\text{tool}}+2t} \approx \frac{4}{3} \tag{44}$$

In addition, the triaxiality ratio σ_m/σ_Y that is known to play an important role in the formability of materials [**22**] is higher in conventional stamping because the radius of the conventional stamping tools is usually much larger than that of the incremental forming tools, $r_{\text{punch}} \gg r_{\text{tool}}$; thus

$$\left(\frac{\sigma_m}{\sigma_Y}\right)_{\text{stamping}} > \left(\frac{\sigma_m}{\sigma_Y}\right)_{\text{biaxial}} > \left(\frac{\sigma_m}{\sigma_Y}\right)_{\text{plane strain}} \Leftrightarrow$$
$$\frac{2}{3}\frac{r_{\text{punch}}-t/2}{r_{\text{punch}}+t} > \frac{2}{3}\frac{r_{\text{tool}}-t}{r_{\text{tool}}+2t} > \frac{1}{2}\frac{r_{\text{tool}}-t}{r_{\text{tool}}+t} \tag{45}$$

As an example the present authors have manufactured a truncated cone shape of 158 mm diameter using a rig with a backing plate of 165 mm diameter and a hemispherical single-point tool of 12 mm diameter. Inserting these forming conditions into equation (45), the relationships obtained when comparing with conventional stamping with punches of 153 mm and 155 mm diameter

respectively are

$$\left(\frac{\sigma_m}{\sigma_Y}\right)_{\text{stamping}} > \left(\frac{\sigma_m}{\sigma_Y}\right)_{\text{biaxial}} > \left(\frac{\sigma_m}{\sigma_Y}\right)_{\text{plane strain}} \Rightarrow$$
$$\begin{cases} 0.66 > 0.42 > 0.36 & (t = 1\,\text{mm}) \\ 0.64 > 0.27 > 0.25 & (t = 2\,\text{mm}) \end{cases} \tag{46}$$

Since the level of the triaxiality ratio σ_m/σ_Y in conventional stamping is higher than that of SPIF, it can be concluded that the rate of accumulated damage in stamping grows more rapidly than in SPIF. This explains why the forming limits of SPIF are higher than those of conventional stamping processes. In addition, the triaxiality ratio in equation (45) also explains the reason why the onset of cracks during the incremental forming of pyramid-shape components is preferentially located at the corners – the corners experience equal biaxial stretching while the side flat surfaces are plastically deformed under plane strain conditions.

It is also interesting to observe that, according to equation (46), different initial thicknesses of the sheet will provide significant variations in the overall triaxiality ratio of SPIF (around 30 per cent in the example based on truncated cone shape) but only very small variations (around 3 per cent) in the triaxiality ratio of conventional stamping, i.e. an increase in the initial thickness of the sheet helps especially to increase the overall formability of SPIF processes.

As a final note on equation (45), it should be observed that the influence of the radius r_{tool} of the tool on the triaxiality ratio σ_m/σ_Y is opposed to that of the thickness and, consequently, formability is expected to increase when the radius of the forming tool decreases. The qualitative predictions based on the new proposed theoretical framework are plausible and in good agreement with experimental observations reported by Jeswiet *et al.* [**5**] and by Fratini *et al.* [**8**].

4.3 Damage and forming limits

A full understanding of the forming limits of SPIF requires a combination of the previous results obtained from ductile damage analysis based on the level of the triaxiality ratio σ_m/σ_Y with an adequate characterization of the morphology of the cracks. From what was mentioned before, it is possible to conclude that plastic deformation in SPIF takes place by uniform thinning (without necking) until fracture. The fracture forming limit in SPIF (see the line labelled FFL in Fig. 10) can be characterized by means of ductile damage mechanics based on void growth models.

Fracture occurs when a damage function, which usually takes the form

$$D = \int_0^{\bar{\varepsilon}_f} f\left(\frac{\sigma_m}{\bar{\sigma}}\right) d\bar{\varepsilon} \tag{47}$$

reaches a critical value D_c [**22**]. When necking occurs, the integral is split into two parts (up to necking, and after necking to fracture) because the normalized hydrostatic stress varies with loading path before necking but is the same within all necks (since they form and propagate in plane strain). This means that the rate of growth of damage 'changes gear' on necking [**22**]. However, since necking is absent in SPIF, the integral is performed in one step. Assuming the Tresca yield criterion, linear loading paths, and that $f(\sigma_m/\bar{\sigma})$ takes the simple form $\sigma_m/\bar{\sigma}$, the total amount of accumulated damage for plane strain SPIF conditions is

$$D_c = \int_0^{\bar{\varepsilon}_f} \frac{\sigma_m}{\bar{\sigma}} d\bar{\varepsilon} = \frac{1}{2}\frac{r_{\text{tool}} - t}{r_{\text{tool}} + t}\varepsilon_1^{\text{plane strain}}$$
$$d\bar{\varepsilon} = d\varepsilon_\phi = d\varepsilon_1, \qquad \bar{\sigma} = \sigma_Y \tag{48}$$

and in equal biaxial stretching SPIF conditions it is (the Tresca yield criterion is utilized and a linear loading path is assumed)

$$D_c = \int_0^{\bar{\varepsilon}_f} \frac{\sigma_m}{\bar{\sigma}} d\bar{\varepsilon} = \frac{2}{3}\frac{r_{\text{tool}} - t}{r_{\text{tool}} + 2t} 2\varepsilon_1^{\text{biaxial}}$$
$$d\bar{\varepsilon} = -d\varepsilon_t = 2d\varepsilon_1, \qquad \bar{\sigma} = \sigma_Y \tag{49}$$

If the critical damage value D_c at the onset of cracking is assumed to be path independent, and solving equations (48) and (49) for ε_1, it is possible to set up the identity

$$\frac{\varepsilon_1^{\text{biaxial}} - \varepsilon_1^{\text{plane strain}}}{\varepsilon_2^{\text{biaxial}} - 0}$$
$$= \frac{\frac{3}{4}[(r_{\text{tool}} + 2t)/(r_{\text{tool}} - t)] - 2[(r_{\text{tool}} + t)/(r_{\text{tool}} - t)]}{\frac{3}{4}[(r_{\text{tool}} + 2t)/(r_{\text{tool}} - t)]}$$
$$= -\frac{5(r_{\text{tool}}/t) - 2}{3(r_{\text{tool}}/t) + 6} \tag{50}$$

Equation (50) gives the slope of the fracture forming line in principal strain space (ε_1, ε_2) (see line labelled FFL in Fig. 10). For typical experimental values of

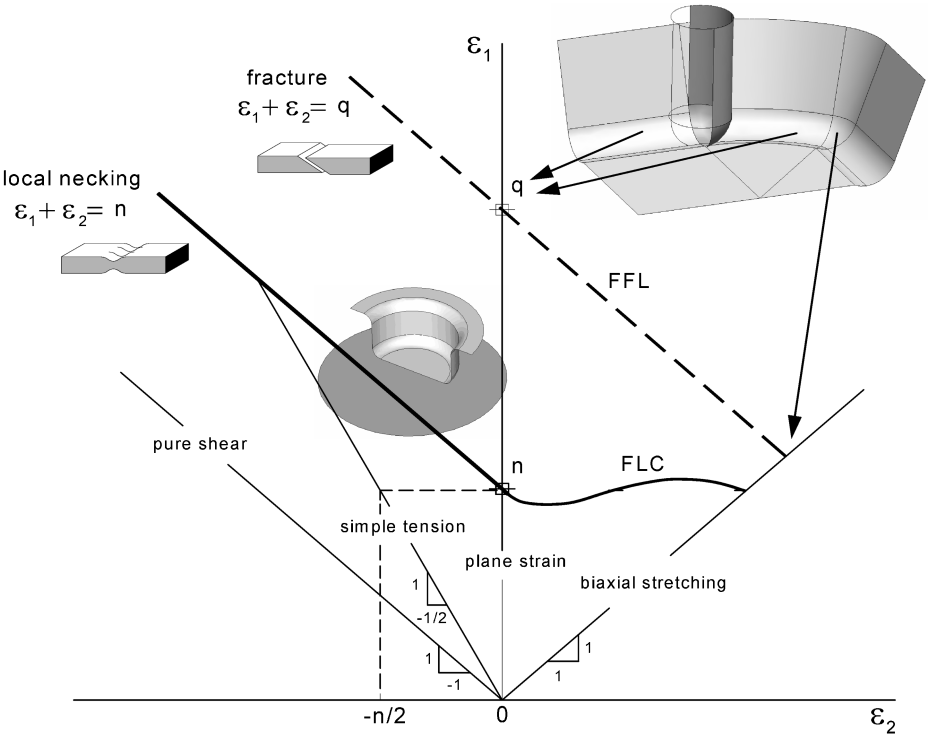

Fig. 10 Schematic representation of the forming limits of SPIF (labelled FFL) against that of conventional stamping and deep-drawing processes (labelled FLC) in the principal strain space (ε_1, ε_2)

r_{tool}/t in the range from 2 to 10, the slope derived from equation (50) will vary between -0.7 and -1.3 and will support the assumption that the fracture forming limit in SPIF can be approximately expressible in the form $\varepsilon_1 + \varepsilon_2 = q$, where $\varepsilon_t = -q$ is the thickness strain at the onset of fracture in plane strain conditions. This result is in close agreement with the typical loci of failure strains in conventional sheet-forming processes, where the slope of the fracture forming line is often about -1 [**25**].

The rotation of the tool seems to be responsible for the two different types of crack growth mechanism that are usually found in SPIF parts (Fig. 11):

(a) the circumferential straight crack propagation path;
(b) the circumferential 'zigzag' crack propagation path.

The circumferential straight propagation path (Figs 11(d) and (e)) is similar to that usually found in conventional stamping operations and this is clear evidence that crack opening in SPIF is triggered by stretching mechanisms due to meridional tensile stresses σ_ϕ. The 'zigzag' crack propagation path (Fig. 11(c)) is also triggered by meridional tensile stresses σ_ϕ but its morphology, bouncing around the circumferential direction, appears to be the result of stretching mechanisms combined with kinematic flow conditions at the contact interface between the tool and the sheet.

Under these circumstances, the difference between straight and 'zigzag' types of crack propagation path observed in Figs 11(c) and (d) are probably caused by friction towards the rotating forming tool. In fact, the position of the neutral velocity line at the contact interface between the tool and the sheet may cause in some cases the crack propagation, after attainment of the onset conditions at point *o*, to follow at some angle δ to the meridional direction (Fig. 11(a)). After reaching point *a* the crack will be considerably away from the small plastic deformation zone, where the level of applied stresses is high, and will be located within the inclined (conical) surface of the component undergoing elastic deformation. In other words, the tip of the crack at *a* will be under a much lower level of meridional stresses than at the onset point *o*. As a consequence, propagation of the crack will stop and the rotation of the tool will drag it to point *b* where the level of applied stresses will be, once again, capable of restoring the onset conditions and restarting crack propagation. This mechanism of crack initiation and

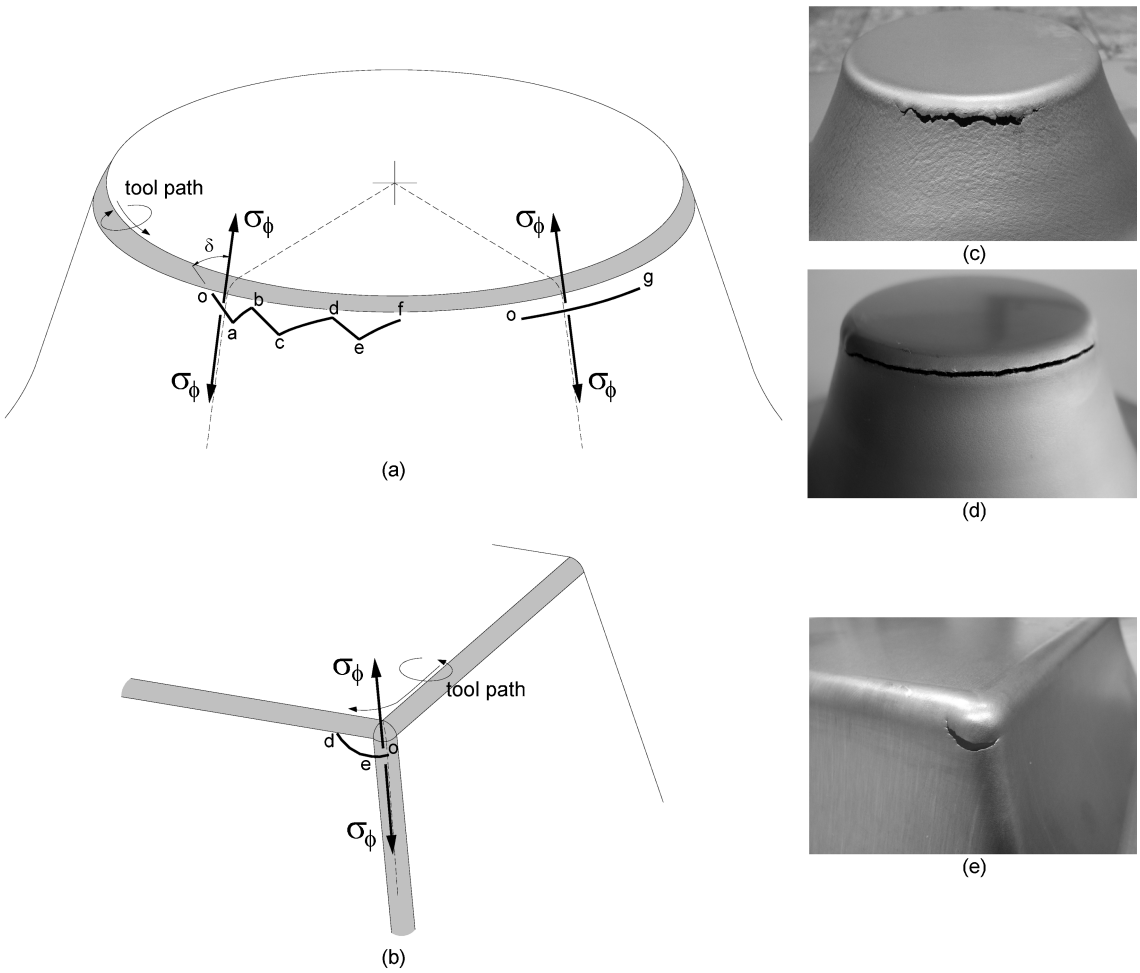

Fig. 11 Crack propagation in SPIF: (a) schematic illustration of two different crack propagation paths in plane strain, rotationally symmetric conditions; (b) schematic illustration of the typical crack propagation path in biaxial stretching, rotationally symmetric conditions; (c) zigzag crack in plane strain, rotationally symmetric conditions; (d) straight crack in plane strain, rotationally symmetric conditions; (e) crack in biaxial stretching, rotationally symmetric conditions. Note that the in-plane stresses σ_θ are not plotted, in order to ensure better readability of the figures

propagation will be recursively repeated, leading to the 'zigzag' morphology of the cracks that can be experimentally observed in Fig. 11(c).

4.4 Maximum drawing angle

Characterizing formability by the maximum drawing angle $\psi_{\max}$ was proposed by Jeswiet *et al.* [**26**], and $\psi_{\max}$ is commonly seen as an artificial index for representing material formability in SPIF [**5**]. The results available in the literature show that the maximum drawing angle $\psi_{\max}$ is directly proportional to the initial thickness t_0 of the sheet and the experimental trend is claimed to be a consequence of the sine law and of the shear spinnability relation due to Kegg [**27**].

It is thus important to verify whether the new proposed theoretical framework for SPIF is capable of providing an analytical relationship between the drawing angle ψ and the initial thickness t_0 of the sheet that is compatible with the experimental trends reported in the literature. If this objective proves to be successful, the determination of formability based on the maximum drawing angle will be provided with a theoretical background that is, for the first time, compatible with the fact that the governing mode of deformation in SPIF is stretching rather than shearing.

Starting from the meridional stress σ_ϕ acting in the local shell element (equations (14) and (18) for plane strain or biaxial stretching conditions respectively) and substituting the actual thickness t by the sine

law $t = t_0 \sin\lambda$, it is found that

$$\frac{\sigma_\phi}{\sigma_Y} = \frac{1}{1+(kt_0\sin\lambda)/r_{tool}} \tag{51}$$

or

$$\sin\lambda = \left(\frac{\sigma_Y}{\sigma_\phi} - 1\right)\frac{r_{tool}}{kt_0} \tag{52}$$

where k is a constant equal to 1 or 2 for plane strain or equal biaxial stretching conditions respectively and $\lambda = \pi/2 - \psi$ is the semicone angle that is the complement of the drawing angle ψ between the inclined wall surface and the initial flat configuration of the sheet (see Fig. 1).

Typical values for the maximum drawing angles of deep-drawing steel, copper, and aluminium alloys in normal sheet-forming qualities are in the range $60^\circ \leqslant \psi \leqslant 80^\circ$ [**5**] implying that sinλ may be approximated by the value of λ, and thereby

$$\psi = \frac{\pi}{2} - \left(\frac{\sigma_Y}{\sigma_\phi} - 1\right)\frac{r_{tool}}{kt_0} \tag{53}$$

It may thus be concluded that the theoretical estimates of the maximum drawing angle ψ_{max}, for values of the meridional stress $\sigma_\phi < \sigma_Y$, are expected to increase with increasing initial thickness t_0 of the sheet and to decrease with increasing radius r_{tool} of the forming tool. This qualitatively agrees with experimentation and provides a background for the determination of material formability by plotting the maximum drawing angle ψ_{max} as a function of the initial thickness t_0 of the sheet.

The theoretical estimate of the drawing angle takes the limiting value $\psi_{max} = \pi/2$ when the meridional stress takes the maximum allowable value $\sigma_\phi = \sigma_Y$ (Fig. 8). Under this extreme forming condition the thickness after deformation is $t = t_0 \sin\lambda = 0$ and, therefore, a link is established between the geometrical relationship provided by the sine law and the states of stress and strain acting in the small localized plastically deforming regions. The shear spinnability relation due to Kegg [**27**] is left out of the analysis owing to the governing mode of deformation in SPIF. Note that the sine law says nothing about the possibility of necking that, in SPIF, does not seem to occur.

Equation (53) is not in a form for calculating theoretical estimates of the maximum drawing angle ψ_{max} because it requires knowledge of the ratio of the yield stress to the meridional stress, which is generally unknown. Thus, it is necessary to rewrite equation (53) in such a way that users may easily obtain their estimates from data readily available from simple material testing conditions.

By substituting σ_t given by equations (11) and (16) into equation (53) and rearranging terms, it is found that (this applies both for plane strain and equal biaxial stretching conditions)

$$\psi = \frac{\pi}{2} - \left(\frac{\sigma_Y}{\sigma_\phi} - 1\right)\frac{r_{tool}}{kt_0} = \frac{\pi}{2} - \left(\frac{kt}{r_{tool}}\right)\frac{r_{tool}}{kt_0} = \frac{\pi}{2} - \exp^{\varepsilon_t} \tag{54}$$

where t is the thickness of the sheet at fracture and ε_t is the value of the thickness strain at the limit of formability. In principle, ε_t is to be determined from the through-thickness fracture limit strain ε_3 in plane strain or equal biaxial tension tests of a sheet metal.

4.5 Maximum drawing angle versus fracture forming limit

Equation (54) has been developed with the objective of estimating the maximum drawing angle ψ_{max} from simple material-testing conditions. However, the equation can alternatively be employed to develop a general correlation between the experimental procedures utilized in the determination of the maximum drawing angle and of the fracture forming limit. Assuming for now that the maximum drawing angle ψ_{max} can be measured at the onset of fracture, the corresponding value of the limiting fracture strain ε_t is calculated from equation (54) as

$$\varepsilon_t = \ln\left(\frac{\pi}{2} - \psi_{max}\right) \tag{55}$$

By taking into consideration the mode of deformation (plane strain or equal biaxial stretching) and the incompressibility condition, the value of the through-thickness fracture strain ε_t provided by equation (55) can be utilized to determine the coordinates of a point in the principal strain space (ε_1, ε_2) that is necessary to plot the fracture forming limit.

Moreover, because recent experimental studies performed by Filice *et al.* [**4**] and Jeswiet and Young [**17**] show that the forming limit in SPIF may be approximately expressed as a straight line with a negative slope, $\varepsilon_2 = -\varepsilon_1 + q$, it follows that by measuring the maximum drawing angle ψ_{max} at the onset of fracture it is possible to characterize fully the fracture forming limit without the need to perform time-consuming circle grid analysis (Fig. 12).

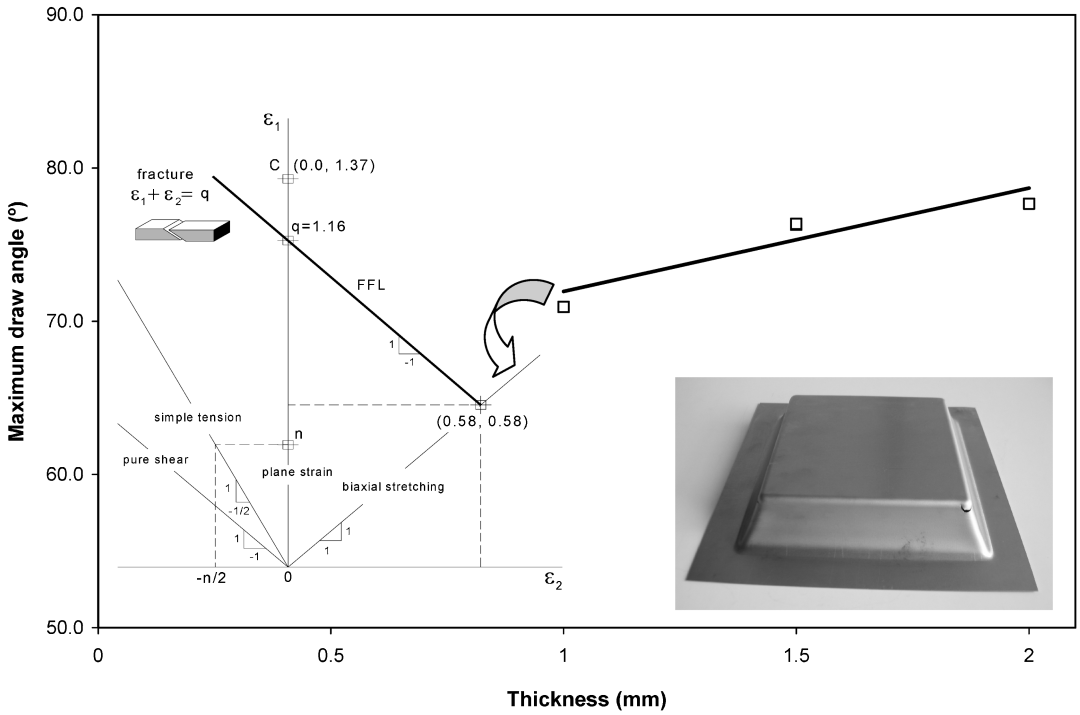

Fig. 12 Schematic representation of the procedure for setting up the fracture forming limit from the experimental measurement of the maximum draw angle $\psi_{\max}$ as a function of the initial thickness of the sheet blank. The inset shows a picture of a pyramid-shaped component after cracking. Note that experimental data are presented for the aluminium AA1050-H111 pyramid-shaped component produced by SPIF, and point C was obtained from measurements of the thickness at fracture for a truncated cone shape of 1 mm thickness (see Fig. 7)

As schematically illustrated in Fig. 12, the experimental value of the maximum draw angle for a pyramid shape component with 1 mm thickness allows calculation of the value of thickness strain at fracture $\varepsilon_t = -1.16$ by means of equation (55). The application of the incompressibility condition under biaxial stretching provides the value of the limiting fracture point $(\varepsilon_1, \varepsilon_2) \equiv (0.58, 0.58)$ in the principal strain space. By taking the assumption that the fracture limit is a line with a negative -1 slope the interception with the ε_1 axis (plane strain) can easily be estimated as $q = 1.16$.

The error between the estimate of the fracture strain for a 1 mm truncated conical shape obtained from the above-mentioned procedure, $\varepsilon_1 + \varepsilon_2 = 1.16$, and from the experimental measurements of the cross-sectional thickness at the onset of fracture (see Fig. 7, and point C in Fig. 12) is 18 per cent ($\varepsilon_t = -1.37$). However, it must be noted that, if instead of using a slope of -1 a slope of -1.17 as predicted from damage analysis was utilized (see equation (50), for $r_{\text{tool}} = 6$ mm and $t_0 = 1$ mm), the new estimate of the intercept would have provided $q = 1.25$ and an overall error to the experimental measurement of point C of below 10 per cent.

To conclude, it is important to state that, conversely, knowledge of the fracture forming limit in the principal strain space $(\varepsilon_1, \varepsilon_2)$ will provide the experimental value of the thickness fracture strain ε_t that is necessary for determining the maximum drawing angle $\psi_{\max}$ at the onset of fracture by means of equation (54). In other words, both experimental procedures utilized for characterizing the formability in SPIF merge into a single concept: the onset of fracture.

5 CONCLUSIONS

The paper extends a new theoretical model for rotationally symmetric SPIF [**14**] to different modes of deformation commonly found in general SPIF processes. The model is built upon membrane analysis and ductile damage mechanics and is based on the experimental observations that fracture is not preceded by localized necking and that the crack

propagates under tensile meridional stresses acting under stretching modes of deformation.

Experimentation by the present authors, together with data retrieved from the literature, confirms that the proposed theoretical framework is capable of successfully addressing the influence of the major parameters and explaining the enhanced formability of the process.

It has been shown that necking in SPIF is suppressed, unlike conventional sheet forming. Forming limit diagrams that give the loci of necking strains are not therefore relevant to limits in SPIF. It is the fracture forming limit diagram that should be employed.

Strain hardening and anisotropy were not taken into consideration, while bending effects were only indirectly included in the analysis. However, the proposed model can be further enhanced to include some of these limitations.

ACKNOWLEDGEMENTS

The first author and the corresponding author would like to acknowledge PTDC/EME-TME/64706/2006 FCT/Portugal for financial support. The corresponding author would like to acknowledge the support of the Institut for Produktion og Ledelse, Danmarks Tekniske Universitet, during his sabbatical licence in Denmark.

REFERENCES

1 **Leszak, E.** Apparatus and process for incremental dieless forming. US Pat. 3342051A, 1967.
2 **Kitazawa, K., Wakabayashi, A., Murata, K.,** and **Yaejima, K.** Metal-flow phenomena in computerized numerically controlled incremental stretch-expanding of aluminum sheets. *Keikinzoku (J. Japan Inst. Light Metals)*, 1996, **46**, 65–70.
3 **Jeswiet, J.** Incremental single point forming. *Trans. North Am. Mfg Res. Inst.*, 2001, **29**, 75–79.
4 **Filice, L., Fratini, L.,** and **Micari, F.** Analysis of material formability in incremental forming. *Ann. CIRP*, 2002, **51**, 199–202.
5 **Jeswiet, J., Micari, F., Hirt, G., Bramley, A., Duflou, J.,** and **Allwood, J.** Asymmetric single point incremental forming of sheet metal. *Ann. CIRP*, 2005, **54**, 623–650.
6 **Hagan, E.** and **Jeswiet, J.** A review of conventional modern single point sheet metal forming methods. *Proc. Instn Mech. Engrs, Part B: J. Engineering Manufacture*, 2003, **217**, 213–225.
7 **Leach, D., Green, A. J.,** and **Bramley, A. N.** A new incremental sheet forming process for small batch and prototype parts. In Proceedings of the Ninth International Conference on Sheet Metal, Leuven, Belgium, 2001, pp. 211–221.
8 **Fratini, L., Ambrogio, G., Di Lorenzo, R., Filice, L.,** and **Micari, F.** Influence of mechanical properties of the sheet material on formability in single point incremental forming. *Ann. CIRP*, 2004, **53**, 207–210.
9 **Allwood, J. M., King, G. P. F.,** and **Duflou, J. R.** A structured search for applications of the incremental sheet forming process by product segmentation. *Proc. IMechE, Part B: J. Engineering Manufacture*, 2005, **219**, 239–244.
10 **Bambach, M., Hirt, G.,** and **Ames, J.** Quantitative validation of FEM simulations for incremental sheet forming using optical deformation measurement. *Advd Mater. Res.*, 2005, **6–8**, 509–516.
11 **Duflou, J. R., Lauwers, B., Verbert, J., Gelaude, F.,** and **Tunckol, Y.** Medical application of single point incremental forming: cranial plate manufacturing. In *Virtual modelling and rapid manufacturing*, 2005, pp. 161–166 (Taylor & Francis, London).
12 **Tekkaya, A. E.** State-of-the-art of simulation of sheet metal forming. *J. Mater. Processing Technol.*, 2000, **103**, 14–22.
13 **Henrard, C., Bouffioux, C., Duchene, L., Duflou, J. R.,** and **Habraken, A. M.** Validation of a new finite element for incremental forming simulation using a dynamic explicit approach. *Key Engng Mater.*, 2007, **344**, 495–502.
14 **Silva, M. B., Skjoedt, M., Martins, P. A. F.,** and **Bay, N.** Revisiting the fundamentals of single point incremental forming by means of membrane analysis. *Int. J. Mach. Tools and Mf.*, 2008, **48**(1), 73–83.
15 **Emmens, W. C.** and **van den Boogaard, A. H.** Strain in shear and material behaviour in incremental forming. *Key Engng Mater.*, 2007, **344**, 519–526.
16 **Allwood, J. M., Shouler, D. R.,** and **Tekkaya, A. E.** The increased forming limits of incremental sheet forming processes. *Key Engng Mater.*, 2007, **344**, 621–628.
17 **Jeswiet, J.** and **Young, D.** Forming limit diagrams for single point incremental forming of aluminium sheet. *Proc. ImechE, Part B: J. Engineering Manufacture*, 2005, **219**, 359–364.
18 **Hirt, G., Junk, S., Bambach, M.,** and **Chouvalova, I.** Process limits and material behaviour in incremental sheet forming with CNC-tools. *Mater. Sci. Forum*, 2003, **426–432**, 3825–3830.
19 **Hirt, G., Ames, J.,** and **Bambach, M.** Validation of FEA for asymmetric incremental sheet forming by on-line measurements of deformation and tool forces. *Prod. Engng*, 2006, **13**(1), 39–44.
20 **Carrino, L., Di Meo, N., Sorrentino, L.,** and **Strano, M.** The influence of friction in negative dieless incremental forming. In Proceedings of the Ninth International ESAFORM Conference on Materials Forming, Glasgow, UK, 2006, pp. 203–206.

21 **Rodrigues, J. M. C.** and **Martins, P. A. F.** *Tecnologia da deformação plástica: aplicações industriais*, 2005 (Escolar Editora, Lisbon).
22 **Atkins, A. G.** and **Mai, Y.-W.** *Elastic and plastic fracture*, 1985 (John Wiley, New York).
23 **Arndt, S., Swillo, S.,** and **Atkins, A. G.** Multiple necks around biaxially loaded holes in sheets. *Int. J. Mech. Sci.*, 2001, **43**, 245–263.
24 **Hu, X.** and **Daehn, G. S.** Effect of velocity on flow localization in tension. *Acta Materialia*, 1996, **44**, 1021–1033.
25 **Atkins, A. G.** Fracture mechanics and metal forming: damage mechanics and the local approach of yesterday and today. In *Fracture research in retrospect* (Ed. H. P. Rossmanith), 1997, pp. 327–350 (A. A. Balkema, Rotterdam).
26 **Jeswiet, J., Hagan, E.,** and **Szekeres, A.** Forming parameters for incremental forming of aluminium alloy sheet metal. *Proc. Instn. Mech. Engrs, Part B: J. Engineering Manufacture*, 2002, **216**, 1367–1371.
27 **Kegg, R. L.** A new test method for determination of spinnability of metals. *Trans. ASME, J. Engng Industry*, 1961, **83**, 119–124.

APPENDIX

Notation

r	radial coordinate
r_1	radius of curvature of meridian at the element (radius of the single-point incremental forming tool)
r_2	radius of the element normal where it cuts the z axis
t	thickness of the sheet
t_f	final thickness of the sheet
t_0	initial thickness of the sheet
λ	half-cone angle of the component
μ	coefficient of friction
σ_t	thickness stress
σ_Y	yield stress
σ_θ	circumferential stress
σ_ϕ	meridional stress
ψ	draw angle between the inclined wall and the initial flat configuration of the sheet

February 2008

Joint author statement

If a thesis contains articles made in collaboration with other researchers, a joint author statement about the PhD-student's part of the article shall be made by each of the co-authors, cf. article 12, section 4 of the Ministerial Order No. 18 February 2008 about the PhD degree

Title of the article: Single point incremental forming of tailored blanks produced by friction stir welding

Author(s): M.B. Silva, M. Skjoedt, P. Vilaça, N. Bay, P.A.F. Martins

Journal: Journal of Materials Processing Technology, (2008), accepted for publication.

PhD-student: Martin Skjødt Cpr.nr: _____

Signature of the PhD-student: _____ Date: _____

Co-author: _____ Signature: _____

Description of each author's contribution to the above-mentioned article:

M. B. Silva: Planning and conduction of experiments, analysis of results, friction stir welding, pictures and graphics for paper, literature study, final editing.

M. Skjoedt: CAD drawing of parts, CAM programming of parts, planning and conduction of experiments, final editing.

P. Vilaça: Friction stir welding, Final editing.

N. Bay: Final editing.

P. A. F. Martins: Planning of experiments, writing of paper, graphics for paper, final editing.

SINGLE POINT INCREMENTAL FORMING OF TAILORED BLANKS PRODUCED BY FRICTION STIR WELDING

*Silva M. B.[(1)], Skjoedt M.[(2)], Vilaça P.[(1)], Bay N.[(2)] and Martins P. A. F.[(1, *))]*

[(1)] IDMEC, Instituto Superior Tecnico, TULisbon
Av. Rovisco Pais, 1049-001 Lisboa, Portugal

[(2)] Technical University of Denmark, Department of Manufacturing Engineering and Management,
DTU - Building 425, DK-2800, Kgs. Lyngby, Denmark

(*) Corresponding author: Fax: +351-21-8419058 E-mail: pmartins@ist.utl.pt

ABSTRACT

This paper is focused on the single point incremental forming of tailored welded blanks produced by friction stir welding. Special emphasis is placed on the know-how for producing the tailored blanks and on the utilization of innovative forming strategies to protect the welding joint from the rotating single point forming tool. Formability of the tailor welded blanks is evaluated by means of benchmark tests carried out on truncated conical and pyramidal shapes and results are compared with similar tests performed on conventional reference blanks of the same material. Results show that the combination of single point incremental forming with tailored welded blanks produced by friction stir welding seems promising in the manufacture of complex sheet metal parts with high depths.

Keywords: Single point incremental forming, tailored blanks, formability

NOTATION

σ_θ - circumferential stress
σ_ϕ - meridional stress
σ_t - thickness stress
σ_Y - yield stress
λ - half cone angle of the component
ψ - draw angle between the inclined wall and the initial flat configuration of the sheet
t - thickness of the sheet
t_0 - initial thickness of the sheet
r_{tool} - radius of the SPIF tool

1. INTRODUCTION

Single point incremental forming (SPIF) is a new sheet metal forming process with a high potential economic payoff for rapid prototyping applications and for small quantity production. The process was patented by Leszak (1967) and was proven to be feasible by Kitazawa et al. (1996) in forming rotational symmetric parts in aluminium.

Figure 1 presents the basic components of the process; (i) the sheet metal blank, (ii) the blankholder, (iii) the backing plate and (iv) the rotating single point forming tool. The tool path is generated in a CNC machining centre and is utilized to progressively form the sheet into a component. During the process there is no backup die supporting the back surface of the sheet.

The capability study of using an ordinary CNC milling machine instead of a special purpose machine-tool apparatus performed by Jeswiet (2001) and Filice et al. (2002) was the starting point for the successful and rapid development of the process within the metal forming research community. However, the industrial spin-off of the process is far from being consolidated. In fact, SPIF is not currently in regular commercial use although some researchers have been suggesting a wide range of potential applications and fabricated a variety of prototypes to demonstrate its feasibility (Jeswiet et al., 2005).

Until recently, most studies on SPIF have concerned experimental investigations on applications and formability limits of traditional blanks having a constant sheet thickness and uniform surface finishing and mechanical properties (Allwood et al., 2004) (Jeswiet et al., 2005). This also applies to the limited number of theoretical (Silva et al., 2008a, 2008b) and numerical (Bambach et al., 2005) studies that have been carried out. The first attempts to utilize tailored blanks having a non-uniform thickness profile was performed by Kopp et al. (2005) and Hirt et al. (2005) who concluded that incremental forming of tailored blanks produced by flexible rolling (also known as tailor rolled blanks (TRB)) allows for the reduction of weight and is suitable for new design approaches in lightweight construction. The alternative utilization of tailor welded blanks (TWB) produced by laser welding is claimed to be disadvantageous because of welding seams and corresponding heat-affected zones and unsmooth thickness transitions. In addition, the studies also showed that TRB have better formability properties than alternative laser-based TWB enabling higher drawing depths.

However, the flexible rolling technology that is required for producing TRB is limited by the fact that it is not capable of producing tailored blanks having non-uniform thickness

profiles and different surface finishing or mechanical properties resulting from joining two or more different materials.

The utilization of tailored blanks is expected to enhance the range of possible applications of SPIF and to drive the process towards the actual needs and demands of the industry regarding new lightweight design philosophies. The objective is to form dedicated sheet metal parts with higher thickness only in the areas where higher loads are expected to occur, similarly to what is being done nowadays in conventional sheet forming of transportation vehicles. The application of tailored blanks in transportation vehicles is known to increase the safety of passengers and at the same time it allows the reduction of the overall weight of the structures. Structural integration is improved, the number of reinforcements and stiffeners is reduced and major parts can be downsized allowing savings in energy consumption and reductions in gas emissions.

Potential applications of the combination between SPIF and tailored blanks span from aerospace carriers to high speed trains and exclusive top model and racing cars manufactured in very small batches. However, there is also potential for innovation in the manufacturing of home appliances as well as in modern design and architectural applications that may want to take advantage of the different aesthetical features provided by the combined utilization of aluminium, copper and steel with diverse colours and different types of surface textures derived from dissimilar finishing options.

Surprisingly, the reference literature in the field reveals that single point incremental forming of aluminium tailored blanks has not been, as far as authors are aware, a key research topic. This is unexpected and somehow contradictory to the primacy and importance of aluminium in the majority of the published research dealing with SPIF of conventional sheet metal blanks. Possible explanations for this situation might be related to the investment costs for setting-up a process chain for producing TRB or to the technological difficulties in producing aluminium TWB by means of the CO_2 laser systems currently utilized for producing tailor welded steel blanks.

Laser-welding of aluminium is a challenge due to its high surface reflectivity and high thermal conductivity. The energy of the laser beam is not properly absorbed and the quality of the welding joints is usually very poor. The utilization of coatings based on graphite can successfully eliminate the difficulties related to surface reflectivity but gives rise to another type of problems related to its application and subsequent removal.

Resort to alternative fusion welding processes for producing aluminium TWB is not possible due to economic and technical reasons. Electron beam welding (EBW), like

laser beam welding, is capable of providing high power density and high penetration with the advantage of not being sensitive to surface reflectivity problems. However, EBW requires large set-up times (the positioning of the parts to be welded with respect to the beam must be very precise) and high capital investments (the cost of the equipment and of its operation is very high). Conventional fusion welding processes cannot be utilized for producing TWB because its lower power densities and slow welding velocities give rise to large heat-affected zones that would considerably diminish the overall formability of the tailored blanks.

From what was mentioned before it is possible to conclude that there is a need to identify and evaluate new low cost alternative technological solutions that can effectively produce aluminium tailored blanks with good forming properties. Buffa et al. (2006) took the first step in the right direction with the numerical and experimental investigation of the feasibility of using friction stir welding (FSW) to join aluminium blanks of different thicknesses. They utilized AA7075-T6 sheets with thicknesses varying from 3 to 4 mm and concluded that FSW can be successfully utilized for producing TWB. However, the thickness of the sheets employed in the investigation is considerably above the values commonly utilized in sheet metal forming applications and no studies were performed to check the formability of TWB produced by FSW.

This paper draws from the idea of producing tailored blanks by FSW to present an innovative research work aimed at evaluating the formability of these tailored blanks in SPIF (formability in SPIF is also known as spifability). The investigation, which is based on IDMEC's know-how to produce TWB by FSW, makes use of innovative solutions based on the utilization of dummy sheets to protect the welding joints from the rotating single point forming tool, and utilizes experimental benchmark tests to evaluate the spifability of TWB produced by FSW against that of conventional reference blanks of the same material.

2. EXPERIMENTATION

This section starts by describing the experimental procedure utilized for producing TWB by FSW and follows by presenting the work plan and identifying the process parameters that were considered more relevant for the analysis of the spifability of TWB. Although the production of TWB by FSW allows joining sheet metals with different surface finishing and mechanical properties it was decided to only produce tailored blanks of the

same material with varying thickness combinations in order to focus the investigation on the influence of the welding joints on the overall formability of SPIF.

2.1 Tailor friction stir welded blanks

The tailored blanks were made of AA1050-H111 sheets (σ_Y = 28 N/mm^2) with 1.5 and 2 mm thickness and the welded joints were produced by FSW. FSW is a solid-phase joining process developed and patented by TWI-The Welding Institute (Thomas et al., 1991). The process is currently utilized by many companies around the world for joining structural components made of aluminium and other light metals and it is commonly considered to be the largest step forward in welding technology of the last decade.

FSW is performed by means of a non-consumable cylindrical rotational tool that is mounted on a milling machine, a machining centre or a special purpose machine-tool. The FSW tool consists of a profiled pin end and a shoulder (figure 2a)). The pin is rotationally plunged into the adjoining edges of the sheets to be welded and performs plastic deformation by stirring the material of the sheets while moving along the welding joint. The motion of the pin and shoulder against the material undergoing local plastic deformation, causes frictional work and generates most of the heat required for welding (Vilaça et al., 2005). The welding joint is created by the combined action of frictional heating and plastic deformation.

The FSW tool employed in the production of TWB was made of hot work tool steel AISI H13 hardened and tempered to 52 HRc in the working region. Ionic nitriding and oxidizing were further employed to enhance the mechanical properties of the surface of the tool (up to a final hardness of 72 HRc) and its resistance to corrosion. The diameter of the shoulder is equal to 14 mm with 2 spiral striates and the pin consists of an ISO M3 with 3 conical flats. The utilization of a shoulder with 2 spiral striates allowed the tilt angle of the FSW tool to be set to zero degrees in all cases. This is very important for welding sheets with small thicknesses because the utilization of a FSW tool with a tilt angle would result in undesirable variations in the nominal thickness of the sheets along the welding joints. The pin with conical flats provides excellent material flow around the FSW tool. This is critical when the thickness of the sheets to be welded is reduced because material flow can easily drift from 3D to undesirable 2D conditions.

The TWB were produced in a milling machined equipped with a clamping system to rigidly fix the sheets to be welded and prevent the abutting joint faces being forced apart during welding (figure 2b)). The rotational velocity of the FSW tool was set to 1120 r.p.m.

and the welding velocity was chosen to be equal to either 320 mm/min or 160 mm/min depending on whether the sheets to be joined were having equal or different thicknesses.

The preforms utilized in the production of the TWB were slightly larger than the dimensional requirements of the experimental SPIF set-up so that the initial and final regions of the weld joint could be discarded. This was necessary to eliminate the unsteady-state welding conditions typical of the beginning and ending of FSW and to eliminate the hole that is left behind when the weld is completed and the tool is withdrawn. Before being welded the edges of the sheets were carefully prepared in order to guarantee a precise positioning of the two parts to be joined and subsequently degreased for eliminating possible contamination of the weld. After welding the burr generated by FSW was carefully removed. The weld joints were performed along parallel and perpendicular orientations to the rolling direction (figure 2c)) in order to check the influence of the position of the weld seam on the overall spifability of the TWB produced by FSW.

2.2 Single point incremental forming

The experimental benchmark tests to evaluate the spifability of TWB produced by FSW were performed in a Cincinnati Milacron machining centre equipped with a rig, a backing plate, a blankholder for clamping the sheet metal blanks and a rotating single point forming tool (figure 1). The forming tool has a diameter of ø12 mm and a spherical tip and was made of cold working tool steel (120WV4-DIN) hardened and tempered to 60 HRc in the working region. The speed of rotation is 35 rpm and the feed rate is 1000 mm/min. The tool path is helical with a step size per revolution equal to 0.5 mm and was generated with the program HeToPaC (Skjoedt et al., 2007a). The lubricant applied between the forming tool and the sheet is diluted cutting fluid.

The benchmark tests were designed to evaluate the spifability of TWB having a uniform thickness profile of 1.5 and 2 mm and a non-uniform profile with 1.5 mm thickness in the thinner and 2 mm thickness in the thicker regions (hereafter referred as 1.5+2 mm TWB) against that of conventional reference blanks with 1.5 and 2 mm thickness.

SPIF of AA1050-H111 sheets with thickness equal to and above of 1.5 mm thickness are known to experience surface quality problems due severe damage characterized by pick-up of workpiece material on the tool and subsequent scoring of its surface usually involving the detachment of large fragments of material (a phenomenon that is usually

designated as 'galling', refer to figure 3a)). In a previous paper Skjoedt et al. (2007b) investigated this phenomenon and proposed the utilization of a dummy sheet on top of the conventional sheet metal blanks in order to avoid direct contact of the tribologically difficult material of the sheet metal blank to be formed with the rotating tool. They found that the utilization of a dummy sheet avoids surface damage by galling and, therefore, greatly improve the final surface quality of the sheet metal blank (figure 3b and 3c).
The original idea proposed by Skjoedt et al. (2007b) is now further developed for the SPIF of TWB because it can additionally protect the welding seam from the single point rotating tool even for sheets with thickness below the critical value for the occurrence of galling. In case of the benchmark tests that were performed by the authors it was decided to utilized a DC04 deep drawing steel dummy sheet of thickness 0.63 mm in all the experiments.
Table 1 presents the experimental work plan. The experiments were designed in order to isolate the influence of the process parameters that are considered most relevant for the analysis of the spifability of TWB; (i) orientation of the welding joint relative to the rolling direction, (ii) orientation of the welding joint relative to the geometry of the workpiece to be formed, (iii) relative position of the root of the welding joint with respect to the rotating tool, (iv) thickness of the sheet and (v) thickness profile of the sheet metal blank. The benchmark tests were performed in truncated conical and pyramidal shapes characterized by varying drawing angles ψ with the depth (figure 4). The experiments were done in a random order and at least two replicates were produced for each combination of method and geometry in order to provide statistical meaning.

3. RESULTS AND DISCUSSION

In a recent work Silva et al. (2008a) showed that it is possible to characterize tool paths in SPIF as combinations of three basic modes of deformation that are associated with; (i) flat surfaces under plane strain stretching conditions, (ii) rotational symmetric surfaces under plane strain stretching conditions and (iii) corners under equal bi-axial stretching conditions. They also showed that the stress field in the instantaneous small localized zone BC undergoing plastic deformation (figure 5) can be analytically derived from membrane analysis with in-plane contact frictional forces. Table 2 contains a resume of the stress equations along the principal directions and details can be obtained in Silva et al. (2008a).

The first part of this section qualitatively extends the above mentioned analysis to the case of conventional sheet metal parts produced by SPIF with the help of dummy sheets, the objective being to investigate the influence of the dummy sheet on the formability of the process. This knowledge is crucial to the overall research work because SPIF of TWB with dummy sheets is considered necessary for protecting the welding joint from the rotating single point forming tool. The second part of this section is fully focused on the evaluation of the spifability of TWB produced by FSW by means of benchmark tests carried out on truncated conical and pyramidal shapes.

3.1 Influence of the dummy sheet in the overall formability of SPIF

The left side of figure 5 presents a schematic evolution of the stress field in a radial slice of a component being produced by SPIF without dummy sheet. As can be concluded from the combined analysis of the figure with the equations included in table 2 the relative values of the principal stresses may vary with process parameters related to the thickness t of the sheet and to the radius r_{tool} of the forming tool but the term $\sigma_1 - \sigma_3$ should be constant according to Tresca yield criterion and equal to the flow stress of the sheet (σ_Y, under perfectly plastic material assumptions).

From a theoretical point of view, the utilization of a dummy sheet on top of conventional sheet metal blanks to avoid direct contact with the rotating single point forming tool is expected to influence formability. This is due to fact that the dummy sheet artificially increases the radius r_{tool} of the tool acting on the sheet metal blank and since the dummy sheet distributes the contact over a more extended area of the sheet metal blank. The increase of the tool radius from r_{tool} to $r_{tool\_artificial}$ (figure 5) leads to an increase of the meridional stress σ_ϕ acting along BC and, therefore, to an increase of the hydrostatic stress implying a decrease in process formability (refer to table 2 and figure 5).

Experimental measurements of the maximum drawing angle ψ_{max} that conventional AA 1050-H111 blanks can undertake when forming a truncated pyramid shape with and without the utilization of a dummy sheet are in agreement with the theoretical predictions but also reveal that the actual reduction in formability is very small (refer to table 3). This last result is very important because it guarantees that dummy sheets can be utilized for protecting the welding joints of TWB without significantly influencing the spifability for this material.

3.2 Spifability of TWB produced by FSW

Figure 6 shows truncated conical and pyramidal SPIF parts produced from TWB made of aluminium AA1050-H111. The pictures show initial blanks and corresponding final parts having different orientations of the welding joint relative to the rolling direction and to the geometry to be formed. The latter are included in order to assess the spifability of TWB in zones characterized by different states of stress and strain.

As can be seen in figure 7, the final quality of the sheet metal parts is greatly dependent on the quality of the welding joint produced by friction stir-welding. On one hand, it is possible to SPIF friction stir-based TWB parts with high forming depths, similar to those obtained with conventional reference blanks of the same material, in which fracture develops outside the welding joint (figure 7a)). On the other hand, it is also possible to obtain bad SPIF parts where cracking occurs prematurely in the welding joint (figures 7b) and c)). This leads to the conclusion that SPIF of FSW tailored blanks is capable of producing industrial sheet metal parts with high forming depths if a good quality control of the welding joints is ensured. Application of non-destructive methods based on X-ray (figure 7d)), ultrasonic and liquid penetration testing is crucial for the identification of possible welding defects that may diminish the overall formability of SPIF.

In what concerns the present research work, results show that a significant part of the formability problems occurred with TWB having a uniform 1.5 mm thickness profile. Possible explanation for this is two fold and can be attributed to (i) the difficulties of the FSW experimental set-up utilized by the authors for welding sheet metal blanks equal to or below 1.5 mm thickness and to (ii) inherent difficulties of FSW for joining sheet metal blanks with small thicknesses due to the fact that material flow around the cylindrical rotational welding tool progressively drifts from 3D to 2D as the thickness of the sheets to be welded is reduced.

Figure 8 shows a truncated pyramid SPIF part produced from a TWB made of aluminium AA1050-H111 with a uniform 2.0 mm thickness profile. The welding joint is parallel to the rolling direction and is positioned across the corners of the SPIF part in order to evaluate the performance of the TWB in severe forming conditions. As can be seen, cracks are triggered almost simultaneously at the corners with and without welding seam that are marked in the figure (refer also to the detail included in figure 8b). This result together with the detail included in figure 8c) showing a sound welding seam, with no evidence of cracking, at the corner placed in the opposite diagonal further confirms the very good forming potential of the tailored blanks produced by FSW.

Figures 9 and 10 present the experimental values of the maximum drawing angles ψ_{max} that TWB and conventional reference blanks without welding can undertake as a function of the initial thickness t_0 during SPIF of truncated conical and pyramidal shapes. Several test cases were considered in accordance to the experimental work plan listed in table 1, namely the utilization of TWB with uniform and non-uniform thickness profiles, with welding joints parallel ('0º/RD' in the legend) and perpendicular ('90º/RD' in the legend) to the rolling direction, with welding joints positioned along the sides or across the corners ('Diagonal' in the legend) of the final part and with the welding root facing ('Inverted' in the legend) and not facing the rotating single point forming tool.

As can be seen, the experimental values of the maximum drawing angle ψ_{max} that were measured in the parts produced from conventional reference blanks diminish with the decrease of the initial thickness t_0, This result is in close agreement with the theoretical predictions and the experimental observations that are available in the literature (Jeswiet et al., 2005)(Silva et al., 2008a). In case of the SPIF parts produced from TWB it is possible to identify two different groups of results, depending on the initial thickness of the blanks being equal to or greater than 1.5 mm. For both geometries the spifability of TWB with larger thicknesses is similar to that of the conventional reference blanks and shows no sensitivity to the orientation of the welding joint and to the relative position of the welding root against the forming tool. The spifability of TWB with uniform 1.5 mm thickness profile is difficult to characterize due to a large dispersion of the experimental results. Some test cases present a level of spifability similar to that of the conventional reference blanks while other test cases present much smaller values. Such variations have to do with the previously mentioned reasons that are likely to affect FSW of tailored blanks with small thickness profiles.

From what was mentioned before it is possible to conclude on the feasibility of producing sound shapes with a constant drawing angle of $\psi = 60º$ for the truncated pyramid and $\psi = 65º$ for the truncated cone from friction stir-based TWB made of aluminium AA1050-H111 with uniform or non-uniform thickness profiles equal or larger than 1.5 mm. Figure 11 shows an example together with the corresponding dummy sheet that was utilized for protecting the welding joint from the rotating single point forming tool.

4. CONCLUSIONS

This paper evaluates the application of single point incremental forming (SPIF) to the manufacture of sheet metal parts made from tailor welded blanks (TWB) produced by friction stir welding (FSW). The work proposes innovative solutions based on the utilization of dummy sheets to protect the welding joints from the rotating single point forming tool and utilizes experimental benchmark tests to evaluate the formability of TWB produced by FSW against that of conventional reference blanks of the same material.

Experimentation by the authors confirms that combination of SPIF with TWB produced by FSW is capable of successfully manufacturing complex sheet metal parts with high forming depths if a good quality control of the welding joints is ensured. The proposed technology is easy to implement and requires low risk investments because existing machine-tools can be utilized for both producing and forming the tailored blanks.

Further studies are necessary to evaluate the formability of TWB made from dissimilar materials.

ACKNOWLEDGEMENTS

The first author and the corresponding author would like to acknowledge PTDC/EME-TME/64706/2006 FCT/Portugal for the financial support. The corresponding author would like to acknowledge the support of IPL/DTU during his sabbatical license in Denmark.

REFERENCES

Allwood, J.M., King, G. P. F., Duflou, J. R., 2004. A structured search for applications of the Incremental Sheet Forming process by product segmentation, *Journal of Engineering Manufacture*, **219**, 239-244.

Bambach, M., Hirt, G., Ames, J., 2005. Quantitative validation of FEM simulations for incremental sheet forming using optical deformation measurement, *Advanced Materials Research*, **6-8**, 509-516.

Buffa, G., Fratini, L., Hua, J., Shivpuri, R., 2006. Friction stir welding of tailored blanks: Investigation on process feasibility, *Annals of CIRP*, **55**, 279-282.

Filice, L., Fratini, L., Micari, F., 2002. Analysis of material formability in incremental forming. *Annals of CIRP*, **51**, 199-202.

Hirt, G., Abratis, C., Ames, J., Jackel, F., Meyer, A., 2005. Manufacturing and processing of tailored products, In: Schaeffer, L. (Eds.), Proceedings of *25th SENAFOR*, Porto Alegre, Brazil, pp. 11-27.

Jeswiet, J., 2001. Incremental single point forming, *Trans. of North American Manufacturing Research Institute*; **29**, 75-79.

Jeswiet, J., Micari, F., Hirt, G., Bramley, A., Duflou, J., Allwood, J., 2005. Asymmetric single point incremental forming of sheet metal, *Annals of CIRP*, **54**, 623-650.

Kitazawa, K., Wakabayashi, A., Murata, K., Yaejima, K., 1996. Metal-flow phenomena in computerized numerically controlled incremental stretch-expanding of aluminum sheets, *Keikinzoku Journal of Japan Institute of Light Metals*, **46**, 65-70.

Kopp, R., Wiedner, C., Meyer, A., 2005. Forming strategies and process modelling for CNC incremental sheet forming, *Advanced Materials Research*, **6-8**, 81-92.

Leszak, E., 1967. Apparatus and process for incremental dieless forming. Patent US3342051A.

Silva, M.B., Skjoedt, M., Atkins, A.G., Bay, N., Martins, P.A.F., 2008. Single point incremental forming & formability/failure diagrams, *Journal of Strain Analysis for Engineering Design*, **43**, 15-35.

Silva, M.B., Skjoedt, M., Martins, P.A.F., Bay, N., 2008. Revisiting the fundamentals of single point incremental forming by means of membrane analysis, *International Journal of Machine Tools and Manufacture*, **48**, 73–83.

Skjoedt, M., Hancock, M.H., Bay, N., 2007. Creating helical tool paths for single point incremental forming, *Key Engineering Materials*, **344**, 583-590.

Skjoedt, M., Silva, M.B., Bay, N., Martins, P.A.F., Lenau, T., 2007. Single point incremental forming using a dummy sheet, In: Vollertsen, F., Yan, S., (Eds.), *Proceedings of the 2nd ICNFT (2nd Int. Conf. on New Forming Technologies)*, Bremen, Germany, pp. 267-276.

Thomas, W.M., Nicholas, E.D., Needham, J.C., Church, M.G., 1991. Templesmith P and, Dawes C. J. Friction stir butt welding, *International Patent Application No. PCT/GB92/02203*.

Vilaça, P., Santos, J.P., Góis, A., Quintino, L., 2005. Joining aluminium alloys dissimilar in thickness by friction stir welding and fusion process, *Welding in the World - Journal of the International Institute of Welding (IIW)*, **49**, 56-62.

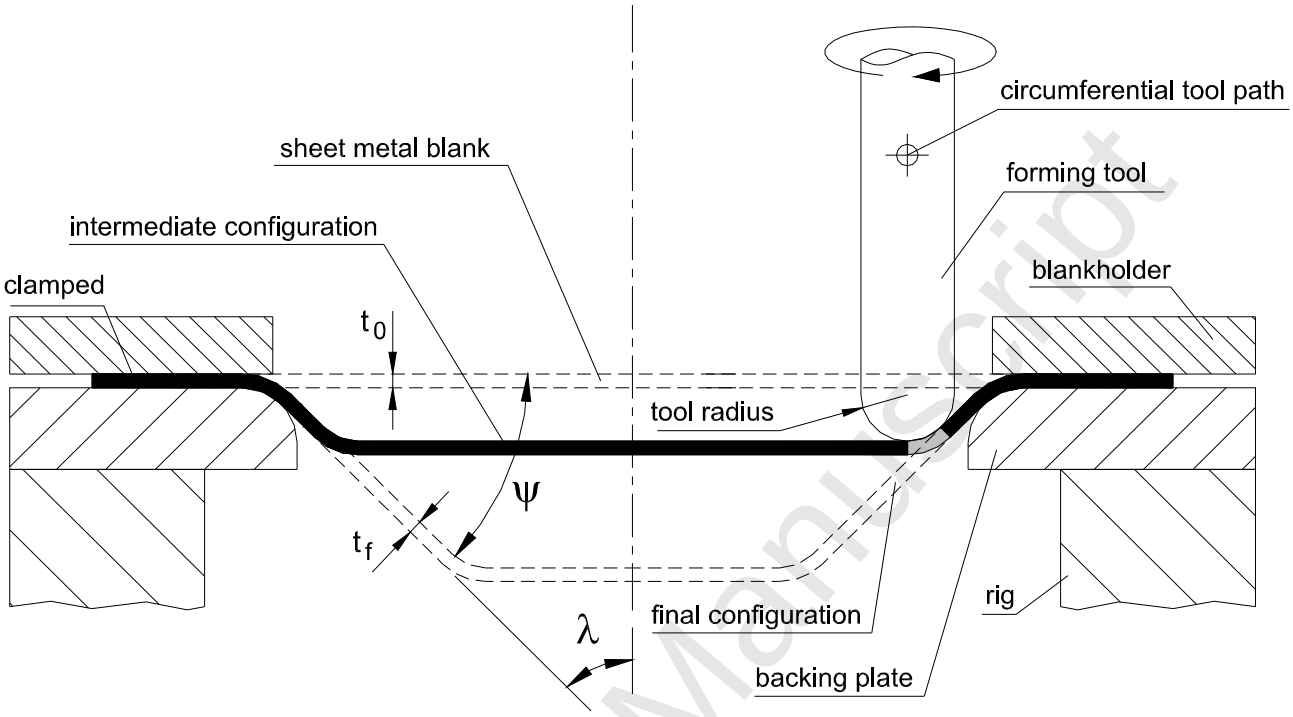

Figure 1 – Schematic representation of a cross section view of the rotational symmetric single point incremental forming (SPIF) process. The tool rotates while performing a round (or helical) path.

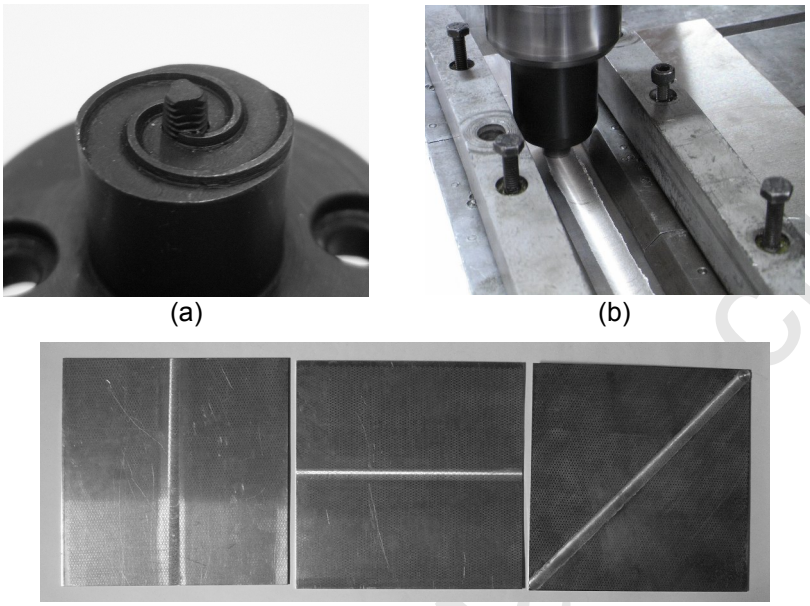

Figure 2 – Production of AA1050-H111 tailor welded blanks by friction stir welding.

a) Detail of the friction stir welding tool showing the shoulder and the pin.

b) Detail of the joint being welded showing the tool and the clamping system utilized for rigidly fixing the sheets.

c) Tailor welded blanks with welding joints parallel and perpendicular to the rolling direction. The welding joint placed across the diagonal of the sheet metal blank is aligned with the rolling direction of each sheet.

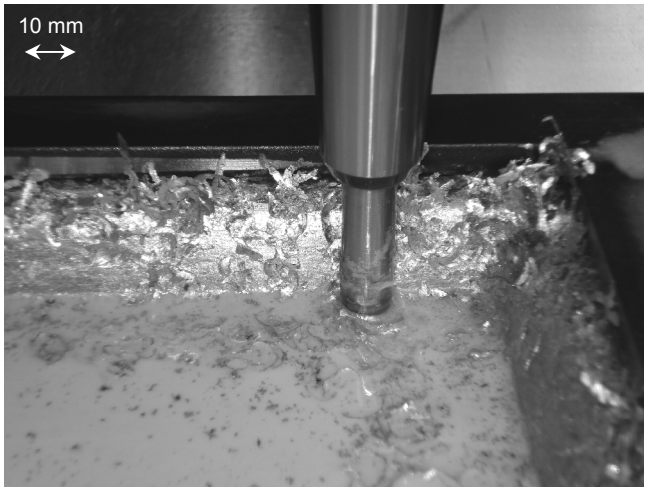

(a)

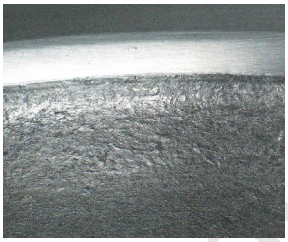

(b)

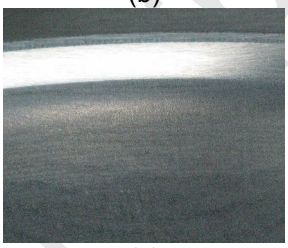

(c)

Figure 3 – SPIF of an Aluminium AA1050-H111 conventional sheet metal blank with 1.5 mm thickness.

a) Evidence of surface damage due to galling.
b) Detail of the poor surface quality due to galling.
c) Detail of the good surface quality due to the utilization of a dummy sheet to avoid direct contact of the sheet metal blank with the rotating forming tool.

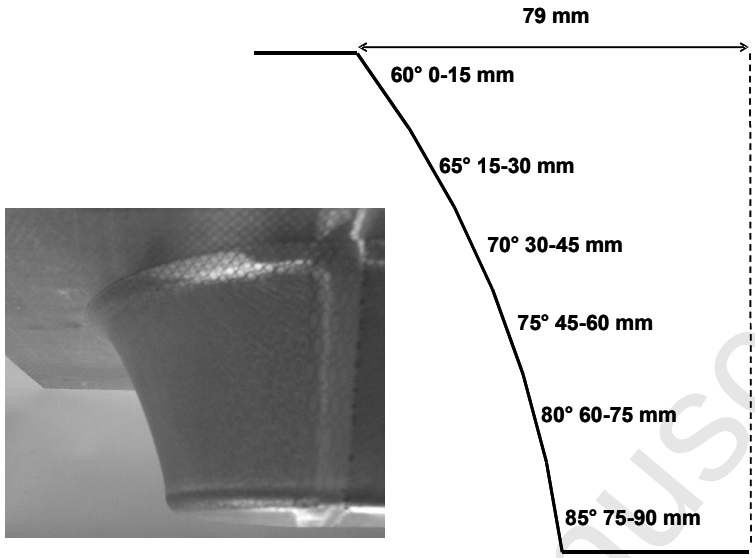

Figure 4 – Detail of the benchmark formability test performed on a truncated conical shape with varying drawing angles ψ with the depth. The picture shows a component made from a tailored welded blank of AA1050-H111 produced by friction stir welding with a uniform thickness of 2 mm.

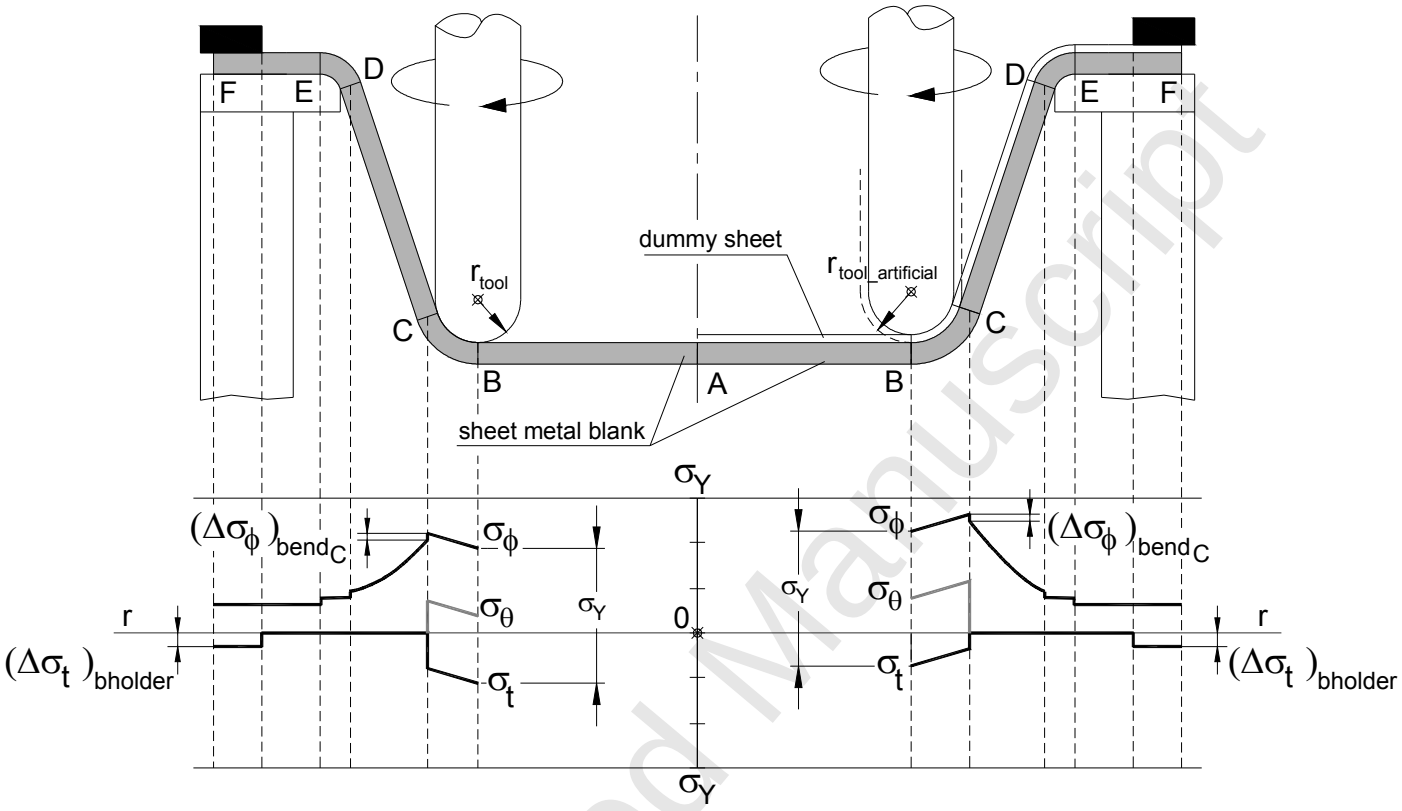

Figure 5 – Schematic representation of the stress field in a radial slice of a SPIF component being produced without (left side) and with (right side) dummy sheet.

Note: The distribution of the stress field shown above is valid only for plane strain conditions because in case of bi-axial stretching $\sigma_\phi = \sigma_\theta$.

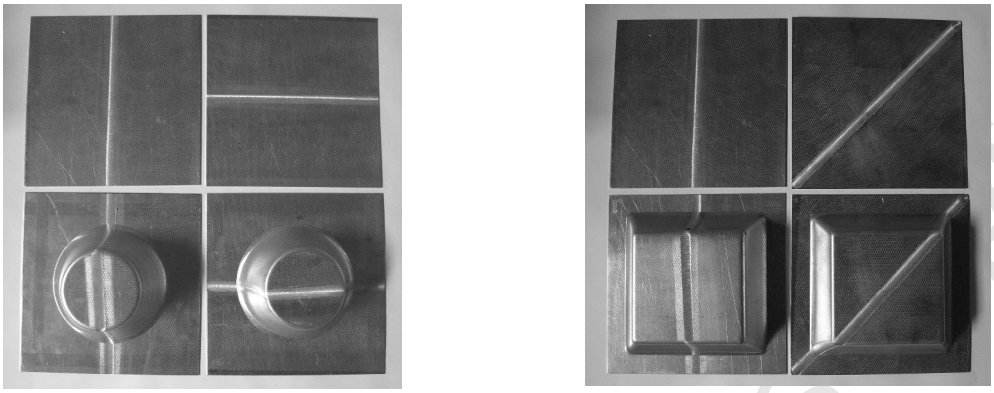

(a) (b)

Figure 6 – Benchmark formability tests of truncated (a) conical and (b) pyramidal shapes characterized by varying drawing angles ψ with the depth (TWB were made of AA1050-H111 sheets with 1.5 and 2 mm thickness).

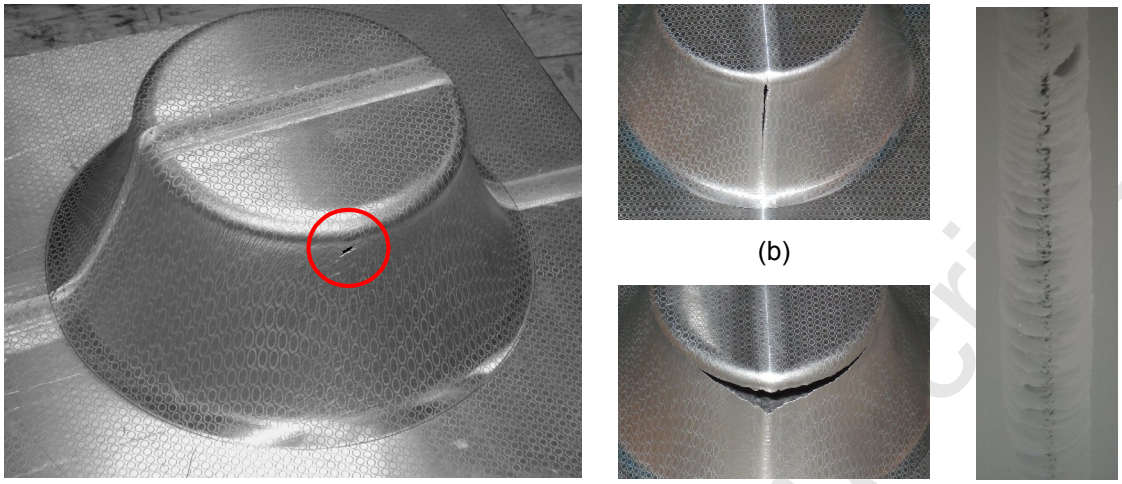

(a) (b) (c) (d)

Figure 7 – Truncated conical benchmark formability parts produced from TWB of Aluminium AA1050-H111 sheets.

a) Good formability showing a crack outside the welding joint (TWB with a uniform 2.0 mm thickness profile)
b) Low formability showing necking and subsequent cracking along the welding joint (TWB with a uniform 1.5 mm thickness profile)
c) Low formability derived from a crack triggered in the welding joint (TMAZ) and subsequently propagated along the circumferential direction perpendicular to the welding joint (TWB with a uniform 1.5 mm thickness profile)
d) Detail of an X-ray of a welding joint showing several defects (TWB with a uniform 1.5 mm thickness profile).

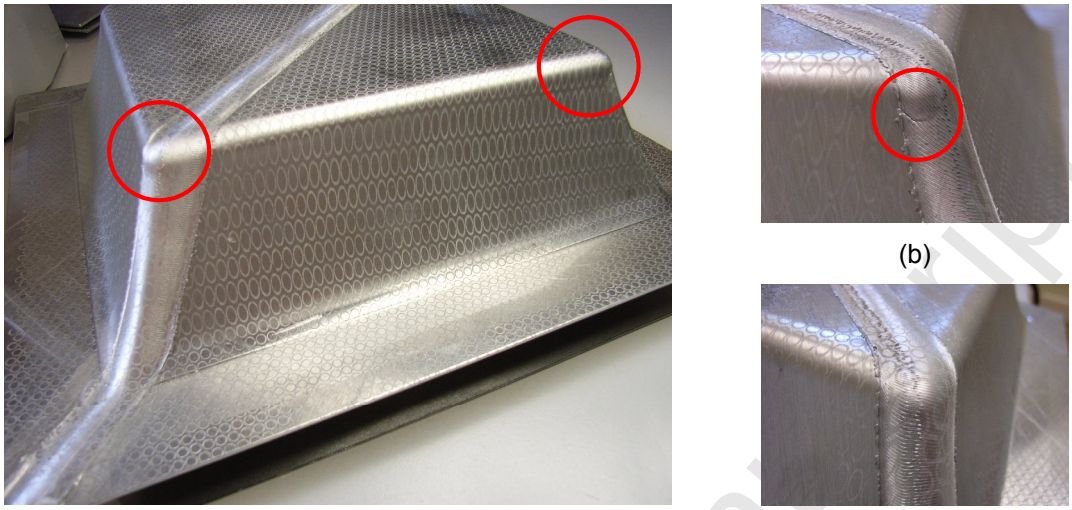

(a) (b) (c)

Figure 8 – Truncated pyramid benchmark formability part produced from a TWB of Aluminium AA1050-H111 with a uniform 2.0 mm thickness profile.

a) Cracks are triggered almost simultaneously at the corners with and without welding joints.
b) Detail of a) showing the crack at the corner.
c) Detail of the corner placed in the opposite diagonal to b) showing no evidence of cracking in the welding joint.

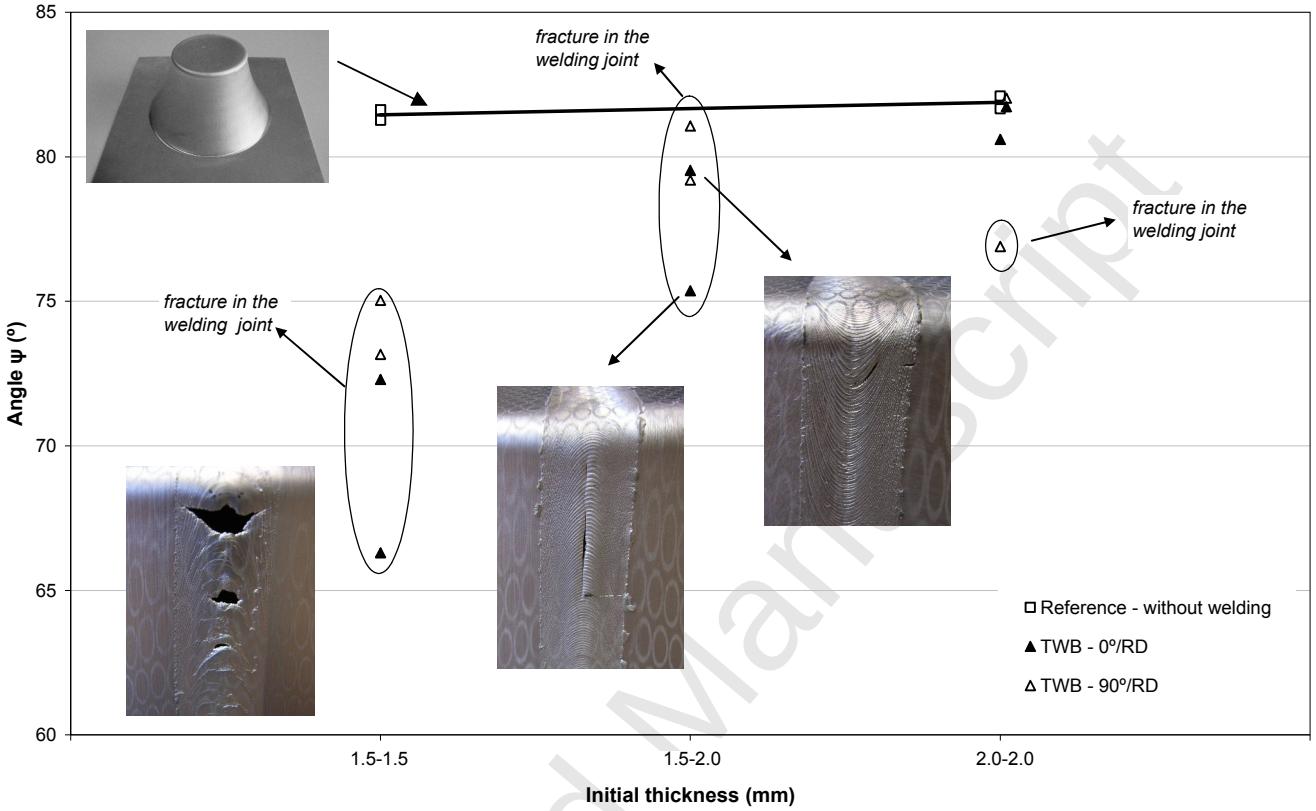

Figure 9 – Maximum drawing angles ψ_{max} that TWB and conventional reference blanks without welding can undertake as a function of the initial thickness t_0 during SPIF of truncated conical shapes made of Aluminium AA1050-H111. A DC04 deep drawing steel dummy sheet with 0.63 mm was utilized in all the experiments.

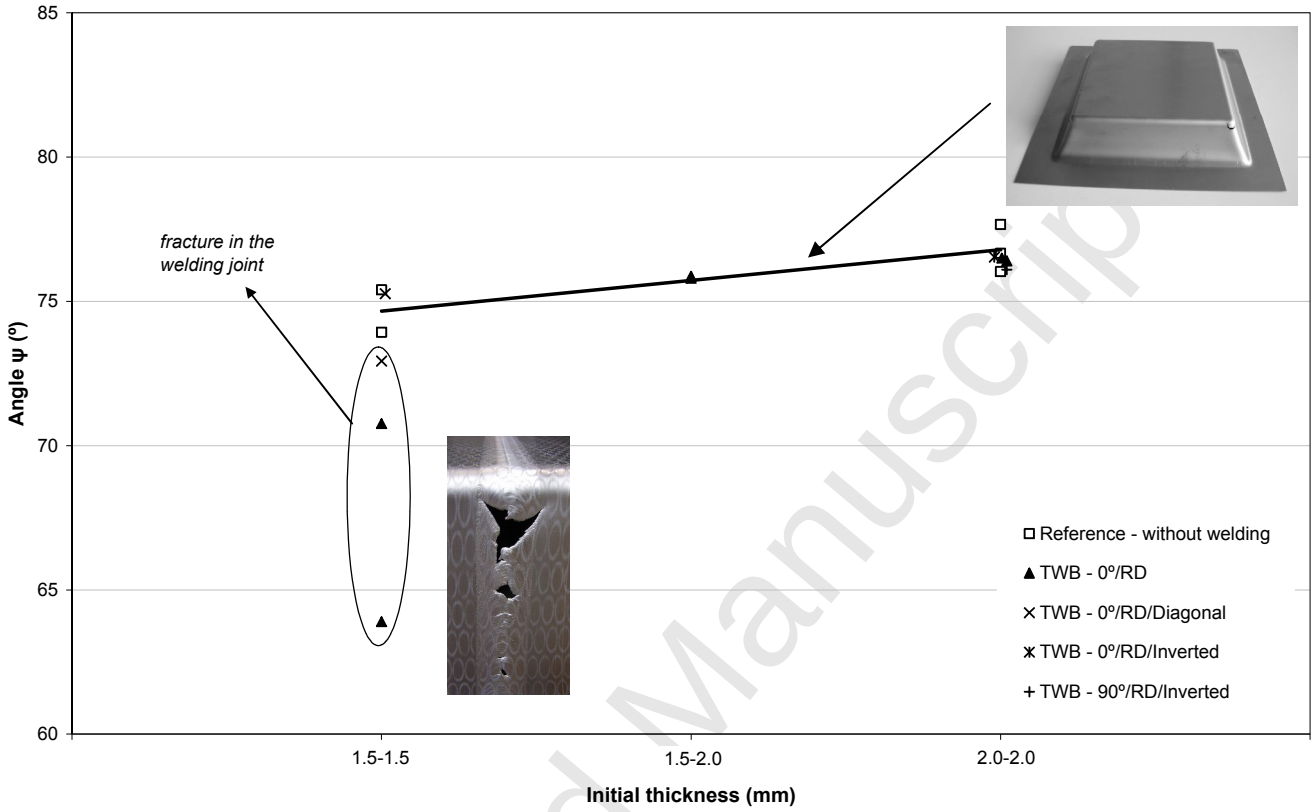

Figure 10 – Maximum drawing angles ψ_{max} that TWB and conventional reference blanks without welding can undertake as a function of the initial thickness t_0 during SPIF of truncated pyramid shapes made of Aluminium AA1050-H111. A DC04 deep drawing steel dummy sheet with 0.63 mm was utilized in all the experiments.

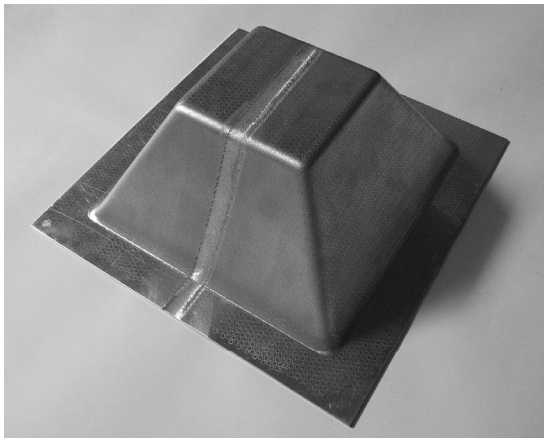

(a)

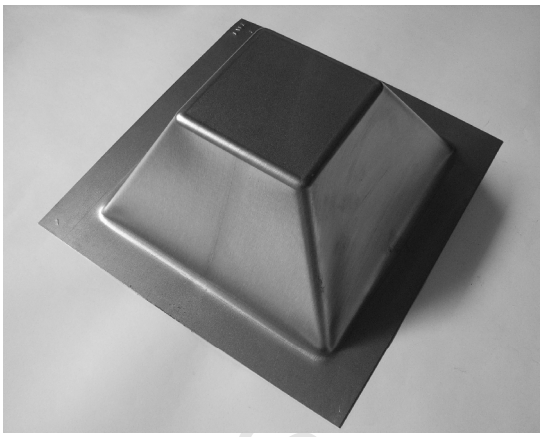

(b)

Figure 11 – (a) Truncated pyramid shape with a constant drawing angle $\psi = 60^{\circ}$ produced by SPIF of a TWB of Auminium AA1050-H111 with a uniform 2.0 mm thickness profile. (b) Dummy sheet of DC04 deep drawing steel with 0.63 mm that was utilized for protecting the welding joint from the rotating single point forming tool.

Geometry	Sheet metal blank	Thickness (mm)	Notes
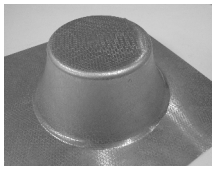	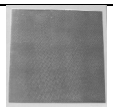	1.5	Single blank
		2.0	
	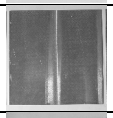	1.5-1.5	TWB – Joint parallel to the rolling direction
		2.0-2.0	
		1.5-2.0	
	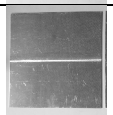	1.5-1.5	TWB – Joint perpendicular to the rolling direction
		2.0-2.0	
		1.5-2.0	
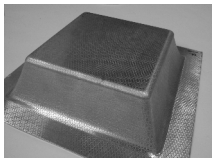	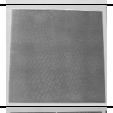	1.5	Single blank
		2.0	
	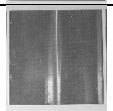	1.5-1.5	TWB – Joint parallel to the rolling direction
		2.0-2.0	
		1.5-2.0	
	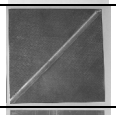	1.5-1.5	TWB – Joint parallel to the rolling direction and positioned across the corners (diagonally) of the final part
	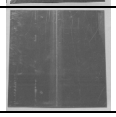	2.0-2.0	TWB – Joint parallel to the rolling direction and root side facing the rotating single point forming tool
	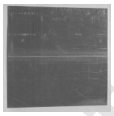	2.0-2.0	TWB – Joint perpendicular to the rolling direction and root side facing the rotating single point forming tool

Table 1 – The plan of experiments

	State of strain	State of stress
Plane strain conditions	$d\varepsilon_\phi = -d\varepsilon_t > 0$ $d\varepsilon_\theta = 0$ $d\varepsilon_t < 0$	$\sigma_\phi = \sigma_1 = \frac{\sigma_Y}{\left(1+\frac{t}{r_{tool}}\right)} + \left(\Delta\sigma_\phi\right)_{friction\_BC} > 0$ $\sigma_\theta = \sigma_2 = \frac{1}{2}\left(\sigma_1 + \sigma_3\right)$ $\sigma_t = \sigma_3 = -\sigma_Y \frac{t}{\left(r_{tool}+t\right)} + \left(\Delta\sigma_\phi\right)_{friction\_BC} < 0$
Equal bi-axial stretching conditions	$d\varepsilon_\phi = d\varepsilon_\theta > 0$ $d\varepsilon_t < 0$	$\sigma_\phi = \sigma_\theta = \sigma_1 = \frac{\sigma_Y}{\left(1+\frac{2t}{r_{tool}}\right)} + \left(\Delta\sigma_\phi\right)_{friction\_BC} > 0$ $\sigma_t = \sigma_3 = -2\sigma_Y \frac{t}{\left(r_{tool}+2t\right)} + \left(\Delta\sigma_\phi\right)_{friction\_BC} < 0$

Table 2 – States of stress and strain that are commonly found in single point incremental forming processes (Silva et al., 2008a).

Note: The meridional stress σ_ϕ increases by an amount $\left(\Delta\sigma_\phi\right)$ from point B to C (refer to figure 5) due to friction.

	Maximum drawing angle ψ_{max} (degrees)	
Thickness t_0 (mm)	**Without dummy sheet**	**With dummy sheet**
1.5	76.4	74.7
2.0	77.7	76.4

Table 3 – Maximum drawing angle ψ_{max} that conventional sheet metal blanks made of Aluminium AA1050-H111 can undertake when forming a truncated pyramid shape with and without the utilization of a DC04 deep drawing steel dummy sheet with 0.63 mm thickness.

February 2008

Joint author statement

If a thesis contains articles made in collaboration with other researchers, a joint author statement about the PhD-student's part of the article shall be made by each of the co-authors, cf. article 12, section 4 of the Ministerial Order No. 18 February 2008 about the PhD degree

Title of the article: Theory of single point incremental forming

Author(s): P.A.F. Martins, N. Bay, M. Skjoedt, M.B. Silva

Journal: CIRP Annals - Manufacturing Technology, (2008), vol. 57, p. 247-252.

PhD-student: Martin Skjødt Cpr.nr: _____

Signature of the PhD-student: _____ Date: _____

Co-author: _____ Signature: _____

Description of each author's contribution to the above-mentioned article:

P. A. F. Martins: Development of initial theory including formulas and assumptions, further discussion and development of theory, planning of experiments, writing of paper, pictures and graphics for paper, final editing.

N. Bay: Planning of experiments, further discussion and development of theory, final editing.

M. Skjoedt: CAD drawing of parts, CAM programming of parts, planning and conduction of experiments, original idea of using a dummy sheet, pictures for paper, literature study, further discussion and development of theory, final editing.

M. B. Silva: Planning and conduction of experiments, friction stir welding, thickness measurements, literature study, further discussion and development of theory, final editing.

CIRP Annals - Manufacturing Technology 57 (2008) 247–252

Contents lists available at ScienceDirect

CIRP Annals - Manufacturing Technology

journal homepage: http://ees.elsevier.com/cirp/default.asp

Theory of single point incremental forming

P.A.F. Martins [a], N. Bay (1)[b,*], M. Skjoedt [b], M.B. Silva [a]

[a] IDMEC, Instituto Superior Tecnico, TULisbon, Portugal
[b] Department of Mechanical Engineering, Technical University of Denmark, Denmark

ARTICLE INFO

Keywords:
Sheet metal
Formability
Single point incremental forming

ABSTRACT

This paper presents a closed-form theoretical analysis modelling the fundamentals of single point incremental forming and explaining the experimental and numerical results available in the literature for the past couple of years. The model is based on membrane analysis with bi-directional in-plane contact friction and is focused on the extreme modes of deformation that are likely to be found in single point incremental forming processes. The overall investigation is supported by experimental work performed by the authors and data retrieved from the literature.

1. Introduction

Single point incremental forming (SPIF) is a new sheet metal forming process with a high potential economic payoff for rapid prototyping applications and for small quantity production. Fig. 1 presents the basic components of the process; (i) the sheet metal blank, (ii) the blankholder, (iii) the backing plate and (iv) the rotating single point forming tool. The blankholder is utilized for clamping and holding the sheet in position during SPIF. The backing plate supports the sheet and its opening defines the working area of the single point forming tool. The tool is utilized to progressively shape the sheet into a component and its path is generated by a CNC machining centre. During the forming process there is no backup die supporting the back surface of the sheet.

Most investigations of SPIF have concerned applications and formability limits of the process. So far, the investigations lead to the conclusion that the formability of the process can be defined in terms of four major parameters [1]: (i) thickness of the sheet, (ii) size of the vertical step down per revolution, (iii) speed (both rotational and feed rate) and (iv) radius of the forming tool. The influence of the first parameter is commonly explained by means of the sine law. In what concerns the second parameter, although the general opinion has been that formability decreases with increasing step size, new results provided by Ham and Jeswiet [2] seem to indicate that step size itself does not have a significant effect on the formability. The speed of the forming tool is known to influence formability because of its direct influence on the frictional conditions at the tool–sheet interface. Smaller radius of the forming tools is claimed to provide better formability due to concentration of the strains at the zone of deformation in the sheet under the forming tool. Larger tool radius tends to distribute the strains over a more extended area making the process more similar to conventional stamping.

Despite the major contributions made by Jeswiet et al. [1], Fratini et al. [3] and Allwood et al. [4] and many others on the development of industrial applications and better characterization of the forming limits of the process, the mechanics of deformation remains little understood. In fact, nowadays, SPIF is one of the very few if not the only sheet metal forming process in which the advantage of experimentation over theoretical and numerical analysis is absolute even for solving the simplest practical problem.

This paper presents a closed-form analysis, modelling the fundamentals of SPIF and explaining the experimental and numerical results available in the literature for the past couple of years. The model is based on membrane analysis with bi-directional, in-plane contact friction and is focused on the extreme modes of deformation that are likely to be found in SPIF. The formability limits of the process are analysed by combining the proposed membrane analysis with ductile damage mechanics. An explanation to the increased formability compared to conventional stamping and deep drawing operations is provided through the utilization of fracture forming limit diagrams based on the onset of fracture instead of the conventional forming limit diagrams based on the onset of necking. New versions of SPIF based on the utilization of dummy sheets inserted between the workpiece and the tool are also addressed and the overall investigation is supported by experimental work performed by the authors and by data retrieved from the literature.

2. Theoretical background

Circle-grid analysis in conjunction with the observation of the smear-mark interferences between the tool and the surface of the sheet allow the classification of all possible tool paths as combinations of the three basic modes of deformation that are depicted in Fig. 2; (A) flat surfaces under plane strain stretching conditions, (B) rotational symmetric surfaces under plane strain stretching conditions and (C) corners under equal bi-axial stretching conditions.

* Corresponding author.

0007-8506/$ – see front matter © 2008 CIRP.
doi:10.1016/j.cirp.2008.03.047

Table 1
States of stress and strain in SPIF and conventional stamping

	Assumption	State of strain	State of stress	Hydrostatic stress
SPIF (flat and rotational symmetric surfaces)	Plane strain conditions (A) and (B)	$d\varepsilon_\phi = -d\varepsilon_t > 0$ $d\varepsilon_\theta = 0$ $d\varepsilon_t < 0$	$\sigma_\phi = \sigma_1 = \frac{\sigma_Y}{1+(t/r_{tool})} > 0$ $\sigma_\theta = \sigma_2 = \frac{1}{2}(\sigma_1+\sigma_3)$ $\sigma_t = \sigma_3 = -\sigma_Y \frac{t}{r_{tool}+t} < 0$	$\sigma_m = \frac{\sigma_Y}{2}\left[\frac{r_{tool}-t}{r_{tool}+t}\right]$
SPIF (corners)	Equal bi-axial stretching (C)	$d\varepsilon_\phi = d\varepsilon_\theta > 0$ $d\varepsilon_t < 0$	$\sigma_\phi = \sigma_\theta = \sigma_1 = \frac{\sigma_Y}{1+(2t/r_{tool})} > 0$ $\sigma_t = \sigma_3 = -2\sigma_Y \frac{t}{r_{tool}+2t} < 0$	$\sigma_m = \frac{2\sigma_Y}{3}\left[\frac{r_{tool}-t}{r_{tool}+2t}\right]$
Conventional stamping (rotational symmetric surfaces)	Equal bi-axial stretching	$d\varepsilon_\phi = d\varepsilon_\theta > 0$ $d\varepsilon_t < 0$	$\sigma_\phi = \sigma_\theta = \sigma_1 = \frac{\sigma_Y}{1+(t/r_{punch})} > 0$ $\sigma_t = \sigma_3 = -\sigma_Y \frac{t}{r_{punch}+t} < 0$	$\sigma_m = \frac{2\sigma_Y}{3}\left[\frac{r_{punch}-t/2}{r_{punch}+t}\right]$

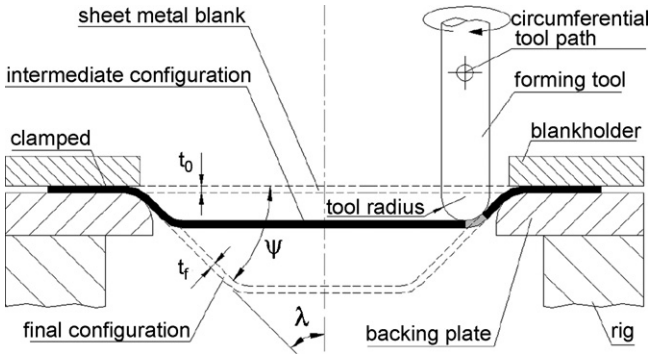

Fig. 1. Schematic representation of SPIF.

It is worth to notice that in between these modes of deformation there are other possibilities where neither plane strain stretching nor equal bi-axial stretching appear. However, the analytical model to be derived in this section of the paper will only be focused on the extreme modes of deformation that are likely to be found in SPIF.

2.1. State of stress and strain

In SPIF the local shell element CDEF (Fig. 3) is subjected to normal forces, shear forces and bending moments, so that it conforms to the hemispherical shape of the tip of the pin tool, forming a contact area (A, B or C in Fig. 2) between the tool and the part of the sheet placed immediately ahead of the moving tool.

The state of strain and stress acting in these areas can be derived from the membrane equilibrium conditions if bending moments are neglected and circumferential, meridional and thickness stresses are assumed to be principal stresses.

Further simplifying assumptions are the following: the material is assumed to be rigid, perfectly plastic and isotropic and the resultant friction stress acting in the tool–sheet contact interface is assumed to consist of two in-plane components—a meridional component $-\mu_\phi\sigma_t$ due to the downwards movement of the tool and a circumferential component $-\mu_\theta\sigma_t$ due to the circumferential feed combined with the rotation of the tool. This last assumption, which is an untraditional way of modelling friction introduced for convenience implies that the coefficient of friction $\mu = \sqrt{\mu_\phi^2 + \mu_\theta^2}$.

Resolving the force equilibrium along the thickness, circumferential and meridional directions, results in:

$$\begin{aligned}
&\sigma_t r\,d\theta\,r_1\,d\alpha + \sigma_\phi r\,d\theta\,t\sin\frac{d\alpha}{2} + (\sigma_\phi + d\sigma_\phi)(r+dr)\,d\theta(t+dt)\sin\frac{d\alpha}{2} + \sigma_\theta r_1\,d\alpha\,t\sin\frac{d\theta}{2}\cos\alpha + (\sigma_\theta + d\sigma_\theta)\,r_1\,d\alpha\,t\sin\frac{d\theta}{2}\cos\alpha = 0\\
&\sigma_\theta r_1 d\alpha\left(t+\frac{dt}{2}\right) - \mu_\theta\sigma_t r_1 d\alpha\left(r+\frac{dr}{2}\right)d\theta - (\sigma_\theta + d\sigma_\theta)r_1 d\alpha\left(t+\frac{dt}{2}\right) = 0\\
&(\sigma_\phi + d\sigma_\phi)(r+dr)\,d\theta(t+dt) - \sigma_\phi r\,d\theta\,t + \mu_\phi\sigma_t r\,d\theta\,r_1\,d\alpha - \sigma_\theta\frac{d\theta}{2}r_1\,d\alpha\,t\sin\alpha - (\sigma_\theta + d\sigma_\theta)\frac{d\theta}{2}r_1\,d\alpha\,t\sin\alpha = 0
\end{aligned} \tag{1}$$

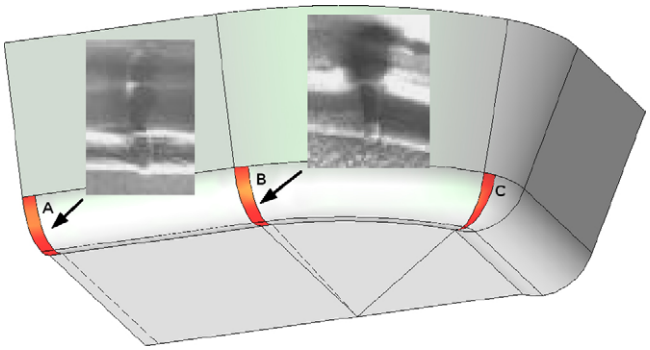

Fig. 2. Instantaneous deformation zone and contact area between forming tool and workpiece during SPIF.

The distribution of stresses in the small localized plastic zones (A, B and C), which as earlier mentioned are the three typical deformation zones in SPIF, can easily be obtained from Eq. (1) after neglecting higher order terms, taking into account geometrical simplifications, considering the Tresca yield criterion and assuming that single point incremental forming of flat and rotationally symmetric surfaces is performed under plane strain conditions, $d\varepsilon_\theta = 0$, see ref. [5].

Table 1 resumes the strains and stresses along the principal directions that are derived from the proposed membrane analysis. Results for conventional stamping are provided for comparison. Further details can be obtained from ref. [5].

2.2. Friction at the tool–sheet contact interface

In recent work [5] the present authors showed that the frictional effects along the circumferential direction can be neglected implying that only the friction forces exerted in the meridional direction need to be taken into account.

Under these circumstances, starting from the membrane equilibrium condition along the meridional direction, Eq. (1), and neglecting the variation in thickness $dt/dr \cong 0$, it is possible to establish the following relationship for the meridional stress distribution σ_ϕ along the curvature from the bottom B to the top C

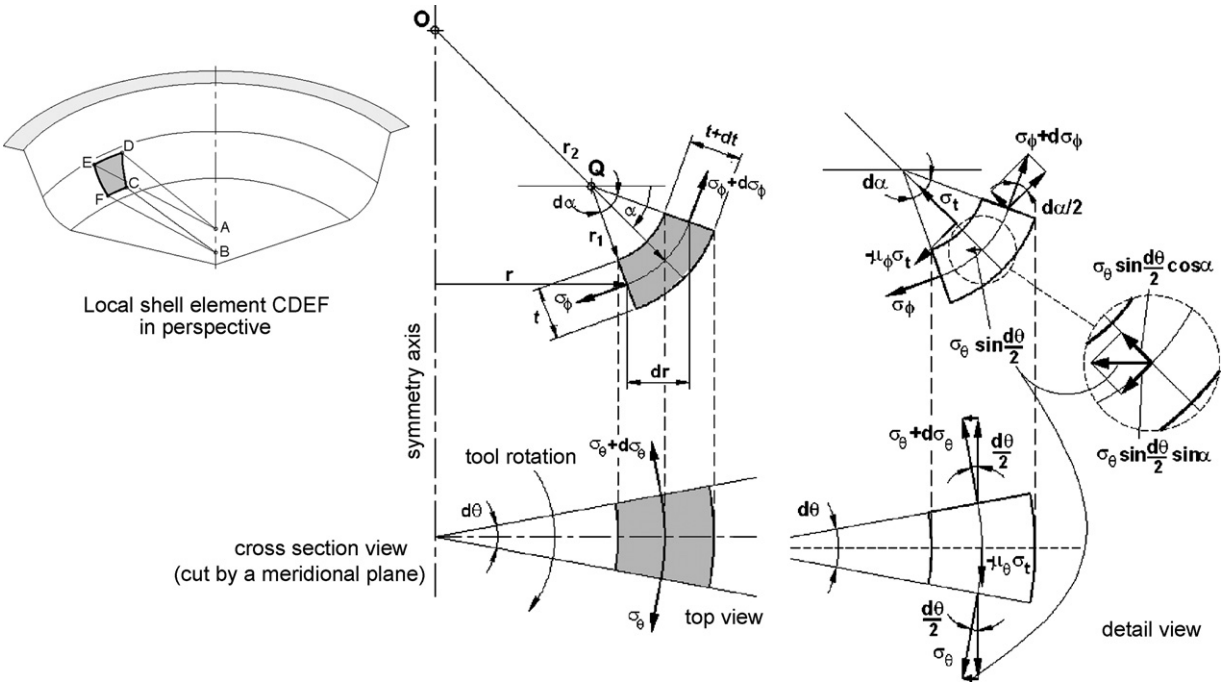

Fig. 3. Membrane analysis of single point incremental forming. Schematic representation of the shell element and details showing the acting stresses in the meridional, circumferential and thickness directions.

of the plastic zone, see Fig. 4:

$$\sigma_\phi = \sigma_{\phi_B} \exp^{k\mu\varphi} \quad (2)$$

where k takes a value equal to 1 or 2 for the plane strain or equal bi-axial strain, respectively, and φ is defined in the detail of the deformed part included in Fig. 4.

In physical terms, Eq. (2) indicates that the meridional stress σ_ϕ will increase with r as a result of friction at the tool–sheet contact interface and that the rate of increase at the corners of the SPIF parts (deformation type C, where $k = 2$) is higher than in the flat and rotationally symmetric surfaces (where, $k = 1$).

2.3. The inclined wall adjacent to the forming tool

Starting from the membrane equilibrium equation (1) along the thickness direction and noticing the absence of curvature $r_1 = \infty$ as well as the absence of contact pressure $\sigma_t = 0$ on the surface of the local element CD (Fig. 4), it may be concluded that $\sigma_\theta = 0$ along the inclined wall adjacent to the forming tool. Thus, since the meridional stresses σ_ϕ are the only stresses acting in this region the following equilibrium condition is valid in the inclined wall of the sheet:

$$\sigma_{\phi_D} = \sigma_{\phi_C} \frac{r_C}{r_D} \quad (3)$$

According to Eq. (3) the meridional stress σ_ϕ decreases along the inclined wall of the sheet being higher at the transition point C and smaller at point D. Because the meridional stress at point C must be kept below the yield stress (for a perfectly plastic material), it follows that the inclined wall surface of the sheet adjacent to the forming tool is elastic.

This result together with the state of stress presented in the previous sections of the paper results in the schematic plot shown in Fig. 4 of the stress field in a radial slice of the SPIF component containing the small, localized plastic zone, for the case of plane strain.

2.4. Thinning at the corner radius

Starting from the simplified form of the membrane equilibrium condition in the meridional direction, neglecting friction and

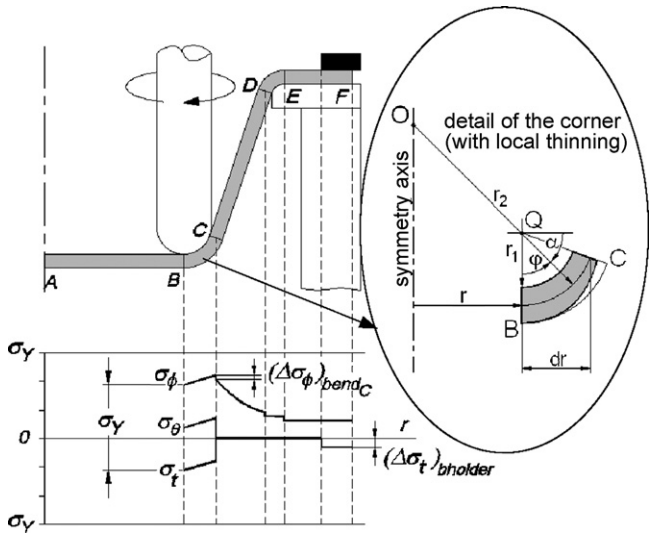

Fig. 4. Schematic representation of the stress field in a radial slice through the instantaneous, small plastic zone.

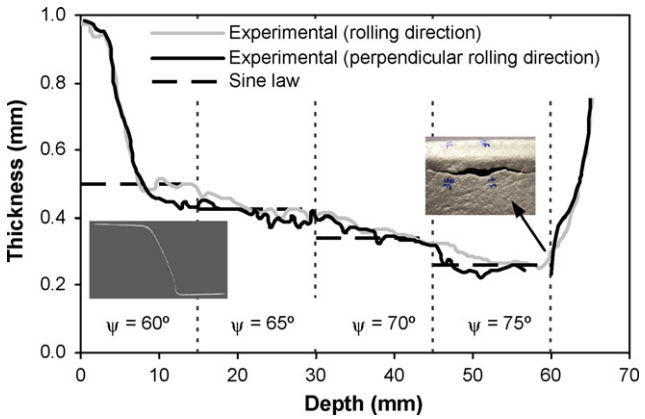

Fig. 5. Variation of the thickness with the depth along two meridional cross sections of a truncated conical shape of AA1050-H111 with varying drawing angles (ψ).

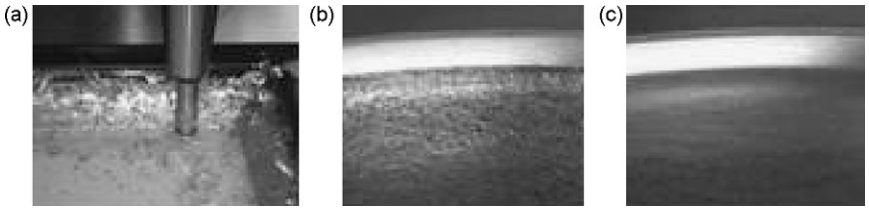

Fig. 6. SPIF of an AA1050-H111 sheet with 1.5 mm thickness. (a) Surface damage due to galling, (b) detail of the poor surface quality due to galling and (c) detail of the good surface quality obtained using a dummy sheet.

introducing the boundary conditions $r = r_B$, $\sigma_\phi = \sigma_{\phi_B}$ and $t = t_0$ it is possible to derive the following identity [5]:

$$\sigma_\phi = \sigma_{\phi_B} \frac{t_0}{t} \tag{4}$$

The physical meaning of Eq. (4) is that reduction in thickness t tends to balance the rise in the meridional stress σ_ϕ so that $\sigma_\phi t$ is constant in the small localized zone being plastically deformed. It follows that although the variation in the wall thickness of the inclined surface of the sheet can be approximately estimated by means of the sine law $t = t_0 \sin\lambda$ (Fig. 5), the reason why thinning occurs has to do with the meridional tensile stresses σ_ϕ rather than shear acting in the small localized zone being plastically deformed. The detail included in Fig. 4 provides a schematic, geometrical interpretation of thinning at the corner radius.

2.5. Dummy sheets and state of stress

SPIF of aluminium AA1050-H111 sheets with thickness equal to and above 1.5 mm thickness are known to experience surface quality problems due to galling, i.e. pick-up of workpiece material on the tool surface and scoring of subsequent workpiece surface as seen in Fig. 6a.

In a previous paper Skjoedt et al. [6] investigated this phenomenon and proposed the use of a dummy sheet inserted between the workpiece and the tool in order to avoid direct contact of the tribologically difficult material of the sheet metal blank with the rotating tool. They found that the dummy sheet prevents surface damage by galling and, therefore, greatly improves the final surface quality of the formed component (Fig. 6b and c).

The idea can be further extended to SPIF of tailor welded blanks (TWB), since the dummy sheet additionally protects the welding seam from the single point rotating tool (Fig. 7).

From a theoretical point of view, the application of a dummy sheet between the sheet metal and the rotating single point forming tool is expected to influence formability. This is due to the fact that the dummy sheet artificially increases the radius r_{tool} of the tool acting on the sheet metal blank. The increase of the tool radius leads to an increase of the meridional stress σ_ϕ acting along BC and, therefore, to an increase of the hydrostatic stress (refer to Table 1 and Fig. 8). This is expected to imply a decrease in the overall process formability in SPIF when utilizing dummy sheets.

Experimental measurements recently performed by the authors [6], comparing the maximum drawing angle ψ_{max}, that conventional AA 1050-H111 blanks can undertake when forming a truncated pyramid shape, with and without a dummy sheet, are in agreement with the theoretical predictions but also reveal that the actual reduction in formability is very small.

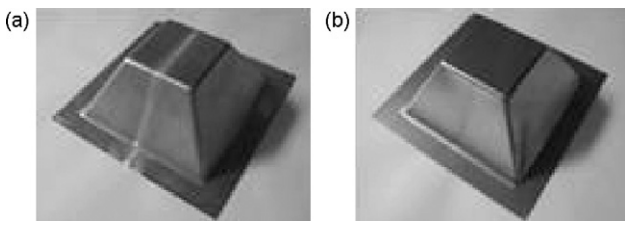

Fig. 7. (a) Truncated pyramid shape produced by SPIF of a TWB of AA1050-H111 with uniform 2 mm thickness profile and (b) dummy sheet of DC04 steel with 0.63 mm.

3. Formability ('SPIFABILITY')

There are two basic experimental procedures for determining if a sheet metal part of a specific material can be made by SPIF. One procedure makes use of conventional circle-grid analysis to characterize the forming limit curve in the principal strain-space (ε_1, ε_2); the other employs the maximum drawing angle ψ_{max} that a material can undertake as a function of the initial thickness of the sheet t_0.

As far as the authors are aware, there is no theoretical background behind the second procedure of using ψ_{max} as a criterion of failure, nor as to how the two procedures may be related. One of the aims of the present paper is to provide the missing background by relating the two experimental procedures.

3.1. FLDs vs. fracture forming limit diagrams

Experimental investigations relating limit strains in SPIF with the limit strains given in conventional forming limit diagrams (FLDs) show that limit strains in SPIF plotted in the principal strain-space (ε_1, ε_2) are usually much greater than those of conventional sheet metal forming processes [1,3].

The usual link between conventional FLD strains with SPIF limiting strains presumes that the failure modes in the two processes are the same, i.e. necking is the limiting criterion. However, the fact that limiting strains in SPIF exceed the FLD, may be due to the presumption of necking as the limit in SPIF being in error.

In fact, the evolution of thickness with depth along two meridional cross sections of a truncated conical shape with varying

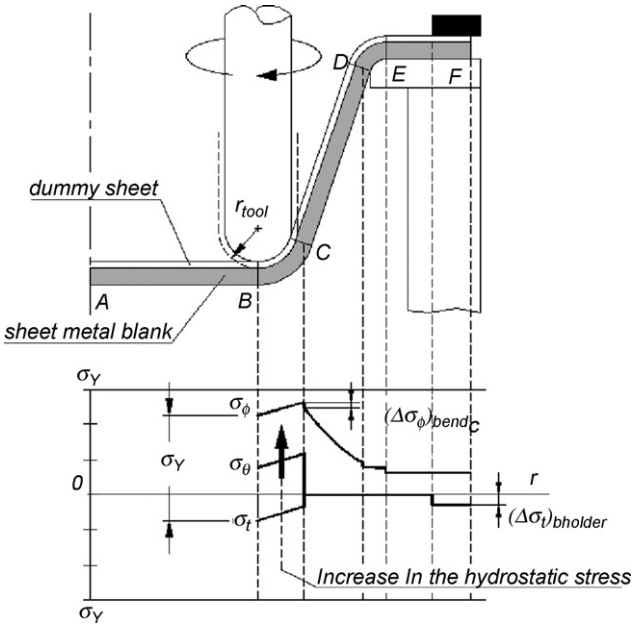

Fig. 8. Schematic representation of the stress field in a radial slice through the instantaneous small plastic zone of a SPIF part being produced with a dummy sheet.

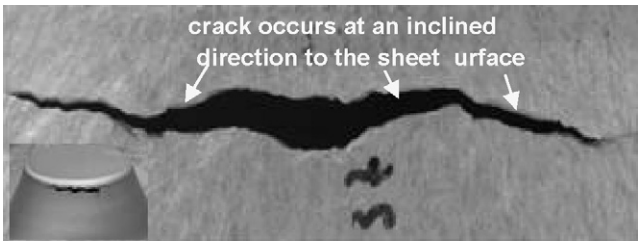

Fig. 9. Experimental evidence that SPIF is limited by fracture without necking.

drawing angles ψ made from an aluminium AA1050-H111 sheet with 1 mm of initial thickness (Fig. 5) reveals, that plastic deformation takes place by uniform thinning until fracture without experimental evidence of localized necking taking place before reaching the onset of fracture.

Additional evidence that formability is limited by fracture without previous necking is the inclined cross sectional shape of the crack to the sheet surface, depicted in Fig. 9.

The suppression of localized necking in SPIF is due to the inability of necks to grow. If a neck was to form at the small plastic deformation zone in contact with the incremental forming tool, it would have to grow around the circumferential bend path that circumvents the tool. This is difficult and creates problems of neck development. Even if the conditions for localized necking could be met at the small plastic deformation zone in contact with the tool, growth would be inhibited by the surrounding material which experiences considerably lower stresses.

The conditions for suppression of localized necking mentioned above do not occur in conventional sheet metal forming processes due to uniform loading and deformation conditions. In fact, differences between neighbouring plastically deforming regions in conventional sheet metal forming processes are much smaller than in SPIF and, therefore, growth of necking is easily ensured.

This last conclusion is crucial, implying that FLDs of conventional sheet metal forming are inapplicable to describe failure in SPIF. Instead, fracture forming limit diagrams (FFLD) placed well above the FLDs should be employed in SPIF (Fig. 10).

3.2. Hydrostatic stress in SPIF

The triaxiality ratio σ_m/σ_Y is known to play an important role in the formability of materials. Assuming proportional loading and realizing that the tool radius in conventional stamping is much greater than in SPIF, $r_{punch} \gg r_{tool}$, it is noticed from Table 1, that σ_m/σ_Y is higher in conventional stamping:

$$\left(\frac{\sigma_m}{\sigma_Y}\right)_{stamping} > \left(\frac{\sigma_m}{\sigma_Y}\right)_{bi-axial} > \left(\frac{\sigma_m}{\sigma_Y}\right)_{plane\ strain}$$
$$\Leftrightarrow \frac{2}{3}\left[\frac{r_{punch}-t/2}{r_{punch}+t}\right] > \frac{2}{3}\left[\frac{r_{tool}-t}{r_{tool}+2t}\right] > \frac{1}{2}\left[\frac{r_{tool}-t}{r_{tool}+t}\right] \quad (5)$$

Since the level of the triaxiality ratio σ_m/σ_Y in conventional stamping is higher than that of SPIF it can be concluded, that the rate of accumulated damage in stamping grows faster than in SPIF. This explains why the forming limits of SPIF are higher than in conventional stamping processes. In addition, the triaxiality ratio in Eq. (5) explains the reason, why the onset of cracks during incremental forming of pyramid shape components is preferentially located at its corners—the corners experience equal bi-axial stretching while the side flat surfaces are deformed under plane strain conditions, where the triaxiality ratio is lower.

As a final note on expression (5), it should be observed that the influence of the radius of the tool, r_{tool}, on the triaxiality ratio σ_m/σ_Y is opposed to that of the thickness and consequently, formability is expected to increase when the radius of the forming tool decreases. The qualitative predictions based on the new proposed theoretical framework are plausible and in good agreement with experimental observations reported in the literature [1].

3.3. Damage and forming limits

The FFLD in SPIF (Fig. 10) can be characterized by means of ductile damage mechanics based on void growth models. Assuming the Tresca yield criterion, linear loading paths, and that $f(\sigma_m/\bar{\sigma})$ takes the simple form $\sigma_m/\bar{\sigma}$, the total amount of accumulated damage for plane strain and equal bi-axial stretching SPIF conditions results in the following critical damage values:

$$D_c = \int_0^{\bar{\varepsilon}_f} \frac{\sigma_m}{\bar{\sigma}}\,d\bar{\varepsilon} = \frac{1}{2}\left[\frac{r_{tool}-t}{r_{tool}+t}\right]\varepsilon_1^{plane\ strain} \quad (6)$$

$$D_c = \int_0^{\bar{\varepsilon}_f} \frac{\sigma_m}{\bar{\sigma}}\,d\bar{\varepsilon} = \frac{2}{3}\left[\frac{r_{tool}-t}{r_{tool}+2t}\right]2\varepsilon_1^{bi-axial} \quad (7)$$

If the critical value of damage D_c at the onset of cracking is assumed to be path-independent, by solving Eqs. (6) and (7) for ε_1 it is possible to set up the following identity:

$$\frac{\varepsilon_1^{bi-axial}-\varepsilon_1^{plane\ strain}}{\varepsilon_2^{bi-axial}-0} = \frac{(3/4)[(r_{tool}+2t)/(r_{tool}-t)]-2[(r_{tool}+t)/(r_{tool}-t)]}{(3/4)[(r_{tool}+2t)/(r_{tool}-t)]} = -\frac{5(r_{tool}/t)-2}{3(r_{tool}/t)+6} \quad (8)$$

Eq. (8) gives the slope of the fracture forming line (FFLD) in the principal strain-space (ε_1, ε_2) (Fig. 10). For typical experimental values of r_{tool}/t in the range 2–10 the slope derived from Eq. (8) will vary between −0.7 and −1.3. This supports the assumption that the fracture forming limit in SPIF can be approximately expressed as $\varepsilon_1 + \varepsilon_2 = q$, where $\varepsilon_t = -q$ is the thickness strain at the onset of fracture in plane strain conditions. This result is in close agreement with the typical loci of failure strains in conventional sheet forming processes, where the slope of the FFLD is often about −1 [1,3].

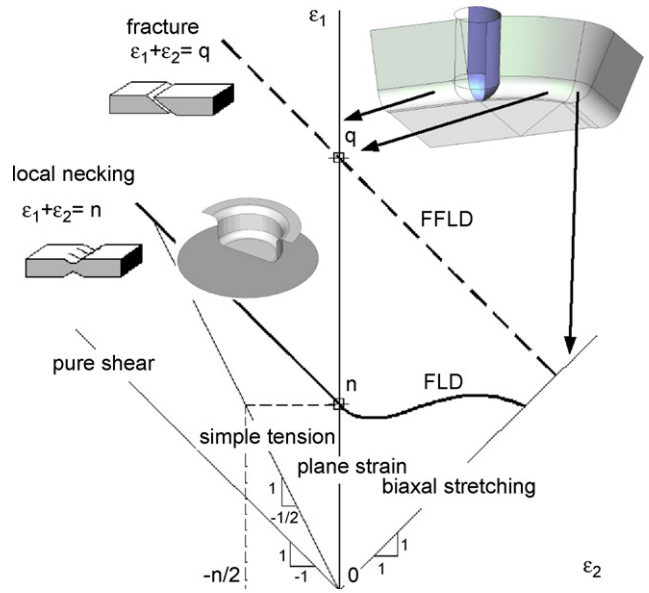

Fig. 10. Schematic representation of the forming limits of SPIF against those of stamping and deep drawing.

3.4. Maximum drawing angle

Starting from the meridional stress σ_ϕ acting in the local shell element for plane strain or bi-axial stretching conditions (refer to Table 1) and substituting the actual thickness t by the sine law

$t = t_0 \sin\lambda$, one obtains:

$$\frac{\sigma_\phi}{\sigma_Y} = \left(1 + \frac{kt_0 \sin\lambda}{r_{tool}}\right)^{-1} \quad (9)$$

where, k is a constant equal to 1 or 2 for plane strain or equal bi-axial stretching conditions respectively, and $\lambda = \pi/2 - \psi$ is the semi-cone angle, which is the complement of the drawing angle ψ between the inclined wall surface and the initial flat configuration of the sheet (Fig. 1). For the typical values of the maximum drawing angles in SPIF $\sin\lambda$ may be approximated by the value of λ, and hereby:

$$\psi = \frac{\pi}{2} - \left(\frac{\sigma_Y}{\sigma_\phi} - 1\right)\frac{r_{tool}}{kt_0} \quad (10)$$

One may thus conclude that the theoretical estimates of the maximum drawing angle ψ_{max}, for values of the meridional stress $\sigma_\phi < \sigma_Y$, are expected to increase with the initial thickness t_0 of the sheet and to decrease with increasing radius of the forming tool, r_{tool}. This agrees qualitatively with experimental results and provides background for the determination of material formability by plotting the maximum drawing angle ψ_{max} as a function of the initial thickness t_0 of the sheet (for example in [1]).

However, Eq. (10) is not in a form allowing theoretical estimation of the maximum drawing angle ψ_{max} since it requires knowledge of the ratio between the yield stress and the meridional stress which is generally unknown. Thus, it is necessary to rewrite Eq. (10) in such a way that users may easily obtain an estimate from data readily available from simple material testing conditions. By substituting σ_t given by the equations included in Table 1 into Eq. (10) and rearranging terms, one obtains the equation below applying for plane strain and as well as equal bi-axial stretching conditions:

$$\psi = \frac{\pi}{2} - \left(\frac{\sigma_Y}{\sigma_\phi} - 1\right)\frac{r_{tool}}{kt_0} = \frac{\pi}{2} - \left(\frac{kt}{r_{tool}}\right)\frac{r_{tool}}{kt_0} = \frac{\pi}{2} - \exp^{\varepsilon_t} \quad (11)$$

where t is the thickness of the sheet at fracture and ε_t is the value of the thickness strain at the limit of formability. In principle, ε_t is to be determined as the through-thickness fracture limit strain ε_3 in plane strain or equal bi-axial stretching test of a sheet metal.

In physical terms Eq. (11) implies that the two experimental procedures utilized for characterizing the formability in SPIF ((1) fracture forming limit in the principal strain-space (ε_1, ε_2) and (2) maximum drawing angle ψ_{max} at the onset of fracture) are merged into a single concept—the onset of fracture.

4. Summary

The paper presents a new theoretical model for the different modes of deformation commonly found in SPIF. The model is built upon membrane analysis and ductile damage mechanics and is based on the experimental observations that fracture is not preceded by localized necking and that crack propagates under tensile meridional stresses acting under stretching modes of deformation.

Experiments by the authors together with data retrieved from the literature confirm that the proposed theoretical framework is capable of successfully addressing the influence of the major parameters and explaining the enhanced formability of the process.

Acknowledgments

The first author would like to acknowledge PTDC/EME-TME/64706/2006 FCT/Portugal for the financial support. The support provided by Prof. Anthony G. Akins during the investigation is also greatly acknowledged.

References

[1] Jeswiet J, Micari F, Hirt G, Bramley A, Duflou J, Allwood J (2005) Asymmetric Single Point Incremental Forming of Sheet Metal. *Annals of CIRP* 54(1):623–650.
[2] Ham M, Jeswiet J (2006) Single Point Incremental Forming and the Forming Criteria for AA3003. *Annals of CIRP* 55(1):241–244.
[3] Fratini L, Ambrogio G, Di Lorenzo R, Filice L, Micari F (2004) Influence of Mechanical Properties of the Sheet Material on Formability in Single Point Incremental Forming. *Annals of CIRP* 53(1):207–210.
[4] Allwood JM, Shouler DR, Tekkaya AE (2007) The Increased Forming Limits of Incremental Sheet Forming Processes. in Micari F, et al. (Eds.) *Key Engineering Materials, ISSN: 1013-9826. Proceeding of SheMet 07—12th International Conerence on Sheet Metal, vol. 344*621–628.
[5] Silva MB, Skjoedt M, Atkins AG, Bay N, Martins PAF (2008) Single Point Incremental Forming & Formability/Failure Diagrams. *Journal of Strain Analysis for Engineering Design* 43(1):15–36.
[6] Skjoedt M, Silva MB, Bay N, Martins PAF, Lenau T (2007) Single Point Incremental Forming Using a Dummy Sheet. in Vollertsen F, Yuan S, (Eds.) *Proceeding. 2nd ICNFT (2nd International Conference on New Forming Technologies)*267–276.

February 2008

Joint author statement

If a thesis contains articles made in collaboration with other researchers, a joint author statement about the PhD-student's part of the article shall be made by each of the co-authors, cf. article 12, section 4 of the Ministerial Order No. 18 February 2008 about the PhD degree

Title of the article: Multi stage strategies for single point incremental forming of a cup

Author(s): M. Skjoedt, N. Bay, B. Endelt, G. Ingarao

Journal: ESAFORM2008, 11th conference on material forming, Lyon, France, Apr. 23-25 (2008), International Journal of Material Forming, (2008), Springer/ESAFORM 2008.

PhD-student: Martin Skjødt Cpr.nr:

Signature of the PhD-student: Date:

Co-author: Signature:

Description of each author's contribution to the above-mentioned article:

M. Skjoedt: Idea and development of multi stage strategies, CAD drawing of parts, CAM programming of parts, FEM simulation, planning and conduction of experiments, analysis of results, writing of paper, pictures and graphics for paper, literature study, final editing.

N. Bay: Discussions and final editing.

B. Endelt: Support during initial FEM simulation, final editing.

G. Ingarao: Providing a working LS-DYNA code for simulation of SPIF which has been the inspiration for the final code used, final editing.

Int J Mater Form
DOI 10.1007/s12289-008-0156-3

Multi Stage Strategies for Single Point Incremental Forming of a Cup

M. Skjoedt[1], N. Bay[1], B. Endelt[2], G. Ingarao[3]

[1]*Department of Mechanical Engineering, Technical University of Denmark, DTU - Building 425, DK-2800, Kgs. Lyngby, Denmark*
URL: www.mek.dtu.dk *e-mail: msk@ipl.dtu.dk; nbay@ipl.dtu.dk*

[2]*Department of Production, Aalborg University, Fibigerstræde 16, DK-9220, Aalborg Ø, Denmark*
URL: www.production.aau.dk *e-mail: endelt@production.aau.dk*

[3]*Department of Manufacturing and Management Engineering, University of Palermo, Viale delle Scienze, 90128 Palermo, Italy*
URL: www.unipa.it *e-mail: p.ingarao@dtpm.unipa.it*

ABSTRACT: A five stage forming strategy for Single Point Incremental Forming of a circular cylindrical cup with a height/radius ratio of one is presented. Geometrical relations are discussed and theoretical strains are calculated. The influence of forming direction (upwards or downwards) is investigated for the second stage comparing explicit FE analysis with experiments. Good agreement is found between calculated and measured thickness distribution, overall geometry and strains. Using the proposed multi stage strategy it is shown possible to produce a cup with a height close to the radius and sides parallel to the symmetry axis in about half of the depth.

Key words: Incremental forming, multi stage, FEM

1 INTRODUCTION

Single Point Incremental Forming (SPIF) is a relative new sheet forming process which offers the possibility of forming complex parts without dedicated dies using only a single point tool and a standard 3-axis CNC machine. The process enables strains much higher than traditional sheet forming processes, but is limited by the type of deformation which is close to plane strain for geometries formed in one stage. A consequence of this is the sine-law, $t = t_0 \cdot \sin(90°-\alpha)$, which relates the drawing angle α with the thickness after forming. This law has proven to give a good description of the thickness distribution and as a result it is not possible to form parts with drawing angles higher than about 60-80° in one stage. For a 90° drawing angle the sine-law predicts a thickness equal to zero and strains going towards infinity. One way to get around the limitations prescribed by the sine-law is to use a multi stage strategy, and this is the subject of the present paper.

2 MULTI STAGE STRATEGIES

Using a multi stage forming strategy is not a new idea in SPIF. Kitazawa et al. [1] used different two stage strategies to produce hemi ellipsoidal shapes and investigated the limits before fracture varying the radius and the height of the geometry. Jeswiet et al. [2] used a three stage strategy to form an automotive headlight reflector. As far as the authors know, no work has yet been presented in literature, where a multi stage strategy allows forming of a part with a 90° drawing angle in SPIF. In two point incremental forming (TPIF) a 90° drawing angle has been achieved, [3,4].

3 MULTI STAGE STRATEGY

3.1 Forming of cups

A fundamental difference between deep drawing and SPIF is the plate area included in the deformation. In deep drawing it is the drawn-in flange, which is deformed, whereas limited deformation is introduced in the bottom of the cup. For deep

drawing steel forming of cups with a height/radius ratio h/r ≈ 2 is possible. SPIF of a cup with a ratio h/r = 1 is considered almost impossible. The plate area included in the deformation in SPIF is the area surrounded by the first round of the tool path or the hole in the backing plate, i.e. forming may be characterized as stretching. Fig. 1 shows the thickness strain for a round and a square cup assuming that thickness is evenly distributed. In SPIF the distribution of thickness is normally far from this.

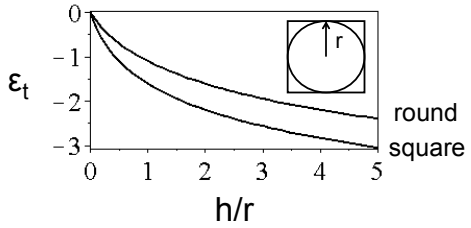

Fig. 1. Thickness strain for different h/r ratios.

3.2 5 stage strategy

The idea in the present work is to extend deformation to all the material available which is indicated by the horizontal, dotted line in Fig. 2. The first stage stretches this into a 45° cone. The following stages will gradually move the middle of this section towards the corner. All stages except the first can be performed going either downwards or upwards. This gives a total of 16 different strategies.

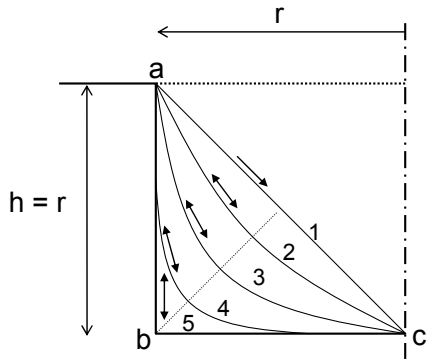

Fig. 2. Five stage strategy for forming a cup with h/r = 1.

In the present paper only the first four stages are considered and in those, two different strategies are investigated, i.e. down-up-down-down (DUDD) and down-down-down-up (DDDU). Influence from direction of forming is investigated in detail for the second stage. Theoretical principal strains can be calculated assuming the deformation to be pure stretching and the meridional strain to be evenly distributed. The circumferential strain is zero at points *a* and *c* and maximum in *b* in Fig. 2. The maximum thickness strain is higher than in Fig. 1 for h/r = 1. This is because the circumferential strain is not evenly distributed.

$$\varepsilon_{\phi} = \ln\left(\frac{2r}{r}\right) = \ln(2) \quad (1)$$

$$\varepsilon_{\theta,\max} = \ln\left(\frac{2\pi r}{\pi r}\right) = \ln(2) \quad (2)$$

$$\varepsilon_{t,\max} = -\ln(4) \approx -1.4 \quad (3)$$

4 SIMULTION AND EXPERIMENTAL SETUP

4.1 Setup of FE model

LS-DYNA version ls971s is adopted to simulate the process using explicit time integration. The forming tool and the backing plate are considered rigid. Time scaling is used simulating the process to be 1500 times faster than the actual experiments. The influence from time scaling and the use of rigid tools are investigated by Qin et al. [5] and the applied settings are considered reasonable. Maximum time step is based on a characteristic length equal to shell area divided by the longest diagonal. As a precaution DYNA uses 0.9 times this value. Fully integrated shells (type 16 in DYNA) are used with five integration points in thickness. Adaptive remeshing is adopted. The movement of the tool in the simulation is identical to that in the experiments including the rotation. The sheet material used is AA1050 H111/O and considered isotropic with a flow stress as stated in equation 4. The values for *C* and *n* are average of what is used by Hirt et al. [6] and Filice et al. [7]. Coulomb friction is assumed with $\mu = 0.1$.

$$\sigma_y = C \cdot \varepsilon^n = 111 \cdot \varepsilon^{0.14}\, MPa \quad (4)$$

4.2 Experimental setup

Experiments are conducted on a 3-axis milling machine. All sheets are 1 mm thick and the forming speed is 1000 mm/min. The tool, which has a radius of 6 mm and a semi-spherical tip, is rotated at 27 rpm. The rotational speed ensures a surface speed at the maximum radius equal to the forming speed. Diluted cutting fluid is used as lubrication, and the part is cleaned between each stage to remove loose wear particles. Tool paths are programmed using Pro/ENGINEER. First stage has a fixed vertical step size of 0.5 mm and following stages have a distance

between tool paths below 1 mm. The geometries used for the different stages are as shown in Fig. 2 with h = 70 mm and r = 80.5 mm. A small undeformed section remains in the middle (r = 0-10 mm) since the tool cannot form a cone with a sharp pointed end.

5 RESULTS

5.1 First two stages

Experiments are compared with simulations for the first two stages only, i.e. down-down (DD) and down-up (DU). A comparison of the achieved geometries can be seen in Fig. 3. There is almost perfect agreement for the DD strategy. Regarding the DU strategy the simulated geometry is more pointed in the center region and about 10 mm too deep.

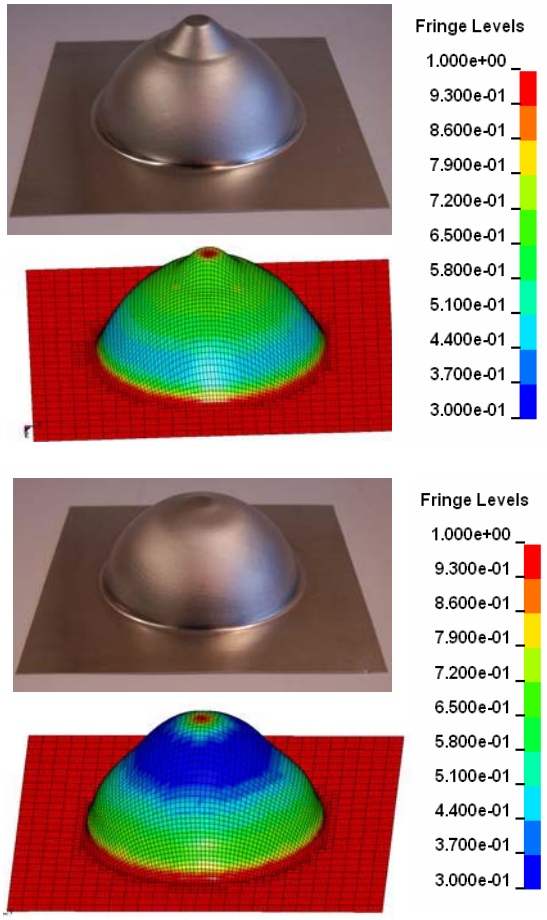

Fig. 3 Comparison of geometry achieved by simulation and by experiment for DD strategy (top) and DU strategy (bottom). Legend displays thickness in mm.

Fig. 4 compares the measured thickness distribution with the calculated one. For both geometries very good agreement is obtained until a depth of 60 mm. The DD strategy causes a distribution similar to a normal, one stage SPIF, where increasing angle causes decreasing thickness. Using the DU strategy this is not the case, and most of the reduction in thickness occurs in the center part where the drawing angle is low. This is necessary if vertical sides are to be achieved in the subsequent stages.

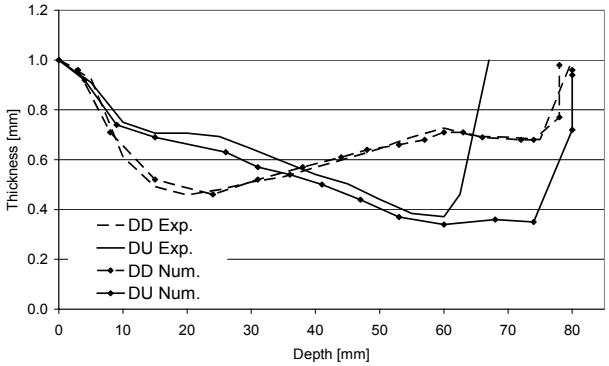

Fig. 4 Comparison of thickness from experiments and simulations as function of depth.

5.1.a Two stages: down-down (DD)

Adopting the strategy DD not all of the geometry is formed during the second stage, leaving a residual cone in the center. This is because the depth of the part is increased in the second stage, whereas the tool path only goes 70 mm down as in the first stage. As the tool moves down during the second stage a small plateau is formed beneath it. This plateau is observed experimentally as well as in the simulation, Fig. 5. Kitazawa et al. [1] obtained similar experimental results.

5.1.b Two stages: down-up (DU)

Adopting the strategy DU no residual cone is observed after the second stage, but material build up in front of the tool is noticed, which changes the point contact to a line contact, Fig. 5. Again this phenomenon is observed in both experiments and simulations. A similar observation is found in experiments by Kitazawa et al. [8]. The line contact causes process forces in the XY plane to increase and care should be taken not to exceed the force limits of the machine when forming harder materials.

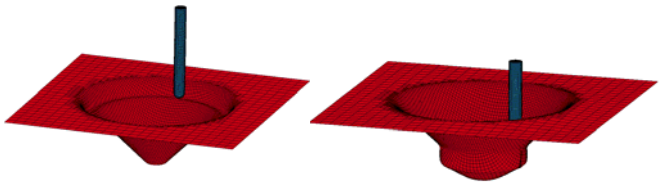

Fig. 5 Left: formation of plateau (DD strategy), right: formation of line contact (DU strategy).

5.2 Strategy DUDD and DDDU

The DDDU strategy can be performed without fracture, whereas the DUDD strategy results in fracture in stage 4 just after finishing the vertical section of the part, Fig. 6. The fracture appears in a zone with heavy thickness strain, see Fig. 7. Thickness measurements below this point are for the first three stages only since the fourth stage could not be completed. Both strategies give minimum thickness in the bending section between the vertical and the horizontal work piece parts. This corresponds well with the theoretical strains which indicate a maximum thickness strain in the corner of the cup. Using the suggested strategy it seems that the critical area is not the vertical sides themselves but the transition zone between vertical and horizontal. The reason is that this zone experiences a deformation close to equal bi-axial stretching.

Fig. 6 Geometry after 4 stages of forming (left DDDU and right DUDD).

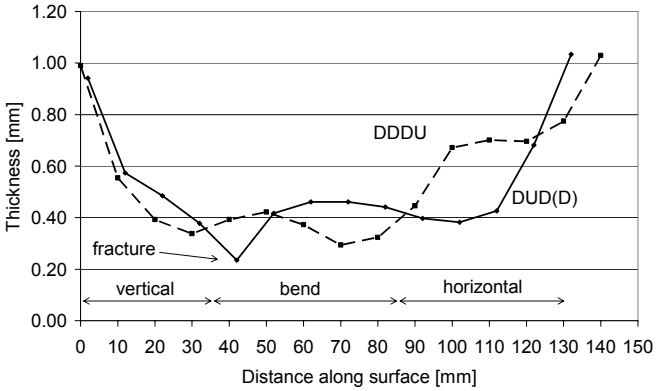

Fig. 7 Measured thickness as function of the distance along the surface for the two strategies DDDU and DUDD.

Both strategies increase the maximum drawing angle since they allow forming of the third stage. Experiments show, that the geometry obtained after this stage cannot be formed in single stage SPIF. The DDDU strategy also allows forming of the fourth stage which has vertical sides to a depth equal to 35 mm and a total depth approximately equal to the radius.

6 CONCLUSION

The multi stage strategy presented is able to produce a cup with a 90° drawing angle which has not been possible before. It demonstrates that strains far from plane strain can be achieved in SPIF and that strain paths may be far from linear. The distribution of strains is not only depending on the geometry of the tool path but also on the direction (downwards or upwards). The proposed strategy needs to be refined by further research but presents a promising concept for forming parts with vertical sides in SPIF.

ACKNOWLEDGEMENTS

The authors would like to thank Professor Joachim Danckert and Mr. Mikkel Steffensen from Department of Production, Aalborg University for their help with LS-DYNA. Furthermore Professor Fabrizio Micari from Department of Manufacturing and Management Engineering, University of Palermo is acknowledged for providing a LS-DYNA model facilitating the start of simulating SPIF in this work.

REFERENCES

1. Kitazawa, K., and Nakane, M., Hemi-ellipsoidal stretch-expanding of aluminum sheet by CNC incremental forming process with two path method, *Keikinzoku/Journal of Japan Institute of Light Metals,* 47, (1997), 440-445, (in Japanese).
2. Jeswiet, J. and Hagan, E., Rapid proto-typing of a headlight with sheet metal, *Technical Paper - Society of Manufacturing Engineers,* (2002), 1-6.
3. Hirt, G., Ames, J., and Bambach, M., A new forming strategy to realise parts designed for deep-drawing by incremental CNC sheet forming, *Steel Research International,* 76, (2005), 160-166.
4. Kitazawa, K., and Nakajima, A., Method for producing aluminum cylindrical shell having uniform wall-thickness by CNC incremental forming process, *Keikinzoku/Journal of Japan Institute of Light Metals,* 47, (1997), 378-384, (in Japanese).
5. Qin Q., Masuku E.S., Bramley A., Mileham A.R., and Owen G.W., Incremental sheet forming simulation and accuracy, *Proceedings of 8th ICTP*, (2005).
6. Hirt, G. and Bambach, M., Modelling incremental sheet forming using a meshless surface representation based on radial basis functions, *Proceedings of 8th ICTP*, (2005).
7. Filice, L., Fratini, L., and Micari, F., Analysis of material formability in incremental forming, *CIRP Annals - Manufacturing Technology,* 51, (2002), 199-202.
8. Kitazawa, K., Wakabayashi, A., Murata, K., and Yaejima, K., Metal-flow phenomena in computerized numerically controlled incremental stretch-expanding of aluminum sheets, *Keikinzoku/Journal of Japan Institute of Light Metals,* 46, (1996), 65-70, (in Japanese).

February 2008

Joint author statement

If a thesis contains articles made in collaboration with other researchers, a joint author statement about the PhD-student's part of the article shall be made by each of the co-authors, cf. article 12, section 4 of the Ministerial Order No. 18 February 2008 about the PhD degree

Title of the article: Strain paths and fracture in multi stage single point incremental forming

Author(s): M. Skjoedt, M.B. Silva, P.A.F. Martins, N. Bay

Journal: Conference paper, 9th international conference on technology of plasticity, (2008) Submitted.

PhD-student: Martin Skjødt Cpr.nr:

Signature of the PhD-student: Date:

Co-author: Signature:

Description of each author's contribution to the above-mentioned article:

M. Skjoedt: Idea and development of multi stage strategies, CAD drawing of parts, CAM programming of parts, FEM simulation, planning and conduction of experiments, analysis of results, writing of paper, graphics for paper, literature study, final editing.

M. B. Silva: Planning of experiments, material testing, surface grid, measurement of strains (fracture and necking), pictures for paper, final editing.

P. A. F. Martins: Planning of experiments, final editing.

N. Bay: Discussions and final editing.

.

Strain Paths and Fracture in Multi Stage Single Point Incremental Forming

M. Skjoedt[1], M.B. Silva[2], P.A.F. Martins[2], N. Bay[1]
[1] Dept. of Mechanical Engineering, Technical University of Denmark
[2] IDMEC, Instituto Superior Tecnico, TULisbon, Portugal

Summary

A multi stage strategy, which allows forming of SPIF parts with vertical walls, is investigated with emphasis on strain paths and fracture strains. Whereas downwards movement of the tool pin results in deformation close to plane strain upwards moving tool results in biaxial strains. A good correlation is observed between numerical simulation and experiments for the three first stages of forming. Surface strains in the first stage show deformation to be stretching. Strain paths are far from straight except for the first stage of forming. A fracture line with a slope of -1 in the principle strain space is in good agreement with measured strains with and without fracture.

1. Introduction

Single Point Incremental Forming (SPIF) is a rather new sheet forming process which offers the possibility of forming complex parts without dedicated dies using only a single point tool and a standard CNC machine. The process enables strains much higher than traditional sheet forming processes, but is limited by the type of deformation which is close to plane strain for geometries formed in one stage. A consequence of this is the sine-law, $t = t_0 \cdot \sin(90° - \Psi)$, which relates the drawing angle Ψ with the thickness after forming. This law has proven to give a good description of the thickness distribution and as a result it is not possible to form parts with drawing angles higher than 60-80° in one stage, the limiting angle being dependent of the workpiece material, geometry and process parameters. For a 90° drawing angle the sine-law predicts a thickness equal to zero and strains going towards infinity. One way to get around the limitations prescribed by the sine-law is to use a multi stage strategy, and this is the subject of the present paper.

2. Multi stage incremental forming

Using a multi stage forming strategy is not new in SPIF. Kitazawa et al. [1] used different two stage strategies to produce hemi ellipsoidal shapes and investigated the limits before fracture varying the radius and the height of the geometry. Jeswiet et al. [2] used a three stage strategy to form an automotive headlight reflector. In recent work Verbert et al. [3] showed parts made with an automatic multi stage tool path generation, but no details were given on the number of stages or how they were shaped.

2.1 New multistage strategy

In previous work by Skjoedt et al. [4] a new multi stage forming strategy was presented which enables forming of a cup with a 90° drawing angle. The strategy extends deformation to all the material available in SPIF which is indicated by the horizontal, dotted line in Fig. 1. The first stage stretches this into a 45° cone. The following stages will gradually move the middle of this section towards the corner. All stages except the first can be performed with either downwards or upwards moving tool. Theoretical principal strains can be calculated assuming the deformation to be pure biaxial stretching and the meridional strain ε_φ to be evenly distributed see Equations (1) - (3). The circumferential strain ε_θ is zero at points *a* and *c* and maximum in *b*. In [4] only the first four stages were investigated, showing that the strategy of three downward movements followed by an upward one in the fourth stage (DDDU) could be realized without fracture. Production of parts with vertical sides was made, an accomplishment not seen before in literature on SPIF.

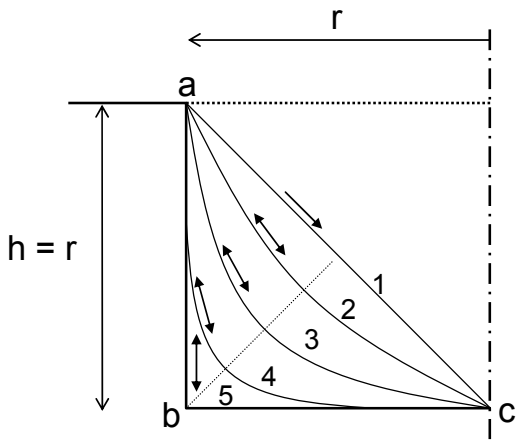

$$\varepsilon_{\phi} = \ln\left(\frac{2r}{r}\right) = \ln(2) \quad (1)$$

$$\varepsilon_{\theta,\max} = \ln\left(\frac{2\pi r}{\pi r}\right) = \ln(2) \quad (2)$$

$$\varepsilon_{t,\max} = -\ln(4) \approx -1.4 \quad (3)$$

Fig. 1: *Five stage forming strategy.*

2.2. Strain paths and fracture

This paper analyzes strain paths for selected representatives of the many different strategies indicated in Fig. 1. This will provide information on the thickness distribution achieved with varying strain paths. It also investigates the strains at fracture and compares these with an analytical model, predicting the fracture line as the forming limit in SPIF, as suggested in earlier work by the authors, [5].

3. Numerical simulation

LS-DYNA version ls971s is adopted to simulate the process using explicit time integration. The forming tool and the backing plate are considered rigid. Time scaling is used simulating the process to be 1500 times faster than the actual experiments in the first stage and 1000 times faster in subsequent stages. Maximum time step is based on a characteristic length equal to shell area divided by the longest diagonal, i.e. no mass scaling is used. As a precaution LS-DYNA applies 0.9 times this value. Fully integrated shells (type 16 in LS-DYNA) are used with five integration points in thickness and mesh refinement is applied in the first stage. Movement of the tool in the simulation is identical to that in the experiments. The sheet material used is AA1050 H111/O and considered isotropic with a stress-strain curve: $\sigma = C\,\varepsilon^{n} = 153\,\varepsilon^{0.25}$ *MPa*, which is determined as the average of 15 tensile tests distributed in directions 0°, 45° and 90° to the rolling direction.

4. Experimental setup

Experiments are conducted on a 3-axis milling machine. All sheets are 1 mm thick and the forming speed is 1000 mm/min. The tool, which has a radius of 6 mm and a semi-spherical tip, is able to rotate freely, but does not rotate during experiments. Diluted cutting fluid is used as lubrication, and the parts are cleaned between each stage to remove loose wear particles. Tool paths are programmed using Pro/ENGINEER. First stage has a fixed vertical step size of 0.5 mm and following stages have a distance between tool paths below 1 mm. The geometries used for the different stages are as shown in Fig. 1, but with h = 70 mm and r = 80.5 mm instead of $h = r$. A small, undeformed section remains in the middle of the workpiece (r = 0-10 mm) since the tool pin of radius 6 mm cannot form a cone with a sharp pointed end. A grid with 2 mm circles is electrochemically etched on the surface of the sheets. This allows measurement of the principle strains assuming the thickness strain ε_t to be a principle strain.

5. Strain and strain paths

The agreement between simulated and experimental shapes for the strategy DDDU is shown in Fig.

2. A residual cone is present after the second stage and it is still present after the fourth stage. Whereas the first three shapes are predicted rather well the simulated shape after the fourth stage is far from the experimental one. A possible explanation to this is a too course mesh due to the large increase in surface area.

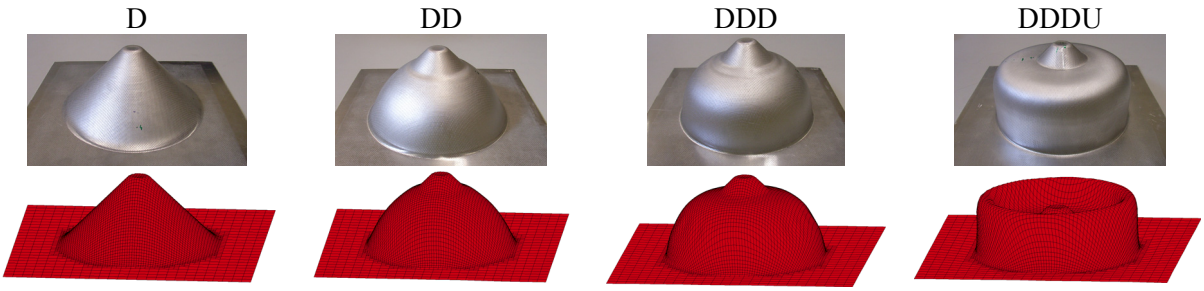

Fig. 2: *Each stage in the strategy DDDU as found in experiments and in simulation.*

5.1. First stage

The first stage can only be performed by downward tool movement. The cone has a constant drawing angle close to 45° and this result in evenly distributed strains, except close to the backing plate and the lowest part of the cone where the radius is approaching the tool radius. Assuming plane strain the meridional strain can be calculated to $\varepsilon_\varphi = 0.35$. This is in good agreement with the plotted strain values in the principle strain space, see Fig. 3.

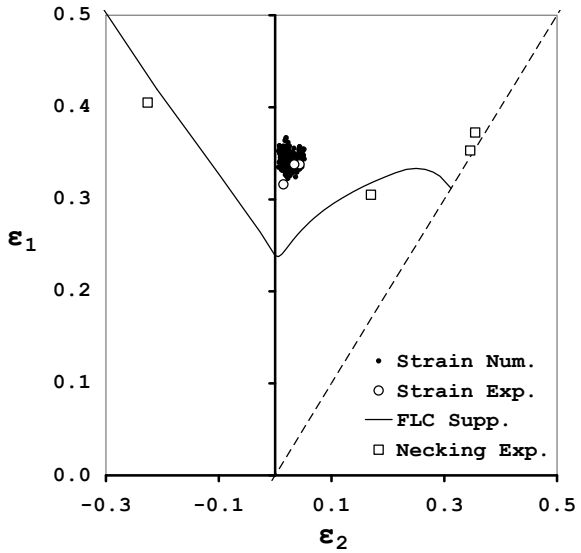

Fig. 3*: Simulated strains after first stage (Z = -10 mm to -60 mm), measured strains, FLC from supplier and experimental necking values.*

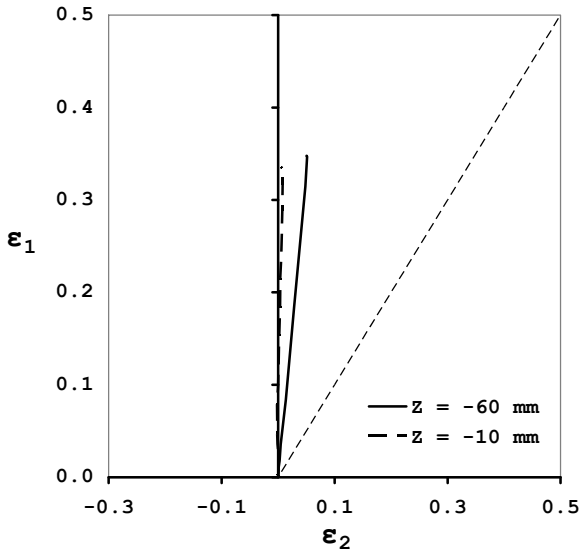

Fig. 4*: Simulated strain paths for element at Z = -10 mm and Z = -60 mm.*

The good agreement between simulated and measured strains indicates, that the surface strains are most likely principle strains, i.e. the deformation is stretching. If deformation was vertical shear or including a large amount of through thickness shear, the surface strains would not be principle strains [6,7]. The strain paths are close to being straight, and the serrated strain path reported by Eyckens et al. [8] is not observed, see Fig. 4. A linear strain path is one of the conditions, which must be fulfilled to adopt the theories for instability proposed by Swift and Hill for isotropic and planar, anisotropic material respectively. According to both theories, the limit before necking in plane strain should be $\varepsilon_1 = n = 0.25$ for the material applied in the present investigation. Applying this value for determining the level of the FLC, good agreement is obtained compared to experimental values for necking found by tensile and bulge tests, and the FLC for same material from material supplier, see Fig. 3. Strains determined after the first forming stage in SPIF are much higher and this supports earlier work by the

authors claming that SPIF is limited by fracture only and not by necking [5].

5.2. Second stage

As regards the two first stages two tool path combinations are possible, i.e. down-down (DD) and down-up (DU). FEM analysis of the strains and strain paths explains the large difference in thickness distribution for the two cases, see Fig. 5. The thickness distribution of DU is almost a mirror image of that of DD having the highest thickness strain near the bottom, Z = -60 mm, where the angle is low. Fig. 6 shows, that the deformation using the DD strategy is close to plane strain, whereas the deformation adopting the DU strategy is close to equal biaxial strain. None of the strain paths are linear, and they all have an initial amount of compression in the direction of ε_1, see Fig. 7. The tendency is that ε_2 increases as ε_1 change a small amount.

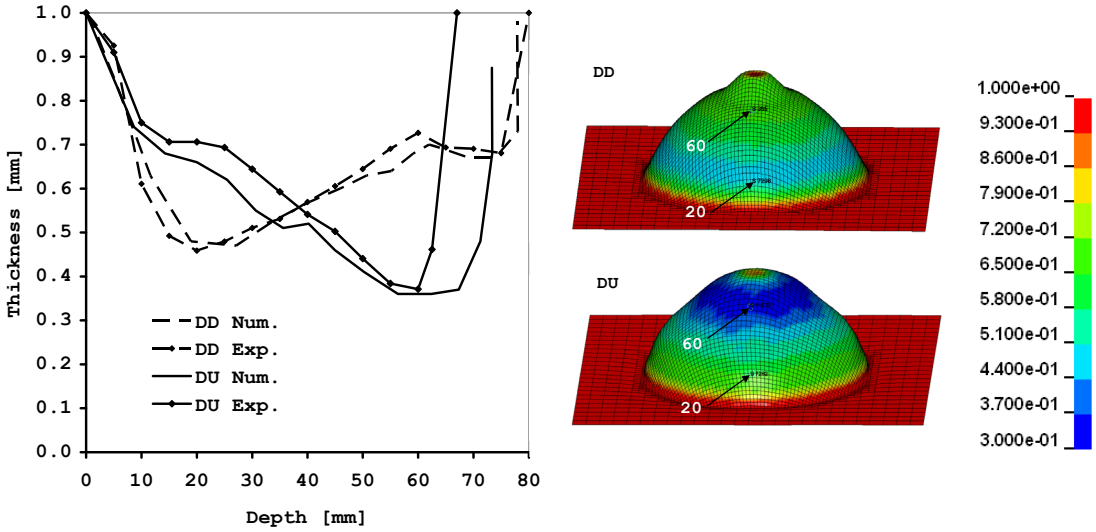

Fig. 5: *Sheet thickness as a function of depth for DD and DU strategy and shapes determined by FE simulation with marking of elements at depths of 20 and 60 mm, scale is thickness in mm.*

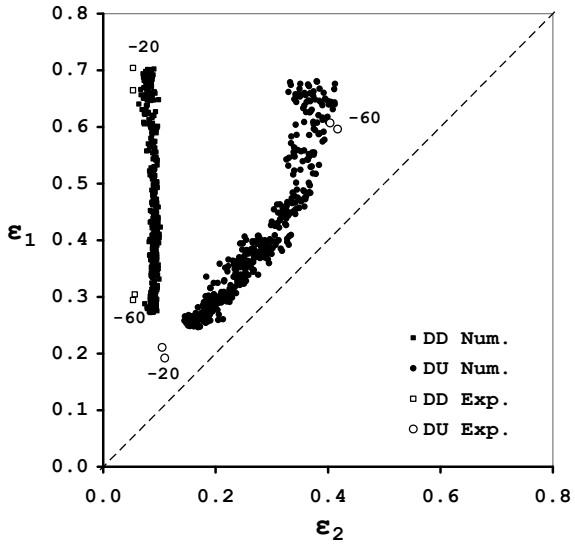

Fig. 6: *Measured and calculated strains for strategies DD and DU in zone -20 < Z < -60 mm.*

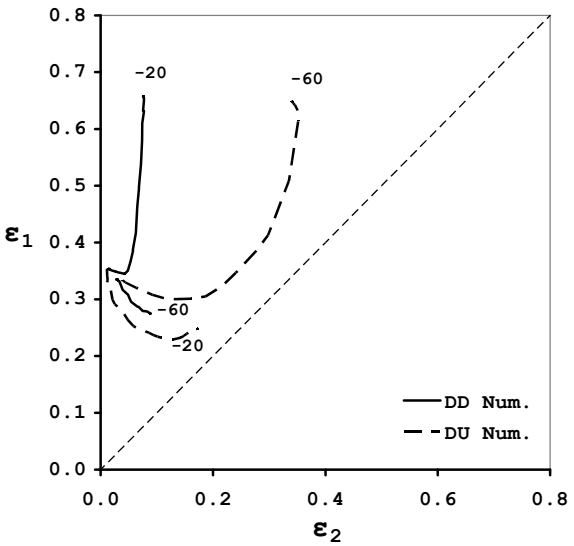

Fig. 7: *Calculated strain paths for elements at Z = -20 mm and Z = -60 mm for strategies DD and DU.*

6. Fracture strains

Fracture strains are measured for the strategies which could not be completed due to fracture, see Table 1. Since no necking occurred, the fracture strains could be measured using the grid technique. All fractures occurred in the fourth stage, indicating that all the strategies investigated distribute the strains more evenly than by single stage deformation, since the geometry of the third stage could not be completed in one stage (strategy #5).

Table 1: Strategies tested and results.

Strategy	**D = down / U = up ( ) = fracture**
#1	DDD(D)
#2	DDDU
#3	DUD(D)
#4	DUD(U)
#5	- - (D) -

Fracture strains are compared with two different, theoretical fracture lines. One is the line of constant thickness strain, i.e. a slope of -1, which has been shown experimentally to describe the forming limits in SPIF rather well. The other is a line with a slope based on ductile damage criterion [5], where the slope can be calculated using Equation (4). To determine the position of the two curves, a cone with section wise increasing angle was formed until fracture. Assuming plane strain, the principal strains may be calculated by volume constancy from the determined angle causing fracture. Based on two experiments the fracture angle is estimated to 77.5°, corresponding to $\varepsilon_1 = 1.5$ and $t = 0.22$ mm. Using Equation (4) this results in a slope of -1.5. Fig. 8 shows a plot of strain values with and without fracture and the two theoretical fracture lines. Strains without fracture are measured as well as simulated for the first three stages (DDD and DUD) and measured for the fourth stage of the DDDU strategy. All these strains representing no fracture are below both fracture lines. The fracture line based on constant thickness strain seems to give a better fit than the fracture line calculated from the ductile damage criterion. The points showing poorest fit are from strategy #4. This could indicate that fracture strains from an upwards tool path are different from a downwards tool path. In Fig. 9 a 10% uncertainty interval is placed around the fracture line based on constant thickness strain. All fracture strains are located within this interval, except those from strategy #4, and all strain points without fracture are outside.

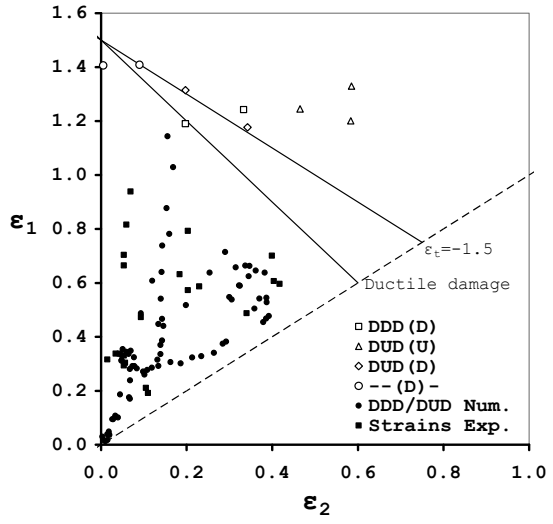

Fig. 8: *Experimental strains and fracture lines.*

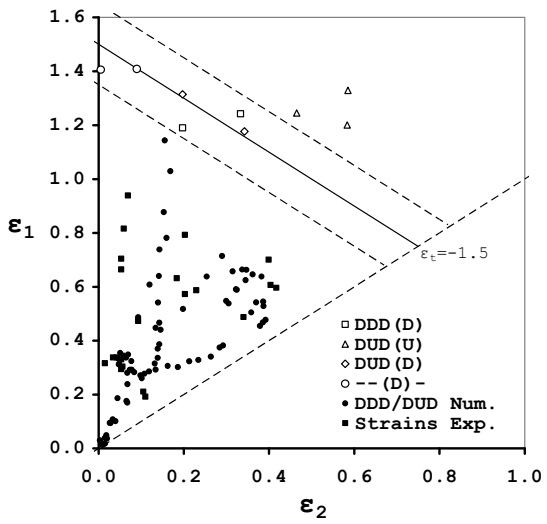

Fig. 9: *Experimental strain points and fracture line for constant thickness strain with a 10% uncertainty interval.*

$$\frac{\varepsilon_1^{biaxial} - \varepsilon_1^{plane\ strain}}{\varepsilon_2^{biaxial} - 0} = \frac{\Delta\varepsilon_1}{\Delta\varepsilon_2} = -\frac{5\left(\frac{r_{tool}}{t}\right) - 2}{3 \cdot \left(\frac{r_{tool}}{t}\right) + 6} \tag{4}$$

Conclusion

The results show good agreement between measured and simulated strain and strain paths. The direction of forming has huge effect on thickness distribution and position of strain points in the principle strain space. Tool paths going upwards imply more biaxial strains than downwards tool paths. With some uncertainty strains are limited by a fracture line with a slope of -1 indicating that the fracture line, on the contrary to the necking line, is not very dependent of strain paths. Strain paths are linear in the first stage, and highly non-linear in the following ones. Surface strains match the deformation as being stretching. Achieved strains are much higher than experimental values for necking in conventional sheet forming tests. Results in general support the theory that SPIF is limited by fracture and not necking [5].

Acknowledgements

The first author would like to thank Otto Mønsteds Fond, Oticon Fonden and Augustinus Fonden for financially supporting his stay at Instituto Superior Tecnico February – May 2008. The second and third author would like to acknowledge PTDC/EME-TME/64706/2006 FCT/Portugal for the financial support.

References

[1] Kitazawa, K. and Nakane, M.: Hemi-ellipsoidal stretch-expanding of aluminum sheet by CNC incremental forming process with two path method, Keikinzoku/Journal of Japan Institute of Light Metals, 47, 1997, 440-445.
[2] Jeswiet, J. and Hagan, E.: Rapid proto-typing of a headlight with sheet metal, Technical Paper - Society of Manufacturing Engineers, 2002, 1-6.
[3] Verbert, J., Belkassem, B., Henrard, C., Habraken, A. M., Gu, J., Sol, H., Lauwers, B., and Duflou, J. R.: Multi-Step toolpath approach to overcome forming limitations in single point incremental forming, ESAFORM 2008, 11th conference on material forming, 2008.
[4] Skjoedt, M., Bay, N., Endelt, B., and Ingarao, G.: Multi stage strategies for single point incremental forming of a cup, ESAFORM 2008, 11th conference on material forming, 2008.
[5] Silva, M. B., Skjoedt, M., Atkins, A. G., Bay, N., and Martins, P. A. F.: Single-point incremental forming and formability-failure diagrams, Journal of Strain Analysis for Engineering Design, 43, 2008, 15-35.
[6] Allwood, J. M., Shouler, D. R., and Tekkaya, A. E.: The increased forming limits of incremental sheet forming processes, Key Engineering Materials, 2007, 621-628.
[7] Emmens, W. C. and van den Boogaard, A. H.: Strain in shear and material behaviour in incremental forming, Key Engineering Materials, 2007, 519-526.
[8] Eyckens, P., He, S., Van Bael, A., Van Houtte, P. and Duflou, J.: Forming Limit Predictions for the Serrated Strain Paths in Single Point Incremental Sheet Forming, AIP Conference Proceedings - American Institute of Physics, 2007, 141-146.

The end!